USTC & ICRANet & UNIFE

A dissertation for doctor's degree

Multiscale Energy Transport and Evolution of Compact Objects in Astrophysical Environments

Author: Shu-Rui Zhang

Speciality: Astrophysics

Supervisor: Prof. Ye-Fei Yuan

Prof. Remo Ruffini

Prof. Jorge Rueda

Completion date: October 22, 2025

ABSTRACT

Astrophysical black holes (BHs) are an active area of research from both theoretical and observational perspectives, each offering crucial insights into the most extreme physics in the universe. This thesis studies both sides. On the theoretical side, the concept of irreducible mass ($M_{\rm irr}$) is a fundamental quantity in BH physics. It plays a key role in the dynamics of BHs, particularly in energy extraction and accretion processes. By examining how the irreducible mass evolves during these processes, we can deepen our understanding of the reversibility and geometric properties of BHs in astrophysical settings. Observationally, supermassive black holes (SMBHs) act as central engines that power the most luminous objects in the universe—active galactic nuclei (AGNs). Meanwhile, a large population of stellar-mass BHs in nuclear star clusters may interact with AGN disks. In particular, gravitational wave detections have sparked growing interest in compact objects embedded in AGN disks. By studying the accretion and dynamical behavior of these compact objects in such environments, we can investigate their ultimate fate and interpret the associated multi-wavelength and multi-messenger signatures.

After providing a background introduction to AGNs and compact objects in the first Chapter, Chapter 2 begins with a discussion of energy extraction from BHs, starting with the well-known Penrose process. We are interested in the change in transformable energy (the rotational part of the mass-energy the a Kerr BH) because it can indicate how the 'reservoir' of BH energy shrinks or expands. We found that the change of transformable energy depends not only on the change of BH mass but also on the increased amount of $M_{\rm irr}$ of BH. During the energy extraction process, M decreases, but $M_{\rm irr}$ increases, both of which lead to a contraction of the transformable energy. As a result, the total energy that can actually be extracted from a BH is less than it would be if no feedback had been considered. Specifically, for an extreme Kerr BH and in the limit $\mu/M \to 0$, all the reduced transformable energy goes into the $M_{\rm irr}$, resulting in high irreversibility. For non-extreme Kerr BHs, the effective potential of particle motion on the equatorial plane in Kerr spacetime is analyzed, and it is demonstrated that the Penrose process can only be undergone by BHs with the dimensionless spin $\hat{a} > 1/\sqrt{2}$ if the decay point coincides with the turning point. Based on that, the lower limit of the change in $M_{\rm irr}$ is provided as a function of the dimensionless spin of the BH.

In Chapter 3, we examine BH accretion, where both the mass and irreducible mass increase. Thus, in contrast to extraction, accretion adds rotational energy to the BH, making it essential to quantify the growth of both mass and irreducible mass. We start with the simplest but widely used model of accretion from the ISCO. We calculated the ratio of mass growth to irreducible mass growth as a function of the dimensionless spin, finding that this ratio increases with spin, reaches a peak near extremal value, then decreases, and ultimately equals the ratio of the BH's mass to its irreducible mass at the extremal limit ($\hat{a} = 1$). This indicates that the dimensionless spin will stabilize at the extremal value, entering a phase of self-similar growth. In reality, however, GWs emitted during the inspiral of massive objects (e. g. EMRIs) carry away energy and angular momentum, causing the dimensionless spin to stabilize before reaching the extremal limit and to enter a self-similar growth phase if the mass ratio of the inspiraling particles is fixed. For the first time, using BH perturbation theory, we accurately computed the stable dimensionless spin and derived an analytical formula for its dependence on the mass ratio.

In Chapter 4, we begin the second part of the thesis—compact objects in AGN disks. A comprehensive analysis of the accretion processes of various compact objects embedded in AGN disks is presented.

In Chapter 5, we discuss white dwarfs (WDs) in AGN disks. Accretion-induced collapse is unlikely, as WDs could reach the mass-shedding limit during accretion. This motivates us to investigate their dynamical evolution. By analyzing dynamical processes in close encounters within AGN disks, we find that Jacobi capture in their inner regions can lead to WD-WD collisions, triggering thermonuclear explosions. We simulate the trajectories of the resulting explosion ejecta and calculate their energy transformation, obtaining the corresponding observational features. Due to the influence of both the AGN disk and the SMBH, this transient event differs from typical SN Ia explosions. The explosion energy of SN Ia is primarily stored as kinetic energy within the ejecta. Since the inner regions of AGN disks are typically geometrically thin, the ejecta are not efficiently decelerated and can thus escape from the disk. However, under the gravitational influence of the SMBH, a significant portion of the ejecta eventually falls back onto the AGN disk. The fallback occurs over a dispersed time and spatial distribution, allowing efficient interactions with the disk gas and converting kinetic energy into thermal energy. This process produces a characteristic light curve: a rapid rise followed by a decay obeying $L \propto t^{-2.8}$. The transient timescale ranges from a few hours to several months, depending on the mass of the SMBH. The subsequent disruption of the disk may lead to the changing-look AGN phenomenon. The high-energy radiation generated by the impact of fallback debris on the disk material primarily spans from hard X-rays to soft γ-rays, with luminosities reaching up to $\sim 10^{43}$ erg s^{-1}, making it a promising target for future MeV detectors. Moreover, debris from WD collisions may significantly enhance heavy-element production in AGNs, potentially turning AGNs into factories of chemical enrichment.

In Chapter 6, we investigate neutron stars (NSs) in AGN disks. We analyze the characteristic effects in both AGN disks and NSs, determining the NS accretion rates, feedback mechanisms, and multimessenger signatures. We classify potential accretion modes of NSs in AGN disks, proposing a hierarchical model of NS accretion: accretion flow from the Bondi scale to the accretion column. NS accretion in AGN disks differs from that of BHs, particularly within the magnetosphere, due to the NS's hard surface and possibly strong magnetic field. As accreting material approaches the magnetosphere, the magnetic field channels the inflow into accretion columns, primarily dominated by neutrino cooling. While neutrinos emitted from individual NS accretion events may not be directly detectable, their cumulative contribution could form a sub-MeV neutrino background comparable to that from supernovae. Furthermore, NS accretion may induce mass quadrupole moments, generating GWs characterized by periodic modulations and echoes, which could be observed by third-generation GW detectors. The emission of neutrinos and GWs extracts energy and angular momentum from the accreting material, reducing feedback on the AGN disk. This leads to an exceptionally high NS accretion rate, resulting in a collapse timescale shorter than the migration-merger timescale, making binary NS mergers in AGN disks less likely.

Lastly, in Chapter 7, we report on a binary BH merger candidate, LVK S241125n, which is probably associated with a short gamma-ray burst (GRB) and X-ray afterglow emission. We model it as radiation linked to a binary BH merger in an AGN disk, where the remnant rapidly accretes surrounding disk material at hyper-Eddington rates. The jet launched in this process may give rise to the GRB observed in coincidence with the GW signal. This GRB, captured by Swift-BAT, displays a Comptonized spectrum characterized by an unusually soft photon index—consistent with emission arising from jet–disk interaction in a dense AGN environment. The accompanying X-ray afterglow exhibits an unusually hard spectral shape, suggesting strong absorption due to a high column density commonly found in AGN disks. We also highlight the importance of further fitting the orbital eccentricity of the merger and conducting deep-field observations of the host galaxy to test our explanation.

KEY WORDS: Active Galactic Nucleus (AGN), Accretion Disk, Black Hole (BH), Neutron Star (NS), White Dwarf (WD), Mutimessenger

Contents

Notation

G	The gravitational constant
c	The speed of light in vacuum
m_{H}	The hydrogen atomic mass
m_{p}	The proton mass
m_{e}	The electron mass
σ_{T}	The Thomson cross-section
k_{B}	The Boltzmann constant
$M_{\odot}$	The solar mass
$R_{\odot}$	The solar radius
M_{SMBH}	The mass of SMBH
R_{g}	The gravitational radius of SMBH
$\dot{M}$	The accretion rate of SMBH
$\dot{M}_{\mathrm{Edd}}$	The Eddington accretion rate of SMBH
$\tilde{R}$	The AGN disk radius
$\tilde{H}$	The scale height of AGN disk
$\tilde{\rho}_{\mathrm{c}}$	The middle plane density of AGN disk
$\tilde{T}_{\mathrm{c}}$	The middle plane temprature of AGN disk
$\tilde{\alpha}$	The viscosity of AGN disk
m_{bh}	The mass of sBH
m_{ns}	The mass of NS
m_{wd}	The mass of WD
r_{g}	The gravitational radius of sBH
r_{ns}	The radius of NS
r_{wd}	The radius of WD
r_{Hill}	The Hill radius

Abbreviations

AGN Active Galactic Nucleus

NSC Nuclear Star Cluster

CO Compact Object

BH Black Hole

NS Neutron Star

WD White Dwarf

sBH stellar-mass Black Bole

IMBH Intermediate-Mass Black Hole

SMBH supermassive black hole

BBH Binary Black Hole

EMRI Extreme Mass Ratio Inspiral

IMRI Intermediate Mass Ratio Inspiral

GW Gravitational Wave

EM Electromagnetic

SED Spectral Energy Distribution

GRB Gamma Ray Burst

FRB Fast Radio Burst

TDE Didal Disruption Event

SN / SNe Supernova / Supernovae

IMF Initial Mass Function

AIC Accretion-Induced Collapse

ISM Interstellar Medium

AI Artificial Intelligence

ML Machine Learning

Chapter 1 Introduction

1.1 Brief Introduction of AGN

The development of radio astronomy led to the discovery of active galaxies. The spectral measurement of the optical counterpart of the radio source 3C 273 by Schmidt (1963) first revealed that quasars are at cosmological distances. Observations across multiple electromagnetic wavelengths have revealed that approximately 2% of galaxies in the universe exhibit intense activity, referred to as active galaxies. The characteristic scales of these activities typically range from tens of light-minutes to light-hours, with some extending up to light-years. This suggests that the activity is primarily confined to a very small region near the galactic nucleus, known as an active galactic nucleus (AGN).

1.1.1 Observation of AGNs

AGNs generally share several common electromagnetic observational characteristics, including (Beckmann et al., 2012): (1) A bright and compact nuclear region; (2) Variability in radiation intensity over time (i.e., exhibiting flux variations); (3) Continuous non-thermal emission, often with pronounced bumps in the infrared and blue optical bands; (4) The presence of atomic and ionic emission lines, including forbidden lines; (5) Stronger emission across the radio, infrared, X-ray, and gamma-ray bands compared to typical galaxies.

In addition to their common characteristics, different types of active galaxies exhibit distinct observational features. They are generally classified into two main categories through radio classification: radio-quiet and radio-loud AGNs.

- The radio-quiet category includes Low-Ionization Nuclear Emission-Line Regions (LINERs), Seyfert galaxies (Seyfert 1 and Seyfert 2), and radio-quiet quasars. It also includes a newly identified type, known as ”Little Red Dots (LRDs) (e.g., Latif et al., 2025).”
- The radio-loud category includes radio-loud quasars, blazars (which comprise BL Lac objects and Optically Violent Variable (OVV) quasars), and radio galaxies. Note that some LINERs may also be radio-loud (e.g., Chiaberge et al., 2005).

Their key observational characteristics are summarized in the Table 1.1.

Apart from the characteristics listed in the table, LRDs exhibit several notable features. They are characterized by a red optical continuum, and most are extremely compact—on average, only about 2% the radius of the Milky Way(Labbe et al., 2025). They appear remarkably clean, with almost no surrounding gas(Chen et al., 2025a). LRDs are found to be ∼1 - 2 orders of magnitude more abundant than luminous quasars at redshifts $z \sim 4$–7 (e.g., Kocevski et al., 2025). They also display a distinctive V-shaped spectral energy distribution (SED) with a turnover wavelength near the Balmer limit, (e.g., Kocevski et al., 2023). Interestingly, the occurrence of star formation in the outer regions of the AGN disk has been proposed as a possible explanation for a "V"-shaped SED (Zhang et al., 2025a), even though LRDs do not show evidence of significant gas extinction (Chen et al., 2025a), as is typical in normal AGNs.

Table 1.1 Features of different types of galaxies

Galaxy type	Active nuclei	EmissionLines Narrow	Broad	X-rays	Excess UV	Excess Far-IR	Strong radio	Jets	Variable
Non-AGN	no	weak	no	weak	no	no	no	no	no
LINER	?	weak	weak	weak	no	no	some	some	no
Seyfert I	yes	yes	yes	some	some	yes	few	no	yes
Seyfert II	yes	yes	no	some	some	yes	few	no	yes
Quasar	yes	yes	yes	some	yes	yes	some	some	yes
Blazar	yes	no	some	yes	yes	no	yes	yes	yes
BL Lac	yes	no	no/faint	yes	yes	no	yes	yes	yes
OVV	yes	no	> BL Lac	yes	yes	no	yes	yes	yes
Radio galaxy	yes	some	some	some	some	yes	yes	yes	yes
LRDs	yes	?	yes[a]	no[b]	some[c]	no[d]	no[e]	?	no[f]

Note. a Greene et al. (2024); b Ananna et al. (2024); c Tee et al. (2025); d Chen et al. (2025a); e Latif et al. (2025); f Kokubo et al. (2024).

In addition, the emergence of multi-messenger observations of AGNs in recent years has attracted increasing attention, despite their continuing rarity. Notable examples include the detection of a 79 TeV neutrino from NGC 1068 (IceCube Collaboration et al., 2022) and the possibility that the gravitational wave (GW) source GW190521 originated from an AGN (e.g., Samsing et al., 2022). Additionally, LHAASO has, for the first time, observed very high-energy photons from the low-luminosity AGN NGC 4278 (Cao et al., 2024). Furthermore, quasars have been found to exhibit super-solar metallicity that shows little evolution with redshift (e.g., Warner et al., 2003; Nagao et al., 2006; Shin et al., 2013; Du et al., 2014; Maiolino et al., 2019). Moreover, AGNs may not always remain active but could transition between different states, leading to the so-called "changing-look" AGNs (e.g., Ricci et al., 2023). Quasi-periodic oscillations (QPOs) and quasi-periodic eruptions (QPEs) have also been identified in AGNs (Song et al., 2020; Miniutti et al., 2023). These new observations have expanded our traditional understanding of AGNs, driving deeper exploration into their nature and underlying physical processes.

1.1.2 The Unified Model of AGNs

The differences among various types of AGNs may arise from differences in the central black hole mass and accretion rate, as well as the presence or absence of relativistic jets. These differences may also result from varying observational perspectives —meaning that AGNs could be intrinsically the same, but appear different depending on the viewing angle, as illustrated in Fig. 1.1. The unified model of AGNs proposes that AGNs consist of the following components:

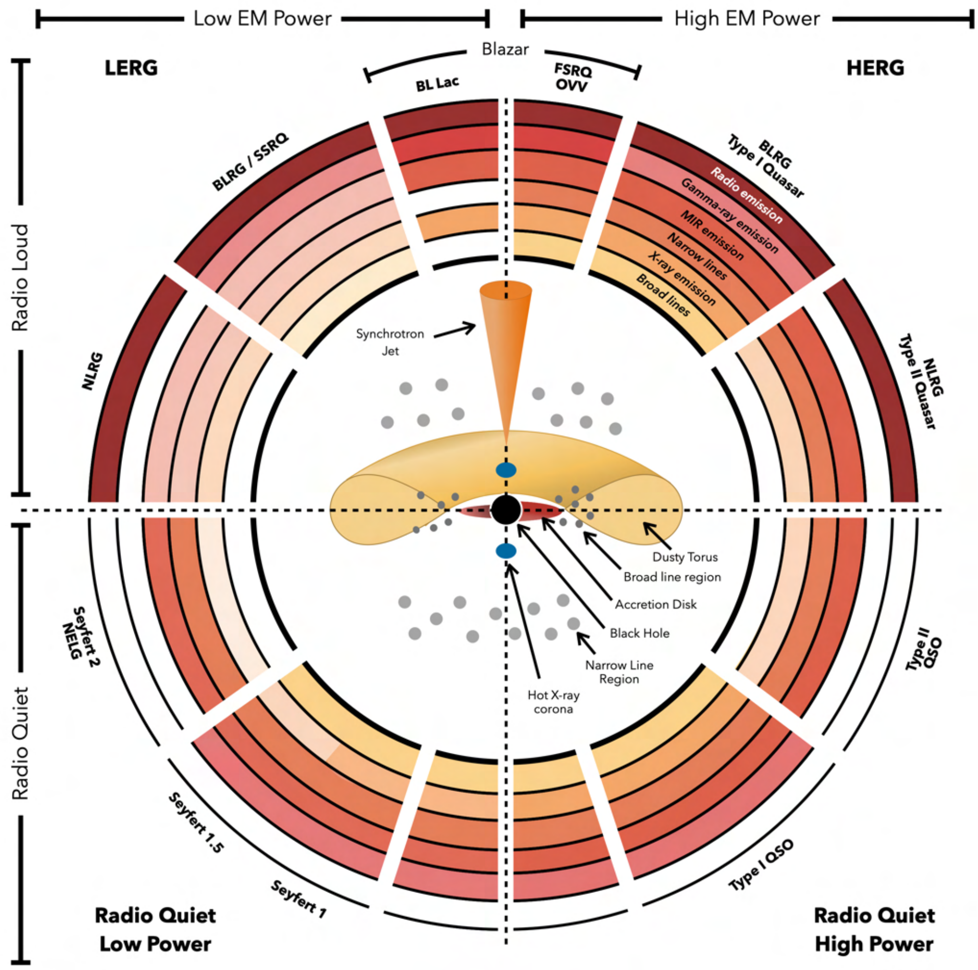

Figure 1.1 The schematic diagram of the AGN unified model. Note that the NSC is not depicted. The figure is taken from Thorne et al. (2022).

(1) **Supermassive Black Hole (SMBH)**: At the center of an AGN lies a SMBH with a mass ranging from 10^5 to $10^9 M_\odot$. Some studies also suggest the possible existence of binary black hole systems within AGNs (Graham et al., 2015).

(2) **Accretion Disk**: The accretion disk surrounding the central SMBH can extend

up to $\sim 10^4 R_g$, emitting radiation from optical to X-ray wavelengths (see Chapter 4 for a detailed discussion of the physical parameters).

(3) **Corona**: The corona is a region of highly ionized plasma, typically located a few to a few dozen gravitational radii from the SMBH. It is a magnetically confined plasma structure (e.g., Bisnovatyi-Kogan et al., 1977; Sunyaev et al., 1980), where hot electrons upscatter optical and ultraviolet photons from the accretion disk via inverse Compton scattering, producing X-ray emission (Haardt et al., 1993).

(4) **Broad-Line Region (BLR)**: The BLR is typically composed of discrete cloud structures with electron densities of $n_e \sim 10^9 - 10^{10}\ \mathrm{cm}^{-3}$. It is located within a region approximately 0.1 to a few parsecs from the SMBH, where the gas clouds can reach orbital velocities of up to $v_{\mathrm{BLR}} \sim 10^4$ km/s. The emission lines from this region exhibit significant Doppler broadening.

(5) **Narrow-Line Region (NLR)**: The NLR is situated farther from the SMBH than the BLR, extending over several parsecs. The electron density in the NLR is about $10^5\ \mathrm{cm}^{-3}$, and the gas clouds orbit the SMBH at velocities of $v_{\mathrm{NLR}} \sim 10^2 - 10^3$ km/s. The lower velocities of the gas produce less Doppler broadening compared to those in the BLR, leading to the formation of narrow emission lines.

(6) **Dusty Torus**: The torus is a ring-like structure composed of dust and molecular material, typically extending from the outer region of the accretion disk to scales of a few parsecs to hundreds of parsecs (e.g., Isbell et al., 2022). It absorbs radiation from the central source and re-emits it primarily in the infrared.

(7) **Relativistic Jets**: Jets are collimated outflows composed of high-energy particles and radiation (Blandford et al., 1982), extending from 0.1 to 10^6 parsecs. Nonthermal radiation processes within the jet, such as synchrotron radiation and inverse Compton scattering, play crucial roles in shaping the broadband emission spectrum.

In addition, most galaxies host an extremely dense and massive **Nuclear Star Cluster (NSC)** at their center, with a characteristic radius of a few parsecs. As shown in the Fig. 1.2, the NSC supplies the AGN core with a large number of stars and objects, which are typically neglected in the unified model. For instance, within 0.1 pc of our Galactic Center, observations have revealed thousands of stars (von Fellenberg et al., 2022), and reproducing the quasi-thermal distribution of the S-star orbital eccentricities requires $\gtrsim 1000$ black holes in this region (Antonini, 2014). Typically, the NSC dominates in low-mass galaxies, while the SMBH takes the lead in high-mass galaxies; they exhibit different scaling relations to the mass of the host galaxy (Scott et al., 2013). Nevertheless, both the NSC and the SMBH typically coexist in the galactic nucleus, and their masses generally exhibit a positive correlation with the mass of the host galaxy (Neumayer et al., 2020). The dynamical evolution and stellar distribution within the NSC are influenced by the SMBH and other components of the galaxy. Taking the NSC into account, along with the large number of stars and compact objects in the AGN disk, is essential for a complete understanding of the physical processes in AGNs. Including the NSC is necessary for making accurate predictions and explanations of the rich observational effects of AGNs and refining the unified model of AGNs.

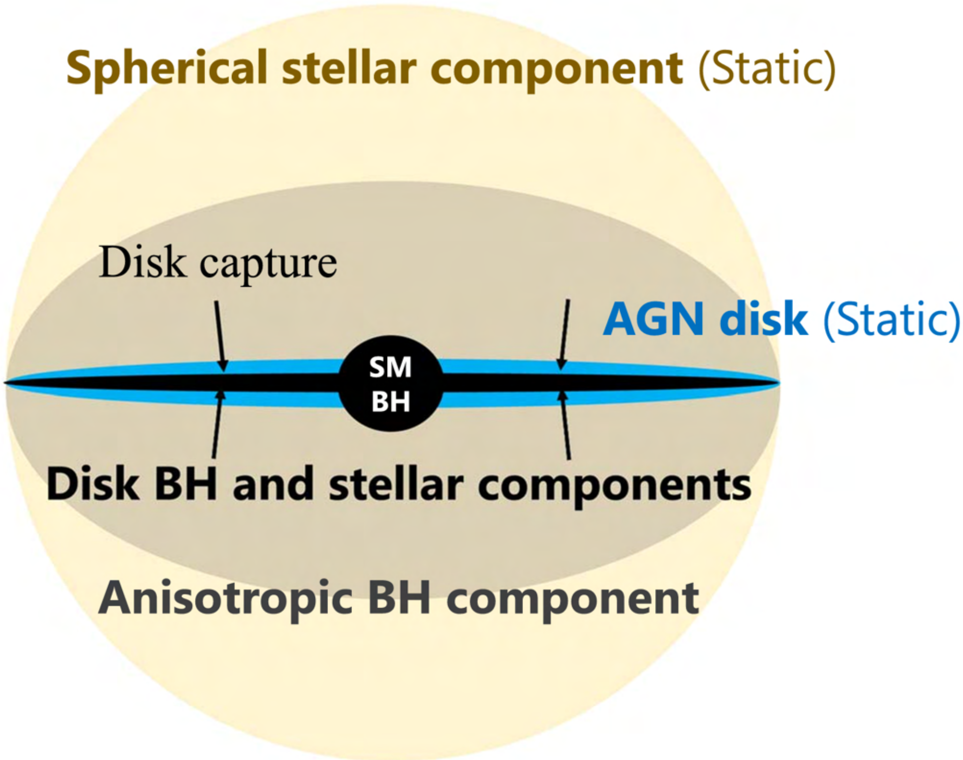

Figure 1.2 Schematic diagram of an AGN including the NSC component, which contains stars and sompact objects. The figure is taken from Tagawa et al. (2020).

1.2 Brief Introduction of Compact Objects

Compact objects (COs) have compactness in the range $10^{-4} \lesssim \mathcal{C} \leqslant 1$, where $\mathcal{C} \equiv \frac{G m_{\rm CO}}{r_{\rm CO} c^2}$. The most common types of COs include black holes (BHs), neutron stars (NSs), and white dwarfs (WDs).

1.2.1 Black Holes

Black holes are solutions to Einstein's field equations. Within the framework of classical general relativity, a physically meaningful black hole is fully described by three quantities: mass, spin, and charge—an idea encapsulated in the "no-hair theorem" (Hawking, 1972), as illustrated in the left panel of Fig. 1.3. If both spin and charge are zero, the solution corresponds to a Schwarzschild black hole (Schwarzschild, 1916). If only spin is zero, the solution corresponds to a Reissner-Nordström black hole (Reissner, 1916; Nordström, 1918). If only charge is zero, the solution corresponds to a Kerr black hole (Kerr, 1963a). In the most general case, where all three quantities are nonzero, the solution corresponds to a Kerr-Newman black hole (Newman et al., 1965).

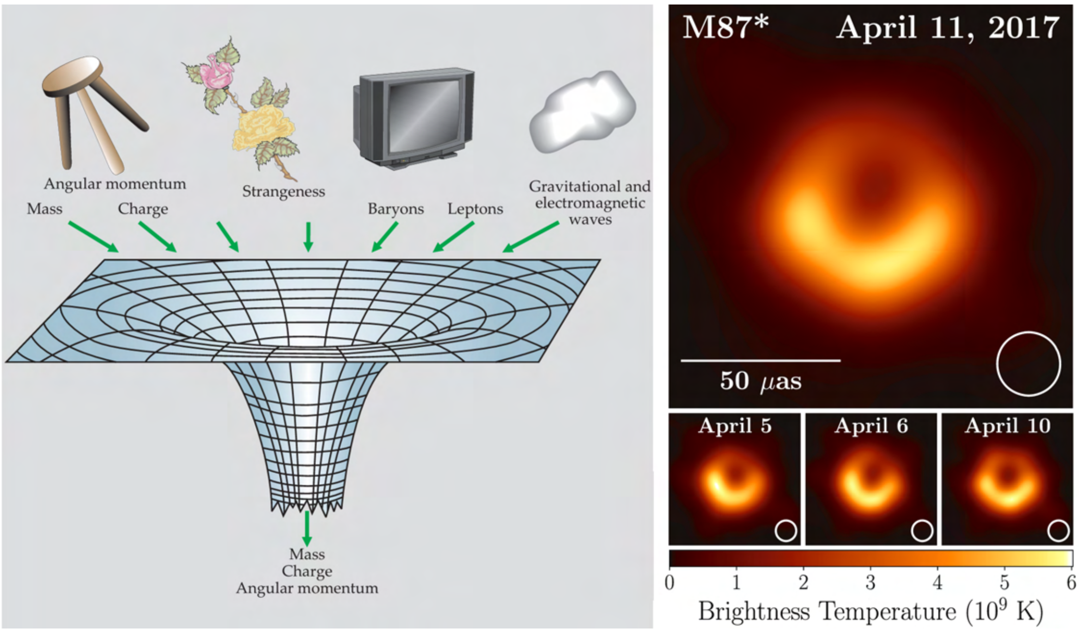

Figure 1.3 Left: The concept of black holes as introduced by Ruffini et al. (1971b). Right: The first image of the black hole M87*, obtained using a global very long baseline interferometry array (Event Horizon Telescope) observing at a wavelength of $\lambda = 1.3\,\mathrm{mm}$. The color bar indicates the brightness temperature $T_{\mathrm{B}} = \frac{S\lambda^2}{2k_{\mathrm{B}}\Omega}$, where S is the flux density, k_{B} is the Boltzmann constant, and Ω is the solid angle of the resolution element (Event Horizon Telescope Collaboration et al., 2019).

Noteworthy, when studying the reversibility of test particle motion in black hole spacetimes, the concept of irreducible mass was introduced (Christodoulou, 1970; Christodoulou et al., 1971). Like mass, spin, and charge, the irreducible mass is a fundamental physical quantity that can fully describe a black hole when combined with any two of the other three parameters. For example, in the case of a Kerr black hole, the irreducible mass is a nonlinear function of mass and spin, meaning that the Kerr black hole can also be described by its mass and irreducible mass. In some cases, using the irreducible mass to discrible a BH is more convenient, such as in studies of black hole energy extraction processes and their feedback on the black hole itself (Zhang et al., 2024b; Ruffini et al., 2025), since the square of the irreducible mass is directly proportional to the horizon area or entropy of the black hole.

In astrophysics, black holes are categorized into four types based on mass:

- Primordial black holes (PBHs; with masses ranging from much below one solar mass up to $\sim 10^6 M_\odot$)
- Stellar-mass black holes (sBHs; typically a few to tens of solar masses)
- Intermediate-mass black holes (IMBHs; with masses from hundreds to hundreds of thousands of solar masses)
- Supermassive black holes (SMBHs; typically exceeding $10^5 M_\odot$, and can reach billions of solar masses)

In AGN environments, black holes spanning three distinct mass ranges may be present. The most prominent of these is the SMBH located at the center of galaxies. Observational evidence indicates that, except for dwarf galaxies, nearly all galaxies, including AGNs, harbor at least one SMBH at their center. The right panel of Fig. 1.3 displays the first resolved shadow of the SMBH, as imaged by the Event Horizon Telescope (EHT) (Event Horizon Telescope Collaboration et al., 2019). In addition to SMBHs, stellar-mass black holes are known to exist in massive star clusters and could also be present in AGN disks. Furthermore, intermediate-mass black holes may reside in star clusters or AGN disks. As the dominant gravitational source at the center of the galaxy, the SMBH plays a central role in shaping the surrounding environment, accumulating matter, and creating extreme physical conditions, as well as interacting with black holes of other mass scales. Therefore, AGN environments serve as an exceptional natural laboratory for studying the formation, evolution, dynamics, and accretion of black holes, as well as for testing fundamental theories of physics.

1.2.2 Neutron Stars

Neutron stars are formed from the core-collapse supernova explosions of stars with masses in the range of ~ 8–$20 M_\odot$. They may also result from the merger of two white dwarfs (Saio et al., 1985). Neutron stars exhibit several distinctive properties: due to the conservation of angular momentum and magnetic flux, those formed from the collapse of progenitor stars are expected to typically rotate rapidly and possess strong magnetic fields. Additionally, unlike black holes, neutron stars have a solid surface. Structurally, neutron stars are thought to have a layered composition, progressing from the outer atmosphere and ocean to the crust, inner crust, interior, and core. However, the exact state of matter in the core remains uncertain.

The mass range of neutron stars is a key research topic. The neutron degeneracy pressure is the primary 'force' counteracting gravity within a neutron star. As mass increases, gravity strengthens, and if degeneracy pressure can no longer resist gravitational collapse, the neutron star may further collapse into a black hole. Consequently, there exists an upper mass limit for neutron stars, though the precise collapse threshold depends on the equation of state (EoS) of neutron star matter. Since the internal composition of neutron stars is not yet well understood, this upper mass limit remains uncertain. Generally, the maximum mass for non-rotating neutron stars is estimated to be around $2.2 M_{\odot}$, while for rotating neutron stars, it can reach up to $2.9 M_{\odot}$.

The minimum neutron star mass also has significant implications. Unlike the upper limit, the lower mass limit is determined by astrophysical formation processes rather than being an intrinsic property of neutron stars or their equation of state. The best-established formation channels for low-mass neutron stars involve the gravitational collapse of the iron core of massive stars or the O-Ne-Mg core of super asymptotic giant branch (SAGB) stars. Three-dimensional simulations of neutrino-driven supernova explosions suggest that neutron stars with masses $\geqslant 1.19 M_{\odot}$ are expected (Müller et al., 2025), which aligns well with observations—except for XMMU J1732. The compact object in XMMU J1732 has a recently measured mass of $0.77^{+0.2}_{-0.17} M_{\odot}$, and its radius $10.4^{+0.86}_{-0.78}$ km (Doroshenko et al., 2022). While some studies suggest that it could be a strange star (see, e.g., Di Clemente et al., 2022; Horvath et al., 2023), a hybrid star, or a dark matter-admixed neutron star (see, e.g. Sagun et al., 2023; Laskos-Patkos et al., 2024), it is also possible that it is a low-mass neutron star formed from a progenitor star with significant rotation (Zhang et al., 2025b). Nevertheless, further simulations are needed to verify this possibility.

Neutron stars are among the most common multi-wavelength or multimessenger sources in the universe, associated with many exotic explosive events, such as gamma-ray bursts (GRBs), fast radio bursts (FRBs), supernovae, kilonovae, giant flares, and X-ray bursts. For instance, NS formation is associated with supernova explosions and long GRBs, which can produce significant amounts of neutrinos, gravitational waves, and multi-wavelength signals. The merger of neutron star binaries generates gravitational waves, as well as electromagnetic counterparts such as short GRBs and kilonovae, which emit across multiple wavelengths. Accreting neutron stars can produce strong electromagnetic emission and continuous gravitational waves, and, if the accretion rate is super-Eddington, neutrino emission may even dominate, as illustrated in the Fig. 1.4. Notably, these exotic events are not only prevalent in our galaxy but also widely distributed throughout the universe. This raises intriguing questions about the physical processes that neutron stars might undergo across cosmic time and in extreme environments such as AGNs, where strong gravitational fields and high-density gas are present. Many of these research topics remain open and merit further investigation.

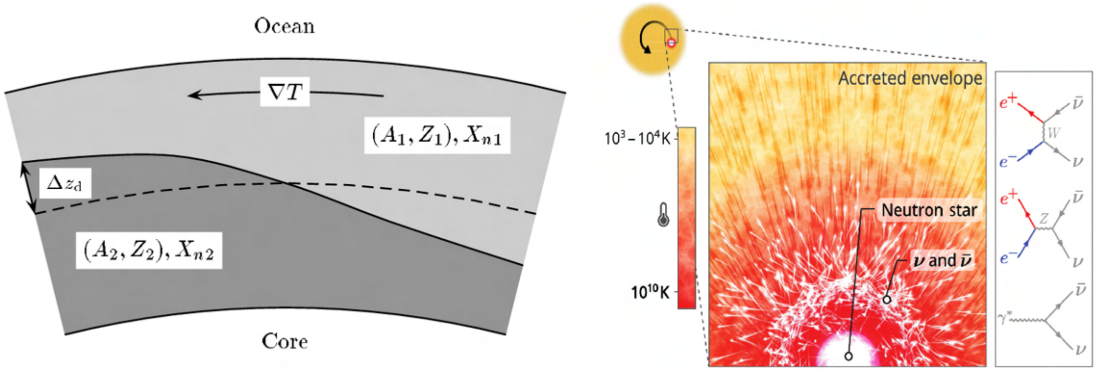

Figure 1.4 Left: Illustration of accretion-induced lateral temperature gradients in the neutron star crust, which cause spatial variation in electron capture depths and lead to a non-axisymmetric mass distribution (Ushomirsky et al., 2000). This non-axisymmetric structure can result in continuous gravitational wave emission when the neutron star is rotating. Right: Neutrino production from super-Eddington accretion onto a neutron star in gas-rich environments, e.g., common envelope systems (Esteban et al., 2025).

1.2.3 White Dwarfs

White dwarfs are the end products of stellar evolution for stars with masses below $\approx 8M_\odot$. Their mass range falls between 0.17 and $1.44M_\odot$, with radii on the order of 10^4 km. Notably, the more massive a white dwarf is, the smaller its radius, following the relation $MV \approx$ constant, where V represents the volume of the white dwarf. The lower mass limit is closely related to stellar evolution pathways and mass-loss processes, while the upper mass limit is determined by the balance between electron degeneracy pressure and gravitational force. As mass increases, the strengthening gravitational force can overcome electron degeneracy pressure, leading the white dwarf to further contract. If its mass exceeds the Chandrasekhar limit ($\approx 1.44M_\odot$), a thermonuclear explosion may be triggered, resulting in a Type Ia supernova.

Type Ia supernovae are explosive events intimately connected to white dwarfs, with most of the released energy stored as kinetic energy in the ejecta. Although only a small fraction of the energy is emitted as electromagnetic radiation, their peak luminosity can be remarkably high. Thanks to the well-established Phillips relation, Type Ia super-

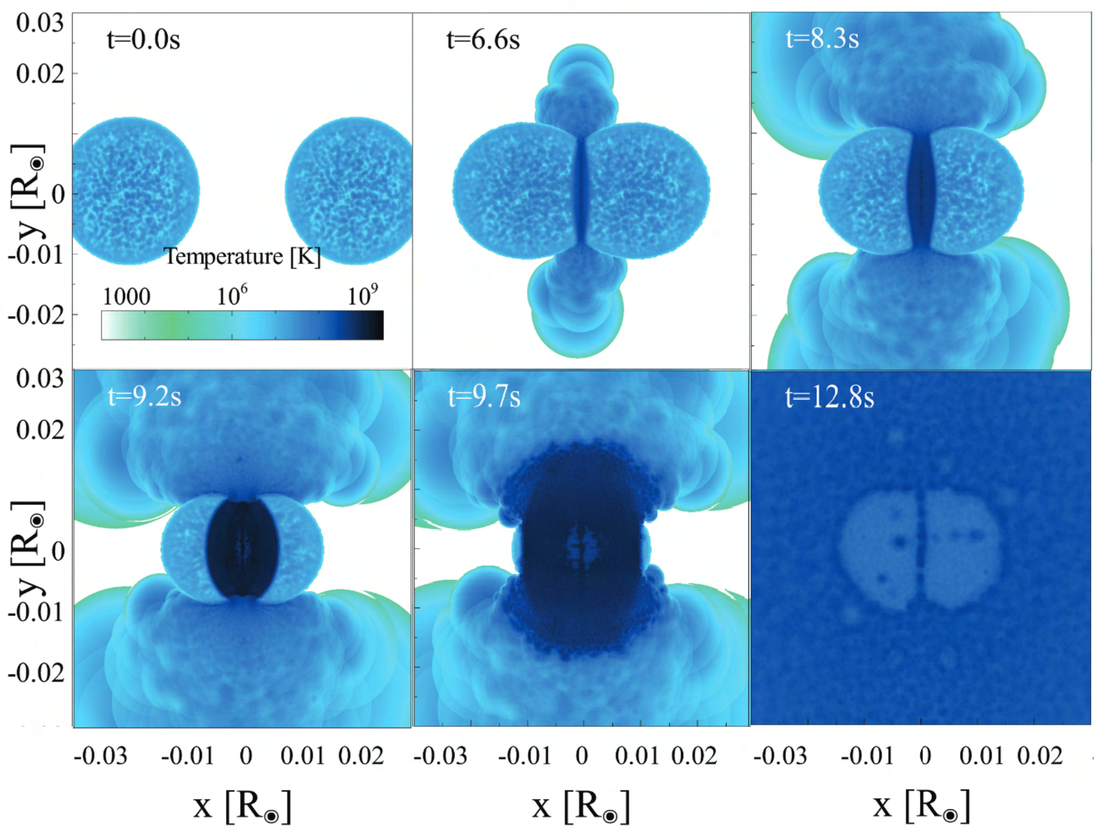

Figure 1.5 A 3D simulation illustrating the head-on collision of two white dwarfs that triggers a thermonuclear explosion. The white dwarfs each have a mass of 0.6 $M_\odot$ and are composed equally of ^{12}C and ^{16}O (Raskin et al., 2009).

novae serve as standard candles for measuring cosmic distances and played a crucial role in the discovery of the accelerating expansion of the universe (Riess et al., 1998; Schmidt et al., 1998; Perlmutter et al., 1999). Nevertheless, their progenitor systems (e.g., Whelan et al., 1973; Hoyle et al., 1960; Webbink, 1984; Taam, 1980; Rosswog et al., 2009; Raskin et al., 2009; Wang et al., 2012) and explosion mechanisms remain subjects of debate (e.g., Hillebrandt et al., 2013; Maoz et al., 2014; McCutcheon et al., 2022).

There are two primary progenitor scenarios for Type Ia supernovae: the single-degenerate and double-degenerate channels. In the single-degenerate scenario, a white dwarf accretes matter from a companion star, which is typically a main-sequence star, subgiant, or red giant. As the white dwarf's mass approaches the Chandrasekhar limit, its core temperature rises, triggering carbon fusion reactions, ultimately resulting in a runaway thermonuclear explosion. In the double-degenerate scenario, a binary white dwarf system loses energy through mechanisms such as gravitational wave radiation, causing the orbit to decay and eventually leading to a merger. If the total mass of the system exceeds the Chandrasekhar limit, a thermonuclear explosion can also occur.

Merging white dwarf binaries are also key targets for space-based gravitational wave detectors such as LISA. Additionally, in some cases, two white dwarfs may directly collide, triggering a thermonuclear explosion even if their combined mass does not exceed the Chandrasekhar limit, as shown Fig. 1.5. Such collisions are more likely to occur in triple systems, where dynamical interactions can drive white dwarf mergers. Intriguingly, AGN disks may serve as natural sites for white dwarf collisions. As discussed below, AGN disks may host a high number density of compact objects, and the confinement of these objects within the disk plane could significantly enhance the probability of collisions.

1.3 Stars and Compact Objects in AGN Disks

The presence of stars or compact objects in AGN disks has increasingly attracted the attention of astronomers. This is due to the relatively high GW detection rate by LIGO-Virgo-KAGRA (LVK), the statistical properties of merging binary systems (e.g., mass, mass ratio, and effective spin), and the detection of super-solar metallicity in AGNs (e.g., Warner et al., 2003; Nagao et al., 2006; Shin et al., 2013; Du et al., 2014; Maiolino et al., 2019), all of which point towards the potential existence of compact objects in AGN disks. The higher-density gas environment in AGN disks, the presence of SMBH at the center, the dense stellar population in nuclear star clusters, and the star formation in the outer regions of AGN disks all affect the formation, capture, accretion, evolution, and dynamics of various types of compact objects. These factors may lead to rich multi-band, multi-messenger observational effects (e.g., Tagawa et al., 2020; Wang et al., 2021a,b). In particular, gravitational wave source GW190521 was discovered with its suspected host, the quasar SDSS J1249+3449 (Graham et al., 2020); the masses of the two merging black holes (85 $M_\odot$ and 66 $M_\odot$) are within the upper mass gap (Abbott et al., 2020), and the pre-merger orbital eccentricity is non-zero (Abbott et al., 2020; Romero-Shaw et al., 2020; Samsing et al., 2022), driving a significant upturn in research interest. The focus of current studies on stars and compact objects in AGN disks can be summarized in the following key areas:

1.3.1 Stellar Evolution in AGN Disks

In this section, we first introduce the formation and evolution of stars in AGN accretion disks. We then summarize the possible outcomes of stellar evolution on the disk, including the formation of compact objects and their contributions to nucleosynthetic yields.

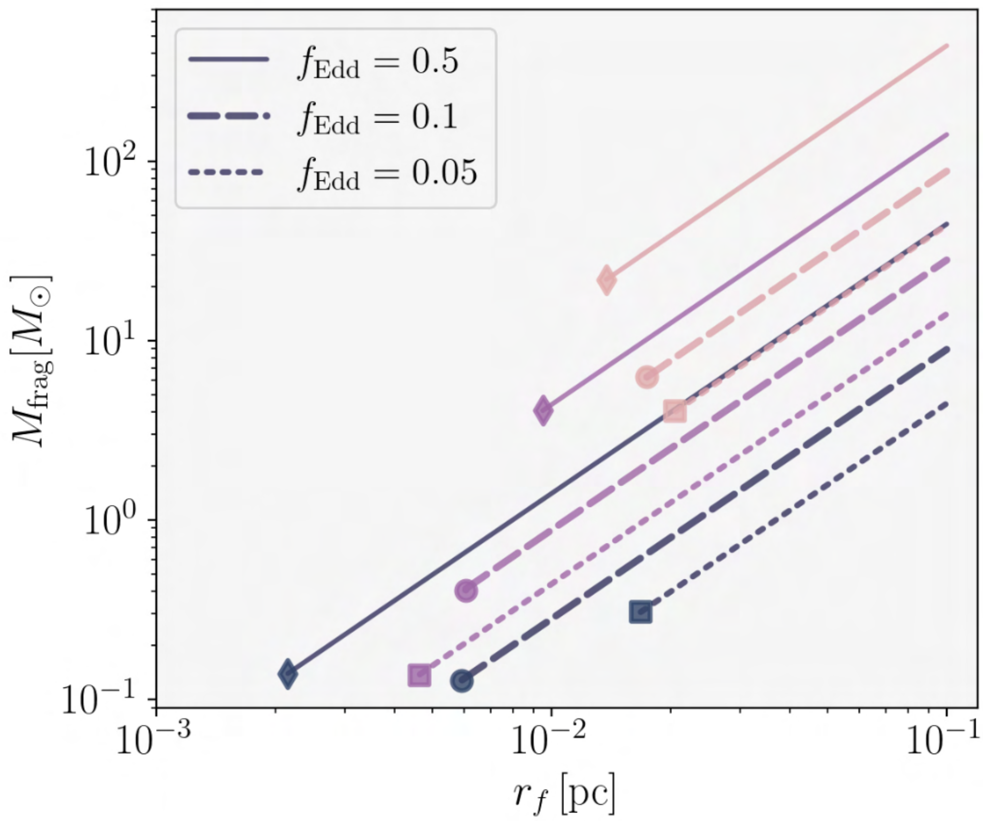

Figure 1.6 The characteristic mass of fragments varies with the disk radius in the region where fragmentation conditions are met. Disks surrounding more massive SMBHs (indicated by lighter lines) yield larger fragment masses. However, this does not align with the initial mass distribution of stars, which is determined by the star formation efficiency and can be assumed to be constant. The figure is taken from Derdzinski et al. (2023).

1. Formation of stars

Strong radiative cooling in the outer regions of AGN disks can trigger fragmentation due to gravitational instability, particularly in radiation pressure-dominated environments. This fragmentation arises when the heating provided by magnetorotational instability (MRI) and gravitoturbulence becomes insufficient to counteract radiative cooling, thereby disrupting the local energy balance (Chen et al., 2024c). In MRI-dominated disks with a viscous parameter $\tilde{\alpha} \lesssim 10^{-2}$ (Bai et al., 2011), and assuming that radiative losses are balanced solely by accretion heating, gravitational instability is expected to occur (i.e., when Toomre parameter $Q < 1$) at radii $\tilde{R} \gtrsim \tilde{R}_{Q=1} \sim 10^{-2}$ pc around SMBHs with masses in the range $\sim 10^6$–$10^8 M_\odot$ (Paczynski, 1978). The onset of gravitational instability in this regime leads to strong gravitoturbulence, and then the effective viscosity parameter can reach $\tilde{\alpha}_\nu \sim 0.01 - 1$ (Lin et al., 1987; Kratter et al., 2008). Once fragmentation occurs, the resulting clumps can grow via gas accretion and collisions, though they may also be destroyed in collisions, eventually forming mas-

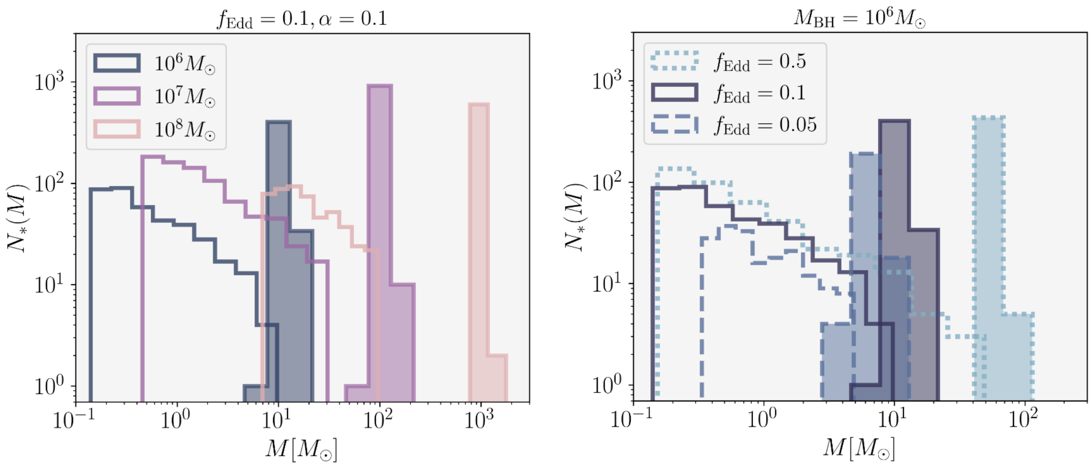

Figure 1.7 The initial mass distributions of in-situ stellar populations in AGN disks. A star formation efficiency of $\alpha = 0.1$ is assumed. The shaded histograms represent the mass distribution after stars have accreted through the (limited) Bondi-rate prescription over a period of 10^6 years without taking into account feedback. The left panel shows different SMBH masses, while the right panel displays varying accretion rates, expressed in terms of the Eddington rate. The figure is taken from Derdzinski et al. (2023).

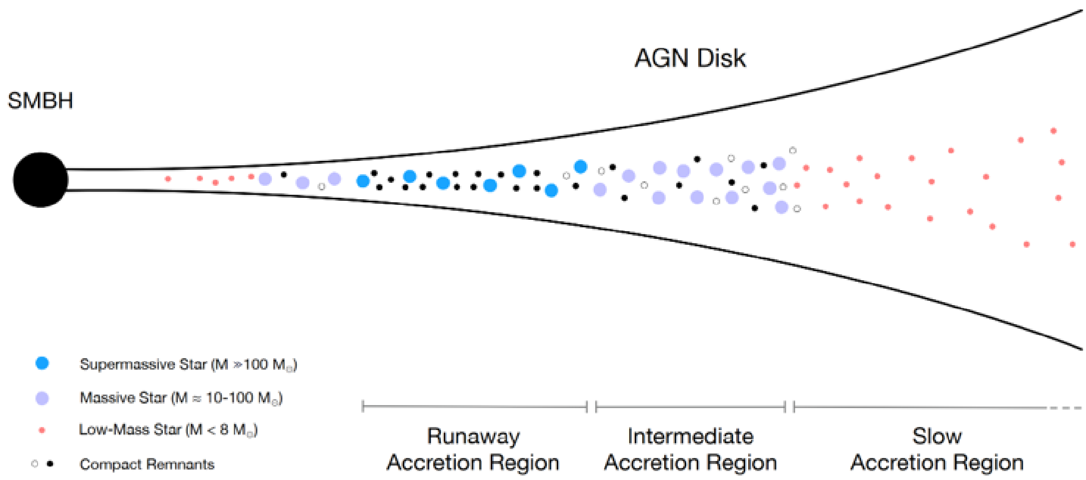

Figure 1.8 Illustration of different regimes of accretion in an AGN disk. The figure is taken from Dittmann et al. (2021).

sive stars. These stars, in turn, play a crucial role in maintaining the extended structure of AGN disks and reducing the accretion rate toward the SMBH, since a significant fraction of the mass flux is continuously diverted into star formation.

Stars formed in the dense environments of AGN disks evolve very differently from field stars. The stars on the disk may either form in situ within the disk or be captured from the nucleus stellar cluster. The mass distribution of stars captured in the disk depends on the stellar distributions (spatial, kinematic, and mass) in the nuclear stellar cluster. For stars formed in situ in the AGN accretion disk, the characteristic mass of fragments as a function of disk radius in the region where fragmentation conditions are satisfied is shown in the Fig. 1.6. The corresponding mass distribution of the formed

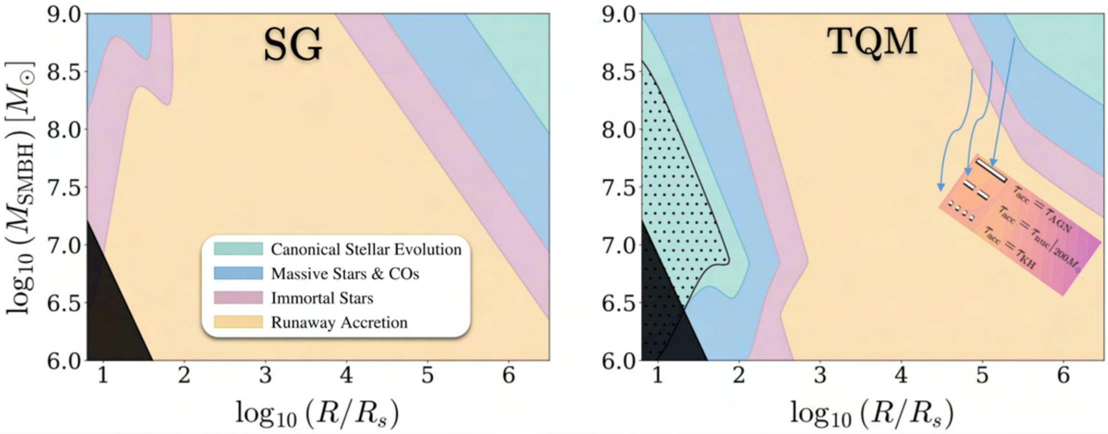

Figure 1.9 The various stellar evolution outcomes are presented based on the comparison of timescales: canonical stellar evolution (green), massive stars and COs (blue), immortal stars (pink), and runaway accretion (yellow). The dotted contour marks the region where the models become unphysical ($c_s \sim c$). The dark area in the lower corner of each panel denotes the tidal limit for a star. The figure is taken from Fabj et al. (2024).

stars, shown in Fig. 1.7, is top-heavy compared to the conventional Salpeter initial mass function (IMF) (Derdzinski et al., 2023), with a fitted IMF slope of $\frac{dN}{dm} \propto m^{\Gamma}$, where $\Gamma \sim -0.7$. This is considerably flatter than the Salpeter IMF, where the slope is $\Gamma_{\mathrm{SP}} = -2.35$. Furthermore, the mass of these stars increases further through accretion. The comparison of the mass distribution of accreted stars to those formed in situ is also shown in the Fig. 1.7. Although note that in this figure, the Bondi-rate prescription without taking into account feedback is assumed, so the overall accretion rate is an overestimate.

2. Evolution of stars

The dense circumstellar material in AGN disks leads to continued accretion onto the stars, which also affects their evolution and classification (Fig. 1.8) (Dittmann et al., 2021; Fabj et al., 2024). Generally, as shown in the Fig. 1.9, stars in AGN disks can be divided into four categories. In the innermost regions of the AGN, if stars accrete faster than they can thermally adjust, runaway accretion occurs, potentially preventing a quasi-steady state and altering the disk structure. In the outer regions of the disk, stars evolve similarly to those in the interstellar medium. While, in the intermediate regions, accretion rapidly transforms low-mass stars into massive stars, and their fate depends on the rate at which they accrete. Independent of their initial mass, these stars can acquire up to several hundred solar masses before efficiently shedding mass through intense stellar winds. If the accreted material in the envelope is well mixed with the helium ashes in the nuclear-burning (CNO cycle) core, this metabolic process allows the massive stars embedded in the dense inner regions of AGN disks to remain on the main sequence indefinitely (Jermyn et al., 2022). These are referred to as "immortal" stars, and their accretion occurs at a faster rate than nuclear burning. However, if their radiative zone provides an effective buffer to prevent significant mixing, the helium and nitrogen abundances in these stars' cores would increase through the CNO cycle on the main sequence. Once nearly all the hydrogen in their cores is exhausted and a significant portion of their total mass is lost, these stars undergo post-main sequence evolution. Subsequently, they release several solar masses of helium and carbon-oxygen-enriched yields. Technically, their evolution calculations with the MESA code are halted at the onset of silicon burning (Ali-Dib et al., 2023). Shortly thereafter, the magnesium- and silicon-laden cores collapse.

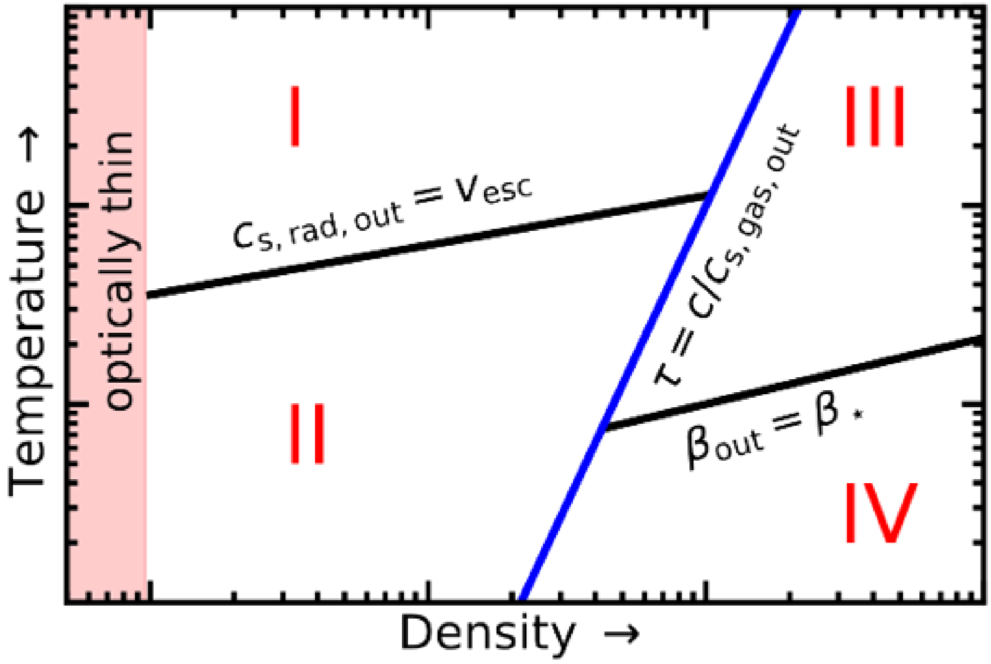

Figure 1.10 Schematic illustration of different accretion regimes of stars in AGN disks and the criteria that separate them. (I) fast diffusion, radiation enthalpy feedback dominated; (II) fast diffusion, gravitational feedback dominated; (III) slow diffusion, non-self-gravitating; (IV) slow diffusion, selfgravitating. The typical numerical values are $\sim 10^{-9}$–10^{-8} g cm^{-3} along the X-axis and $\sim 10^4-10^5$ K along the Y-axis for a star with a mass of 50−100 $M_\odot$. For stars of different masses, the values of β_* and v_{esc} vary accordingly. The figure is taken from Chen et al. (2024d).

Radiation hydrodynamic simulations were performed to study the accretion of stars in isotropic, gas-rich environments (Chen et al., 2024d). Generally, based on the background density and temperature, the outcome of accretion onto a given stellar envelope can be summarized into the four regions shown in the schematic Fig. 1.10. By applying the scaling results obtained from their simulations to a wide range of boundary conditions—using AGN disk models over extended radial scales as depicted by Sirko et al. (2003) and Thompson et al. (2005)—it was found that stars typically accrete in the fast diffusion regime. For the outer star-forming region, the accretion rate of embedded stars is primarily limited by gravitational feedback (region II). Although in situ star formation is quenched by local gravitational stability, embedded stars may still migrate to or be captured at the innermost regions of the AGN disks. At this location, the stars' infalling envelope is optically thick, and their accretion rate is mainly limited by the enthalpy-feedback effect (region I). If the energy cannot be radiated away, the star will remain bound in a metastable state.

Table 1.2 Comparison of Accretion-modified Stars with Known Stellar Populations. The table is taken from Wang et al. (2023a).

Population	X	Y	Z	$m_* \,/\, \mathrm{M}_\odot$
I	0.6 ~ 0.74	0.22 ~ 0.39	0.01–0.04	massive
II	0.9	0.099	0.001	low mass
III	0.75	0.25	0	massive or very massive
AMS	arbitrary	arbitrary	arbitrary	massive or very massive

Population	Age/Spectra	Wind Properties	Born
I	young (O, B, A)	strong	the Galactic disk, spiral arms
II	old (cold)	weak	spheroid, globular cluster
III	young	no wind	earlier universe
AMS	arbitrary	weak	AGN accretion disks

Note. X, Y, and Z are hydrogen, helium, and metal abundances, respectively.

Additionally, Wang et al. (2023a) proposed that AGN disks could harbor accretion-modified stars (AMSs). Table 1.2 provides a comparative summary of AMSs relative to types I, II, and III stars. As a new class of stars, AMSs can have any metallicity but do not experience significant mass loss from stellar winds, as the winds are choked by the dense medium of the disk and return to the core stars. The mass functions of the AMS population exhibit a pile-up or cutoff-pile-up shape in top-heavy or top-dominant forms if the stellar winds are strong, which is consistent with the narrow range of supernova explosions driven by the well-known pair-instability.

3. Formation of compact objects

The stellar mass distribution in AGN disks is "top-heavy" compared to field stars, thus leading to a higher tendency for the formation of neutron stars and black holes. If these stars are able to continue evolving, most stars produced in AGN disks generate carbon-oxygen (C-O) cores greater than $8M_\odot$ at the onset of silicon burning. Therefore, the residual cores of these stars will collapse to form neutron stars or black holes. In the absence of sufficient spin angular momentum, these stars are not expected to undergo a supernova explosion, and they are unlikely to eject much mass during the collapse. Under such conditions, the remnant's mass will be approximately equal to the mass of the collapsing star, with yields primarily limited to the stellar-wind mass loss (in elements lighter than silicon) during their main-sequence and post-main-sequence evolution (Ali-Dib et al., 2023). However, AGN stars are likely to spin up at the end of their post-main-sequence evolution as they exchange mass (consequently angular momentum) with the AGN disks (Jermyn et al., 2021). The fast-spinning stars would also have enough angular momentum to form a disk outside the remnant's gravitational radius during collapse.

In NS remnants, there could be a relatively higher fraction of magnetars, as strong magnetic fields can be generated via dynamo processes, provided the rotation rates are sufficiently high (Raynaud et al., 2020). Typically, NS magnetic fields may decay over time due to processes like Ohmic dissipation during accretion (Konar et al., 1997; Pan et al., 2021a). However, average magnetic field strengths of $\sim 10^4$ Gauss are observed in AGN disks (Silant'ev et al., 2009; Daly, 2019); as NSs accrete matter from these disks, magnetic flux conservation suggests that their magnetic fields could be enhanced during the accretion process.

In general, white dwarfs are not expected to form in significant numbers within AGN disks due to the top-heavy stellar distribution and ongoing accretion processes. However, the initial mass, accretion, and evolution of stars are influenced by their positions within the disks and the properties of the disks themselves. A star with a mass less than $8 M_\odot$ can evolve into a white dwarf, although the stellar mass at which a star ends its life as a WD is highly uncertain in the accretion disk, because the mass loss of a star is likely completely different from that of stars in a normal environment. Considering these factors, a considerable number of white dwarfs may still form in AGN disks. For example, Fig. 1.7 shows that the peaks of the IMFs are below $8 M_\odot$, except for the case with $M_{\rm SMBH} = 10^6 M_\odot$. Even after 10^6 years of accretion, the peak of the stellar mass function in an AGN disk with $M_{\rm SMBH} = 10^6 M_\odot$ can still remain below $8 M_\odot$. Moreover, the stellar mass function is also influenced by the location within the AGN disk: for instance, the characteristic mass of a protostar formed by in situ collapse is smaller in the inner region of the AGN disk (e.g., Fig. 1.6).

In addition, for captured stars as introduced in the next subsection, the typical mass can be lower than that of stars formed in situ. While accreted stars near the inner disk may grow enough to form BHs, those located further out generally do not (Cantiello et al., 2021). WDs formed in these outer regions can migrate inward without collapsing into BHs. Moreover, AGN disks might not persist long enough for low-mass stars to evolve into WDs within a single active episode. Nevertheless, according to AGN duty cycle models (e.g., Shankar et al., 2009), stellar evolution can continue over multiple AGN phases or during inactive periods, enabling WD formation over extended timescales. Mass segregation in nuclear star clusters typically causes WDs to settle at larger radii than BHs or NSs. However, such segregation is not universally efficient across all nuclear clusters (McKernan et al., 2020). In systems hosting SMBHs with masses $\gtrsim 10^7 M_\odot$, mass segregation becomes less effective, and the IMF may also be less top-heavy.

Table 1.3 Comparison of Abundance ratios by mass. The observed abundance ratio is determined by comparing the observed line intensity ratio in the quasar BLR with the predicted line intensity ratio from the CLOUDY model. The table is taken from Fryer et al. (2025).

Element Ratio	Observed	AGN-disk	CCSN	TNSN	Solar Value
Mg/C	-0.3 ± 0.1	< -2.0	$-1.0 - -0.4$	$-0.1 - 1.0$	-0.55
Si/O	-2.2 ± 0.5	< -2.0	$-2.0 - -1.0$	$-0.7 - -0.5$	-0.91
C/O	-1.5 ± 0.1	$0.0 - 0.4$	$-0.8 - -0.2$	$-1.5 - -0.7$	-0.43
N/O	-0.6	$-4.0 - -2.0$	$-2.0 - -1.2$	$-6.0 - -5.0$	-0.82
Fe/Mg	-0.5 ± 0.5	~ 2	$-1.0 - -0.6$	$1.0 - 2.5$	0.28
Fe/O*	-0.4 ± 0.5	$-0.2 - 0.0$	$-1.9 - -0.5$	$0.3 - 1.7$	-0.69

4. Nucleosynthetic yields

The stellar evolution in AGN accretion disks also influences the element abundances within AGNs. Generally, these AGN disk stars and compact objects formed by collapse produce nucleosynthetic yields. The yields consist of stellar wind ejecta prior to collapse, disk wind ejecta after black hole formation, and stellar disruption as the disk wind and jet interact with the star (Fryer et al., 2025). The full nucleosynthetic yields from these typical stars in AGN disks have very different signatures compared to those of field stars (i.e., through thermonuclear supernovae (TNSN) and core-collapse supernovae (CCSN).), as summarized in the Table 1.3. Given the expected rotation rates of these stars, disks formed outside the remnant generate jet-driven explosions that produce large amounts of iron-peak elements, releasing approximately 1 $M_\odot$ of iron into the AGN disk. Additionally, the disk wind intercepts the delayed infall from the dwindling outer regions of the collapsing cores. This interruption further alters the abundance and ejects modest amounts of magnesium and silicon. On the other hand, if AMSs indeed form in AGN disks, very massive ones with $m > 260 M_\odot$ may directly collapse into black holes, while those in the range $260 M_\odot > m > 140 M_\odot$ may undergo pair-instability supernovae (PISNe). It has been found that iron production primarily comes from very massive stars via PISNe, whereas magnesium production is roughly linear with the progenitor mass (Wang et al., 2023a). This difference provides a method to distinguish the mass functions of AMS in AGN disks, iron-rich broad-line regions (BLRs) indicate the history of such stars. However, stars that directly collapse, including those with low angular momentum or with masses exceeding $260 M_\odot$, produce effectively no yields.

1.3.2 The Capture and Migration of Compact Objects in AGN Disks

1. Capture

Compact objects in AGN disks can originate not only from the evolution of stars within the disk but also through capture from the surrounding nuclear star cluster. Fig. 1.11 illustrates the capture process, where each time a stellar remnant crosses the AGN disk, its velocity and angular momentum are altered due to the accretion of disk material (Yang et al., 2019, 2022). The Bondi-Hoyle-Lyttleton (BHL) drag force, $F_{\rm BHL}$, acts on a compact object traversing the disk and is given by (Antoni et al., 2019; Fabj et al., 2020; Nasim et al., 2023)

$$F_{\rm BHL} = 4\pi G^2 m_{\rm BH}^2 \tilde{\rho}_{\rm disk} v_{\rm rel}^{-2}, \tag{1.1}$$

where $m_{\rm BH}$ is the mass of the compact object, and $\tilde{\rho}_{\rm disk}$ is the local disk density. Considering the influence of the Mach cone trailing the moving body, an additional factor of $\ln(r_{\rm max}/r_*)$ should be multiplied in the above expression, where $r_{\rm max}$ is the effective linear size of the surrounding medium and is larger than r_* (Ostriker, 1999). Additionally, AGN disks may directly capture stars from the nuclear star cluster. As a star repeatedly passes through the disk, it can generate QPEs (Linial et al., 2023). The geometric drag force, $F_{\rm GEO}$, acts on a star crossing the disk and is given by (Passy et al., 2012; Fabj et al., 2020; Nasim et al., 2023)

$$F_{\rm GEO} = \frac{1}{2} C_d (4\pi r_*^2) \tilde{\rho}_{\rm disk} v_{\rm rel}^2, \tag{1.2}$$

where the drag coefficient $C_d \approx 1$, r_* is the stellar radius, and $v_{\rm rel}$ is the relative velocity of the star with respect to the disk. Here the star structure (r_*) is likely modified by collision.

Overall, prograde orbiters (with inclination $i < 90^\circ$; the "orbiters" include both stars and BHs) experience a reduction in inclination, as well as a decrease in semimajor axis (a) and eccentricity (e), eventually leading to orbital alignment with the AGN disk. According to Fabj et al. (2020), approximately 10% of prograde inclined orbiters ($i < 90^\circ$) are captured and aligned with the disk, assuming the SG disk model (i.e., the model proposed by Sirko et al. (2003); see more details in Chapter 2), which is characterized by a density of $\tilde{\rho} > 10^{-11}\,{\rm g\,cm^{-3}}$, given a plausible range of AGN disk lifetimes (0.1–100 Myr) under the assumption of negligible accretion. On the other hand, only a small fraction of prograde orbiters become aligned with a disk of lower gas density, such

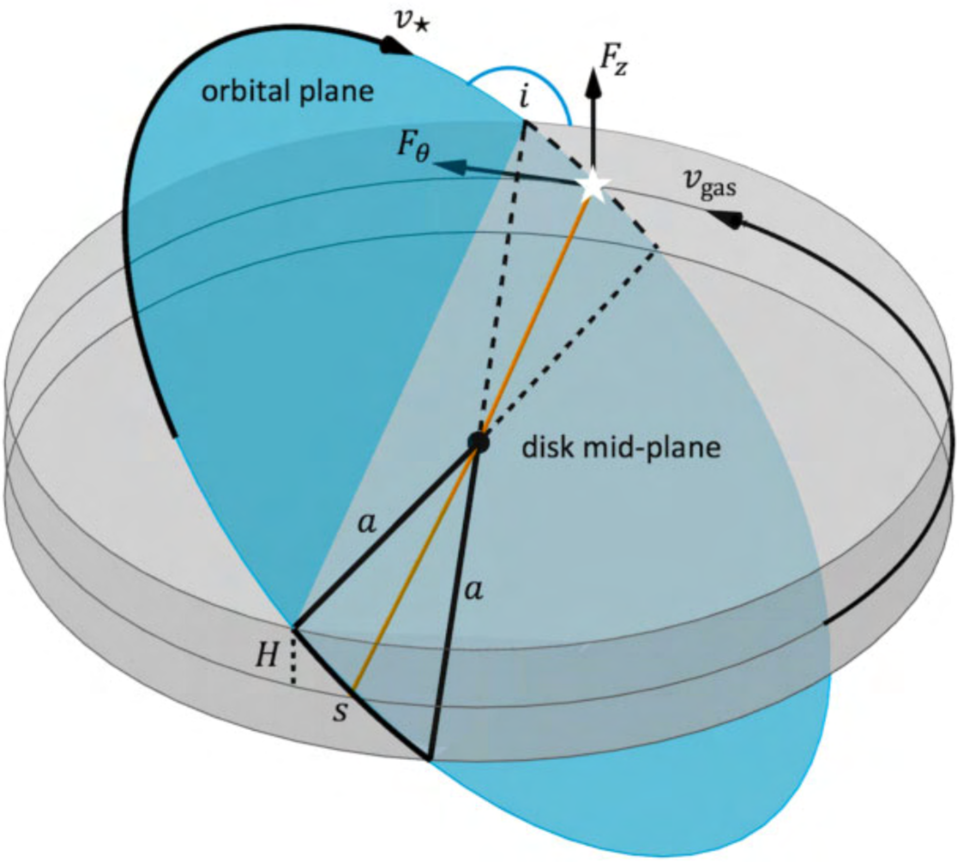

Figure 1.11 The orbital plane (blue) of a retrograde orbiter crossing the schematic representation of an AGN disk; the orange line indicates the intersection between the disk mid-plane and the orbital plane. The figure is taken from Nasim et al. (2023).

as the model proposed by Thompson et al. (2005) (hereafter TQM). And separately, most prograde stars that are aligned have small initial semimajor axis ($a < 10^{3-4} R_{\mathrm{g}}$), which then decreases by at most an order of magnitude during capture, where $R_{\mathrm{g}} = GM_{\mathrm{SMBH}}c^{-2}$ denotes the SMBH gravitational radius; sBHs starting from a wide range of initial $a \leqslant 10^6 R_{\mathrm{g}}$ end up at small disk radii ($a \sim 10^2 R_{\mathrm{g}}$) during capture (Fabj et al., 2020).

Neverthrless, it is anticipated that approximately half of all NSC orbits will be retrograde ($i > 90^\circ$) relative to the AGN disk, with the majority not being aligned with the disk plane. Retrograde stars are alingned more rapidly than their prograde counterparts, undergo a transition to prograde orientation ($i < 90^\circ$) during capture, and experience a significant decrease in a as they migrate toward the SMBH (Nasim et al., 2023). For sBHs, a critical inclination angle of $i_{\mathrm{ret}} \sim 113^\circ$ is identified, below which retrograde sBHs evolve into embedded prograde orbits ($i \to 0^\circ$). Conversely, for $i_0 > i_{\mathrm{ret}}$, sBHs settle into embedded retrograde orbits ($i \to 180^\circ$). The most pronounced reductions in a occur for sBHs on nearly polar orbits ($i \sim 90^\circ$) and stars on nearly embedded retrograde orbits ($i \sim 180^\circ$) (Nasim et al., 2023). Whether a star becomes aligned with the disk within the AGN's lifetime primarily depends on the disk density, with secondary influences from stellar type and initial semimajor axis. For sBHs, the timescale for disk capture is longest for those on polar orbits, with lower masses, or interacting with less dense disks. More massive sBHs are thus expected to reside in AGN disks for a longer time, which has implications for the spin distribution of embedded sBHs (Nasim et al., 2023).

2. Migration

Once a compact object is captured onto the disk, it will undergo further migration within the disk under the influence of torques. The migration of objects in an AGN disk is similar to the migration of planets within their original protoplanetary disks. Generally, the object exchanges angular momentum with the disk, resulting in changes to its orbital parameters. The interaction between the object and the disk depends on the mass of the object and the properties of the disk.

If the object is small (with a mass ratio to the central object $q < 10^{-4}$) and does not significantly disturb the disk, such as Earth-like planets in a protoplanetary disk, or stellar-mass compact objects in an AGN disk, the object will migrate under the opposing force exerted by the disk gas. This type of migration is referred to as Type I migration. The timescale for Type I migration is given by (e.g., Peng et al., 2021)

$$\tau_{\mathrm{I}} = \frac{M_{\mathrm{SMBH}}}{q\tilde{\Sigma}\tilde{R}^2}\frac{1}{\tilde{\Omega}}, \tag{1.3}$$

where q is the mass ratio of the migrating object to the central object and $\tilde{\Omega}$ is the object angular velocity.

However, if an object is sufficiently massive, it can truncate the accretion disk through its own gravitational tidal forces, creating an annular gap around its orbit [90]. This applies to Jupiter-mass planets in a protoplanetary disk or to intermediate-mass black holes in an AGN disk. Under the influence of the gap's edge, the object becomes trapped within the annular gap and migrates inward along with the disk, ultimately accreting onto the central object. This migration process is known as Type II migration. The timescale for Type II migration is determined by the disk height and the disk's viscosity coefficient, as given by (McKernan et al., 2012)

$$\tau_{\mathrm{II}} = \frac{1}{\tilde{\alpha}}\left(\frac{\tilde{H}}{\tilde{R}}\right)^{-2}\frac{1}{\tilde{\Omega}}, \tag{1.4}$$

where $\tilde{\alpha}$ is the viscosity coefficient.

Black holes embedded in accretion disks are also expected to exert feedback on the surrounding gas, which can alter the migration torque. When feedback is present, the torque is adjusted according to the formulation proposed by Hankla et al. (2020)

$$\Gamma_{\text{heat}} \sim 0.07 \left(\frac{c}{\tilde{v}_{\text{k}}}\right) \frac{\eta}{\tilde{\tau}\tilde{\alpha}^{\frac{3}{2}}}, \tag{1.5}$$

where Γ_{heat} represents the heating torque, c is the speed of light, $\tilde{v}_k$ is the Keplerian velocity of the black hole, η is the accretor's Eddington ratio, and $\tilde{\tau}$ is the disk's optical depth. Thus the corespoding timescale is $\tau_{\text{heat}} \sim 2m\tilde{\Omega}\tilde{R}^2/\Gamma_{\text{heat}}$. A notable aspect of this modification is that Γ_{heat} generally exerts an outward force, which means that in disk regions with lower opacity, migration can be driven outward rather than the typical inward direction. This outward runaway migration can occur in low-opacity disks, such as the outer regions of TQM disk.

In certain radial locations within the AGN disk, the total torque may be zero, and such locations are referred to as migration traps. The typical location of migration traps is around $10^3 R_{\text{g}}$ (Bellovary et al., 2016; Derdzinski et al., 2023), with the innermost migration trap potentially reaching the innermost circular orbit (Peng et al., 2021), where the torque due to GW emission is significant. However, migration traps are not always present (Dittmann et al., 2020; Pan et al., 2021b). During differential migration or within trap regions, objects in the disk may undergo two-body or multi-body interactions, which could lead to events such as binary compact objects mergers.

1.3.3 Merger and Accretion of Compact Objects in AGN Disks

1. Merger dynamics

The compact objects in AGN accretion disks undergo complex physical processes, exhibiting a wealth of observational features, with the formation and evolution of binary systems being particularly notable. Driven by gravitational wave observations, research on binary systems in AGN accretion disks has mainly focused on binary black holes. In AGN disk environments, black hole binaries may form from stellar binaries born within the disk, or from originally isolated black holes captured into binary systems through gravitational wave or gas interactions (Tagawa et al., 2020). Three key dynamical ways to tighten these binaries are:

(1) **Disk interaction:** The binary system is surrounded by a circumbinary disk, while each black hole hosts its own circum-BH disk. A snapshot of the gas density for a typical model simulating the binary black hole in an AGN disk is shown in the Fig. 1.12. Interactions between the binary and the circumbinary disk can either expand or shrink the binary orbit. The specific outcome depends on the disk properties, the masses of the black holes, and the orbital configuration of the

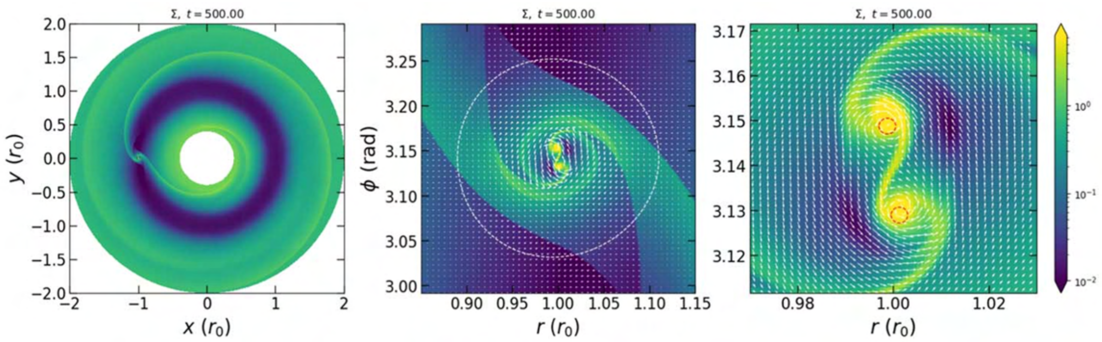

Figure 1.12 Asnapshot of gas density for a typical model simulating the BBH in an AGN disk. Each panel, from left to right, progressively zooms in on the BBH. The dashed white circle represents the BBH Hill radius. Arrows overlaid on the image indicate the gas velocity streamlines in the BBH center-of-mass frame. The dashed red circles in the rightmost panel denote the softening scale for each black hole. The figure is taken from Li et al. (2021).

binary(Li et al., 2021, 2022e,b, 2023c, 2024).

(2) **Interactions with other stellar-mass objects:** Three-body scattering in a coplanar configuration can lead to binary mergers with extremely high eccentricities, leaving observable residual eccentricities in the LIGO band (Samsing et al., 2022; Trani et al., 2024). The illustration of an eccentric LIGO-Virgo source forming in an AGN disk is shown in the Fig. 1.13 Additionally, the gas hardening of the triple further enhances the probability of a merger by a minimum factor of 3.5 to 8 (Rowan et al., 2025), depending on assumptions.

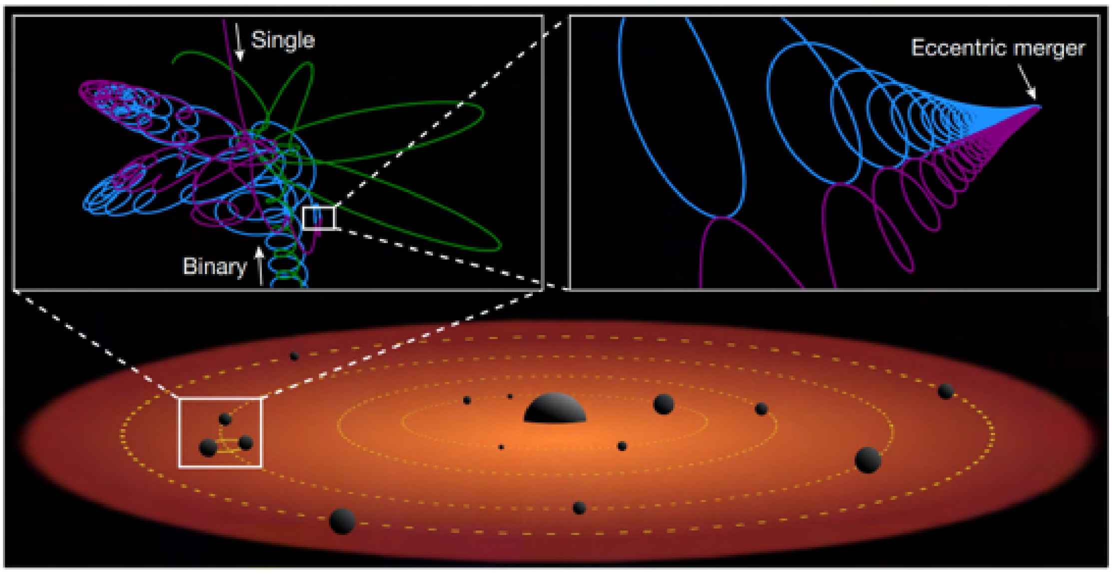

Figure 1.13 Illustration of an eccentric LIGO-Virgo source forming in an AGN disk. The figure is taken from Samsing et al. (2022).

(3) **Interaction with the central SMBH:** As shown in the diagrammatic sketch, i.e., Fig. 1.14, over long timescales, dynamical effects from the SMBH's gravitational perturbations can induce high eccentricities in nearby binaries. Each time the bi-

nary black holes encounter the disk, surrounding gas (Rowan et al., 2024) or gravitational waves (Li et al., 2022a; Boekholt et al., 2023) dissipate orbital energy, accelerating their merger.

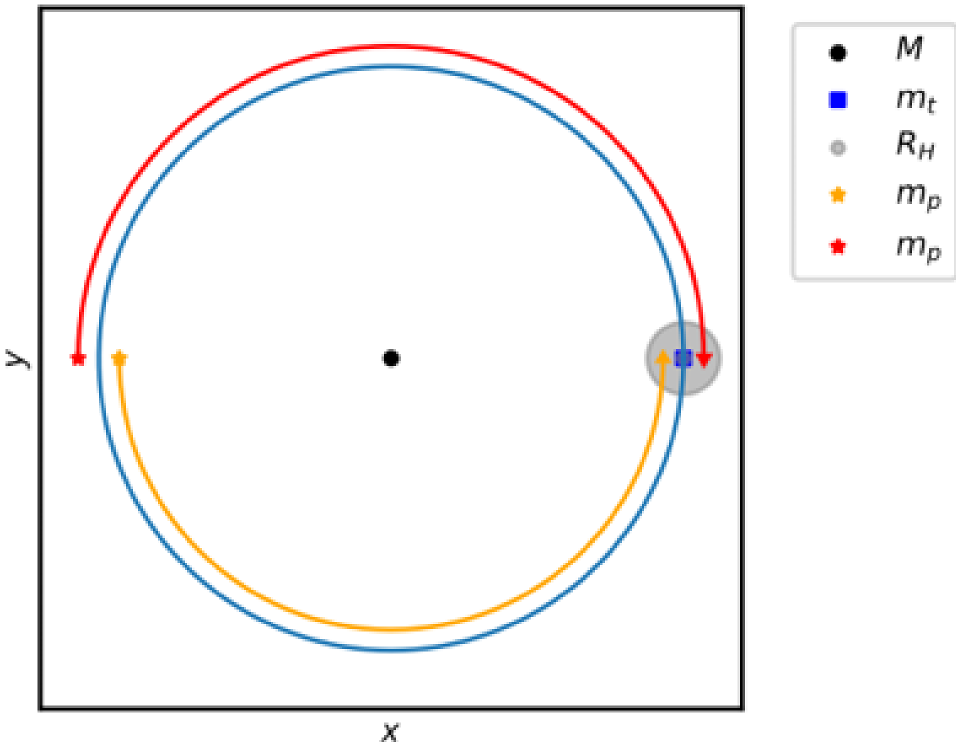

Figure 1.14 Schematic illustration of the binary black hole orbit around SMBH. The frame is centered on the central body (M) and co-rotates with the target body (m_t). The target's Hill radius (R_H) is shaded in grey. For the projectile body (mass m_p), two orbits are shown, one with a positive (red star) and one with a negative (orange star) impact parameter, both of which intersect the target's Hill radius. The figure is taken from Boekholt et al. (2023).

In addition to binary black hole mergers in AGN accretion disks, similar dynamical effects may cause black holes in the disk to have close encounters with stars or white dwarfs, leading to micro-TDEs (tidal disruption events) (Prasad et al., 2024; Yang et al., 2022; Xin et al., 2023). Similarly, in the case of a three-body system consisting of the central SMBH and two white dwarfs in the disk, the two white dwarfs are found not to form a stable binary before merging, but instead collide directly due to their relatively large radii (Luo et al., 2023; Zhang et al., 2023). Moreover, neutron star−neutron star and neutron star−black hole mergers may also occur, producing jets, electromagnetic counterparts, and neutrinos (Zhu et al., 2021d). However, it should be noted that neutron stars in disks may accrete mass and collapse before forming binaries, reducing the likelihood of neutron star mergers in disks (Zhang et al., 2024c).

2. Accretion processes

Due to the dense gas in AGN disks, accretion becomes a key physical process for compact objects. Different types of compact objects exhibit distinct accretion behaviors in AGN disks, potentially leading to diverse observational signatures. The study of how various compact objects accrete within AGN disks is still in its early stages, and many aspects remain unclear. Nevertheless, it is understood that accretion onto compact objects in AGN disks generally shares the following characteristics:

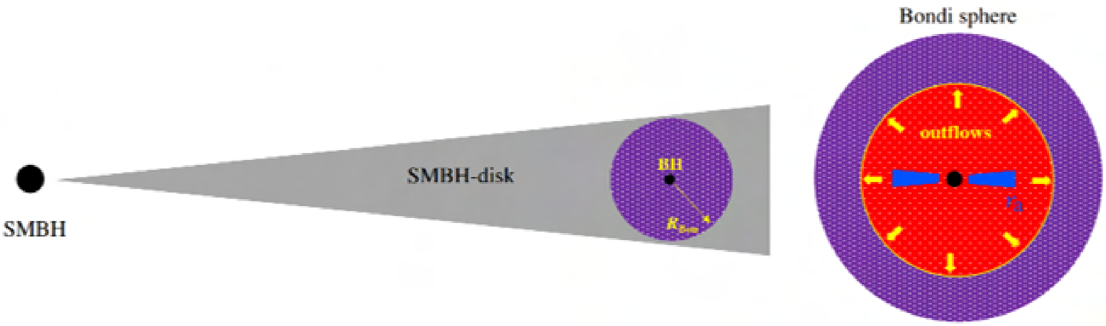

Figure 1.15 Accretion pattern of compact objects in AGN disks, referred to as accretion-modified stars (AMSs) according to Wang et al. (2021a).

(1) **Outer spherical and inner disk accretion pattern:** The typical accretion pattern for compact objects in AGN disks consists of an outer spherical and an inner disk structure, as shown in the Fig. 1.15. Namely, at the Bondi radius scale, the accretion flow is nearly spherical toward the central object. As the flow moves inward by 1–2 orders of magnitude, due to the differential rotation of the AGN disk and the conservation of angular momentum, a circum-CO disk is formed (Wang et al., 2021a; Chen et al., 2023a).

(2) **Hyper-Eddington rates and strong outflows:** Bondi accretion is a reasonable initial assumption for COs accreting in AGN disks; it often occurs at hyper-Eddington rates (reaching up to $\sim 10^9$ times the Eddington rate) given the high-density gas (Wang et al., 2021b). During hyper-Eddington accretion, the CO is typically surrounded by an outflow-dominated circum-CO disk (Wang et al., 2021a; Tagawa et al., 2022; Chen et al., 2023a).

(3) **Intermittent accretion:** Simulations show that super-Eddington accretion produces powerful outflows strongly influencing its surroundings, but the mid-plane still continues accretion with rates from 300 to 10^3 Eddington rates (Takeo et al., 2020). However, in AGN disks, the accretion rate is even stronger, and feedback from outflows prevents accreting gas from reaching the black hole, temporarily creating a cavity around it. This could lead to intermittent accretion onto the

compact object, with accretion resuming once the cavity is replenished. For black holes in the disk, the typical accretion duty cycle may be very small, ranging from $\sim 10^{-5}$ to ~ 0.1 (Wang et al., 2021a; Chen et al., 2023a).

More detailed studies of accretion onto different kinds of compact objects embedded in AGN disks are presented in Chapter 2, especially the investigation of neutron star accretion.

1.3.4 Multimessenger Observational Effects of Compact Objects in AGN Disks

Various physical processes associated with compact objects in AGN disks can produce not only multi-band electromagnetic emission, but also multi-messenger signals such as gravitational waves and neutrinos.

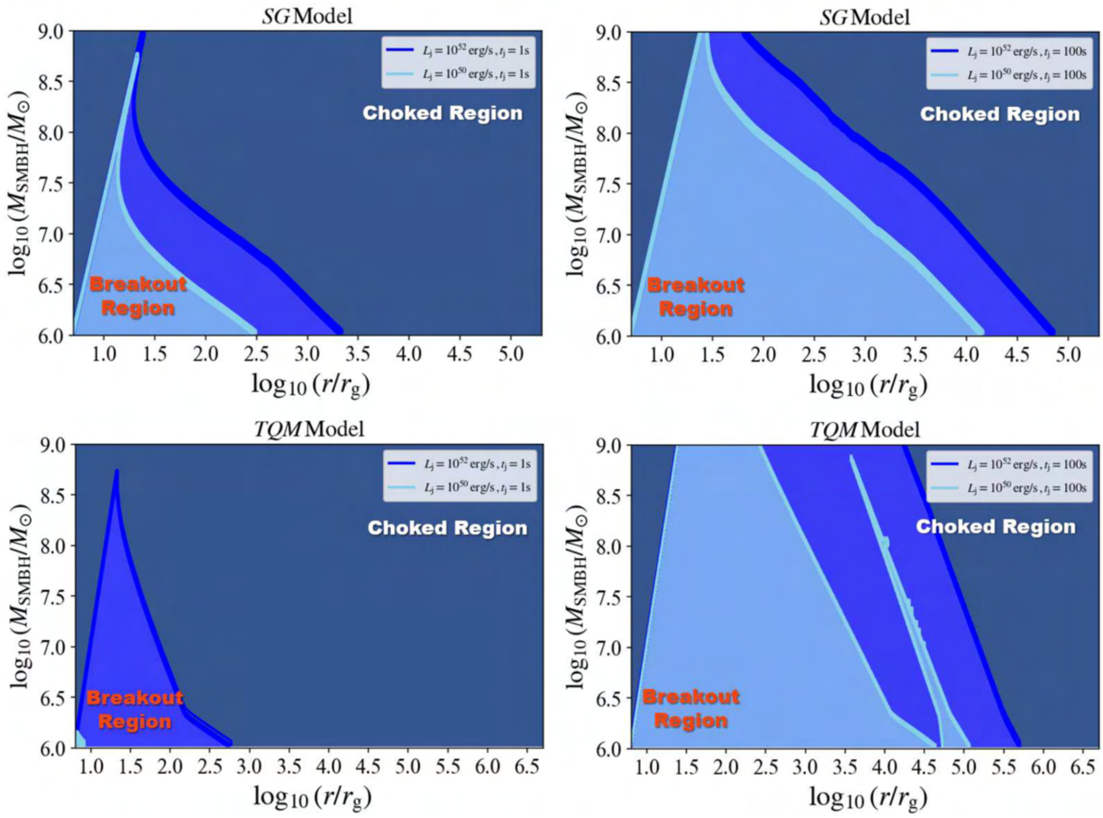

Figure 1.16 Parameter space in the $(R, M_{\rm SMBH})$ plane for jet breakout (blue region) and choking (gray region). The figure is taken from Zhang et al. (2024a).

As discussed in the previous section, once a binary black hole merges in an AGN disk, GWs are produced, typically with residual orbital eccentricity information, such as in the case of GW190521(Abbott et al., 2020; Romero-Shaw et al., 2020; Samsing et al., 2022). Furthermore, the unique dynamics processes of compact objects in AGN disks may imprint distinctive features on the statistical distributions of mass and effective spin in the gravitational waveforms of merging binaries. (e.g., Li et al., 2023a; Li,

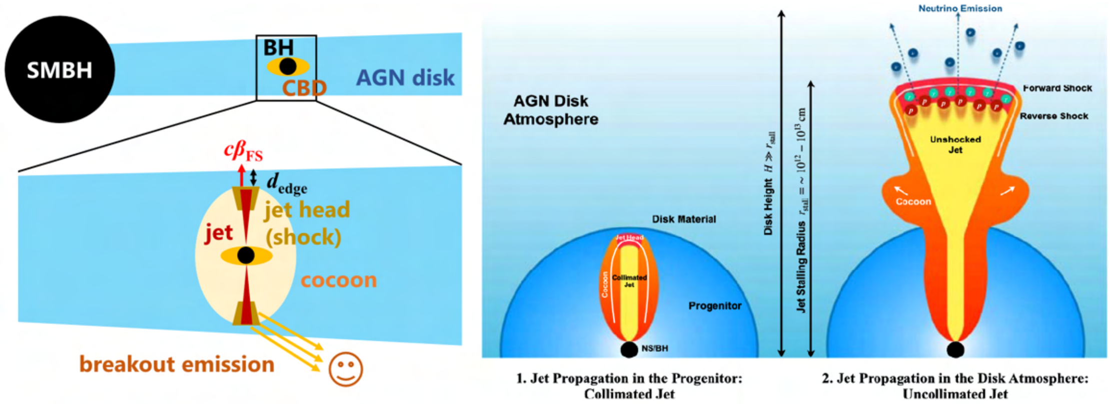

Figure 1.17 Left: Schematic illustration of a jet launched from a black hole embedded in an AGN disk and its breakout, adapted from Tagawa et al. (2023b). Right: Illustration of jet choking and high-energy neutrino emission, adapted from Zhu et al. (2021b).

2022; Santini et al., 2023; Wang et al., 2023b). This may help explain why the mergers detected by LVK are significantly more massive than those observed in our Galaxy, as well as the observed anti-correlation between the mass ratio q and the effective spin $\chi_{\rm eff}$ (Callister et al., 2021). Additionally, GWs can be associated with GRBs, as seen in events like GW150914 (Levan et al., 2023; Lazzati et al., 2023) and LVK S241120n. However, there are still very few confirmed binary merger events with electromagnetic counterparts, let alone definitive observational constraints on the general characteristics or rates of binary compact object mergers in AGN disks. Nevertheless, statistical analyses based on spatial correlations constrain that, at a 95% confidence level, unobscured AGNs with bolometric luminosities above $10^{44.5}$ erg s^{-1} (or 10^{44} erg s^{-1}) contribute no more than 21% (or 11%) of detected GW events, a larger fraction might still originate from fainter or obscured AGNs (Veronesi et al., 2025).

In addition to binary black hole mergers in AGN disks, stellar-mass black holes or intermediate-mass black holes in the disk may migrate inward, under the torque exerted by the disk, forming extreme or intermediate mass-ratio inspirals (EMRIs or IMRIs) (Kocsis et al., 2011; McKernan et al., 2012, 2014; Peng et al., 2023; Pan et al., 2021b). Since the gas in the disk dampens the motion of compact objects, the gravitational wave signals from such EMRIs or IMRIs in AGN disks (”wet” origins) will exhibit phase differences when compared to those from ”dry” origins, and these signals may be detectable by LISA within several years (Dutta Roy et al., 2025). Furthermore, these ’wet’ EMRIs may be used to explain the QPEs associated with mHz GW signals, calibrate other methods for probing SMBH mass and spin, and test AGN disk and jet models (Lyu et al., 2024).

GWs from NSs have received less attention compared with that of BHs, due to both observational and theoretical challenges. Observationally, NS–NS and NS–BH mergers are rare. Theoretically, the formation and evolution of such binaries in AGN disks are significantly more complex than in isolated environments like the Milky Way (Wang et al., 2020a; Deng et al., 2024). Some preliminary studies suggest that binary neutron star or neutron star–black hole mergers could occur in AGN disks (Zhu et al., 2021d), although with larger uncertainty in the predicted merger rates (McKernan et al., 2020). Gravitational waves from the pre-merger phase of binary neutron stars can be detected by LVK, but the postmerger phase is typically hard to detect, despite the unique value such signals could offer in studying neutron star equations of state (Clark et al., 2016; Papenfort et al., 2018). However, if binary neutron star mergers occur in the inner regions of the AGN disk, gravitational waves from the postmerger phase might be detectable by LVK due to Doppler shifts and gravitational redshift caused by the SMBH (Vijaykumar et al., 2022). If NS–NS or NS–BH mergers indeed occur in AGN disks, the corresponding pre-merger binaries could be highly eccentric. This scenario is capable of ejecting significantly more material than typical kilonovae (Radice et al., 2016; East et al., 2012; Foucart et al., 2014; Kyutoku et al., 2015), and may leave behind distinct GW signals (Papenfort et al., 2018; Vick et al., 2019; Wang et al., 2020b).

Meanwhile, it is noteworthy that in the high-density gas environment of an AGN disk, neutron stars could undergo accretion-induced collapse (Perna et al., 2021b). Zhang et al. (2024c) compare the timescale for accretion-induced collapse of neutron stars with the timescale for migration leading to the formation of binary systems and find that binary mergers of NSs are less likely to originate from AGNs. Moreover, the accretion of neutron stars could also produce gravitational waves, primarily at kilohertz frequencies. The accreting neutron stars might drive mass quadrupole growth, releasing gravitational waves. Possible mechanisms include the formation of 'mountains' from shell elastic deformations (i.e., non-axisymmetric deformations that produce mass quadrupoles) due to temperature asymmetry (Ushomirsky et al., 2000) and/or magnetic field support (Haskell et al., 2015). Therefore, at high accretion rates, neutron stars in AGN disks could serve as new kilohertz gravitational wave sources for the next generation of detectors.

Another potential multi-messenger signal associated with compact object activity in AGN is neutrinos. Binary compact object mergers, stellar collapses, or black hole accretion in AGN disks could generate relativistic jets (Tagawa et al., 2023b; Zhu et al., 2021a; Tagawa et al., 2023c) via e.g., the Blandford-Znajek (BZ) mechanism (Blandford et al., 1977). These jets might fail to break out as typical GRBs and instead result in choked GRBs in the disk (Zhu et al., 2021b), as illustrated in the right panel of Fig. 1.17. When the jet interacts with the disk's gas, shockwaves accelerate protons, which then produce high-energy neutrinos through hadronic processes (such as pp or pγ), with energies above GeV, potentially reaching PeV (Zhu, 2024). Additionally, shocks driven by various transients, including supernova explosions, winds from circum-CO disks, compact object coalescences, and tidal disruption events, can also accelerate particles, which subsequently interact with the shocked disk gas or radiation fields via hadronic processes, leading to the production of high-energy neutrinos (e.g., Zhu et al., 2021a; Zhou et al., 2023; Ma et al., 2024). The corresponding expected event rate densities, diffuse fractional fluxes, and detection rates for AGN stellar explosions are shown in Table 1.4. Interestingly, IceCube detected 79 high-energy neutrinos in the 1 − 10 TeV range from NGC 1068 (IceCube Collaboration et al., 2022), along with the absence of TeV gamma photons, suggesting these neutrinos were produced in an environment opaque to high-energy photons (Murase, 2022). These high-energy neutrinos likely originate from a transient event in the disk, where protons and electrons are accelerated by the jet produced from the BH and generate neutrinos via adiabatic cooling, pp, or pγ processes, with the corresponding high-energy photons consistent with observational constraints for NGC 1068 (Tagawa et al., 2023a). Of course, other origins of these high-energy neutrinos cannot be excluded, such as the dense corona around the central SMBH or proton-photon collisions involving disk-produced radiation (Murase et al., 2020).

Table 1.4 The expected event rate densities, diffuse fractional fluxes of high-energy neutrinos, and detection rates from neutrinos for AGN explosion events. This table is taken from Zhu et al. (2021a).

Explosion	$R_0/\mathrm{Gpc}^{-3}\mathrm{yr}^{-1}$	Diffuse Fractional Flux	$\dot{N}/\mathrm{yr}^{-1}$
SN Ia	< 5000	$\lesssim 3\%$	$\lesssim 0.1$
Kilonova	< 460	$\lesssim 0.3\%$	$\lesssim 0.01$
SGRB	< 460	$\lesssim 2\%$	$\gtrsim 0.05$
CCSN	< 100	$\lesssim 1\%$	$\gtrsim 0.03$
GRB-SN	< 1	$\lesssim 0.3\%$	$\lesssim 0.01$
LGRB	< 1	$\lesssim 5\%$	$\gtrsim 0.2$

Electromagnetic signals from the activities of stars or compact objects in the disk could also be very rich. As shown in Fig. 1.16, jets with high energy in AGNs might also break out of the disk, producing multi-band light variations up to the GeV range (Yuan et al., 2022), particularly in cases where the inner AGN disk is thin (Zhang et al., 2024a). Overall, GRBs from AGN disks may differ in their luminosity, duration, and photon index of both prompt emission and afterglow phases compared to normal GRBs (Lazzati et al., 2022; Wang et al., 2022; Ray et al., 2023). Some GRBs with unusual classifications, such as GRB 191019A, could potentially originate from AGN disks (Levan et al., 2023; Lazzati et al., 2023). In addition to jet breakouts, super-Eddington accretion in black holes in the AGN disk could produce powerful outflows, driving electromagnetic bursts known as Bondi explosions (Wang et al., 2021a,b). These outflows can generate light curves from radio to gamma rays (Wang et al., 2021a,b; Chen et al., 2023a). If shockwaves from various supernovae in the disk break out, they could produce light variations such as in the UV to soft X-ray band (Grishin et al., 2021; Zhu et al., 2021c). Stars that are captured by the disk and collide with it may also explain QPEs (Linial et al., 2023). For thermonuclear explosions caused by white dwarf collisions in the inner regions of the AGN disk, we find that they would produce light variations predominantly in the MeV range, potentially even disrupting the AGN disk (Zhang et al., 2023). TDEs can occur in AGNs, including planar TDEs (McKernan et al., 2022; Ryu et al., 2024), perpendicular disk TDEs (Chan et al., 2019, 2020, 2021), and micro-TDEs of stars and white dwarfs (Xin et al., 2023; Yang et al., 2022). Veres et al. (2024) showed that AT2019aalc may be a candidate repeating TDE in an AGN. These TDEs may also disrupt the AGN disk, with related events observed as changing-look AGNs (Wang et al., 2024b). Notably, polarization observations of at least some changing-look AGNs confirm that their variability originates from changes in the accretion rate, rather than from external obscuration. (e.g., Hutsemékers et al., 2017). More direct evidence from infrared variability also confirms this nature of Changing-look AGNs (Sheng et al., 2017).

The combination of these multi-band, multi-messenger signals not only advances the search for compact object mergers in AGNs and improves the understanding of their dynamics and accretion processes, but also potentially opens new avenues for probing cosmology, as the redshift and luminosity distance of the source can be determined separately through EM and GW observations (Bom et al., 2024; Mancarella et al., 2024). As introduced above, gravitational wave sources and AGNs can be used for spatial correlation analysis (Veronesi et al., 2022), and if gravitational waves are determined to originate from an AGN, the event can serve as a standard siren to measure the Hubble constant H_0. By statistically correlating gravitational wave sources with AGN activity, the merger rate of binary black holes in AGNs, the Hubble constant, dark matter state parameters, and other cosmological quantities can be inferred. In the ideal case, after two years of observations with the LVK design sensitivity, the measurement accuracy of H_0 could reach $\approx 2\% - 3\%$ (Bom et al., 2024). Furthermore, wet EMRIs provide a promising avenue for probing cosmological models or constraining parameters by serving as both 'bright' and 'dark' sirens (Lyu et al., 2024).

1.4 The Structure of the Remaining Text

In the previous section, we introduced the background and current research on Multiscale Energy Transport and Evolution of Compact Objects in Astrophysical Environments. There is a clear central topic: astrophysical black holes. There are two general parts still worth exploring: one is the physics of black holes, in particular, the role of the irreducible mass (increase) in astrophysical black holes. Second, the topic is the study of some of the physical processes occurring in the surroundings of astrophysical black holes, in particular, the accretion and dynamics of compact objects in AGN disks, as well as the related multi-messenger signals.

According to classical general relativity, the no-hair theorem states that a BH can be fully described by three parameters: mass, spin, and charge. In astrophysical settings, BHs are typically assumed to be uncharged, so they are often described using only mass and spin. However, they can also be characterized by mass and $M_{\rm irr}$, where $M_{\rm irr}$ is a nonlinear function of mass and angular momentum, and it is equally important as mass and angular momentum. Thus, we focus on the role of irreducible mass in black hole physics, examining how the irreducible mass increases during energy extraction and accretion processes, and its implications. This part is studied in Chapters 2–3.

Another part focuses on processes more closely related to observational effects. Largely driven by gravitational wave observations, many studies investigate stellar-mass black holes in AGN disks. However, only a few candidates of black hole merger events in AGN disks have been reported to date, and most related studies remain theoretical. To mitigate this, we integrate electromagnetic and gravitational wave observations to identify a potential source in AGN disks. On the other hand, WDs and NSs may also reside in AGN disks, yet the physical processes associated with them and their potential observational signatures remain poorly understood. Therefore, our work focuses on how WDs and NSs interact with their surrounding environment, how energy and angular momentum are transferred during these interactions, and what observational phenomena may result. Overall, our study centers on the accretion and dynamical behavior of various types of compact objects in AGN disks. This part is studied in Chapters 4–7.

Finally, Chapter 8 concludes with a summary and outlook.

Chapter 2 Roles of Irreducible Mass of a BH in Energy Extraction Processes

2.1 Background

Longstanding issues include the mechanisms by which the extreme environments of BHs supply and transfer energy. The energy extraction from *ergosphere* of a Kerr black hole (BH) has attracted considerable attention. Up to now, numerous methods and their corresponding extended research for extracting energy from BHs have been proposed (Bekenstein, 1973a; Teukolsky et al., 1974; Ruffini et al., 1975; Piran et al., 1975; Blandford et al., 1977; Bekenstein et al., 1998; Rueda et al., 2022; Zaslavskii, 2022, 2023). Especially, the challenge of using the Kerr BH as an energy source for astrophysical systems and it affect on irreduceble mass has been addressed in context of test magnetic field around a Kerr BH, with examples in the special cases of GRBs and AGNs (Rueda et al., 2023). However, despite the ballistic Penrose process being the most fundamental one, the study of its influence on BHs has not been well-developed.

Penrose et al. (1971) pioneered the idea that ballistic particle fission can be used as a process of Kerr BH energy extraction. It was soon demonstrated that the Penrose process satisfies some constraints. In particular, Wald (1974) provides the energy limit of the Penrose process, demonstrating that one cannot obtain significantly greater energies than those achievable through a similar breakup process in the absence of a BH. This chapter introduces an additional and innovative constraint on the decay position of the Penrose process, particularly when the decay point coincides with the turning point. Additionally, the capture of a counterrotating test particle by the black hole horizon may have specific implications for the surface area or irreducible mass. Both Penrose et al. (1971) and Chandrasekhar (1998) have mentioned that the Penrose process leads to an increase in the surface area of a BH, but a precise quantitative description is currently absent. For this reason, we re-examine this fundamental issue followed by location constraints in this chapter. Meanwhile, the irreducible mass always increases for a BH in classical theory (Christodoulou et al., 1971; Hawking, 1971). Thus, it is fundamental to have a more direct exemplification of how to interact with this fundamental quantity, $M_{\rm irr}$.

This chapter provides a quantitative analysis of the feedback from the Penrose process on the irreducible mass, demonstrating the irreversibility of energy extraction and its impact on the total amount of energy that can be extracted from a BH. This subject is of academic and purely theoretical interest because the irreducible mass is linked to BH area or BH entropy. Additionally, it may have astrophysical implications concerning energy supply in extreme environments.

2.2 Irreducible Mass and Transformable Energy of a Kerr BH

In spheroidal Boyer-Lindquist coordinates (t, r, θ, ϕ), the Kerr BH metric reads (Carter, 1968)[①]

$$ds^2 = -\left(1 - \frac{2Mr}{\Sigma}\right) dt^2 + \frac{\Sigma}{\Delta} dr^2 + \Sigma\, d\theta^2 + \frac{A}{\Sigma} \sin^2\theta\, d\phi^2 \\ - \frac{4aMr}{\Sigma} \sin^2\theta\, dt\, d\phi, \tag{2.1}$$

where $\Sigma = r^2 + a^2\cos^2\theta$, $\Delta = r^2 - 2Mr + a^2$, $A = (r^2 + a^2)^2 - \Delta a^2 \sin^2\theta$, being M and $a = J/M$, respectively, the BH mass and angular momentum per unit mass. The BH horizon is $r_+ = M + \sqrt{M^2 - a^2}$.

The mathematical solution of the Einstein equations by Kerr (1963a), which plays a central role in the description of rotating objects in General Relativity. Building upon Kerr's work, the paper by Christodoulou (1970) introduced the mass-energy formula

$$M^2 = M_{\rm irr}^2 + \frac{J^2}{4M_{\rm irr}^2}, \tag{2.2}$$

and the irreducible mass of a Kerr BH, $M_{\rm irr}$, where $J^2/(4M_{\rm irr}^4) \leqslant 1$. Therefore, the Kerr BH's mass is a function of two parameters J and $M_{\rm irr}$. The papers by Christodoulou et al. (1971) and Hawking (1971) introduced the relation between the irreducible mass and the surface area of the BH,

$$S = 16\pi M_{\rm irr}^2, \tag{2.3}$$

both monotonically increase in irreversible transformations. The surface area further linearly related entropy of BH (Bekenstein, 1973b).

2.2.1 Change of Irreducible Mass

Inverting Eq. (2.2), the irreducible mass can be expressed as a function of the BH mass and angular momentum. There are two negative and two positive roots. For obvious reasons, the two negative roots are discarded, and the two positive roots are

$$M_{\rm irr}^{(\pm)} = \sqrt{\frac{M^2 \pm \sqrt{M^4 - J^2}}{2}}, \tag{2.4}$$

①We use geometric units $c = G = 1$ unless otherwise specified.

which for the extreme Kerr BH coincide, i.e.,

$$M_{\mathrm{irr}} = M_{\mathrm{irr}}^{(+)} = M_{\mathrm{irr}}^{(-)} = \frac{M}{\sqrt{2}}. \tag{2.5}$$

Generally, only the plus sign root in Eq. (3.1) is physical, while the negative sign root is unphysical. For instance, the latter leads to $M_{\mathrm{irr}}^{(-)}(J = 0) = 0$, instead of the correct result, $M_{\mathrm{irr}}^{(+)}(J = 0) = M$.

Now, we consider the change of irreducible mass of a Kerr BH after absorbing the particle "1" with energy E_1 and angler momentum $p_{\phi 1}$ from the equatorial plane:

$$\Delta M_{\mathrm{irr}} = \sqrt{(M + E_1)^2 + \sqrt{(M + E_1)^4 - (\hat{a}M^2 + p_{\phi_1})^2}}/\sqrt{2} - M\sqrt{1 + \sqrt{1 - \hat{a}^2}}/\sqrt{2}. \tag{2.6}$$

It is worth noting that the change in irreducible mass exhibits nonlinear behavior with respect to μ_1 in general. Moreover, in the case of a massive particle, the quantities E_1 and $p_{\phi 1}$ can be expressed as dimensionless values. The symbol "Δ" denotes the difference between the final and the initial physical quantities. For the infinitesimal process (i.e., test particles limit), the discrete symbol "Δ" is substituted with the differential symbol "d", as discussed in the next chapter.

2.2.2 Transformable Energy

Contrasting irreducible mass, we define the transformable energy of a BH as:

$$E_{\mathrm{trans}} = M - M_{\mathrm{irr}} = \left(1 - \sqrt{\frac{1 + \sqrt{1 - \hat{a}^2}}{2}}\right) M, \tag{2.7}$$

which has been referred to in some works as rotational energy (e.g., Camenzind, 2007) and as extractable energy (Ruffini et al., 2019). For the extreme Kerr BH, the $\hat{a} = 1$, and the transformable energy is 29.2893%M. Near the extreme value, the transformable energy decreases sharply with the decrease of spin. We are interested in the change in transformable energy because it can indicate how the 'reservoir' of BH energy shrinks or expands. Differentiating Eq. (2.7), it yields:

$$\Delta E_{\mathrm{trans}} = \Delta M - \Delta M_{\mathrm{irr}}. \tag{2.8}$$

Namely, the change of transformable energy depends not only on the change of BH mass but also on the increased amount of irreducible mass of BH. The quantity ΔM_{irr} can only have a positive value, whereas ΔM can take on positive, zero, and negative values, corresponding to normal BH accretion (Zhang, 2023), the Pollock process (Pollock, 1976; King et al., 1977), and BH energy extraction, respectively.

For the energy extraction process, M decreases, but $M_{\rm irr}$ increases, so the transformable energy shrinks (see the further discussion and examples in the following section). Some studies claim that all extractable energy can be removed (Tursunov et al., 2019). However, this claim is conceptually flawed, as it neglects the feedback of the extraction process on the irreducible mass. As depicted in Fig. 2.1, only $-\Delta M$ represents the extracted energy according to the conservation of energy, while the remaining portion (of the transformable energy change) is converted into irreducible mass. This implies that less energy can be extracted from a BH than previously expected. Therefore, this naturally leads us to investigate the quantitative increase in irreducible mass for specific energy extraction processes, particularly focusing on the fundamental Penrose process.

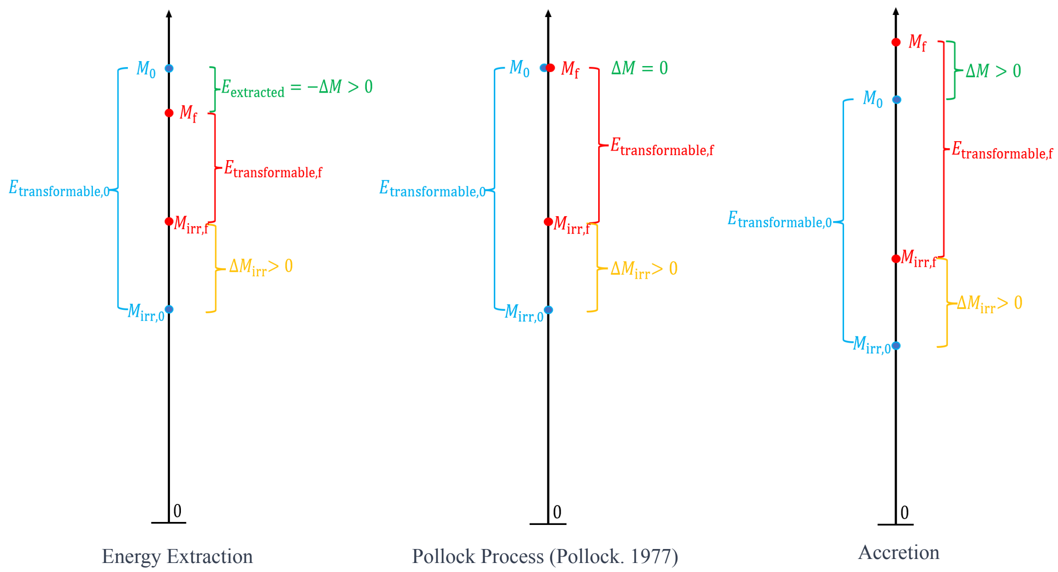

Figure 2.1 Schematic diagrams of the changes in quantities of the BH resulting from various processes. The initial state quantities of the BH are denoted by the blue color, while the final state quantities are represented by red. The green symbol indicates the amount of change in the mass of the BH, and the yellow symbol represents the amount of change in the irreducible mass. The left panel shows the process of BH's energy extraction, leading to a decrease in its mass. Simultaneously, the irreducible mass increases, both resulting in the shrinking of transformable energy. The middle panel illustrates the Pollock process (Pollock, 1976), which demonstrates the presence of a relative torque between a rotating BH and a non-axisymmetrically positioned magnetic field. This torque endeavors to bring the system into an axisymmetric configuration (King et al., 1977). Throughout this process, the mass of the BH remains constant, while the transformable energy is converted into an increase in irreducible mass. The right panel showcases the effects of normal accretion, where both the mass and irreducible mass of the BH increase.

2.3 Basic Equations and Location Constraints for Penrose Processes

The preceding discussion provides a general overview. We now shift our focus to a specific yet fundamental energy extraction process known as the ballistic Penrose process.

2.3.1 Assumptions and Effective Potential

We present the basic assumptions. We consider the classical ballistic Penrose process, namely the decay of an in-going massive particle "0" in the ergosphere of a Kerr BH (usually with initial kinetic energy zero at infinite distance), into two particles "1" and "2" with masses

$$\mu_0, \ \ \mu_1, \ \ \mu_2 \ : \ \ \mu_0 > \mu_1 + \mu_2, \tag{2.9}$$

where μ_1 can be zero as described in the appendix A.2. After decay, the particle "1" counterrotates with the BH and is in a negative energy state as measured from an infinite distance. Meanwhile, particle "2" returns to infinity with mass energy of E_2, which is larger than that of the ingoing particle, E_0, potentially resulting in the extraction of rotational energy from the BH. Following the work of Ruffini et al. (1971a), we assume that the test-particle approximation holds and decay happens at a turning point. Furthermore, the motion of test particles in the equatorial plane is considered, thus the motion is governed by an effective potential.

The effective potential is described in detail in the Appendix A.1. For massive particles, for example, the effective potential is given by

$$\frac{V}{\mu} = \frac{2\hat{a}\hat{p}_\phi \pm \sqrt{\hat{r}\left[\hat{a}^2 + \hat{r}\left(\hat{r}-2\right)\right]\left(\hat{p}_\phi^2\hat{r} + \left[\hat{r}^3 + \hat{a}^2\left(2+\hat{r}\right)\right]\right)}}{\hat{r}^3 + \hat{a}^2\left(\hat{r}+2\right)}, \tag{2.10}$$

that allows analyzing the physical trajectories on the equatorial plane of test particles with conserved energy E. The allowed regions for a particle of E are the regions with $V \leqslant E$, and the turning points occur where $V = E$ (Misner et al., 1973). The above equation introduces dimensionless quantities for the BH, $\hat{a} = J/M^2$, and for a massive test particle, $\hat{E} = E/\mu$, $\hat{p}_\phi = p_\phi/(M\mu)$ and $\hat{r} = r/M$. Here, M and J are the BH mass and angular momentum, μ and p_ϕ are the test-particle rest mass and angular momentum, and r is the radial coordinate. In this study, only the positive sign solution in Eq. (2.10) is considered, deferring discussion of the negative sign solution for future analysis. For the positive sign solution and particle motion outside the event horizon ($\hat{r} > \hat{r}^+ =$

$1+\sqrt{1-\hat{a}^2}$), an important property is revealed by the effective potential:

$$\hat{E} > \frac{\hat{a}\hat{p}_\phi}{2+2\sqrt{1-\hat{a}^2}} \tag{2.11}$$

If precisely on the event horizon, the inequality above becomes equality, but this can never occur for the Penrose process because if a particle decays on the event horizon, no particle can escape. Therefore, only inequality will be utilized in the subsequent analysis.

There are some notes in the above assumptions. Since the minimum energy of a particle is achieved when $p_r = p_\theta = 0$ (Misner et al., 1973), we analyze the decay of a particle at the turning point. Moreover, the equations (see in the Appendix A.2) are simplified when decay occurs at the turning point; otherwise, the situation becomes more intricate due to the increase in free parameters. For the same reason, this process occurs on the equatorial plane, where the ergosphere reaches its maximum width, and where the effective potential for particle motion exists. Additionally, the sum of the two masses in Eq. (2.9), $\mu_1 + \mu_2$, cannot be equal to the initial particle mass μ_0 in this process. If the masses remain equal, the solution of trajectories of μ_1 and μ_2 always coincide, and they do not separate, meaning that these two particles never have a relative velocity. From a physical perspective, mass loss is necessary to generate kinetic energy in the center of the mass frame, allowing the two particles to have a relative velocity and separate.

2.3.2 Particle Decaying Processes

Now, we utilize the equations to describe the scenario in which test particle "1" and particle "2" are created through the decay of particle "0" at a turning point in the ergosphere of a Kerr BH.

The equations controlling the decaying processes are described in detail in the Appendix A.2. In generally, by setting values of $\hat{r}$, E_1 and $p_{\phi 1}$ that fulfill

$$\hat{r}\ :\ \hat{r}_+ < \hat{r} < 2 \tag{2.12a}$$

$$E_1 < 0,\ \ p_{\phi 1} < 0\ :\ \ E_1 > \frac{\hat{a}\frac{p_{\phi 1}}{M}}{2+2\sqrt{1-\hat{a}^2}}, \tag{2.12b}$$

and masses that satisfy Eq. (2.9), one can always find the corresponding positive values of geodesic conserved dimensionless quantities $\hat{E}_0$, $\hat{p}_{\phi 0}$, $\hat{E}_2$, and $\hat{p}_{\phi 2}$ from the set of equations:

$$\hat{p}_{r0} = 0, \tag{2.13a}$$

$$\mu_0 \hat{E}_0 = E_1 + \mu_2 \hat{E}_2, \tag{2.13b}$$

$$\mu_0 \hat{p}_{\phi 0} = p_{\phi 1} + \mu_2 \hat{p}_{\phi 2}, \tag{2.13c}$$

$$\mu_0 \hat{p}_{r0} = p_{r1} + \mu_2 \hat{p}_{r2}. \tag{2.13d}$$

Eq. (2.13a) guarantees that the particle "0" decays at the turning point, Eqs. (2.13b)–(2.13d) represents the conservation of energy, angular momentum, and radial momentum. For massive particle "1", E_1 and $p_{\phi 1}$ can expressed as dimensionless quantities $E_1 = \mu_1 \hat{E}_1$ and $p_{\phi 1} = \mu_1 \hat{p}_{\phi 1}$.

When particle "1" with negative energy and negative angular momentum falls into the BH, it reduces the mass and angular momentum of the BH according to

$$\Delta M = E_1 \tag{2.14}$$

and

$$\Delta J = p_{\phi 1}, \tag{2.15}$$

respectively. The energy extracted from the BH by particle "2" can be expressed as

$$E_{\text{extracted}} = \hat{E}_2 \mu_2 - \hat{E}_0 \mu_0. \tag{2.16}$$

According to the conservation of energy principle (i.e. Eq. (2.13b)), it can obtain

$$E_{\text{extracted}} = -E_1 = -\Delta M. \tag{2.17}$$

By solving Eq. (2.13) with a chosen set of parameters and utilizing the effective potential, examples of Penrose processes can be conveniently demonstrated. Usually, the parameters are chosen so that particle "0" drops from rest at infinity. But it should be noted that the specific energy of particle "0" ($\hat{E}_0$) can be equal to, larger than, or smaller than 1. Some specific examples can be found in Section 2.5.

2.3.3 Location Constraints for Penrose Processes

When the Penrose process occurs and the decay point coincides with the turning point on the equatorial plane, the decay position of the Penrose process can be constrained.

As depicted in the panels corresponding to particle "0" and particle "2" in Figs 2.7 and 2.9, the presence of a turning point is evident when the effective potential exhibits a peak outside (or at) the event horizon. Otherwise, the effective potential monotonically decreases outside the horizon as $\hat{r}$ decreases. In this case, the particles at the turning point cannot escape outward. Additionally, for particle "2" to escape to infinity, the

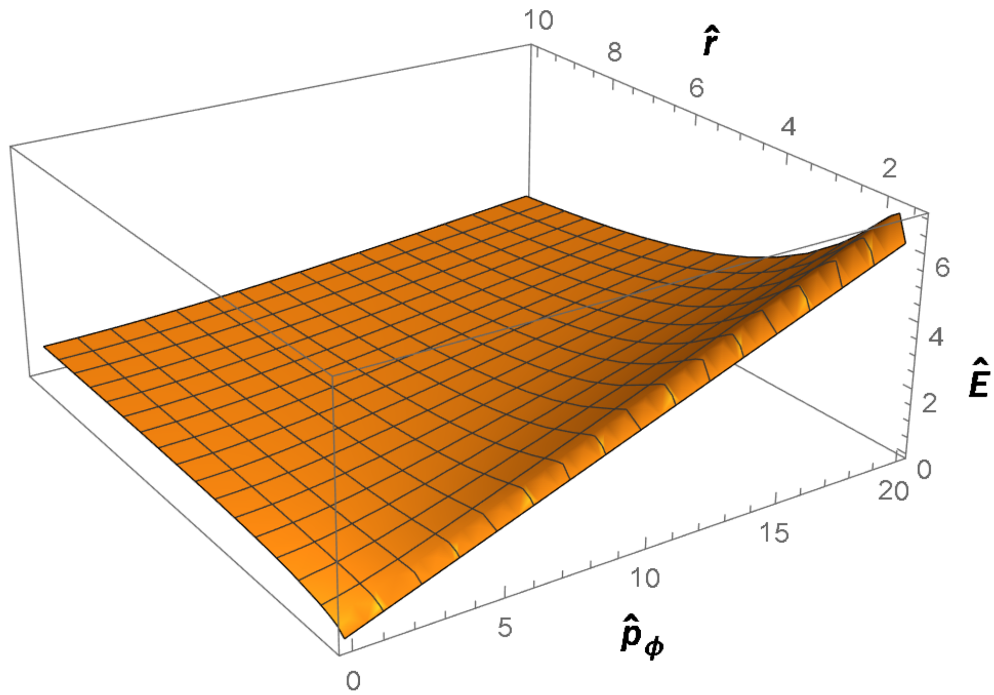

Figure 2.2 The effective potential of the massive test particle motion on the equatorial plane of Kerr space-time. A BH with spin $\hat{a} = 0.9$ is chosen. This figure shows the case of particles with positive angular momentum ($\hat{p}_\phi > 0$) outside the event horizon ($\hat{r} > \hat{r}_+$). The effective potential has a peak near the event horizon.

peak value of the effective potential should exceed 1. The position of this peak, denoted as $\hat{r}_{\rm peak}$, can be determined by

$$\frac{dV}{d\hat{r}}(\hat{r}_{\rm peak}) = 0. \tag{2.18}$$

Both particle "0" and particle "2" can only move at positions where $\hat{r} > \hat{r}_{\rm peak}$, indicating that the decay point occurs outside of $\hat{r}_{\rm peak}$. Any decay point inside of $\hat{r}_{\rm peak}$ is considered non-physical (refer to the example in the section 2.5). Fig. 2.2 also illustrates the effective potential of the massive particle as a function of $\hat{r}$ and $\hat{p}_\phi$. Without loss of generality, $\hat{a} = 0.9$ is selected in Fig. 2.2 as an example. It is observed that $\hat{r}_{\rm peak}$ decreases monotonically with an increase in $\hat{p}_\phi$, and as $\hat{p}_\phi$ tends to infinity, $r_{\rm peak}$ approaches $\hat{r}_{\rm peak,min}$, i.e.

$$\hat{r}_{\rm peak,min} = \lim_{\hat{p}_\phi \to \infty} \hat{r}_{\rm peak}. \tag{2.19}$$

The value of $\hat{r}_{\rm peak,min}$ is solely dependent on the spin, as depicted in Fig. 2.3. It is evident that when $\hat{a} < \frac{1}{\sqrt{2}}$, $\hat{r}_{\rm peak,min} > 2$, which lies beyond the outer radius of the ergosphere of a Kerr BH. This implies that when $\hat{a} < \frac{1}{\sqrt{2}}$, the decay point cannot reside within the ergosphere, thus rendering the Penrose process impossible. Consequently, we will focus solely on the scenario where $\hat{a} > \frac{1}{\sqrt{2}}$ from now on.

Moreover, more precise constraints can be obtained by specifying a given decay location $\hat{r}$ and requiring that the turning points of particles "0" and "2" lie to the

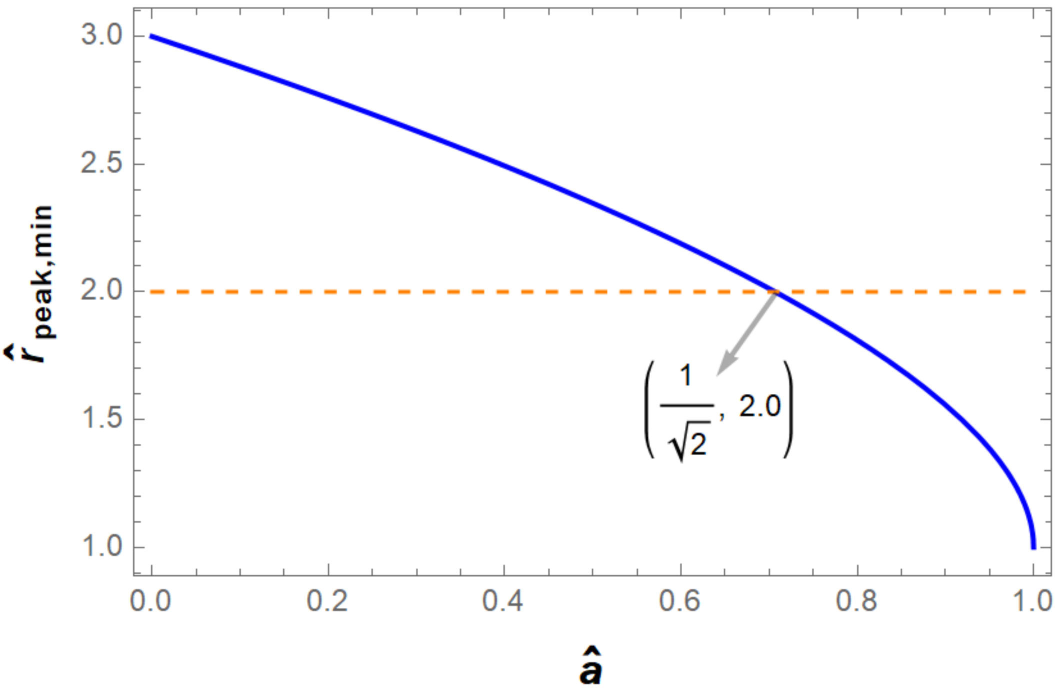

Figure 2.3 The value of $\hat{r}_{\text{peak,min}}$ is defined in Eq. (2.19) as a function of the dimensionless spin of the BH (blue curve). The orange dashed line indicates the outer radius of the ergosphere.

right of the maximum of the effective potential, $V^+_{i,\max}$. For the case $\hat{E}_0 = 1$, the above implies a spin lower limit $\hat{a}_{\min,0} = 2\sqrt{\hat{r}} - \hat{r}$, approached when $V^+_{0,\max} = \hat{E}_0 = 1$. If one allows $\hat{E}_0 > 1$, the limit situation $V^+_{2,\max} = \hat{E}_2$ imposes the spin lower limit $\hat{a}_{\min,2} = (3 - \hat{r})\sqrt{\hat{r}}/2$. Particle "1" turning point exists if the discriminant of the square root of V^+_1 is positive, implying $\hat{a}_{\min,1} = \sqrt{\hat{r}(2 - \hat{r})}$, which occurs when $\Delta = 0$ is approached, i.e., when $\hat{r}_+ = \hat{r}$. It is easy to check that $\hat{a}_{\min,0} > \hat{a}_{\min,2} > \hat{a}_{\min,1}$ for $1 < \hat{r} < 2$. Thus, the relevant spin limit in the present situation is $\hat{a} \geqslant \hat{a}_{\min,0}$. At lower spins, particle "0" reaches a turning point on the left side of $\hat{V}^+_0$, yielding a non-physical solution in classical theory. These location constraints will play a role in the repetitive Penrose process considered later.

2.4 Feedback on Irreducible Mass for Extreme Kerr BH

Up until now, what has remained incomplete is the consideration of the feedback on the irreducible mass resulting from the capture of the counterrotating test particle by the BH horizon. In other words, it involves estimating the amount of rotational energy lost by the Kerr BH through the occurrence of this energy extraction process. We initiate the discussion by examining the case of an extreme Kerr BH in this section.

2.4.1 Massive particle

The general formula of change of irreducible mass after a Kerr BH absorbed a test particle is in Appendix A.3. For the extreme Kerr BH ($\hat{a} = 1$), the change in irreducible mass after the absorption of test particle "1" with negative energy $E_1 = \hat{E}_1\mu_1$ and negative angular momentum $p_{\phi_1} = \hat{p}_{\phi 1} M\mu_1$ is given by:

$$\Delta M_{\rm irr} = \sqrt{\left(M + \hat{E}_1\mu_1\right)^2 + \sqrt{\left(M + \hat{E}_1\mu_1\right)^4 - \left(M^2 + \hat{p}_{\phi 1}M\mu_1\right)^2}}/\sqrt{2} - M/\sqrt{2}. \tag{2.20}$$

The aim is to compare this quantity with the energy extracted from a BH. Thus, the following conditions can be checked:

$$\Delta M_{\rm irr} > \mid \hat{E}_1 \mid \mu_1. \tag{2.21}$$

We introduce the quantity:

$$x_1 = \mu_1/M, \tag{2.22}$$

and rewrite inequality (2.21) as:

$$\sqrt{(1+\hat{E}_1x_1)^2 + \sqrt{(1+\hat{E}_1x_1)^4 - (1+\hat{p}_{\phi_1}x_1)^2}}/\sqrt{2} - 1/\sqrt{2} > |\hat{E}_1|x_1. \tag{2.23}$$

for $x_1 \ll 1$ one can make power expansion in the left-hand side of (2.23) and get:

$$\frac{1}{2}\sqrt{x_1}\sqrt{2\hat{E}_1 - \hat{p}_{\phi_1}} + \frac{1}{8}x_1(2\sqrt{2}\hat{E}_1 + \sqrt{2}\hat{p}_{\phi_1}) > |\hat{E}_1|x_1, \tag{2.24}$$

or:

$$\frac{1}{2}\sqrt{2\hat{E}_1 - \hat{p}_{\phi_1}}/\sqrt{x_1} + \frac{1}{8}(2\sqrt{2}\hat{E}_1 + \sqrt{2}\hat{p}_{\phi_1}) > |\hat{E}_1|. \tag{2.25}$$

It is clear that for small x_1 this inequality tends to the inequality $\hat{E}_1 > \hat{p}_{\phi_1}/2$. Thus, the following theorem is obtained:

$$\text{if } \mu_1 \ll M \text{ then } \Delta M_{\rm irr} > |\hat{E}_1|\mu_1, \tag{2.26}$$

or: for any given $\hat{E}_1 < 0$ and $\hat{p}_{\phi_1} < 0$, there exist $\mu_1 < M$ such that $\Delta M_{\rm irr} > |\hat{E}_1|\mu_1$. Even more, for any given $\hat{E}_1 < 0$ and $\hat{p}_{\phi_1} < 0$, there exist $\mu_1 < M$ such that $\Delta M_{\rm irr} > h|\hat{E}_1|\mu_1$, where h is a any positive number.

In Table 2.1 we present some numerical examples corresponding to different μ_1/M ratios. Note that we regard μ_0, μ_1, and μ_2 as test particles. We adopt the test particle approximation for particles with mass satisfying $\mu/M < 10^{-2}$. Therefore, as long as the ratio of μ_0, μ_1, and μ_2 are kept fixed, their dimensionless solutions from Eqs. (2.13) are the same. From these examples, it follows that the absolute value of ΔE_{trans} becomes smaller and smaller and tends to 0 as μ_1/M decreases, $|\Delta E_{\text{trans}}|/|E_1|$ becomes larger and larger and tends to infinity, standing Eq. (2.26). In the natural and reasonable range where $\mu_1/M \ll 1$, the conditions $\Delta M_{\text{irr}}/|E_1| \gg 1$ and $|\Delta E_{\text{trans}}| \gg |E_1|$ always hold. For the sake of rationality, in the subsequent analysis, we focus exclusively on the scenario where the mass of the test particle is significantly smaller than the mass of the BH, particularly in the case where $\mu_1/M \to 0$. For massless particles, the corresponding situation is considered where $|\frac{E_1}{M}| \to 0$ and $|\frac{p_{\phi 1}}{M^2}| \to 0$.

2.4.2 Massless particle

The proof process for massless particles is similar to that of mass particles, but it should be noted that the energy and angular momentum of massless particles cannot use dimensionless quantities.

In short, for the Penrose process in an extreme Kerr BH, whether it involves a massive particle or a massless particle falling into the BH, the amount of extracted energy from a Kerr BH is much lower than the change in irreducible mass, resulting in high irreversibility and a significant shrinkage of transformable energy.

2.5 Feedback on Irreducible Mass for General Kerr BH

Even in discussions regarding general Kerr BHs, the condition of $\hat{a} > \frac{1}{\sqrt{2}}$ continues to be considered, as specified in the restrictions outlined in the last part of Section 2.3.

Table 2.1 The change of BH angular momentum, the change of BH mass, the change of irreducible mass, their ratio, and the change of transformable energy at different μ_1/M. We keep $\hat{r} = 1.5$, $\hat{E}_1 = -1.7935$, $\hat{p}_{\phi 1} = -10$, and the ratio is maintained as $\mu_0 : \mu_1 : \mu_2 = 2.4428 : 0.1 : 0.4$.

$\mu_1[M]$	$\Delta J = p_{\phi 1}[M^2]$	$\Delta M = E_1[M]$	$\Delta M_{\text{irr}}[M]$	$\frac{\Delta M_{\text{irr}}}{\lvert E_1 \rvert}$	$\Delta E_{\text{trans}}[M]$
10^{-2}	-0.1	-1.7935×10^{-2}	0.1026	5.7181	-0.1205
10^{-3}	-0.01	-1.7935×10^{-3}	0.0376	20.9904	-0.0394
10^{-6}	-10^{-5}	-1.7935×10^{-6}	1.2638×10^{-3}	704.6711	-1.2656×10^{-3}
10^{-57}	-10^{-56}	-1.7935×10^{-57}	4.0041×10^{-29}	2.2326×10^{28}	-4.0041×10^{-29}
0	0	0	0	∞	0

2.5.1 Feedback on irreducible mass

As shown in Appendix A.3, the change in the irreducible mass of a general Kerr BH after absorbing the test particle "1" is given by:

$$\Delta M_{\rm irr} = \sqrt{(M + \hat{E}_1\mu_1)^2 + \sqrt{(M + \hat{E}_1\mu_1)^4 - (\hat{a}M^2 + \hat{p}_{\phi_1}M\mu_1)^2}}/\sqrt{2} - M\sqrt{1 + \sqrt{1 - \hat{a}^2}}/\sqrt{2}. \tag{2.27}$$

Similar to the example of an extreme BH, we aim to verify the following condition:

$$\Delta M_{\rm irr} > h|\hat{E}_1|\mu_1, \tag{2.28}$$

here, h is currently an arbitrary positive constant, but its corresponding relationship with $\hat{a}$ will be established in the subsequent analysis.

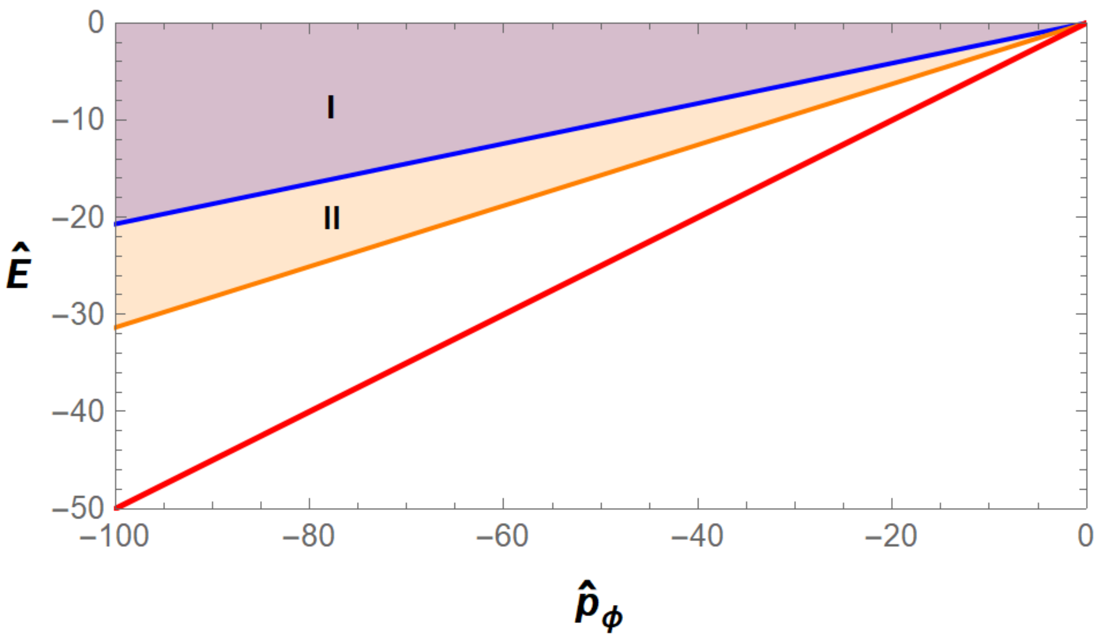

Figure 2.4 The region given by Eq. (2.31) and Eq. (2.32). The blue line gives the boundary of Eq. (2.31), and the orange line gives the boundary of Eq. (2.32). $\hat{a} = 0.9$ has been chosen here. When $\hat{a} = 1$, the regions given by Eq. (2.31) and Eq. (2.32) coincide, and the red solid line indicates their boundary.

The quantity $x_1 = \mu_1/M$ can be introduced, and inequality (2.28) can be rewritten as:

$$\sqrt{(1 + \hat{E}_1x_1)^2 + \sqrt{(1 + \hat{E}_1x_1)^4 - (\hat{a} + \hat{p}_{\phi_1}x_1)^2}}/\sqrt{2} - \sqrt{1 + \sqrt{1 - \hat{a}^2}}/\sqrt{2} > h|\hat{E}_1|x_1. \tag{2.29}$$

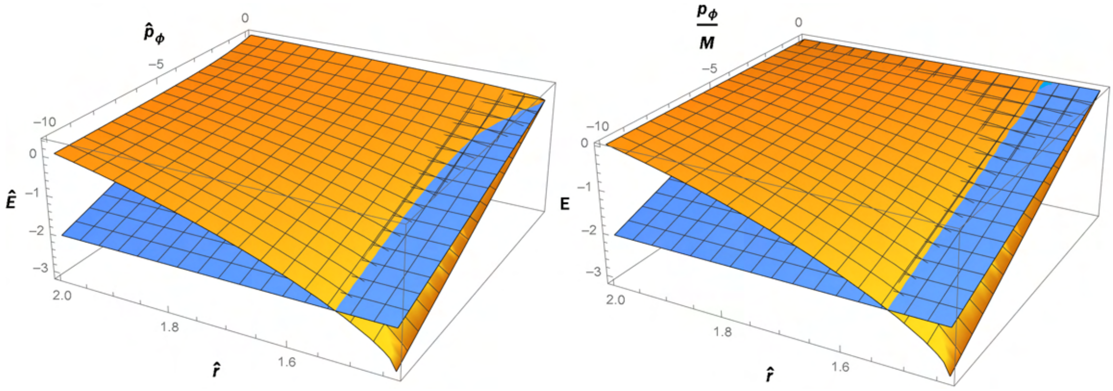

Figure 2.5 The effective potential surface (shown in orange), and the plane representing the increase in irreducible mass equal to the decrease in BH mass, i.e., Eq. (2.33) (shown in blue). The left panel illustrates the case of a massive particle, with the corresponding effective potential surface described by Eq. (2.10), while the right panel depicts the scenario of a massless particle, with the corresponding effective potential surface described by Eq. (A.9). The figure is drawn within the energy ergosphere ($\hat{r}^+ < \hat{r} < 2$), and for particles with negative angular momentum ($p_\square < 0$), a BH spin of $\hat{a} = 0.9$ is selected.

for $x_1 \ll 1$ one can make power expansion in the left-hand side of Eq. (2.29) and get:

$$\frac{2\hat{E}_1 + \frac{2\hat{E}_1 - \hat{a}\hat{p}_{\phi 1}}{\sqrt{1-\hat{a}^2}}}{2\sqrt{2}\sqrt{1+\sqrt{1-\hat{a}^2}}} x_1 + O\left(x_1^2\right) > h|\hat{E}_1|x_1, \tag{2.30}$$

or

$$\frac{1+\frac{1}{\sqrt{1-\hat{a}^2}}}{\sqrt{2+2\sqrt{1-\hat{a}^2}}}\left(\hat{E}_1 - \frac{\hat{a}\hat{p}_\phi}{2+2\sqrt{1-\hat{a}^2}}\right) x_1 + O\left(x_1^2\right) > h|\hat{E}_1|x_1. \tag{2.31}$$

While the inequality (2.11) is currently valid for any position outside the horizon, thus, we are able to demonstrate:

$$\frac{2\hat{E}_1 + \frac{2\hat{E}_1 - \hat{a}\hat{p}_{\phi 1}}{\sqrt{1-\hat{a}^2}}}{2\sqrt{2}\sqrt{1+\sqrt{1-\hat{a}^2}}} x_1 > 0. \tag{2.32}$$

However, we are unable to prove the Eq. (2.30) as we did in the last section.

Set $\hat{a} = 0.9$ and given $h = 1$, the regions given by inequalities (2.31) and (2.32) are shown in Fig. 2.4. The blue line represents the boundary of inequality (2.31), and the orange line represents the boundary of inequality (2.32), corresponding to the event horizon where the inequality (2.32) becomes equality. That is, region I satisfies $\Delta M_{\mathrm{irr}} > |E_1|$, while region II has $\Delta M_{\mathrm{irr}} < |E_1|$. Indeed, an extreme Kerr BH offers a fortunate case where the condition $\Delta M_{\mathrm{irr}} > |E_1|$ can be reduced to $\hat{E}_1 > \hat{p}_{\phi 1}/2$, resulting in the coincidence of the two boundary lines, as depicted in the red line. However, the same advantageous feature is not present for a non-extreme Kerr BH. The region where $\Delta M_{\text{irr}} > |E_1|$ becomes significantly constrained. Nevertheless, further limitations on the irreducible mass feedback can be explored according to the location constraints of the Penrose process.

2.5.2 Restrictions on Irreducible Mass Feedback

The main objective of the following analysis is to find the lower limit of irreducible mass feedback (as a function of BH spin) in the Penrose process.

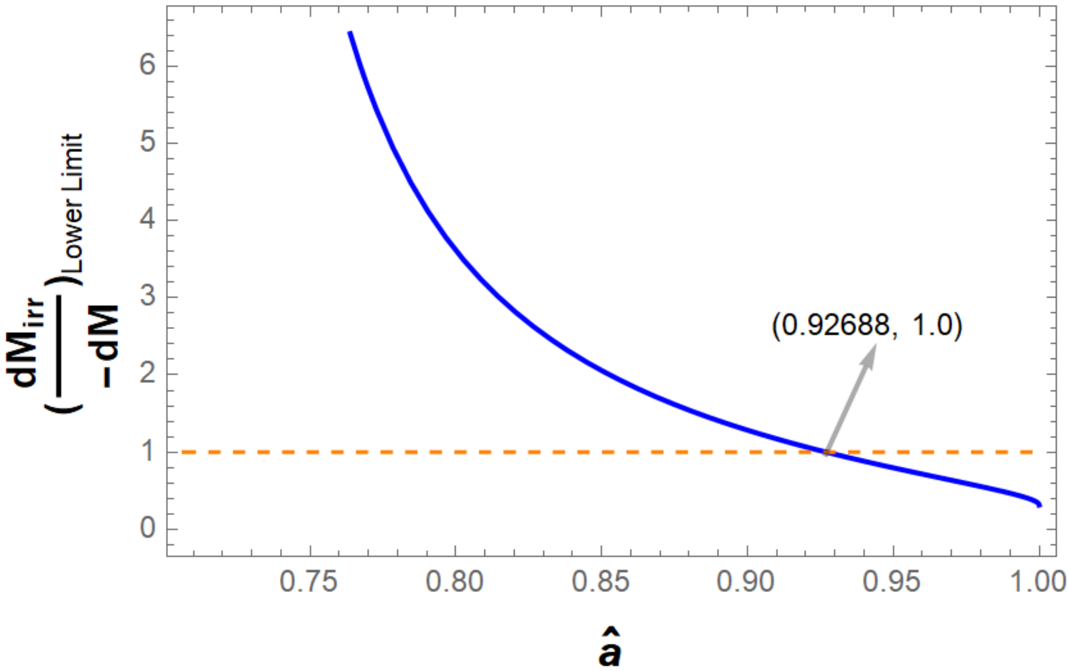

Figure 2.6 Restrictions on irreducible mass feedback for different spin of the BH, i.e the lower limit of increased irreducible mass as function of dimensionless spin from Eq. (2.34). The assumptions needed for this constraint are that these particles are test particles, and particle "0" decays at the turning point (while there is no need for particles "1" and "2" to be at the turning points).

We begin with the extension of Fig. 2.4, transforming it into a 3D depiction. First, we note that the effective potential given by Eq. (2.10) depends on the radius, whereas Eq. (2.31) does not contain radius. The boundary of Eq. (2.31) is

$$\frac{1 + \frac{1}{\sqrt{1-\hat{a}^2}}}{\sqrt{2+2\sqrt{1-\hat{a}^2}}}\left(\hat{E}_1 - \frac{\hat{a}\hat{p}_\phi}{2+2\sqrt{1-\hat{a}^2}}\right) = h|\hat{E}_1|, \tag{2.33}$$

from which one can express $\hat{E}_1$ as a function of $\hat{p}_\phi$. This function can be plotted as a plane. The intersection curve between this plane and the effective potential surface corresponds to the values of $\hat{r}$, denoted as $\hat{r}_{\text{crit}}$. This 3D depiction and its intersection are shown in Fig. 2.5. For massive particles, $\hat{r}_{\text{crit}}$ is a function of $\hat{p}_{\phi}$, while for massless particles, $\hat{r}_{\text{crit}}$ is a constant related to $\hat{a}$. Selecting the radius $\hat{r}$ at the event horizon ($r = r_+$) on Fig. 2.5 will give the boundary lines on Fig. 2.4. The region where particles can move is situated above the effective potential surface (orange surface), coinciding with the orange surface when particles reach the turning point. The region above the blue plane signifies $\varDelta M_{\text{irr}} > |E_1|$, while the area below the blue plane indicates $\varDelta M_{\text{irr}} < |E_1|$.

The $\hat{r}_{\text{crit}}(\hat{p}_{\phi})$ corresponding to the intersection curve in Fig. 2.5 can be solved using the combined Eq. (2.10) and Eq. (2.33). For negative $\hat{p}_{\phi}$ values, $\hat{r}_{\text{crit}}$ is a monotonically increasing function as $\hat{p}_{\phi}$ decreases. When $\hat{p}_{\phi} = 0$, $\hat{r}_{\text{crit}} = r_+$, and when $\hat{p}_{\phi}$ approaches negative infinity, $\hat{r}_{\text{crit}}$ approaches $\hat{r}_{\text{crit,max}}$. In the case of massless particles, $\hat{r}_{\text{crit}}$ remains a constant value independent of p_{ϕ} and precisely matches the $\hat{r}_{\text{crit,max}}$ value of massive particles. $\hat{r}_{\text{crit,max}}$ is solely dependent on the values of a and h. For a specific value such as $\hat{a} = 0.9$ and $h = 1$, the corresponding $\hat{r}_{\text{crit,max}}$ is 1.53. In short, any position that violates $\varDelta M_{\text{irr}} < |E_1|$ cannot exceed $\hat{r}_{\text{crit,max}}$, i.e. the condition $\varDelta M_{\text{irr}} < |E_1|$ can only occur within a limited region where $\hat{r}$ is smaller than $\hat{r}_{\text{crit,max}}$, particularly in proximity to the horizon.

On the other hand, recalling the limit value $\hat{r}_{\text{peak,min}}(\hat{a})$ that was determined in Section 2.3, we equate these two limits, i.e.,

$$\hat{r}_{\text{peak,min}}(\hat{a}) = \hat{r}_{\text{crit,max}}(\hat{a}, h). \tag{2.34}$$

By doing so, $h(\hat{a})$ can be solved as the lower limit of the increase in irreducible mass, providing the constraint on the irreducible mass feedback. This is because any physically valid solution for the decay point lies outside $\hat{r}_{\text{peak,min}}$, equated to $\hat{r}_{\text{crit,max}}$. Consequently, $\varDelta M_{\text{irr}} > h|E_1|$ holds for any physically valid solution (above the blue plane in the example of $h = 1$). The function of h with respect to $\hat{a}$ is numerically solved, as illustrated in Fig. 2.6. Therefore, the restriction on the growth of irreducible mass in the Penrose process is derived as $\varDelta M_{\text{irr}} > h|\varDelta M|$. As $\hat{a}$ approaches $\frac{1}{\sqrt{2}}$, h tends to infinity; however, in this case, the Penrose process can only occur at the outer boundary of the ergosphere. When $\hat{a}$ is less than 0.92688, h is greater than 1, indicating that the Penrose process is highly irreversible for values of below 0.92688. As $\hat{a}$ approaches 1, h approaches 0. However, it is important to note that when $\hat{a}$ equals 1, the restrictions obtained in this section are invalid, and the discussion in Section 2.4 should be referred to.

In summary, for the Penrose process occurring in a general Kerr BH, when the decay point coincides with the turning point, we can not only constrain the decay position (as shown in Fig. 2.3), but also impose a restriction on the irreducible mass feedback, $\Delta M_{\rm irr} > h|\Delta M|$, where h is a function of $\hat{a}$ as depicted in the Fig. 2.6. Based on this differential relationship, it can be further calculated that a maximum of $11.6117\%M$ of energy can be extracted, rather than $29.2893\%M$. It is noteworthy that the above proof remains applicable in the case where particle "1" is a massless particle, as $\hat{r}_{\rm crit,max}$ serves as the critical radius for massless particles.

2.5.3 Examples

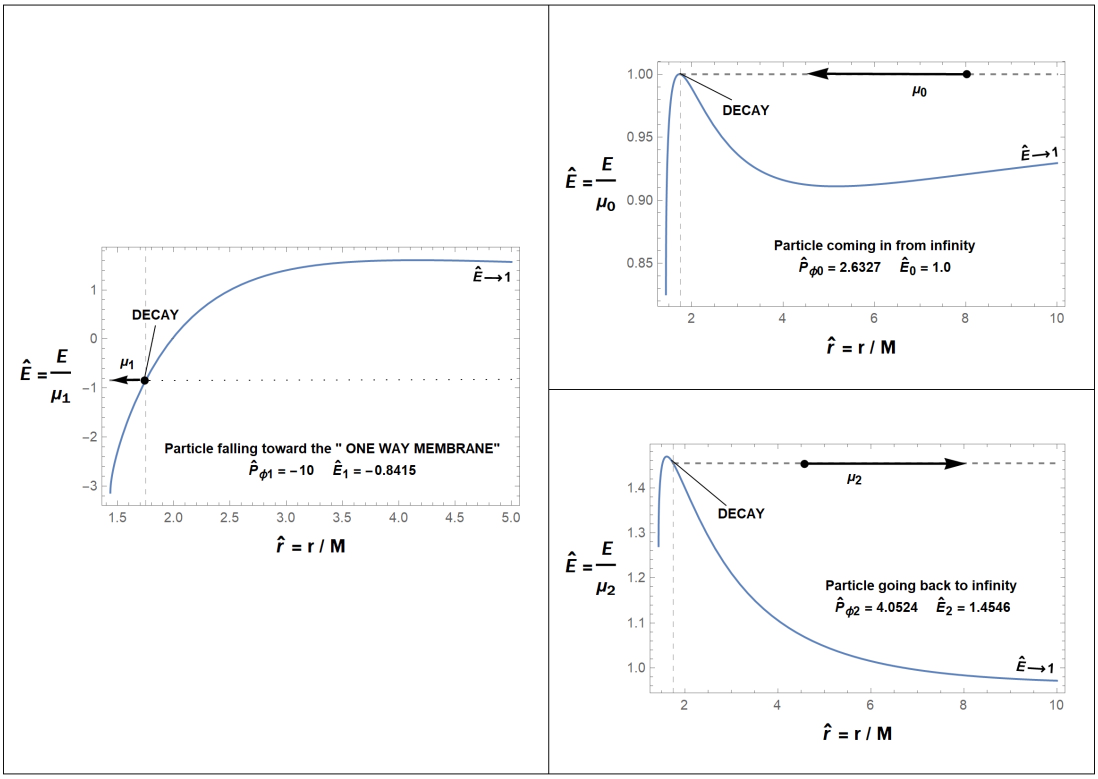

Figure 2.7 The physically feasible solution for particle "0" and particle "2" in region I of the Fig. 2.4. This process is highly irreversible ($\Delta M_{\rm irr} > | E_1 |$). In the example, $\hat{a} = 0.9$, $\hat{r} = 1.75$ is maintained, and the ratio is kept as $\mu_0 : \mu_1 : \mu_2 = 1 : 0.02 : 0.6990$.

Table 2.2 The summary of irreducible mass feedback when the mass of the test particle $\mu/M \to 0$. The columns, from left to right, represent the case number, the dimensionless spin of the BH, the location of the decay point, the ratio between the growth of irreducible mass and extracted energy in the limit of $\mu/M \to 0$, and a judgment of whether it is a physical solution. For the remaining parameters, please refer to the values in the corresponding case diagram.

Case	$\hat{a}$	$\hat{r}$	$\frac{\Delta M_{\rm irr}}{\lvert E_1 \rvert}$	physical solution?
1	0.9	1.75	$5.2955 > 1$	Yes
2	0.9	1.5	$0.7109 < 1$	No
3	0.98	1.27	$0.8962 < 1$	Yes

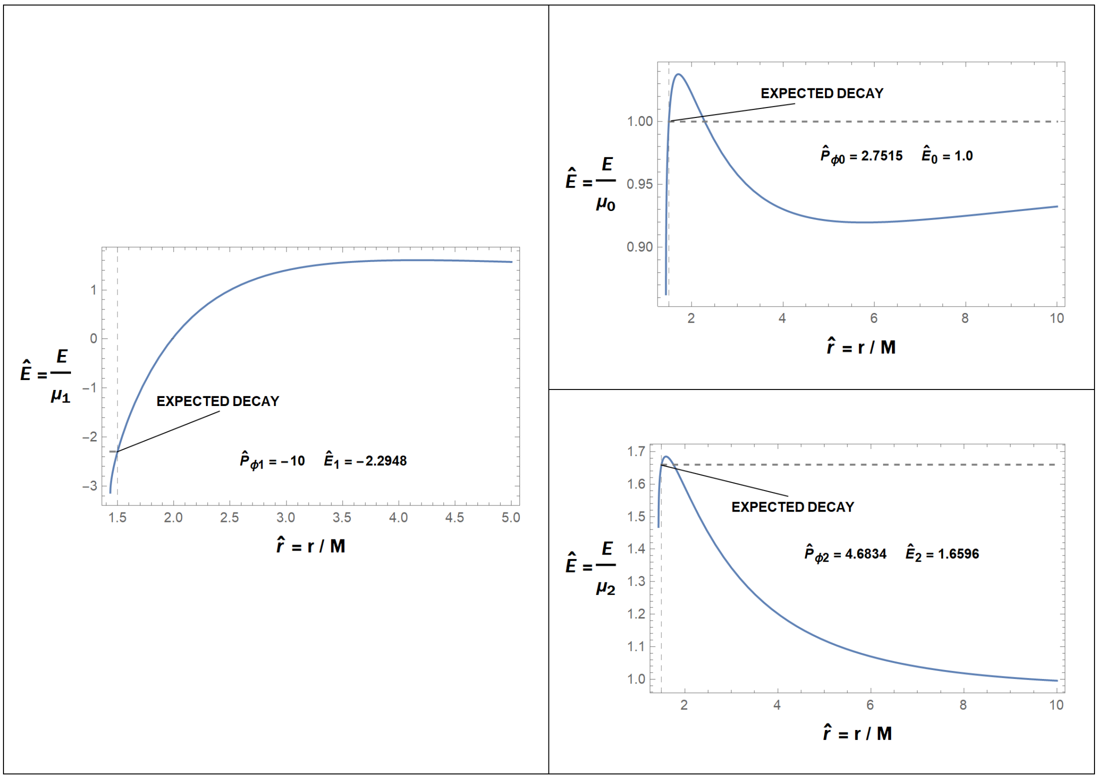

Figure 2.8 The nonphysical solution of particle "0" and particle "2" in region II of the Fig. 2.4. This process is not expected to be a highly irreversible process ($\Delta M_{\rm irr} <| E_1 |$). The vertical dashed line is the position where the particle "0" is expected to decay. In the example, $\hat{a} = 0.9$, $\hat{r} = 1.5$, $\hat{E}_1 = -2.2948$, $\hat{p}_{\phi 1} = -10$ is maintained, and the ratio kept as $\mu_0 : \mu_1 : \mu_2 = 1 : 0.02 : 0.6302$.

We have already given the general restrictions on irreducible mass feedback of the Penrose process. Now, we present several illustrative examples to improve understanding of the Penrose process in general Kerr BH and its impact on the irreducible mass.

The first case is for $\hat{a} = 0.9$ and decay point of $\hat{r} = 1.75$. The schematic diagram and corresponding parameters are presented in Fig. 2.7, and the corresponding irreducible mass feedback is summarized in the first row of values in Table 6.2. It is noteworthy that the effective potential peaks associated with particle "0" and particle "2" are both located to the left of the decay point, indicating the physical validity of this set of solutions. Furthermore, the increase in irreducible mass exceeds the decrease in the BH mass.

The second case is still for $\hat{a} = 0.9$ but the decay point of $\hat{r} = 1.5$. The schematic diagram and corresponding parameters are presented in Fig. 2.8, and the corresponding irreducible mass feedback is summarized in the second row of values in Table 6.2. Although the expected increase in irreducible mass is smaller than the decrease in the BH mass, the effective potential peaks associated with particle "0" and particle "2" are

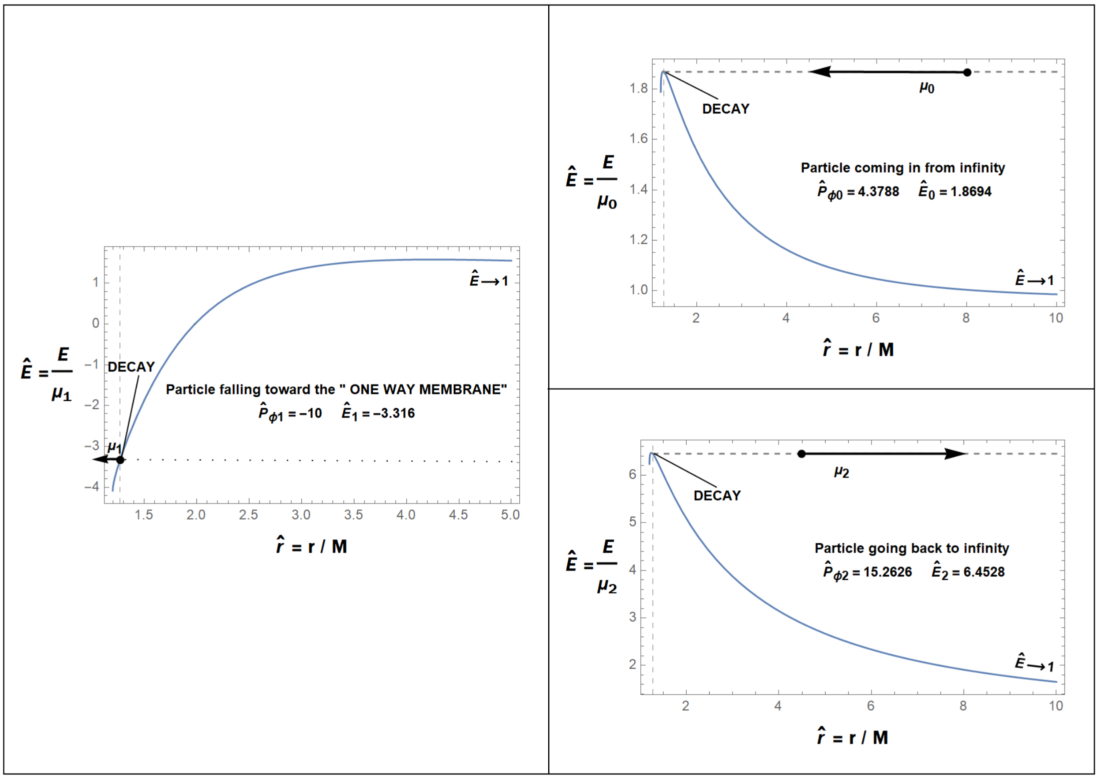

Figure 2.9 The physically feasible solution where the increase in irreducible mass is smaller than the decrease in the BH mass ($\Delta M_{\text{irr}} <\mid E_1 \mid$), i.e., this process is not a highly irreversible process. In the example, $\hat{a} = 0.98$, $\hat{r} = 1.27$ is maintained, and the ratio kept as $\mu_0 : \mu_1 : \mu_2 = 1 : 0.02 : 0.3$.

both located to the right of the decay point, indicating that these particles would need to overcome the potential barrier to reach the decay point or escape to infinity. As a result, this set of solutions is considered non-physical in classical theory. However, it is possible that the solutions may become physically meaningful when accounting for the quantum effects of the particles. Nonetheless, discussing the quantum effects is beyond the scope of this paper.

The third one is for $\hat{a} = 0.98$ and the decay point of $\hat{r} = 1.27$. The schematic diagram and corresponding parameters are presented in Fig. 2.9, and the corresponding irreducible mass feedback is summarized in the third row of values in Table 6.2. This case represents a physically valid solution, where the increase in irreducible mass is smaller than the decrease in the BH mass.

In the above examples, the first one represents a physical solution, while the second one corresponds to a non-physical solution. This distinction arises because the decay point in the first example is outside the $\hat{r}_{\text{peak,min}}(\hat{a} = 0.9)$, while the decay point in the second example falls within the $\hat{r}_{\text{peak,min}}(\hat{a} = 0.9)$. Both examples maintain $\hat{p}_\phi = -10$, resulting in relatively larger feedback on the irreducible mass in the first example due to the larger decay radius. Bringing the decay point closer to the event horizon reduces the feedback on the irreducible mass, but it may also lead to a non-physical solution, as observed in example 2. Moreover, particular attention should be given to example 3, which presents a physical solution where the increase in irreducible mass is smaller than the decrease in the BH mass. This suggests that the Penrose process is not consistently highly irreversible.

2.6 The Repetitive Nonlinear Process

We now extend the single decay to a sequence of decays, each of which follows the laws described in the previous sections and proceeds until limited by the location constraint. The BH mass and angular momentum at the nth process depends on the energy $E_{1,n-1}$ and angular momentum $p_{\phi 1}$ of the particle that the BH captured in the preceding $n-1$ process, as follows

$$M_n = M_{n-1} + \Delta M_{n-1}, \quad \Delta M_{n-1} = \hat{E}_{1,n-1}\mu_{1,n-1}, \tag{2.35a}$$

$$L_n = L_{n-1} + \Delta L_{n-1}, \quad \Delta L_{n-1} = \hat{p}_{\phi 1}\mu_{1,n-1}M_{n-1}, \tag{2.35b}$$

leading to the changes in $\hat{a}$, $\hat{r}_+$, and $M_{\rm irr}$

$$\Delta\hat{a}_{n-1} = \frac{L_n}{M_n^2} - \frac{L_{n-1}}{M_{n-1}^2}, \tag{2.36a}$$

$$\Delta r_{+,n-1} = M_n\left(1+\sqrt{1-\hat{a}_n^2}\right) - M_0\left(1+\sqrt{1-\hat{a}_0^2}\right), \tag{2.36b}$$

$$\Delta M_{{\rm irr},n-1} = M_n\sqrt{\frac{1+\sqrt{1-\hat{a}_n^2}}{2}} - M_0\sqrt{\frac{1+\sqrt{1-\hat{a}_0^2}}{2}}. \tag{2.36c}$$

Fig. 2.10 shows the final BH parameters after the sequence of Penrose processes, following the analogous calculation described above, for decay radii in the range $\hat{r}$ = 1.01 to 1.99. The plot shows that the larger the decay radius, the lower the final spin, so the lower the rotational and extractable energy. The larger the radius, the lower the final spin at the end of the sequence, so one could think the process extracts the rotational energy efficiently. However, inspecting the irreducible mass shows it becomes larger and larger, approaching the BH mass and explaining the decrease of the extractable energy. Notice that also the extracted energy decreases for larger radii. The above demonstrates a dramatic conclusion for the Penrose process: instead of being transferred to the escaping particle, the BH rotational energy lost mostly converts into irreducible mass.

2.7 Conclusions

Determining the increase in the irreducible mass of a BH is crucial, as it not only reflects the irreversibility of the corresponding process but also renders the calculation of changes in the surface area and BH entropy effortless. Moreover, the energy extraction process in a BH reduces the BH mass while increasing the irreducible mass, both of which lead to a contraction of the transformable energy. As a result, the total energy that can actually be extracted from a BH is less than what would have been possible if no feedback had been considered. For instance, Tursunov et al. (2019) indicate that all the initial transformable energy is available for extraction. However, our results show that the energy extraction process may be highly irreversible and result in significantly less energy being extractable from a BH compared to the initial transformable energy.

To illustrate the relationship between the released energy of a BH and the increase in its irreducible mass, the Penrose process is examined as an example. We have re-derived the fundamental equations describing test particle motion and decay on the equatorial plane of a Kerr BH, considering both massive and massless particles. These equations allow us to quantitatively demonstrate the feedback of irreducible mass.

In the case of an extreme Kerr BH, as the limit $\mu_1/M \to 0$ is approached, the ratio $\Delta M_{\rm irr}/|E_1|$ tends to infinity, indicating that all the reduced transformable energy contributes to the increase in irreducible mass. This high irreversibility is demonstrated in Table 1. The amount of energy extracted from a Kerr BH using massive particles is significantly lower than the change in transformable energy.

For non-extreme Kerr BHs, the effective potential of particle motion on the equatorial plane in Kerr spacetime is analyzed. It is demonstrated that only BHs with a dimensionless spin $\hat{a}$ greater than $1/\sqrt{2}$ can undergo the Penrose process if the decay point coincides with the turning point. Based on this analysis, the lower limit for the change in irreducible mass as a function of the BH's dimensionless spin is provided (Fig. 2.6).

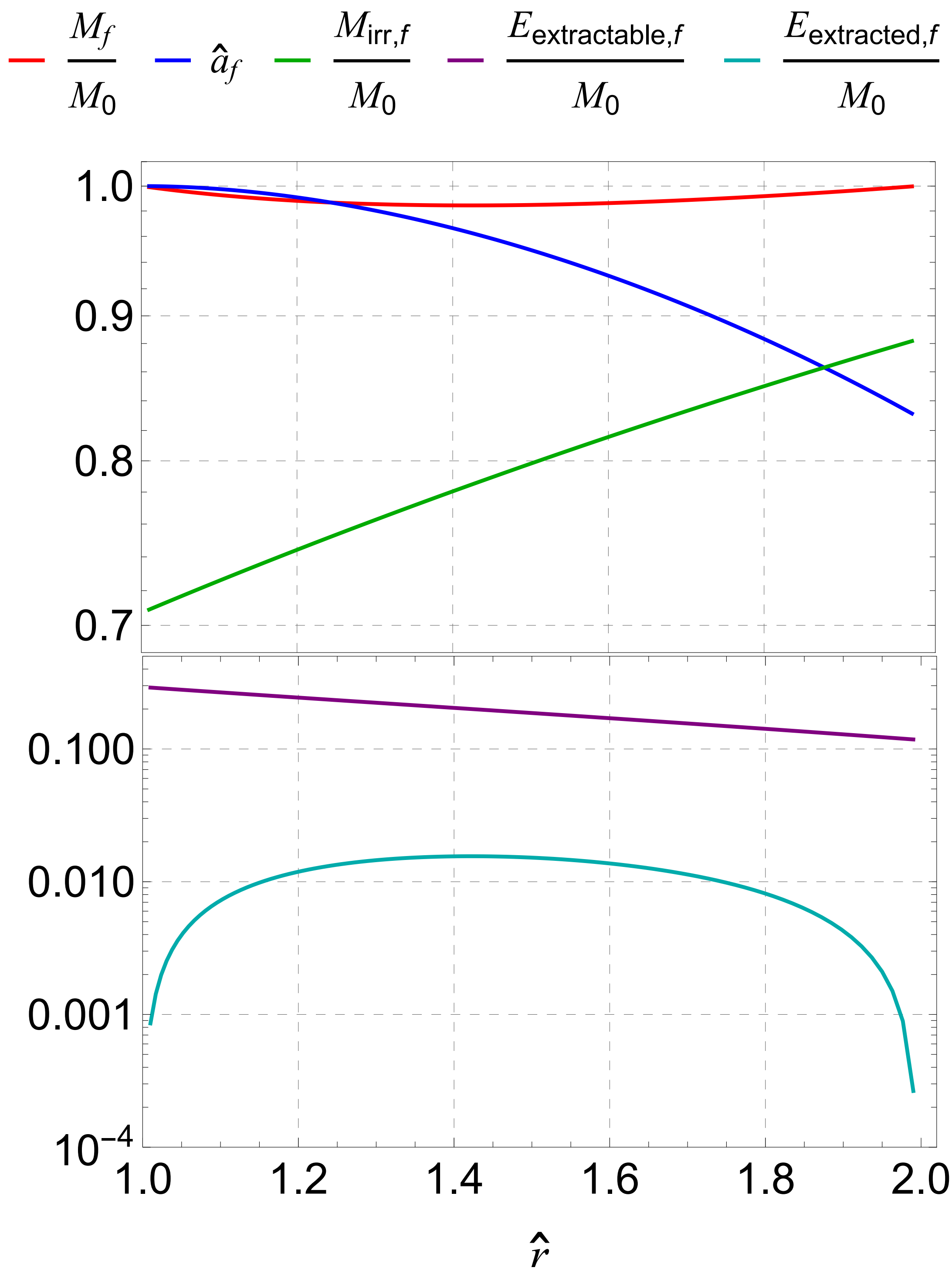

Figure 2.10 BH properties at the end of the Penrose process sequence, for $\hat{E}_0 = 1$, $\hat{p}_{\phi 1} = -19.434$, $\mu_2/\mu_1 = 0.78345$, and $\mu_0/M_0 = 10^{-2}$. The decay radii vary from $\hat{r} = 1.01$ to 1.99. Upper: BH mass, spin, and irreducible mass. Lower: Extractable and extracted energy. Notice the different scales of the vertical axis of the upper and lower plots.

Chapter 3 Roles of Irreducible Mass of a BH in Accretion Processes

3.1 Background

The previous chapter focused on energy extraction processes from black holes, during which the black hole mass decreases while the irreducible mass increases. In contrast to energy extraction, accretion serves to recharge the rotational energy reservoir harbored within, during which both the mass and the irreducible mass increase.

Accretion of matter onto black holes is a prevalent phenomenon in the cosmos. During accretion, the accreting material possesses angular momentum and forms an accretion disk around the BH. Particles gradually lose angular momentum due to friction as they approach the inner region of the accretion disk, eventually reaching the innermost stable circular orbit (ISCO) (Bardeen et al., 1972), and ultimately falling into the BH. For particles during the infall process, neglecting further loss of energy and angular momentum, they move along geodesics starting from the ISCO. The conserved quantities for the ISCO are analytically given (Hobson et al., 2006). The trajectories of particles moving along geodesics starting from the ISCO have also recently been elucidated (Mummery et al., 2022). Nevertheless, the feedback to the BH from particles falling into it, particularly concerning the irreducible mass, has not been thoroughly explored, despite its significant importance. In fact, by combining previous work (Bardeen et al., 1972; Hobson et al., 2006; Mummery et al., 2022), a quantitative computation of the irreducible mass growth can be easily performed.

This paper focuses on the accretion process onto a black hole, calculating the variations in its physical quantities induced by (test) particles falling from the ISCO. Furthermore, this framework can be extended to extreme mass-ratio inspirals (EMRIs), provided that corrections due to gravitational wave emission are properly taken into account.

3.2 Irreducible Mass Increase by Particle Capture

We start from the mass–energy formula of a Kerr black hole (Eq. 2.2). The irreducible mass can be expressed as a function of the black hole mass and angular momentum, i.e.,

$$M_{\rm irr}^2 = \frac{1}{2} M r_+, \tag{3.1}$$

whose infinitesimal change is given by

$$\mathrm{d}M_{\mathrm{irr}}^2 = \frac{Mr_+}{\sqrt{M^2 - a^2}}(\mathrm{d}M - \Omega_+ \mathrm{d}J), \tag{3.2}$$

where $\Omega_+ = a/(2Mr_+)$ is the angular velocity of the black hole, and the horizon radius is $r_+ = M + \sqrt{M^2 - a^2}$.

Let us assume the BH captures a particle of energy $E \ll M$, and angular momentum $L \ll J$. Therefore, the BH mass and angular momentum change as $\mathrm{d}M = E$ and $\mathrm{d}J = L$, then Eq. (3.2) tells that the irreducible mass changes by

$$\mathrm{d}M_{\mathrm{irr}}^2 = \frac{Mr_+}{\sqrt{M^2 - a^2}}(E - \Omega_+ L). \tag{3.3}$$

For time-like trajectories, $E \geqslant \Omega_+ L$, which implies $\mathrm{d}M_{\mathrm{irr}}^2 \geqslant 0$, as expected from Hawking's BH area increase theorem and Christodoulou-Ruffini irreversible transformations. It is clear that in the present case, the increase of M_{irr}^2 also implies the increase of M_{irr}:

$$\mathrm{d}M_{\mathrm{irr}} = \sqrt{\frac{\hat{r}_+}{2}}\frac{(E - \Omega_+ L)}{\sqrt{1 - \hat{a}^2}} \geqslant 0, \tag{3.4}$$

where we have introduced the dimensionless spin $\hat{a} \equiv a/M$ and horizon $\hat{r}_+ = r_+/M$, and used Eq. (3.1). Thus, the change of M_{irr} relative to the change of M is

$$\frac{\mathrm{d}M_{\mathrm{irr}}}{\mathrm{d}M} = \sqrt{\frac{\hat{r}_+}{2}}\frac{(1 - \Omega_+/\omega)}{\sqrt{1 - \hat{a}^2}}, \tag{3.5}$$

where we have used $\mathrm{d}M = E$ and written $\omega \equiv E/L$.

The variation of the dimensionless spin of a Kerr black hole with respect to its mass and irreducible mass is of particular interest. Equation (2.2) can be rewritten as

$$\hat{a} = \pm\frac{2M_{\mathrm{irr}}}{M^2}\sqrt{M^2 - M_{\mathrm{irr}}^2}. \tag{3.6}$$

Differentiate the above equation, we obtain

$$|\mathrm{d}\hat{a}| = \frac{4M_{\mathrm{irr}}^2 - 2M^2}{\left(M^2 - M_{\mathrm{irr}}^2\right)^{\frac{1}{2}}}\left(\frac{M_{\mathrm{irr}}}{M}\mathrm{d}M - \mathrm{d}M_{\mathrm{irr}}\right). \tag{3.7}$$

Therefore:

(i) if $\hat{a} > 0$, then $\mathrm{d}\hat{a} \geqslant 0$ is equivalent to $\frac{\mathrm{d}M}{\mathrm{d}M_{\mathrm{irr}}} \geqslant \frac{M}{M_{\mathrm{irr}}}$. When equality holds, it indicates that $\hat{a}$ has reached a stable value and will no longer increase;

(ii) if $\hat{a} < 0$, then $\mathrm{d}\hat{a} \geqslant 0$ is equivalent to $\frac{\mathrm{d}M}{\mathrm{d}M_{\mathrm{irr}}} \leqslant \frac{M}{M_{\mathrm{irr}}}$;

(iii) if $\hat{a} = 0$, then $\mathrm{d}\hat{a} \geqslant 0$ always holds as long as $L \geqslant 0$, and $\frac{\mathrm{d}M}{\mathrm{d}M_{\mathrm{irr}}}$ is always equal to $\frac{M}{M_{\mathrm{irr}}}$.

The last case can also easily be verified from

$$\mathrm{d}\hat{a} = \frac{\mathrm{d}J - 2a\,\mathrm{d}M}{M^2}. \tag{3.8}$$

3.3 Massive Particle Plunging from the ISCO

3.3.1 Energy and Angular Momentum Conservation Approximation

We first consider circular orbits of a massive particle with mass μ on the equatorial plane, $\theta = \pi/2$. We recall the effective potential for the radial motion (Ruffini et al., 1971a; Rees et al., 1974) (see also in the Appendix A):

$$V_{\rm eff} = 1 - \frac{2}{\hat{r}} + \frac{\tilde{L}^2 - \hat{a}^2(\tilde{E}^2 - 1)}{\hat{r}^2} - \frac{2(\tilde{L} - \hat{a}\tilde{E})^2}{\hat{r}^3}, \tag{3.9}$$

which leads to a radial equation of motion

$$\tilde{E}^2 = \left(\frac{dr}{d\tau}\right)^2 + V_{\rm eff}, \tag{3.10}$$

where $\tilde{E} \equiv E/\mu$ and $\tilde{L} \equiv L/(\mu M)$ are the dimensionless particle's energy and angular momentum, and τ is the proper time. Circular orbits are obtained from the conditions $\mathrm{d}r/\mathrm{d}\tau = 0$ and $\partial V_{\rm eff}/\partial r = 0$), which have energy and orbital angular momentum given by Ruffini et al. (1971a); Bardeen et al. (1972); Rees et al. (1974)

$$\tilde{E} = \frac{\rho^3 - 2\rho \pm \hat{a}}{\rho^{3/2}\sqrt{\rho^3 - 3\rho \pm 2\hat{a}}}, \tag{3.11a}$$

$$\tilde{L} = \pm\frac{\rho^4 \mp 2\hat{a}\rho + \hat{a}^2}{\rho^{3/2}\sqrt{\rho^3 - 3\rho \pm 2\hat{a}}}, \tag{3.11b}$$

where we have introduced $\rho \equiv \sqrt{\hat{r}}$, with $\hat{r} = r/M$, and the upper(lower) sign corresponds to co(counter)-rotating circular orbits.

The ISCO is given by the inflection point of the effective potential, i.e., the radius for which $\partial^2 V_{\rm eff}/\partial r^2 = 0$. The radius of the ISCO is given by Bardeen et al. (1972)

$$\hat{r}_{\rm lco} = 3 + Z_2 \mp \sqrt{(3 - Z_1)(3 + Z_1 + 2Z_2)}, \tag{3.12a}$$

$$Z_1 = 1 + (1 - \hat{a}^2)^{1/3}[(1 + \hat{a})^{1/3} + (1 - \hat{a})^{1/3}], \tag{3.12b}$$

$$Z_2 = \sqrt{3\hat{a}^2 + Z_1^2}. \tag{3.12c}$$

Thus, the ISCO's energy and angular momentum are given by $\tilde{E}_{\rm lco} = \tilde{E}(\hat{r} = \hat{r}_{\rm lco})$ and $\tilde{L}_{\rm lco} = \tilde{L}(\hat{r} = \hat{r}_{\rm lco})$, with $\hat{r}_{\rm lco}$ obtained via Eqs. (3.12), which can be rewritten as (see, e.g., Mummery et al. (2022))

$$\tilde{E}_{\rm lco} = \left(1 - \frac{2}{3\hat{r}_{\rm ico}}\right)^{\frac{1}{2}} \tag{3.13a}$$

$$\tilde{L}_{\rm lco} = 2\sqrt{3}\left(1 - \frac{2\hat{a}}{3\rho_{\rm lco}}\right). \tag{3.13b}$$

For a Schwarzschild BH ($\hat{a} = 0$), $\hat{r}_{\rm lco} = 6$, $\tilde{E}_{\rm lco} = 2\sqrt{2}/3$ and $\tilde{L}_{\rm lco} = 2\sqrt{3}$. For an extreme Kerr BH ($\hat{a} = 1$), $\hat{r}_{\rm lco} = \hat{r}_+ = 1$, and $\tilde{E}_{\rm lco} = \sqrt{3}/3$, $\tilde{L}_{\rm lco} = 2\sqrt{3}/3$.

Assuming no energy and angular momentum losses from the ISCO to the BH, we readily obtain from Eq. (3.5) the BH irreducible mass change:

$$\left(\frac{dM_{\rm irr}}{dM}\right)_{\rm lco} = \sqrt{\frac{\hat{r}_+}{2}}\frac{(1 - \Omega_+/\omega_{\rm lco})}{\sqrt{1 - \hat{a}^2}}, \tag{3.14}$$

where $\omega_{\rm lco} = E_{\rm lco}/L_{\rm lco}$.

3.3.2 Ori & Thorne Approximation

Ori et al. (2000) (hereafter OT) considered a correction of the conservative approximation, deriving approximate equations of motion and semi-analytic solutions for the transition from the adiabatic to the plunge regime. In their approximation, the angular velocity and the energy radiated in gravitational waves (GWs) are assumed equal to their ISCO values, and the boundary conditions that the solution of the equation of motion matches before the ISCO, the adiabatic motion, and, after it, a geodesic plunge. We refer to Ori et al. (2000) for the technical details.

Using the OT notation, the particle's energy and angular momentum when it crosses the BH horizon are

$$\tilde{E}_{\rm OT} = \tilde{E}_{\rm lco} - \tilde{\Omega}_{\rm lco}(\kappa\tau_0 T_{\rm plunge})\eta^{4/5}, \tag{3.15a}$$

$$\tilde{L}_{\rm OT} = \tilde{L}_{\rm lco} - (\kappa\tau_0 T_{\rm plunge})\eta^{4/5}, \tag{3.15b}$$

where $\eta = \mu/M$, $T_{\rm plunge} = 3.412$, $\tau_0 = (\alpha\beta\kappa)^{-1/5}$, $\tilde{\Omega}_{\rm lco} = 1/(\hat{r}_{\rm isco}^{3/2} + \hat{a})$, and

$$\kappa = \frac{32}{5}\frac{1 + \hat{a}/\hat{r}_{\rm lco}^{3/2}}{1 - 3/\hat{r}_{\rm lco} + 2\hat{a}/\hat{r}_{\rm lco}^{3/2}}\tilde{\Omega}_{\rm lco}^{7/3}\dot{E}_{\rm lco}, \tag{3.16}$$

$$\begin{aligned}\alpha = {} & \frac{3}{\hat{r}_{\rm lco}^6}\{\hat{r}_{\rm lco}^2 + 2[\hat{a}^2(\tilde{E}_{\rm lco}^2 - 1) - \tilde{L}_{\rm lco}^2]\hat{r}_{\rm lco} \\ & + 10(\tilde{L}_{\rm lco} - \hat{a}\tilde{E}_{\rm lco})^2\},\end{aligned} \tag{3.17}$$

$$\begin{aligned}\beta = {} & \frac{2}{\hat{r}_{\rm lco}^4}\{(\tilde{L}_{\rm lco} - \hat{a}^2\tilde{\Omega}_{\rm lco}\tilde{E}_{\rm lco})\hat{r}_{\rm lco} \\ & - 3(\tilde{L}_{\rm lco} - \hat{a}\tilde{E}_{\rm lco})(1 - \hat{a}\tilde{\Omega}_{\rm lco})\},\end{aligned} \tag{3.18}$$

with $\dot{E}_{\rm lco}$ the general relativistic correction to the energy loss (per unit μ) of a binary in circular orbit (of radius $r_{\rm lco}$ by quadrupolar gravitational-wave emission within the classic point-like approximation (Peters et al., 1963; Peters, 1964a). OT adopted the numerical values of $\dot{E}_{\rm lco}$ given for specific BH spins in Table II of Finn et al. (2000).

In this case, the increase of the BH irreducible mass given by Eq. (3.5) reads:

$$\left(\frac{\mathrm{d}M_{\mathrm{irr}}}{\mathrm{d}M}\right)_{\mathrm{OT}} = \sqrt{\frac{\hat{r}_+}{2}}\frac{(1-\Omega_+/\omega_{\mathrm{OT}})}{\sqrt{1-\hat{a}^2}}, \tag{3.19}$$

where $\omega_{\mathrm{OT}} = E_{\mathrm{OT}}/L_{\mathrm{OT}}$, with E_{OT} and L_{OT} given by Eq. (3.15). Figure 3.1 compares the change in the BH irreducible mass in the conservative and OT approximations given by Eqs. (3.14) and (3.19), for co-rotating ($\hat{a} > 0$) and counter-rotating ($\hat{a} < 0$) orbits.

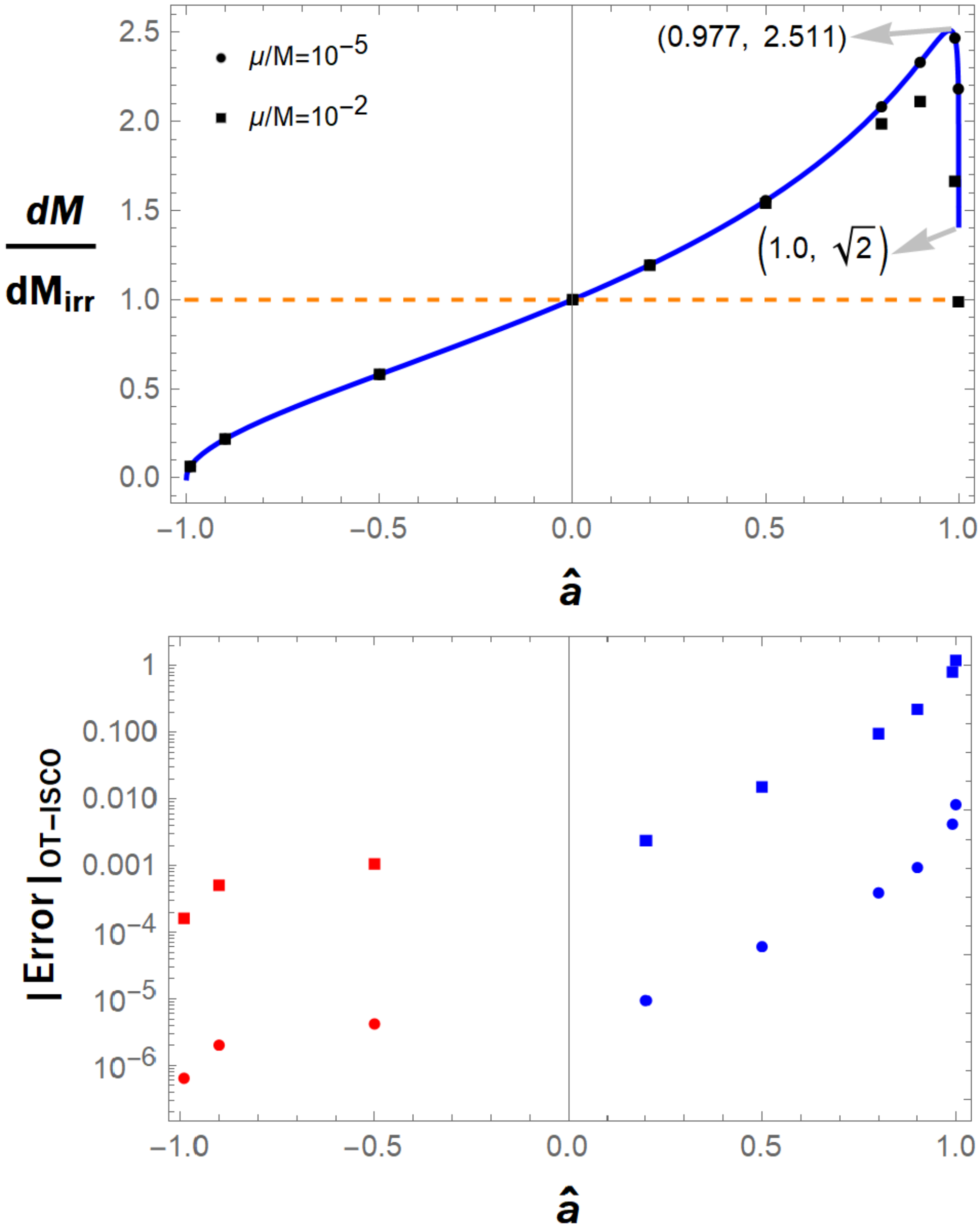

Figure 3.1 Comparison of the change in the BH irreducible mass in the conservative (blue curve) and OT (dots, $\eta = 10^{-5}$, and squares, $\eta = 10^{-2}$) approximations using Eqs. (3.14) and (3.19), respectively, for co-rotating ($\hat{a} > 0$) and counter-rotating ($\hat{a} < 0$) orbits. The lower panel shows the absolute value of the difference between the OT and the conservative approximations. The red color indicates where the difference is positive, and the blue color where it is negative. At $\hat{a} = 0$, there is no difference between the two approximations.

3.3.3 Helicoidal-Drifting-Sequence (HDS) Approximation

In Rodriguez et al. (2018), a still different approximation of the particle infalling to the BH from the ISCO was presented, the helicoidal-drifting-sequence (HDS). The HDS abandons the adiabatic approximation accounting for the radial momentum in the particle's motion in the entire trajectory, even before the ISCO. Purely circular motion is kept only to calculate the energy and angular momentum losses by gravitational-wave radiation using the Sasaki-Nakamura method (Sasaki et al., 1982a,b) to solve the Teukolsky's radial equation (Teukolsky, 1972, 1973; Teukolsky et al., 1974). The final plunge is assumed geodesic from the ISCO radial distance. We refer to Rodriguez et al. (2018) for further technical details.

In the HDS, the particle's energy and angular momentum at the BH horizon can not be reduced to analytic or semi-analytic functions; they are given by

$$\tilde{E}_{\rm HDS} = \tilde{E}_{\rm lco} - |\Delta E|, \tag{3.20a}$$

$$\tilde{L}_{\rm HDS} = \tilde{L}_{\rm lco} - |\Delta L|, \tag{3.20b}$$

where $\Delta E < 0$ and $\Delta L < 0$, measure the deviations from the purely circular motion due to the gravitational-wave radiation and the radial drift and depend upon the BH spin and the particle to BH mass ratio, η. More quantitatively, it approximately follows $\Delta E/\mu \propto (\eta)^{0.72}$ and $\Delta L/(\mu M) \propto \eta^{0.81}$ (Rodriguez et al., 2018), rather than scaling as $\eta^{4/5}$ in the OT approximation shown in Eq. (3.15).

In this case, similar to the previous section, the increase of the BH irreducible mass given by Eq. (3.5) reads:

$$\left(\frac{{\rm d}M_{\rm irr}}{{\rm d}M}\right)_{\rm HDS} = \sqrt{\frac{\hat{r}_+}{2}}\frac{(1-\Omega_+/\omega_{\rm HDS})}{\sqrt{1-\hat{a}^2}}, \tag{3.21}$$

where $\omega_{\rm HDS} = E_{\rm HDS}/L_{\rm HDS}$, with $E_{\rm HDS}$ and $L_{\rm HDS}$ given by Eq. (3.20). Figure 3.2 compares the change in the BH irreducible mass in the conservative and HDS approximations given by Eqs. (3.14) and (3.21) for only co-rotating ($\hat{a} \geqslant 0$) orbits. This method has smaller corrections to the conservation approximation and is more accurate than the OT method.

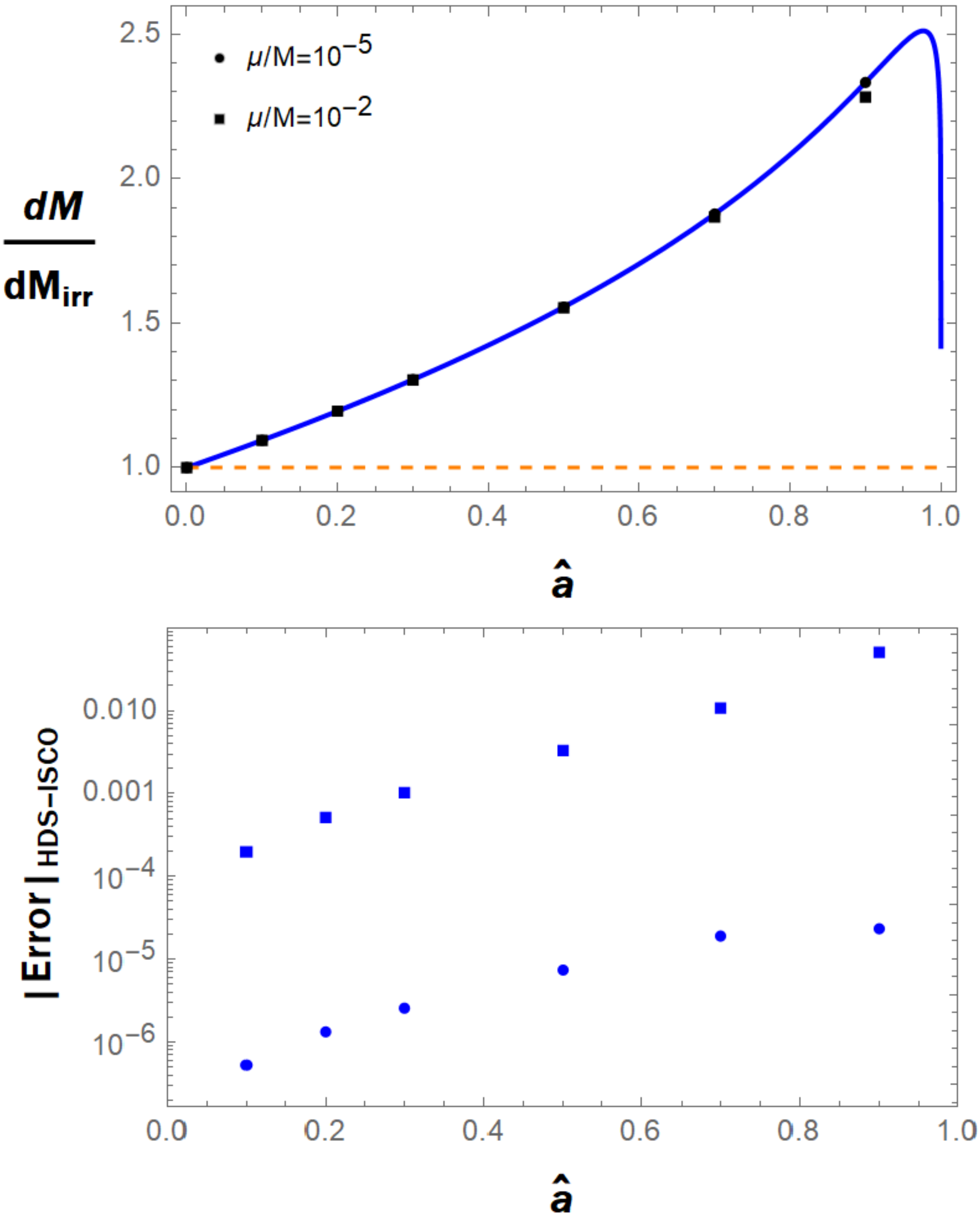

Figure 3.2 Comparison of the change in the BH irreducible mass in the conservative (blue curve) and HDS (dots, $\eta = 10^{-5}$, and squares, $\eta = 10^{-2}$) approximations using Eqs. (3.14) and (3.21), respectively, for co-rotating ($\hat{a} \geqslant 0$) orbits. The lower panel shows the absolute value of the difference between the OT and the conservative approximations. At $\hat{a} > 0$, the difference is negative, with the absolute value shown in blue. At $\hat{a} = 0$, there is no difference between the two approximations.

3.4 Massless Particle Plunging from the Unstable Circular Orbits

In a manner similar to massive particles, massless particles can also follow circular orbits known as photon rings. These photon rings, however, are unstable circular orbits. The increase in the BH's irreducible mass caused by massless particles falling from the photon ring into the BH can be computed. It is important to note that all the conservation quantities associated with the massless particles cannot be expressed in dimensionless units. The radius of the photon ring, determined by Bardeen et al. (1972), yields the function of $\frac{dM}{dM_{\rm irr}}$ with respect to the BH's spin, as depicted in Fig. 3.3. Unlike the scenario where massive particles fall from the ISCO into the BH, massless particles falling from the photon ring lead to a monotonically increasing trend of $\frac{dM}{dM_{\rm irr}}$ with respect to the BH's spin. This increase approaches the value of the extremal black hole, but not asymptotically.

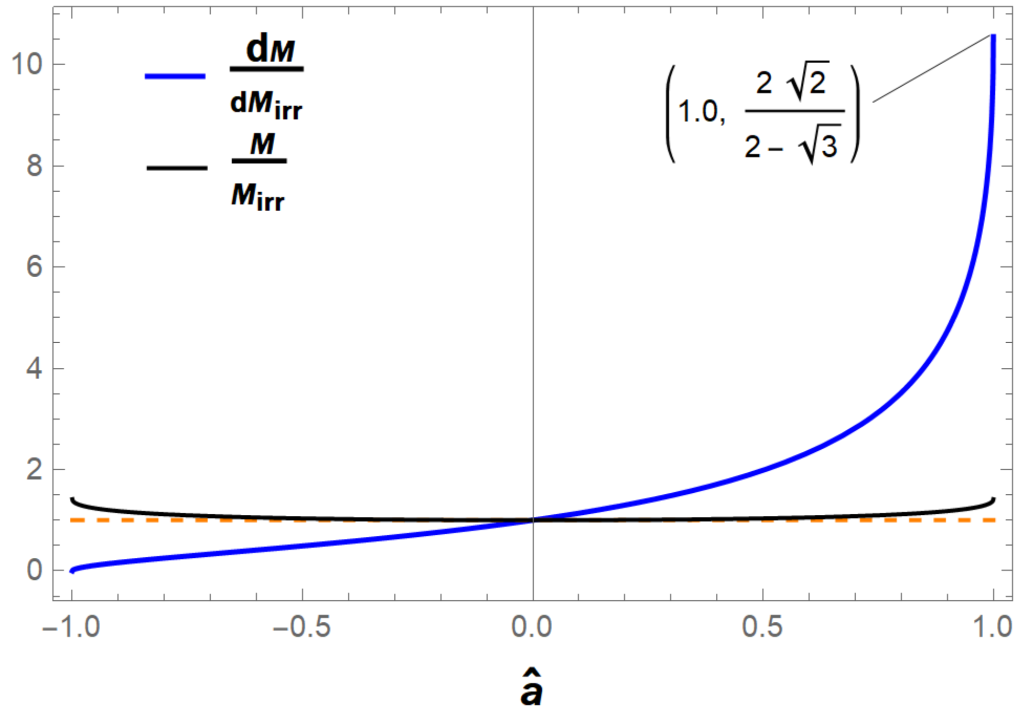

Figure 3.3 Comparison of $\frac{M}{M_{\rm irr}}$ and $\frac{{\rm d}M}{{\rm d}M_{\rm irr}}$ during the accretion of massless particles along the unstable circular orbit (corresponding to the photon ring).

3.5 Final Black Hole Parameters

We now estimate the final BH parameters, namely its mass, angular momentum, and irreducible mass, after absorbing the particle. Following the above, we can write them as

$$M_f = M + E, \tag{3.22a}$$

$$J_f = J + L, \tag{3.22b}$$

$$M_{\rm irr,f} = M_{\rm irr} + \sqrt{\frac{M r_+}{2}} \frac{E - \Omega_+ L}{\sqrt{M^2 - a^2}}, \tag{3.22c}$$

where E and L are the particle's final energy and angular momentum, i.e., their values when the particle reaches the geodesic plunge into the BH. In the conservative approximation, $E = E_{\rm lco}$ and $L = L_{\rm lco}$, in the OT approximation, $E = E_{\rm OT}$ and $L = L_{\rm OT}$, and in the HDS approximation, $E = E_{\rm HDS}$ and $L = L_{\rm HDS}$.

3.5.1 Accretion

1. Conservative approximation of massive particles

Let us assume a continuous accretion process of test particles falling to the BH from the ISCO. Each accreted particle produces an infinitesimal increase of the BH mass, $\mathrm{d}M = M_f - M = E$, angular momentum, $\mathrm{d}J = J_f - J = L$, and irreducible mass, $\mathrm{d}M_{\rm irr} = M_{\rm irr,f} - M_{\rm irr}$. Thus, the evolution of the BH mass as a function of the increasing spin parameter is given by the solution of the differential equation

$$\frac{\mathrm{d}M}{\mathrm{d}\hat{a}} = \frac{\tilde{\omega} M}{1 - 2\hat{a}\,\tilde{\omega}}, \tag{3.23}$$

where $\tilde{\omega} = M\omega = \tilde{E}/\tilde{L}$ and $\tilde{\Omega}_+ = M\Omega_+$. Thus, by integrating Eq. (3.23) one obtains $M(\hat{a})$, which can be inserted into Eq. (3.1) to get the irreducible mass as a function of the spin, $M_{\rm irr}(\hat{a})$.

In the conservative approximation, $\tilde{\omega} = \tilde{\omega}_{\rm lco} = \tilde{E}_{\rm lco}/\tilde{L}_{\rm lco}$, which is a function only of $\hat{a}$. Thus, Eqs. (3.23) can be rewritten as

$$M = M_0 \exp\left(\int_{\hat{a}_0}^{\hat{a}} \frac{\tilde{\omega}_{\rm lco}}{1 - 2\hat{a}\,\tilde{\omega}_{\rm lco}} d\hat{a}\right), \tag{3.24}$$

where we have denoted the BH initial mass and spin by M_0 and $\hat{a}_0 = J_0/M_0^2$. The evolution results in the conservative case, i.e., the mass and irreducible mass as a function of the dimensionless spin during accretion along the ISCO, are shown in Fig. 3.4. We find that if a Kerr BH begins accreting from $\hat{a} = -1$, the mass and irreducible mass will increase by a factor of approximately 3.0 to reach $\hat{a} = 1$. Therefore, if accretion starts at any other initial spin, the increase factor to reach $\hat{a} = 1$ is less than 3.0.

After reaching $\hat{a} = 1$, the BH then enters self-similar growth. Namely, the dimensionless spin will remain constant at $\hat{a} = 1$, but the mass will continue to grow as long as accretion continues along the ISCO. This is illustrated in Fig. 3.5: in the limit $\hat{a} = 1$, we have $\frac{\mathrm{d}M}{\mathrm{d}M_{\rm irr}} = \sqrt{2}$, which equals the ratio between the mass and the irreducible mass of an extremal Kerr black hole. Thus, the ratio between mass and irreducible mass no longer changes, and the dimensionless spin is fixed.

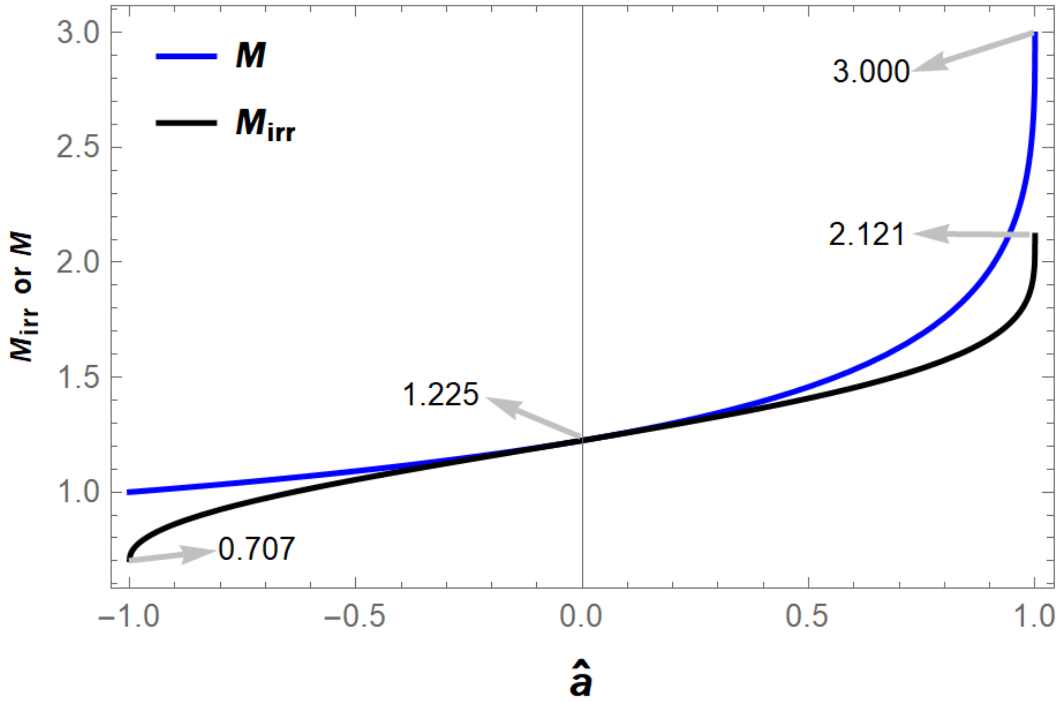

Figure 3.4 The evolution curves of the mass and irreducible mass of a Kerr BH are shown as functions of the dimensionless spin during accretion along the ISCO. The evolution always proceeds in the direction of increasing $\hat{a}$, with the values normalized to the mass at $\hat{a} = -1$. The initial spin can take any value between $-1 \leqslant \hat{a} \leqslant 1$, as long as the values are re-normalized using their initial value.

2. Massless particles

As a comparison, we also considered massless particles falling into black holes along the unstable circular orbit. As shown in Fig. 3.3, it is clear that when $\hat{a} > 0$, the inequality $\frac{\mathrm{d}M}{\mathrm{d}M_{\mathrm{irr}}} \geqslant \frac{M}{M_{\mathrm{irr}}}$ always holds. The ratio $\frac{\mathrm{d}M}{\mathrm{d}M_{\mathrm{irr}}}$ consistently increases and approaches a value of about 10 in the extremal limit, rather than $\sqrt{2}$. Although this may not be physically realistic, if a continuous stream of photons were to fall into the black hole along its unstable circular orbit, it would suggest that $\hat{a}$ does not stabilize at $\hat{a} = 1$, and may even $\hat{a} > 1$. Thus, directing a stream of photons toward an extremal black hole could potentially lead to the formation of a naked singularity.

3.5.2 Black Bole Binary Merger

The present problem of the test particle infalling progressively to the BH in circular orbits can be readily applied to the two-body problem of a merging binary. In this case, the masses μ and M of the test particle and the BH must be read as the binary reduced mass and total mass, respectively. In this case, Eqs. (3.22) give the parameters of the final BH formed from the binary merger. In particular, the test particle case accurately

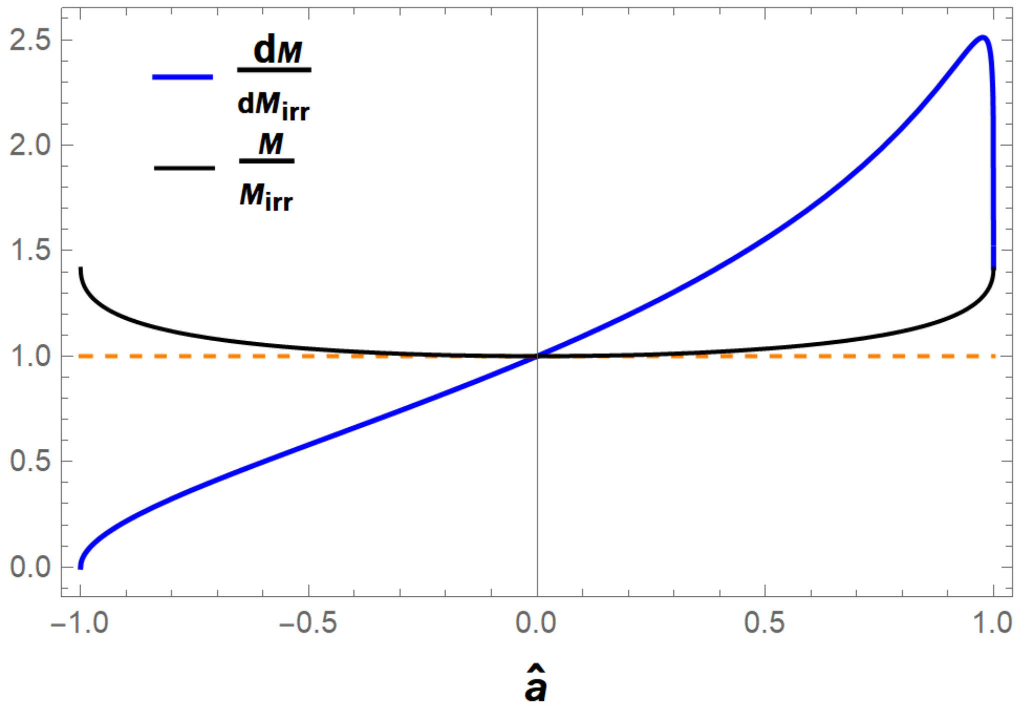

Figure 3.5 Comparison of $\frac{M}{M_{\rm irr}}$ and $\frac{\mathrm{d}M}{\mathrm{d}M_{\rm irr}}$ in the conservative approximation of particle accretion along the ISCO. The two curves coincide exactly at $\hat{a}=1$ within the range $\hat{a}>0$.

describes the so-called EMRIs, binary mergers with mass ratio $\eta=\mu/M\ll 1$.

1. EMRIs

When the secondary in EMRIs falls into the primary BH, GWs are emitted, carrying away energy and angular momentum. This emission prevents the BH's spin parameter from reaching its extremal value, instead stabilizing near it which denoted as $a_{\rm stable}$. To determine $a_{\rm stable}$, we continue to use the HDS method to calculate $\frac{\mathrm{d}M}{\mathrm{d}M_{\rm irr}}$ in cases very close to extremal spin. However, the numerical method in Section III.C for calculating the GW flux fails near extremal spin, and the transition region extends to the BH's event horizon. Therefore, we adopt the analytical formula (23) of Burke et al. (2020) to replace the numerical solution from Sasaki-Nakamura's equation, the formula reads as

$$\frac{\mathrm{d}\tilde{E}_{\rm GW}}{\mathrm{d}\tilde{t}}\approx\eta\,\tilde{C}_{\infty}\frac{r-r_+}{r_+},\tag{3.25}$$

where $\tilde{C}_{\infty}=-0.133$, which is summing the contribution of the first $|m|\leqslant l=30$ modes. Since our goal is to determine the feedback effect of EMRIs on BHs to obtain the stable spin parameter, so we just consider GWs that propagate to infinity, as waves falling into the BH would also alter the BH.

The results are shown in Fig. 3.6, illustrating $\frac{\mathrm{d}M}{\mathrm{d}M_{\rm irr}}$ of the BH for different mass ratios when a massive particle falls into a BH close to extremal spin. We compare this with $\frac{M}{M_{\rm irr}}$, and their intersection corresponds to the stable spin parameter, given in Table 6.1 for different EMRI mass ratios. This stable spin parameter can be well-described by the analytic formula,

$$1 - \hat{a}_{\rm stable} = 0.79 \times \eta^{2.06}, \tag{3.26}$$

provided the mass ratio is below 0.01. After reaching $\hat{a}_{\rm stable}$, the BH enters self-similar growth if the mass ratio of the inspiraling particles is fixed. If a series of EMRIs with random mass ratios occurs, the spin parameter of the black hole will fluctuate near the extremal value, but never reach the extremal value.

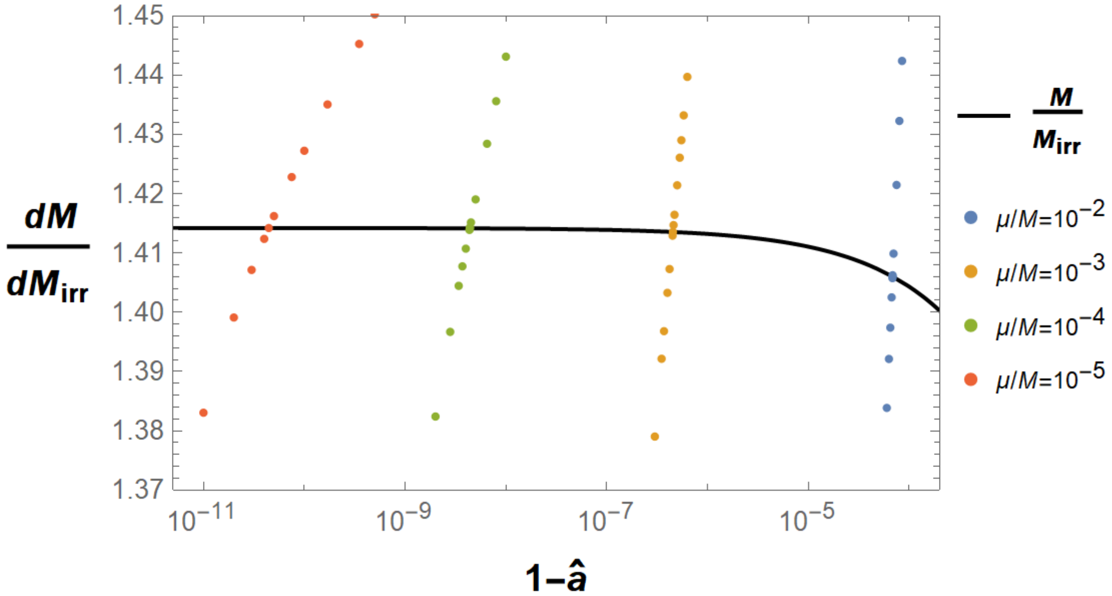

Figure 3.6 The values of $\frac{\mathrm{d}M}{\mathrm{d}M_{\rm irr}}$ in the HDS approximation during the extreme $\hat{a}$ range for different mass ratio (dots) compared with $\frac{M}{M_{\rm irr}}$ (curve).

Recall that Thorne (1974) considered a scenario where a BH simultaneously accretes matter from a disk and radiation generated by the disk. The radiation applies a negative torque to the BH, stabilizing the spin parameter at $a \approx 0.998$. Here, we follow the same philosophy but consider GWs instead of photon radiation. The GW-induced negative torque is smaller than that of photon radiation, resulting in a stable spin parameter closer to the extremal value. Even for a mass ratio of 0.01, our $1 - \hat{a}_{\rm stable}$ is approximately one order of magnitude smaller than Thorne's result. Additionally, our quantitative results align with the predicted order of magnitude for the maximum

Table 3.1 Stable $\hat{a}$. The formula $1 - \hat{a}_{\rm stable} = 0.79 \times \eta^{2.06}$ provides a good fit for mass ratios $\eta \leqslant 10^{-2}$.

$\eta = \mu/M$	10^{-2}	10^{-3}	10^{-4}	10^{-5}
$\hat{a}_{\rm stable}$	$1 - 6.84 \times 10^{-5}$	$1 - 4.53 \times 10^{-7}$	$1 - 4.38 \times 10^{-9}$	$1 - 4.44 \times 10^{-11}$

attainable spin given by Compère et al. (2020), expressed as $\sqrt{1-\hat{a}^2} \sim \eta$.

Additionally, the qualitative behavior of the BH's mass change with the spin parameter due to EMRIs can be estimated. In this case,

$$M = M_0 \exp\left(\int_{\hat{a}_0}^{\hat{a}} \frac{\tilde{\omega}_{\rm f}}{1-2\hat{a}\,\tilde{\omega}_{\rm f}} d\hat{a}\right), \tag{3.27}$$

where $\tilde{\omega}_{\rm f} = \tilde{E}_{\rm f}/\tilde{L}_{\rm f}$. We find that, whether using the OT approximation or the HDS approximation, $\tilde{\omega}_{\rm f} > \tilde{\omega}_{\rm lco}$. Consequently, the mass change between any two spin parameters due to EMRIs is greater than that in the accretion process (i.e., the conservation approximation, as shown in Fig. 3.4).

2. Binary with comparable mass components

When dealing with binaries with comparable-mass components, the perturbative methods typically used for EMRIs are generally thought to break down. However, Rodríguez et al. (2018) found that by adopting the HDS of a test particle as an effective body—essentially a Newtonian center-of-mass description—to model the merger of two black holes with comparable masses, the resulting GW waveform shows a surprisingly close agreement with numerical-relativity (NR) waveform templates. Specifically, if one adopts in the HDS treatment the same mass ratio as that used in the NR simulations, it is always possible to identify an effective spin of the Kerr black hole in the HDS framework for which the waveforms from the two approaches are in excellent agreement. In this picture, the effective spin is proportional to the mass ratio, reaching zero only in the limiting case of a vanishing mass ratio.

Nevertheless, despite the agreement in the waveforms, the mass of the newly formed black hole in NR simulations is systematically smaller than that obtained from the HDS of the test particle (Rodríguez et al., 2018). This may suggest the presence of additional gravitational radiation in the NR simulations, emitted after the passage of the particle over the ISCO. The physical origin of the remarkable agreement between the NR waveforms and those predicted by the HDS remains to be clarified, and the precise determination of the mass of the newly formed black hole will be addressed in future work.

3.6 Conclusions

Understanding the change in irreducible mass is crucial for knowing how the of BH rotational energy contracts or expands, as well as its spin evolution for BH accretion and EMRIs.

Starting from the conservation approximation, and massive particles fall into BHs along the ISCO, we find that the ratio of mass change to irreducible mass change is a non-monotonic function of dimensionless spin. It initially rises with spin, reaches a peak at $\hat{a} \approx 0.977$, and then declines sharply, ultimately stabilizing the BH as an extreme one and entering a self-similar growth phase.

In reality, however, GWs emitted during the inspiral of massive objects introduce corrections to the conservative approximation. The counter-rotating case leads to a positive correction of the change ratio to the conservative approximation, while the co-rotating case also leads to a negative correction. For a Schwarzschild BH, there is no difference between the OT method and the conservative approximation. Consequently, the dimensionless spin stabilizes before reaching the extremal limit if the mass ratio of the inspiraling particles is fixed. For the first time, using BH perturbation theory, i.e., the HDS approximation, we accurately computed the stable dimensionless spin and derived an analytical formula for its dependence on the mass ratio.

Chapter 4 Compact Object Accretion in AGN Disks

4.1 AGN Accretion Disk Profiles

The accretion of compact objects in AGN disks is greatly influenced by the physical properties of the AGN disk. Therefore, in this section, the commonly used AGN disk models in the literature, along with the corresponding physical parameters as a function of radius, are introduced.

The thin, Keplerian, steady-state accretion disk model (Shakura et al. (1973), summarized in the book Kato et al. (2008)) is commonly used as a primary approximation to describe the AGN disk. Additionally, the disk models proposed by Sirko et al. (2003) and Thompson et al. (2005), referred to as SG03 and TQM05 respectively, are also widely adopted as AGN disk models. Both models feature an inner, thin accretion disk that extends to larger radii to explain the observed AGN luminosities. In comparison to the standard thin-disk solution by Shakura et al. (1973), the SG03 model uses tabulated opacities (from Iglesias et al. (1996), and Alexander et al. (1994)) instead of analytical opacity. Moreover, it assumes the presence of a heating mechanism that generates radiation pressure, which can support the outer regions of the disk against collapse. The TQM05 model is a further development of the SG03 model, with its most notable change being that mass advection is driven by non-local torques instead of local viscous stresses. Additionally, the accretion rate in the Sirko et al. (2003) model is constant across the disk, while in Thompson et al. (2005), it varies to account for the mass lost to star formation.

4.1.1 Basic Assumptions and Equations for the Standard Thin Disk

Here, we first revisit the standard thin accretion disk model, including its analytical formulas. The radial structure of the disk is described based on the following assumptions:

(1) The gravitational field is dominated by the central object, and the disk's self-gravity is negligible.

(2) The disk is in a steady-state configuration.

(3) The disk is axisymmetric.

(4) The disk is geometrically thin in the sense that $\tilde{H}/\tilde{R} \ll 1$.

(5) The disk follows nearly Keplerian rotation, with radial inflow velocity much smaller than the rotational velocity.

(6) The disk maintains vertical hydrostatic equilibrium.

(7) The disk is optically thick in the vertical direction.

(8) The $\tilde{R}\tilde{\phi}$ component of the viscous stress tensor is proportional to the pressure.

Under these assumptions and simplifications, a set of equations describing the standard disk can be derived (see Shakura et al. (1973) for details). In summary, the model is governed by the following 11 fundamental equations:

$$\dot{M} = -2\pi \tilde{R}\tilde{v}_{\rm R}\tilde{\Sigma}, \tag{4.1}$$

$$\tilde{\Omega} = \tilde{\Omega}_K = \sqrt{\frac{GM}{\tilde{R}^3}}, \tag{4.2}$$

$$\tilde{\nu}\tilde{\Sigma} = \frac{1}{3\pi}\dot{M}\left(1 - \sqrt{\frac{\tilde{R}_{\rm in}}{\tilde{R}}}\right), \tag{4.3}$$

$$\tilde{H} = \frac{\tilde{c}_s}{\tilde{\Omega}_K}, \tag{4.4}$$

$$\frac{9}{4}\tilde{\nu}\tilde{\Sigma}\tilde{\Omega}_{\rm K}^2 = \frac{8ac\tilde{T}_{\rm c}^4}{3\tilde{\tau}}, \tag{4.5}$$

$$\tilde{p} = \frac{2\tilde{\rho}_{\rm c}k_B\tilde{T}_{\rm c}}{m_H} + \frac{a\tilde{T}_{\rm c}^4}{3}, \tag{4.6}$$

$$\bar{\kappa} = \kappa_{\rm es} + \kappa_0\tilde{\rho}\tilde{T}_{\rm c}^{-3.5}, \tag{4.7}$$

$$\frac{3}{2}\tilde{\nu}\tilde{\Omega}_K = \tilde{\alpha}\tilde{p} \quad (= -\tilde{t}_{r\varphi}), \tag{4.8}$$

$$\tilde{\Sigma} = 2\tilde{\rho}_{\rm c}\tilde{H}, \tag{4.9}$$

$$\tilde{c}_s = \left(\frac{\tilde{p}}{\tilde{\rho}_{\rm c}}\right)^{1/2}, \tag{4.10}$$

$$\tilde{\tau} = \frac{1}{2}\bar{\kappa}\tilde{\Sigma}, \tag{4.11}$$

where a is the radiation constant, $k_{\rm B}$ is the Boltzmann constant, $m_{\rm H}$ is the hydrogen atomic mass, $\kappa_{\rm es} = 0.4\ {\rm cm^2g^{-1}}$ is the electronic scattering opacity, and $\kappa_0 = 6.4 \times 10^{22}\ {\rm cm^2g^{-1}}$ for pure hydrogen plasma. The above 11 equations, from top to bottom, describe mass conservation, momentum conservation, angular momentum conservation, hydrostatic equilibrium, energy balance, the equation of state, opacity, the viscosity assumption, surface density, sound speed, and optical depth respectively. Given the black hole mass, accretion rate, and viscosity parameter (i.e., M, $\dot{M}$, and $\tilde{\alpha}$), 11 physical quantities can be determined as functions of the radius $\tilde{R}$: i.e., the radial velocity $\tilde{v}_{\rm R}$, surface density $\tilde{\Sigma}$, angular velocity $\tilde{\Omega}$, disk scale height $\tilde{H}$, density $\tilde{\rho}_{\rm c}$, kinematic viscosity coefficient $\tilde{\nu}$, sound speed $\tilde{c}_{\rm s}$, pressure $\tilde{p}$, midplane temperature $\tilde{T}_{\rm c}$, opacity $\bar{\kappa}$, and optical depth $\tilde{\tau}$. Fig. 4.1 presents numerical solutions for some basic physical quantities of the disk as functions of radius.

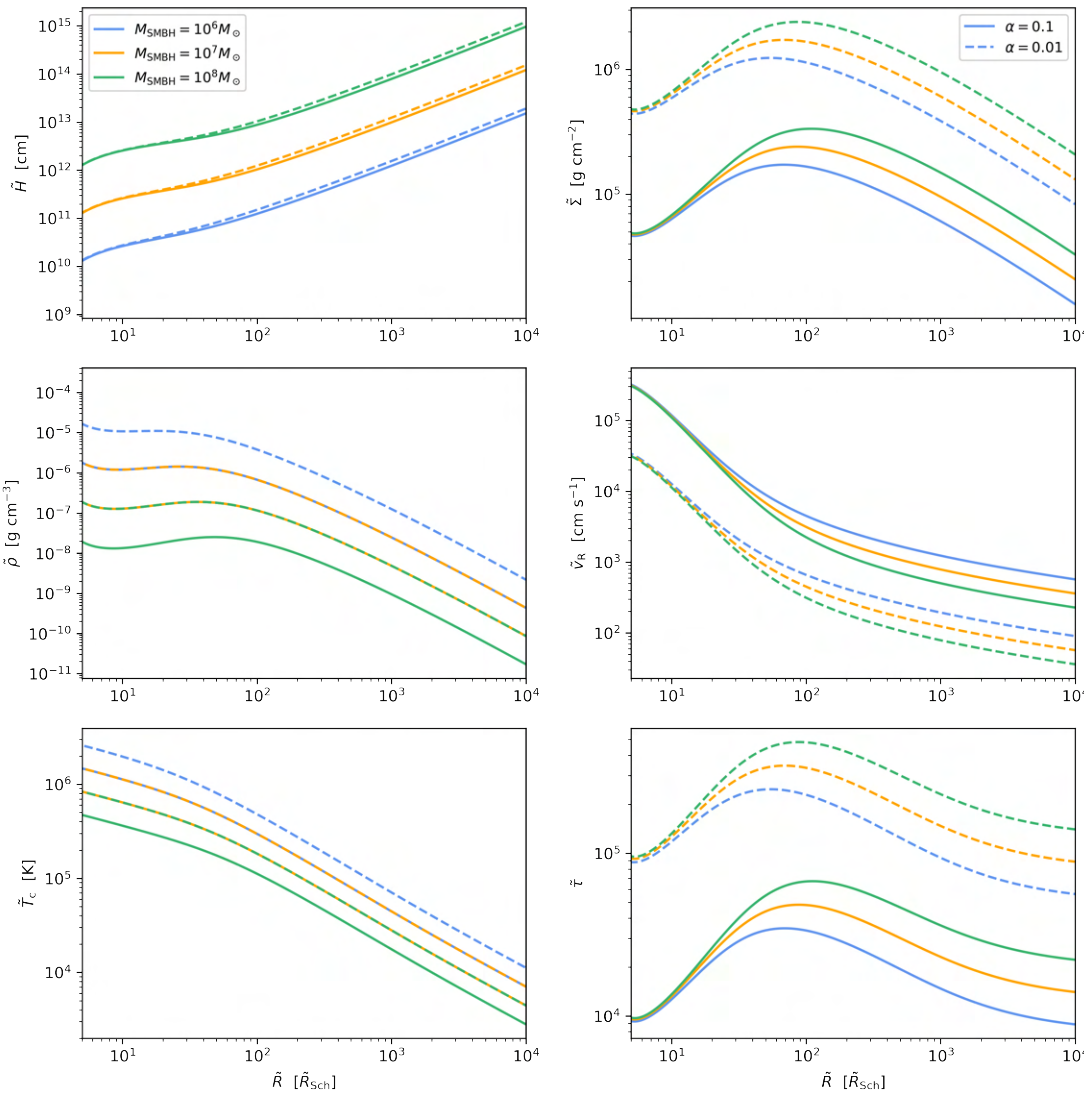

Figure 4.1 Solutions of the standard thin disk model profiles for various central SMBH masses and alpha parameters. The accretion rate of the central SMBH is assumed to be $\dot{M} = \dot{M}_{\rm crit} = 0.1\dot{M}_{\rm Edd}$.

4.1.2 Analytical Solutions of the Standard Thin Disk

The above equations can also yield analytical solutions, which are often more convenient for practical use. Depending on the dominant sources of opacity and pressure, the disk can be approximately divided into three different regions, each corresponding to a distinct analytical solution.

1. Inner region

Since the density and temperature are high enough, $\tilde{p} \sim \tilde{p}_{\rm rad}$ and $\kappa \sim \kappa_{\rm es}$ are assumed, it follows that:

$$\tilde{H} = 5.5 \times 10^4 \left(\frac{M}{M_\odot}\right)\left(\frac{\dot{M}}{\dot{M}_{\rm crit}}\right) f \text{ cm}, \tag{4.12}$$

$$\tilde{\Sigma} = 1.0 \times 10^2\, \tilde{\alpha}^{-1} \left(\frac{\dot{M}}{\dot{M}_{\rm crit}}\right)^{-1} \left(\frac{\tilde{R}}{R_{\rm Sch}}\right)^{3/2} f^{-1} \text{ g cm}^{-2}, \tag{4.13}$$

$$\tilde{\rho} = 9.0 \times 10^{-4}\, \tilde{\alpha}^{-1} \left(\frac{\dot{M}}{\dot{M}_{\rm crit}}\right)^{-1} \left(\frac{M}{M_\odot}\right)^{-2} \left(\frac{\tilde{R}}{R_{\rm Sch}}\right)^{3/2} f^{-2} \text{ g cm}^{-3}, \tag{4.14}$$

$$|\tilde{v}_R| = 7.6 \times 10^8\, \tilde{\alpha} \left(\frac{\dot{M}}{\dot{M}_{\rm crit}}\right)^{2} \left(\frac{\tilde{R}}{R_{\rm Sch}}\right)^{-5/2} f \text{ cm s}^{-1}, \tag{4.15}$$

$$\tilde{T}_c = 4.9 \times 10^7 \left(\tilde{\alpha}\frac{M}{M_{\rm crit}}\right)^{-1/4} \left(\frac{\tilde{R}}{R_{\rm Sch}}\right)^{-3/8} \text{ K}, \tag{4.16}$$

where:

$$f \equiv 1 - \sqrt{\frac{3R_{\rm Sch}}{\tilde{R}}}. \tag{4.17}$$

The Schwarzschild radius of central SMBH is

$$\tilde{R}_{\rm Sch} \equiv \frac{2GM}{c^2}. \tag{4.18}$$

The critical accretion rate is defined as

$$\dot{M}_{\rm crit} \equiv \frac{L_E}{c^2}, \tag{4.19}$$

where $L_E = 4\pi GMm_pc/\sigma_T$ is the Eddington luminosity, and σ_T is the Thomson scattering cross-section. The Eddington accretion rate is further defined as $\dot{M}_{\rm Edd} = \dot{M}_{\rm crit}/\eta$, where η represents the energy conversion efficiency; for the accretion disk of a Schwarzschild black hole, $\eta \approx 0.1$.

Note that this region exists only when the constraint is met:

$$\frac{\dot{M}}{\dot{M}_{\rm crit}} \geqslant \frac{1}{170}\left(\tilde{\alpha}\frac{M}{M_\odot}\right)^{-1/8}. \tag{4.20}$$

2. Middle region

Since the density and temperature are not too high, $\tilde{p} \sim \tilde{p}_{\rm gas}$ and $\kappa \sim \kappa_{\rm es}$are assumed, it follows that:

$$\tilde{H} = 2.7 \times 10^3\, \tilde{\alpha}^{-1/10} \left(\frac{M}{M_\odot}\right)^{9/10} \left(\frac{\dot{M}}{\dot{M}_{\rm crit}}\right)^{1/5} \left(\frac{\tilde{R}}{R_{\rm Sch}}\right)^{21/20} f^{1/5}\,\mathrm{cm}, \tag{4.21}$$

$$\tilde{\Sigma} = 4.3 \times 10^4\, \tilde{\alpha}^{-4/5} \left(\frac{M}{M_\odot}\right)^{1/5} \left(\frac{\dot{M}}{\dot{M}_{\rm crit}}\right)^{3/5} \left(\frac{\tilde{R}}{R_{\rm Sch}}\right)^{-3/5} f^{3/5}\,\mathrm{g\,cm^{-2}}, \tag{4.22}$$

$$\tilde{\rho} = 8.0\, \tilde{\alpha}^{-7/10} \left(\frac{M}{M_\odot}\right)^{-7/10} \left(\frac{\dot{M}}{\dot{M}_{\rm crit}}\right)^{2/5} \left(\frac{\tilde{R}}{R_{\rm Sch}}\right)^{-33/20} f^{2/5}\,\mathrm{g\,cm^{-3}}, \tag{4.23}$$

$$|\tilde{v}_R| = 1.7 \times 10^6\, \tilde{\alpha}^{4/5} \left(\frac{M}{M_\odot}\right)^{-3/10} \left(\frac{\dot{M}}{\dot{M}_{\rm crit}}\right)^{2/5} \left(\frac{\tilde{R}}{R_{\rm Sch}}\right)^{-2/5} f^{-3/5}\,\mathrm{cm\,s^{-1}}, \tag{4.24}$$

$$\tilde{T}_c = 2.2 \times 10^8\, \tilde{\alpha}^{-1/5} \left(\frac{M}{M_\odot}\right)^{-1/5} \left(\frac{\dot{M}}{\dot{M}_{\rm crit}}\right)^{2/5} \left(\frac{\tilde{R}}{R_{\rm Sch}}\right)^{-9/10} f^{2/5}\,\mathrm{K}. \tag{4.25}$$

The boundary between Region 1 and Region 2 is located at

$$\frac{\tilde{R}_{\rm bc}}{R_{\rm Sch}} \approx 150 \left(\tilde{\alpha}\frac{M}{M_\odot}\right)^{2/21} \left(\frac{\dot{M}}{\dot{M}_{\rm crit}}\right)^{-16/21}. \tag{4.26}$$

Since the usual case is $\tilde{R}_{\rm ab} >> 3R_{\rm Sch}$, the approximation $f(\tilde{R}_{\rm ab}) \approx 1$ is used.

3. Outer region

Since the density and temperature are low, $\tilde{p} \sim \tilde{p}_{\rm gas}$ and $\kappa \sim \kappa_{\rm ff}$are assumed, it follows that:

$$\tilde{H} = 1.5 \times 10^3\, \tilde{\alpha}^{-1/10} \left(\frac{M}{M_\odot}\right)^{9/10} \left(\frac{\dot{M}}{\dot{M}_{\rm crit}}\right)^{3/20} \left(\frac{\tilde{R}}{R_{\rm Sch}}\right)^{9/8} f^{3/20}\,\mathrm{cm}, \tag{4.27}$$

$$\tilde{\Sigma} = 1.4 \times 10^5\, \tilde{\alpha}^{-4/5} \left(\frac{M}{M_\odot}\right)^{1/5} \left(\frac{\dot{M}}{\dot{M}_{\rm crit}}\right)^{-7/10} \left(\frac{\tilde{R}}{R_{\rm Sch}}\right)^{-3/4} f^{7/10}\,\mathrm{g\,cm^{-2}}, \tag{4.28}$$

$$\tilde{\rho} = 47\, \tilde{\alpha}^{-7/10} \left(\frac{M}{M_\odot}\right)^{-7/10} \left(\frac{\dot{M}}{\dot{M}_{\rm crit}}\right)^{11/20} \left(\frac{\tilde{R}}{R_{\rm Sch}}\right)^{-15/8} f^{11/20}\,\mathrm{g\,cm^{-3}}, \tag{4.29}$$

$$|\tilde{v}_R| = 5.4 \times 10^5\, \tilde{\alpha}^{4/5} \left(\frac{M}{M_\odot}\right)^{-1/5} \left(\frac{\dot{M}}{\dot{M}_{\rm crit}}\right)^{3/10} \left(\frac{\tilde{R}}{R_{\rm Sch}}\right)^{-1/4} f^{-7/10}\,\mathrm{cm\,s^{-1}}, \tag{4.30}$$

$$\tilde{T}_c = 6.9 \times 10^7\, \tilde{\alpha}^{-1/5} \left(\frac{M}{M_\odot}\right)^{-1/5} \left(\frac{\dot{M}}{\dot{M}_{\rm crit}}\right)^{3/10} \left(\frac{\tilde{R}}{R_{\rm Sch}}\right)^{-3/4} f^{3/10}\,\mathrm{K}. \tag{4.31}$$

The boundary between Region 2 and Region 3 is located at

$$\frac{\tilde{R}_{\rm bc}}{R_{\rm Sch}} \approx 6.3 \times 10^3 \left(\frac{\dot{M}}{\dot{M}_{\rm crit}}\right)^{2/3}, \tag{4.32}$$

where the approximation $f(\tilde{R}_{\rm bc}) \approx 1$ is once again used.

4.1.3 SG03 and TQM05 Models

For the SG03 and TQM05 models, we use the pAGN code (Gangardt et al., 2024) to directly compute the radial profiles of various physical quantities. The results are shown in Fig. 4.2.

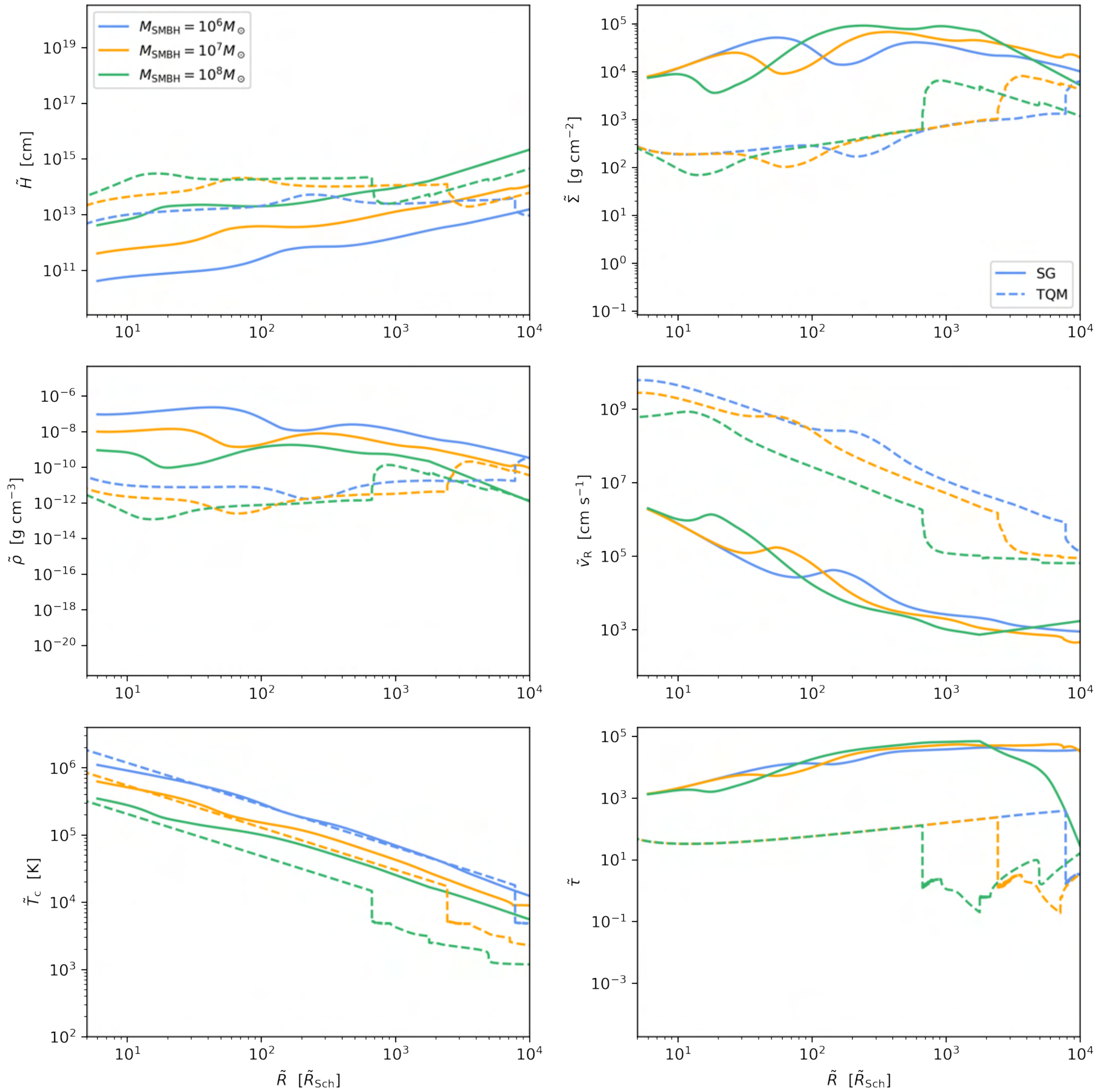

Figure 4.2 Disk profile solutions in the SG03 and TQM05 models for different central SMBH masses. The accretion rate of the central SMBH in SG03 model is assumed to be $\dot{M} = \dot{M}_{\rm crit} = 0.1\dot{M}_{\rm Edd}$. In the TQM05 model, the star formation efficiency is assumed to be $\epsilon_{\rm T} = 10^{-3}$, the global torque efficiency $m_{\rm T} = 0.2$, and the supernova radiative efficiency $\xi = 1$, as suggested by Thompson et al. (2005).

In the following analysis, we primarily adopt the standard thin disk model. To compare the effects of different AGN disk models on compact objects, it is sufficient to replace the relevant physical quantities in the analysis with those corresponding to the chosen AGN disk model and follow the same procedure.

4.2 Balck Hole Accretion in AGN Disks

In general, the accretion of various compact objects embedded in AGN disks follows a common pattern characterized by an “outer spherical, inner disk” structure, as shown in Fig. 1.15 (Wang et al., 2021a). Specifically, at the Bondi radius, accretion occurs in an approximately spherical manner. However, as the material moves inward, reaching a distance 1–2 orders of magnitude closer to the compact object, it circularizes due to the differential rotation of the AGN disk, forming a circum-CO disk (Pan et al., 2021a).This circum-CO disk is dominated by outflows. When the accretion rate surpasses roughly 1000 times the Eddington rate, no steady-state solution exists, causing outflow-driven feedback to induce episodic accretion from the AGN disk onto the compact object (Wang et al., 2021a; Chen et al., 2023a). Consequently, the average accretion rate is determined by both the instantaneous accretion rate and the duty cycle. Despite this intermittency, both the instantaneous and average accretion rates in AGN disks significantly exceed the Eddington limit. Nevertheless, the accretion processes differ significantly among BHs, NSs, and WDs, primarily due to variations in magnetic field configurations and inner accretion radii.

For BHs in AGN disks, the large-scale accretion structure is qualitatively similar to that of NSs, particularly at the Bondi scale. Consequently, when estimating characteristic scales—such as the modified Bondi radius and the circularization radius—as well as the associated accretion rates and feedback effects on the AGN disk, one can just substitute the NS mass with the BH mass in the corresponding equations (i.e., Equations (4.34)-(4.41)). The detailed calculation process for neutron stars is presented in the following section. However, for the inner region of the circum-BH disk, Chen et al. (2023a) suggests taking $r_{\rm in} \sim 10\, r_{\rm g}$ as the inner radius beyond which self-similar solutions remain valid and outflow cooling is efficient. This choice is motivated by several factors: when $r \lesssim 10\, r_g$, relativistic effects of the central compact object become significant, the strong gravitational force suppresses outflows (Jiao et al., 2015), and cooling is dominated by advection rather than outflows (Wu et al., 2022).

Additionally, during accretion, the magnetic fields surrounding the BH may accumulate (Cao, 2011) and be further amplified by outflows (e.g., Liska et al., 2020). Simultaneously, disk accretion increases the BH’s angular momentum, although turbulence within the AGN disk may prevent it from reaching high values (Chen et al., 2023b). Under these conditions, the BZ mechanism (Blandford et al., 1977) enables the extraction of spin energy through jet formation; it has a power output of $P_{\rm BZ} \propto B^2 a_{\rm BH}^2$, where B represents the magnetic field threading the black hole horizon, and $a_{\rm BH}$ denotes the dimensionless spin parameter of the BH.

As shown in left panel of the Fig. 1.17, the jet produced from the accretion of the BH interacts with the disk material, creating shocks. The diffusion of photons is slower than the propagation of the shock, causing photons to be initially trapped (Zhu et al., 2021b; Yuan et al., 2022). If the disk material is dense, jets are more likely to be choked within the disk (Zhang et al., 2024a). However, efficient shock acceleration at the reverse shock may still produce high-energy cosmic rays and neutrinos through processes like $p\gamma$ and pp (Zhu et al., 2021b; Yuan et al., 2022). While, in the case of a powerful jet and relatively low-density gas regions (Zhang et al., 2024a), the jet may penetrate the disk, possibly producing a shock breakout event associated with the GRB.

Binary black hole mergers in AGN disks are promising events for triggering intense accretion onto the remnant. The recoil kick from the merger can further enhance the accretion rate and duty cycle (Chen et al., 2024a; Tagawa et al., 2023b), and may also boost high-energy neutrino production from outflows (Ma et al., 2024). The reason the recoil kick from the merger can enhance the accretion rate is that the circum-BH accretion structure is altered. First, the gas in the annulus between the radii of the totally bound and unbound regions is perturbed by the kick, and it immediately experiences shocks. As a result of the shock, the gas is stripped of angular momentum and moves inward on a dynamical timescale. Consequently, the gas density in the inner regions of the circum-BH disk and the accretion rate onto the BH are enhanced (Tagawa et al., 2023b). Thus, if jets are launched and can break out of the disk, this could lead to an association between gravitational waves from binary black hole mergers and GRBs. Actually, even single black holes in AGN disks could accrete and produce jets, accompanied by corresponding electromagnetic signals (Tagawa et al., 2023c). However, without a merger kick to enhance accretion, their accretion rates are typically lower, leading to dimmer luminosities and the absence of associated gravitational wave counterparts, making them harder to detect.

4.3 Neutron Star Accretion in AGN Disks

Since the accretion structure of NSs is the most complex (general) and is rarely discussed comprehensively in the literature, this section provides a more detailed examination of their accretion behavior within AGN disks.

4.3.1 General Picture

NS accretion in AGN disks should have the same general properties as that of other COs, i.e., an "outer spherical, inner disk" accretion structure. However, their small radii, hard surfaces, and possibly strong magnetic fields lead to unique accretion behavior of NSs within the magnetosphere regions. Therefore, we shall demonstrate a hierarchical pattern in the accretion behavior of NSs in AGN disks, as illustrated in Fig. 4.3. The following subsections will address models at various scales and the feedback on the AGN disk.

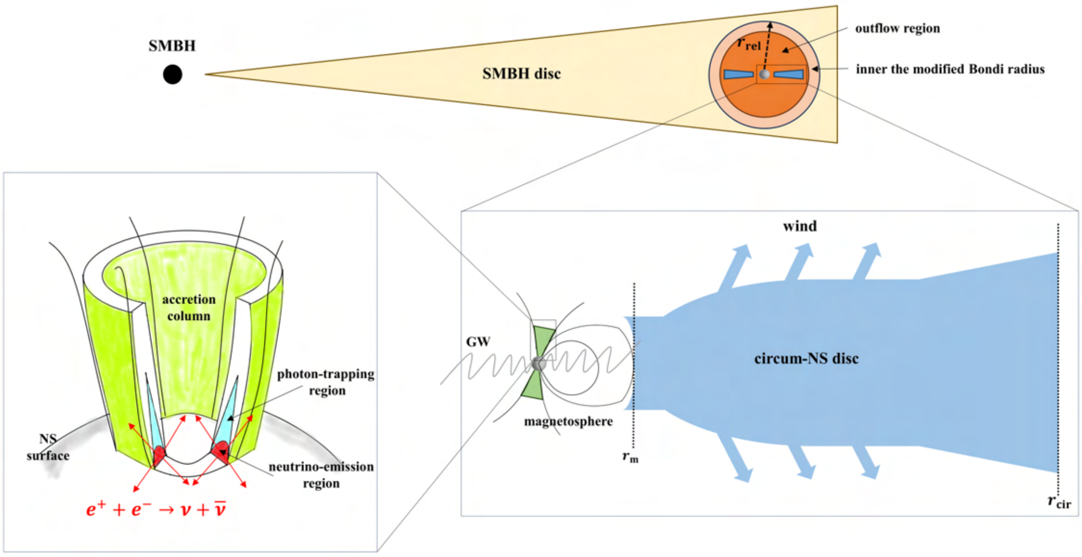

Figure 4.3 Diagram illustrating NS accretion within an AGN disk. Top panel: Accretion structure at the Bondi scale. The light orange region marks the inner part of the modified Bondi radius, while the dark orange represents the outflow region, initially surrounding the circularization radius. The formation of the circum-NS disk within this radius is shown in blue. Bottom right panel: A close-up of the circum-NS disk and its inner structure. The circum-NS disk is dominated by outflows (winds) and extends from the circularization radius ($r_{\rm cir}$) to the magnetosphere radius ($r_{\rm m}$). Then, accreted material is funneled by magnetic fields into accretion columns near the NS's polar caps, represented in green. The accreting NS may emit GWs, illustrated by gray wave lines. Bottom left panel: A close-up of the accretion column. The photon-trapping region is depicted in blue, while the neutrino-emission-dominated region appears in red. As accretion rates increase, these regions extend upward, potentially disturbing the base of the hollow accretion column, causing partial infill of the center-walled area and eventually leading to a solid column. Note that this diagram focuses on the hollow accretion column, and the fully developed cylindrical solid column is not included.

For quantitative study, we apply the numerical solution of the standard thin accretion disk to the AGN disk model. As this model excludes the effects of disk self-gravity, it is expected to more accurately describe the inner regions (up to $\sim 10^4 R_{\rm g}$) of AGN disks. Consequently, our numerical simulations are restricted within a radial range of

$2 \times 10^4 R_g$. The fiducial parameters employed in these calculations include an accretion rate of $\dot{M} = 0.1\dot{M}_{\rm Edd}$ and a viscosity parameter of $\tilde{\alpha} = 0.1$, where $\dot{M}_{\rm Edd}$ denotes the Eddington accretion rate. To simplify the treatment of vertical structure, a constant density $\tilde{\rho}_0$ is assumed within the vertical height $\tilde{Z} \leqslant \tilde{H}$, where $\tilde{H}$ is the scale height, acknowledging that for disks with an exponentially declining vertical density, the density drops significantly when $\tilde{Z} > \tilde{H}$ (Netzer, 2013). For discussions including the correction of star accretion in disks with vertical structure, see Mac Low et al. (1988); Dittmann et al. (2021); Tagawa et al. (2022). We consider a typical NS with a mass of $1.4\ M_\odot$ and a radius of 13 km. For NSs of different masses, we assume the mass-radius relationship for degenerate stars, i.e., $m_{\rm ns} r_{\rm ns}^3 = $ const., where $m_{\rm ns}$ and $r_{\rm ns}$ denote the mass and radius, respectively. In our work, the Eddington accretion rate is adopted as the reference unit for accretion rates, and is defined as

$$\dot{m}_{\rm Edd} = \frac{4\pi G m_{\rm ns} m_{\rm p}}{0.1\sigma_{\rm T} c} \approx 9.8 \times 10^{17} \left(\frac{m_{\rm ns}}{1.4 M_\odot}\right) {\rm g\ s^{-1}}, \tag{4.33}$$

where $m_{\rm p}$ represents the proton mass and $\sigma_{\rm T}$ denotes the Thomson scattering cross-section.

4.3.2 Bondi Scale

For a given AGN disk model with an NS embedded in it at a distance $\tilde{R}$ from the SMBH, we initially examine the accretion flow far from the NS, namely at the Bondi scale. In general, the accretion process for a compact object moving through a medium with uniform density is characterized by the Bondi-Hoyle-Lyttleton (BHL) accretion framework (e.g. Shapiro et al., 2008). The BHL accretion radius is expressed as:

$$r_{\rm BHL} = \frac{G m_{\rm ns}}{\left(v_{\rm rel}^2 + \tilde{c}_{\rm s}^2\right)}; \tag{4.34}$$

and the associated mass accretion rate is given by:

$$\dot{m}_{\rm BHL} = \frac{4\pi G^2 m_{\rm ns}^2 \tilde{\rho}_0}{\left(v_{\rm rel}^2 + \tilde{c}_{\rm s}^2\right)^{3/2}}, \tag{4.35}$$

where $v_{\rm rel}$ denotes the relative velocity between the NS and the surrounding disk gas, and $\tilde{c}_{\rm s}$ is the local sound speed in the AGN disk. The relative velocity is approximated by:

$$v_{\rm rel} = \frac{1}{2}\tilde{\Omega}_{\rm K} r_{\rm rel}, \tag{4.36}$$

with $\tilde{\Omega}_{\rm K}$ representing the Keplerian angular velocity of the AGN disk, and $r_{\rm rel}$ being the effective Bondi radius modified by the central SMBH tidal force and the thickness of the AGN disk. Therefore, the effective radius that defines the accretion region, termed the modified Bondi radius, is:

$$r_{\rm rel} = \min\{r_{\rm BHL}, r_{\rm Hill}\}, \tag{4.37}$$

where the Hill radius is calculated as $r_{\rm Hill} = \left(m_{\rm ns}/3M_{\rm SMBH}\right)^{1/3}\tilde{R}$. Taking into account geometric and tidal constraints, the corrected accretion rate is written as (Pan et al., 2021a):

$$\dot{m}_{\rm rel} = \min\{1, \frac{\tilde{H}}{r_{\rm Hill}}\} \times \min\{1, \frac{r_{\rm Hill}}{r_{\rm BHL}}\} \times \dot{m}_{\rm BHL}, \tag{4.38}$$

which quantifies the actual inflow rate onto the NS at the Bondi scale under the AGN disk conditions.

In the fiducial setting, the modified Bondi radii and their corresponding accretion rates at various radial locations in the AGN disk are illustrated by the blue curves in Fig. 4.4. Overall, NSs at the Bondi scale exhibit extremely high accretion rates, typically exceeding $10^5\dot{m}_{\rm Edd}$ and varying by nearly three orders of magnitude. At this scale, the inflow is roughly radial; however, as the material continues to move inward, it gradually circularizes due to the differential rotation inherent in the AGN disk.

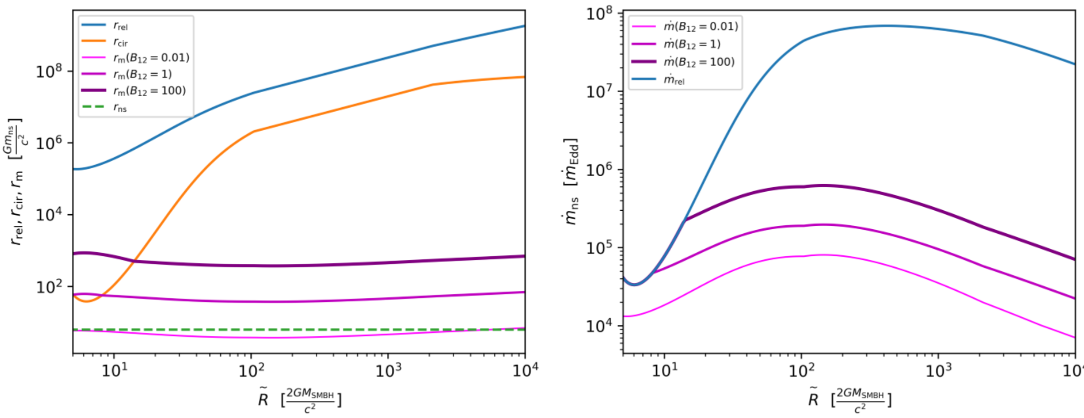

Figure 4.4 Left panel: Various characteristic radii as functions of AGN disk radius $\tilde{R}$ in the fiducial model, including the Bondi scale (Eq. (4.37)), circularization radius (Eq. (4.39)), and magnetospheric radii (Eq. (4.46)). The purple curves indicate the magnetosphere radii under different magnetic field strengths, with darker shades representing stronger fields and lighter shades indicating weaker ones. Right panel: Accretion rates at the Bondi scale (Eq. (4.38)) and at the magnetosphere are shown as functions of AGN disk radius for the fiducial setup. The fiducial parameters adopted in this analysis are: $M_{\rm SMBH} = 10^8 M_\odot$, $\tilde{\alpha} = 0.1$, $\dot{M} = 0.1\dot{M}_{\rm Edd}$, $m_{\rm ns} = 1.4M_\odot$, $r_{\rm ns} = 13$ km, and $s = 0.5$ in Eq. (4.40).

4.3.3 Circum-NS Disk

As the accreted material approaches the NS, it circularizes to form a circum-NS disk. The circularization radius $r_{\rm cir}$ is estimated via angular momentum conservation as

$$\left(Gm_{\rm ns}r_{\rm cir}\right)^{\frac{1}{2}} = v_{\rm rel}(r_{\rm rel})r_{\rm rel}. \tag{4.39}$$

This circularization radius defines the outer boundary of the circum-NS disk, where the inflow rate is assumed to match the modified Bondi accretion rate $\dot{m}_{\rm rel}$, implying that mass loss due to outflows between $r_{\rm rel}$ and $r_{\rm cir}$ is negligible. In the fiducial model, $r_{\rm cir}$ is illustrated as the yellow curve in Fig. 4.4. Generally, this radius is one to two orders of magnitude smaller than the corresponding modified Bondi radius. However, toward the inner AGN disk region, a substantial decrease in the circularization radius is observed. This trend arises because the local sound speed $\tilde{c}_{\rm s}$ increases significantly in the inner disk, which reduces $r_{\rm rel}$ and consequently leads to a substantial drop in $r_{\rm cir}$, as described by Eqs. (4.34) and (4.39).

The circum-NS disk is dominated by outflows due to the hyper-Eddington accretion rate. The inflow rate as a function of radius in the disk is modeled as (e.g. Blandford et al., 1999; Chen et al., 2023a)

$$\dot{m}_{\rm in}(r) = \dot{m}_{\rm cir}\left(r/r_{\rm cir}\right)^{s}, \tag{4.40}$$

where s is a free parameter within the range $0 < s \leqslant 1$, and the fiducial value adopted in this chapter is $s = 0.5$.

Radiation-driven outflows can carry away a significant fraction of viscous heating in the circum-NS disk. This fraction, denoted by $f_{\rm w}$, is assumed to be removed via disk winds and radiation, expressed as (Chen et al., 2023a)

$$L_{\rm w} = f_{\rm w}\dot{m}_{\rm cir}c^2 r_{\rm g} r_{\rm inner}\left(\frac{r_{\rm cir}}{r_{\rm inner}}\right)^{-s} \times \left[\frac{1-(r_{\rm outer}/r_{\rm inner})^{s-1}}{1-s} - \frac{1-(r_{\rm outer}/r_{\rm inner})^{-3/2}}{3/2}\right]. \tag{4.41}$$

Here, the outer edge of the disk is taken as $r_{\rm outer} = r_{\rm cir}$, and the inner boundary is defined by $r_{\rm inner} = \max\{r_{\rm ns}, r_{\rm m}\}$. Throughout this work, a fiducial value of $f_{\rm w} = 0.5$ is adopted. The expression for the magnetospheric radius $r_{\rm m}$ will be introduced in the following subsection.

It's worth noting that despite the high accretion rate of the circum-NS disk, it does not reach the threshold for neutrino emission. The critical rate at which disk accretion becomes neutrino-dominated can be estimated as (Chevalier, 1996)

$$\dot{m}_{\rm cn} = \max\{\dot{m}_{\rm cn1}, \dot{m}_{\rm cn2}\}, \tag{4.42}$$

where

$$\begin{aligned} \dot{m}_{\rm cn1} &= 23.0\, \beta_1^{-0.22} \left(\frac{\kappa}{0.2\ {\rm cm^2 g^{-1}}}\right)^{-0.73} \\ &\times \left(\frac{m_{\rm ns}}{1.4 M_\odot}\right)^{-0.03} \times \left(\frac{r_{\rm cir}}{10^{10}\ {\rm cm}}\right)^{1.08} M_\odot {\rm yr}^{-1}, \end{aligned} \tag{4.43a}$$

$$\begin{aligned} \dot{m}_{\rm cn2} &= 8.2 \times 10^{11} \beta_1^{-0.80} \left(\frac{r_{\rm rel}}{10^{11}\ {\rm cm}}\right)^{-2.70} \\ &\times \left(\frac{m_{\rm ns}}{1.4 M_\odot}\right)^{-0.10} \times \left(\frac{r_{\rm cir}}{10^{10}\ {\rm cm}}\right)^{4.0} M_\odot {\rm yr}^{-1}, \end{aligned} \tag{4.43b}$$

with a gas opacity $\kappa \approx 0.34\ {\rm cm^2 g^{-1}}$ and β_1 of order unity. In the above equations, $\dot{m}_{\rm cn1}$ represents the condition where the disk's shock radius equals the photon trapping radius, while $\dot{m}_{\rm cn2}$ corresponds to the shock radius matching the modified Bondi radius $r_{\rm rel}$. Fig. 4.5 presents a comparison between the estimated Bondi accretion rate and the critical rate required for neutrino-dominated disk accretion. It is evident that the circum-NS disk is insufficient to produce neutrinos. However, although neutrino emission is not possible from the circum-NS disk itself, when the NS accretion becomes nearly spherical or undergoes column accretion influenced by magnetic fields, the critical accretion rate needed for neutrino generation is significantly lowered.

4.3.4 Inner the Magnetosphere

Due to the magnetic field and solid surface of NSs, their accretion behavior in AGN disks exhibits distinct features within the magnetosphere, compared to that of BHs. The magnetic field of the NS is commonly assumed to be dipolar. The inner boundary of the circum-NS disk is governed by the magnetic field strength. When the gas pressure in the disk surpasses the magnetic pressure, the disk is truncated at the magnetospheric radius, denoted as $r_{\rm m}$, also referred to as the Alfvén radius. Therefore, the inner edge of the circum-NS disk is set by

$$\frac{B(r_{\rm m})^2}{8\pi} = \rho(r_{\rm m}) v(r_{\rm m})^2. \tag{4.44}$$

It should be noted that in some literature, the location where the disk is truncated by the magnetic field is not strictly identical to the Alfvén radius—there can be a discrepancy by a factor of order unity.

As a qualitative approximation, we consider a steady, transonic inflow proceeding at nearly free-fall velocity (Shapiro et al., 2008)

$$v(r) = \left(\frac{G m_{\rm ns}}{r}\right)^{\frac{1}{2}}, \tag{4.45a}$$

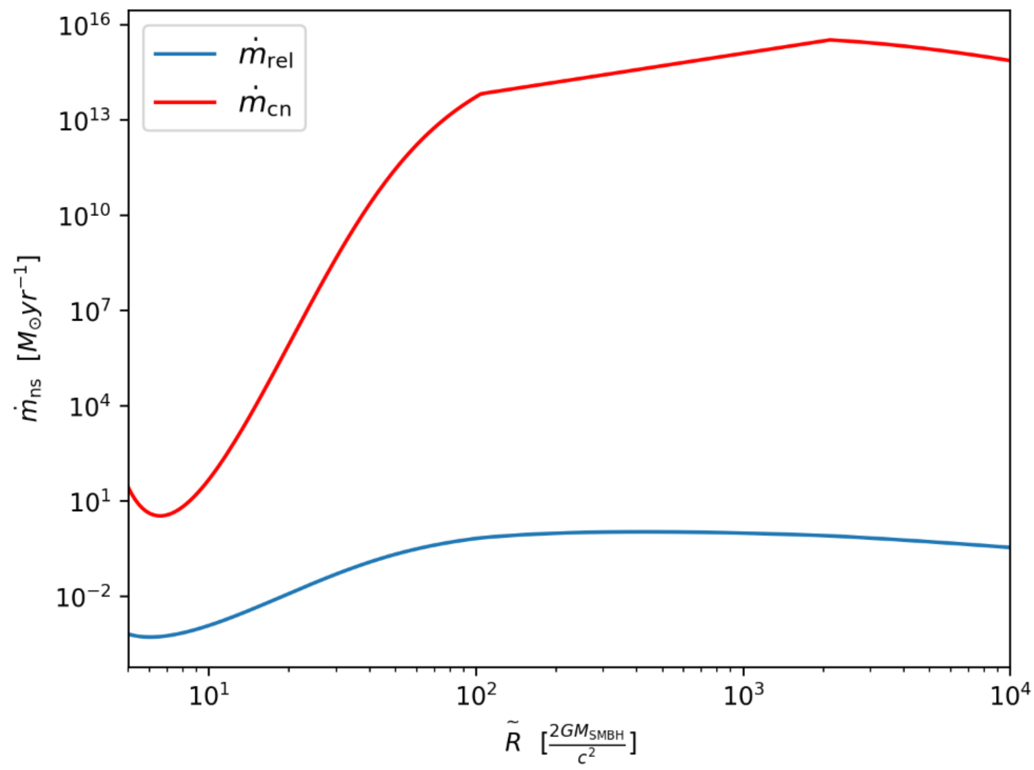

Figure 4.5 Comparison of the accretion rate at the outer edge of the circum-NS disk with the critical accretion rate required for neutrino-dominated disks. The blue line matches that in Fig. 4.4, showing the modified Bondi accretion rate in the fiducial model, whereas the red line indicates the critical accretion rate for neutrino-dominated disks.

$$\rho(r) = \frac{\dot{m}_{\rm in}(r)}{4\pi v r^2}. \tag{4.45b}$$

Inserting Eq. (4.40) into the above expressions, the inner truncation radius of the circum-NS disk can be estimated as:

$$r_{\rm m} = \left(\frac{B_0^4 r_{\rm ns}^{12} r_{\rm cir}^{2s}}{G m_{\rm ns} \dot{m}_{\rm rel}^2}\right)^{\frac{1}{7+2s}}, \tag{4.46}$$

where B_0 denotes the surface dipole magnetic field strength of the NS. Accordingly, the accretion rate reaching the NS surface is given by $\dot{m} = \dot{m}_{\rm in}(r_{\rm inner})$, under the assumption that no additional outflows occur between the inner edge of the disk and the NS surface due to magnetic confinement.

Fig. 4.4 shows the inner radius of the circum-NS disk and its associated accretion rate for different magnetic field strengths, in addition to $r_{\rm rel}$, $r_{\rm cir}$, and $\dot{m}_{\rm rel}$ (accretion rate at the outer radius). Overall, these results consistently align with the hierarchical accretion structure shown in Fig. 4.3. Namely, as matter flows inward from the modified Bondi radius, it circularizes to form a disk, followed by truncation of the disk's inner region (i.e., $r_{\rm cir} > r_{\rm m}$). However, within the innermost regions of the AGN disk, where

$r_{\rm cir} < r_{\rm m}$, magnetic truncation sets in before the material has a chance to circularize. In this case, the disk structure vanishes and the accretion flow remains nearly spherical at the magnetosphere. This spherical inflow, further channeled by the magnetic field, forms a filled accretion column above the NS polar cap. By contrast, when a circum-NS disk is present, the resulting accretion column is hollow, consisting of a narrow wall along the field lines, as illustrated in Fig. 4.3. The trends of scale radii and accretion rates as a function of AGN disk radius with different parameters, as shown in Fig. 4.6, qualitatively resemble those of the fiducial case. In summary, the hierarchical accretion scenario proposed in Fig. 4.3 is generally supported, and the accretion rate onto the NS remains in the hyper-Eddington regime in most cases.

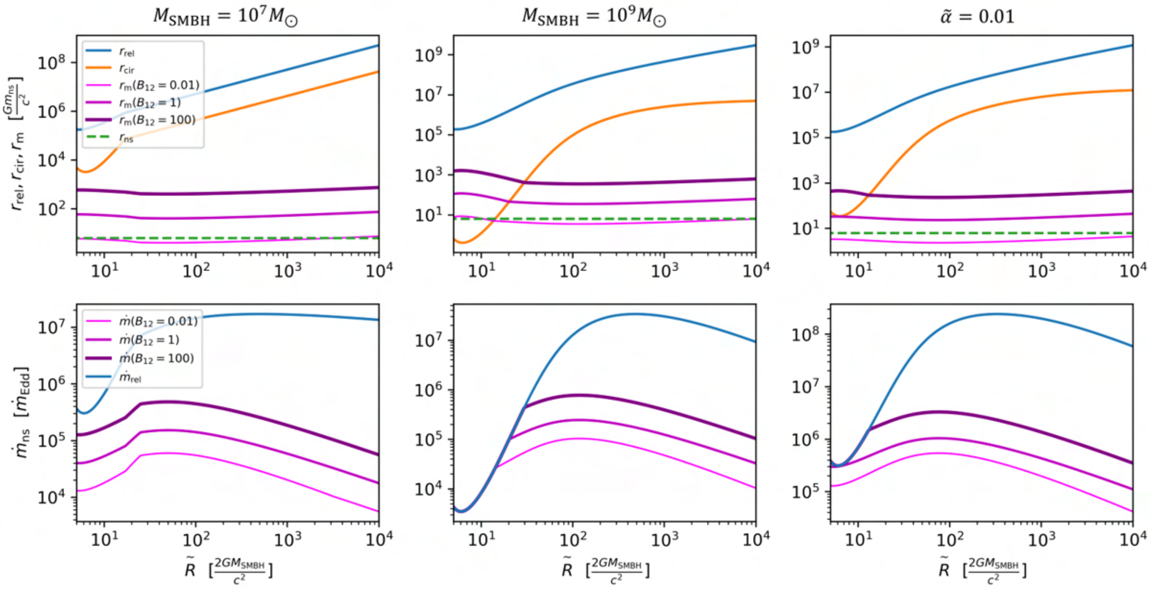

Figure 4.6 Accretion scales and rates for neutron stars embedded in AGN disks, under conditions that deviate from the fiducial model. The top panels illustrate characteristic radii, while the bottom panels present the corresponding accretion rates. From left to right, the variations considered are $M_{\rm SMBH} = 10^7 M_\odot$, $M_{\rm SMBH} = 10^9 M_\odot$, and $\tilde{\alpha} = 0.01$, with all other parameters held identical to those in the fiducial setup. Each curve follows the same definitions as those in Fig. 4.4.

Owing to the presence of a hard surface, NSs can attain relatively high mass-energy conversion efficiencies. For instance, considering a fiducial NS with $m_{\rm ns} = 1.4 M_\odot$ and $r_{\rm ns} = 13$ km, the efficiency can be expressed as

$$\eta = 1 - \left(1 - \frac{2Gm_{\rm ns}}{r_{\rm ns}c^2}\right)^{\frac{1}{2}} \approx 17.4\%, \tag{4.47}$$

under the assumption that the external spacetime is described by the Schwarzschild metric. This general relativistic estimate is slightly higher than the Newtonian value of approximately 15.9%. For reference, nuclear fusion yields a efficiency only reaches up to 0.7%, and accretion onto a Schwarzschild black hole reaches only up to 5.7%. In a scenario where the infalling matter consists of ionized hydrogen, and assuming that all gravitational potential energy is converted into thermal energy within the accretion column without loss, the following relation holds:

$$\eta m_{\mathrm{p}} c^2 = 2 \times \frac{3}{2} k_{\mathrm{B}} T, \tag{4.48}$$

where k_{B} is the Boltzmann constant. As a result of the extremely high accretion rate, the temperature at the base of the accretion column can become exceedingly high, reaching $T \approx 6.3 \times 10^{11}$ K(≈ 54 MeV). This intense heat leads to substantial neutrino emission, which acts as a main cooling mechanism. Thus, the actual temperature remains lower, as a portion of the energy is carried away by neutrinos. The dominant channel for neutrino production is the annihilation of electron-positron pairs. Other processes—such as bremsstrahlung, plasmon decay, photoneutrino emission, and synchrotron neutrino radiation—also contribute, though their effects are subdominant compared to pair annihilation (Mushtukov et al., 2018; Bernal et al., 2010). Moreover, while magnetic fields can slightly alter the neutrino production rate from pair annihilation, the correction is generally small (Kaminker et al., 1992).

The neutrino luminosity can be estimated by considering the fraction of photons trapped within the advection-dominated accretion column. A good approximate expression is given as (Asthana et al., 2023)

$$L_{\nu} \approx 0.64\, \eta \dot{m} c^2 \arctan\left(\frac{\eta \dot{m} c^2}{8 \times 10^{40} \mathrm{erg\ s^{-1}}}\right). \tag{4.49}$$

When the neutrino luminosity exceeds half of the total available accretion power $\eta \dot{m} c^2$, we classify the flow as neutrino-dominated. Thus, the corresponding threshold accretion rate for such neutrino-dominated columnar flows is approximately $\dot{m}_{\mathrm{cn}} \sim 500\, \dot{m}_{\mathrm{Edd}}$. This condition is readily fulfilled in the case of neutron star accretion within AGN disks. Furthermore, non-axisymmetric accretion, as well as an asymmetric temperature distribution in the crust, can induce changes in the mass quadrupole moment of the NS when it rotating. The magnetic field may also enhance this asymmetry, thereby contributing to GW emission.

In short, given the large optical depth of AGN environments, observable electromagnetic signals might be limited (for further details, refer to the next chapter). However, due to three factors—high accretion rates, efficient energy conversion, and the formation of an accretion column—neutrinos and gravitational waves can potentially be produced.

4.3.5   Feedback

Since the circum-NS disk is dominated by outflows, it directly affects both the inflow rate and the feedback intensity on the AGN disk, thereby influencing the accretion duty cycle.

The feedback calculations are based on Chen et al. (2023a), with the additional consideration that neutrinos emitted during the NS accretion process carry away most of the released gravitational potential energy. As a result, the feedback arises almost solely from the wind of the circum-NS disk. The timescale over which the circum-NS disk sustains effective accretion is given by

$$t_{\rm acc} = \alpha^{-1} h^{-2} \Omega_{\rm K}^{-1}, \tag{4.50}$$

where $\alpha \approx \tilde{\alpha}$, $h \approx 0.5$, and $\Omega_{\rm K}$ represent the viscosity parameter, the disk height-to-radius ratio, and the Keplerian angular velocity of the circum-NS disk, respectively.

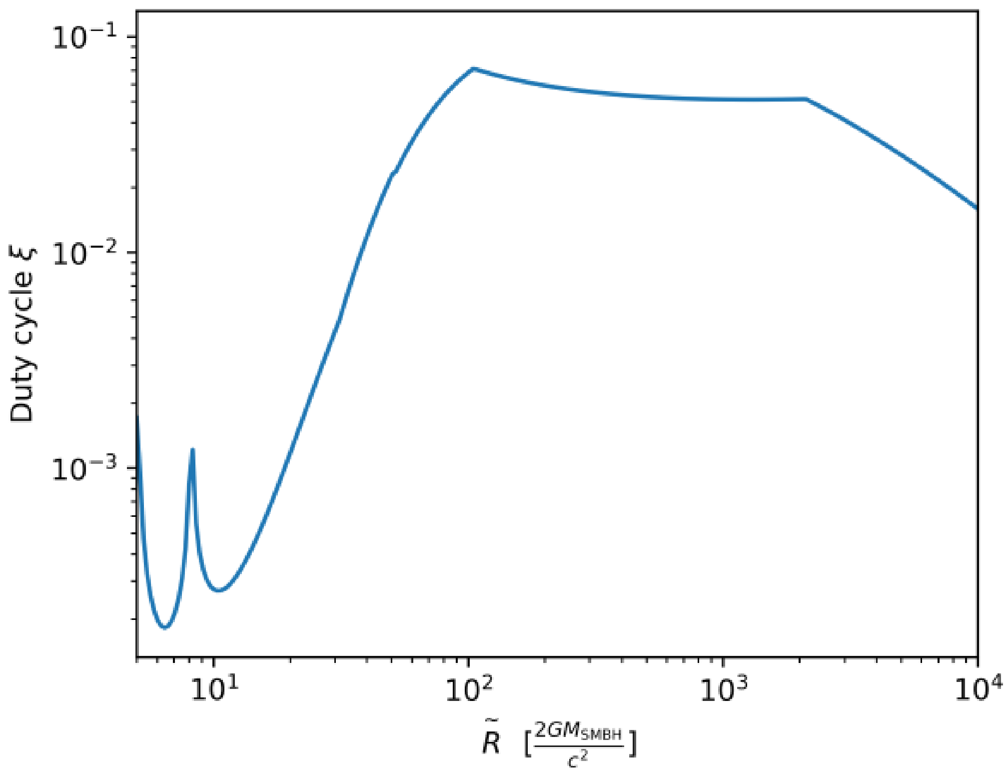

Figure 4.7   Duty cycle of NS accretion in AGN disks for the fiducial setting.

The wind originating from the circum-NS disk drives a forward shock into the surrounding AGN disk gas, forming a shell of shocked disk gas. The radius of this expanding shell evolves over time as (Weaver et al., 1977)

$$r_{\rm shell} = 0.88 \left(\frac{L_{\rm w} t^3}{\tilde{\rho}_0} \right)^{\frac{1}{5}}, \tag{4.51}$$

and its velocity is given by

$$v_{\rm shell} = 0.53 \left(\frac{L_{\rm w}}{\tilde{\rho}_0 t^2} \right)^{\frac{1}{5}}, \tag{4.52}$$

where $L_{\rm w}(\dot{m}_{\rm rel}, r_{\rm cir}, r_{\rm m}, s)$, taken from Equation (4.41), represents the rate at which energy is injected into the AGN disk via the wind. The breakout timescale, $t_{\rm bre}$, is determined by the condition $r_{\rm shell}(t_{\rm bre}) = \tilde{H}$. The cavity's formation and recovery times depend on the two characteristic timescales, $t_{\rm acc}$ and $t_{\rm bre}$. The time required for the cavity to expand outward can be expressed as

$$t_{\rm cav} = \begin{cases} \frac{r_{\rm cav}^3 - r_{\rm shellb}^3(t_{\rm acc})}{3 r_{\rm shellb}^2(t_{\rm acc}) v_{\rm shellb}(t_{\rm acc})} + t_{\rm acc}, & t_{\rm acc} \gtrsim t_{\rm bre} \\ \frac{r_{\rm cav}^3 - \tilde{H}^3}{3 \tilde{H}^2 v_{\rm shellE}(t_{\rm breE})} + t_{\rm breE}, & t_{\rm acc} \lesssim t_{\rm bre}, \end{cases} \tag{4.53}$$

where

$$r_{\rm cav} = \begin{cases} \left[r_{\rm shellb}^2(t_{\rm acc}) v_{\rm shellb}(t_{\rm acc}) / \tilde{c}_{\rm s} \right]^{\frac{1}{2}}, & t_{\rm acc} \gtrsim t_{\rm bre} \\ \left[r_{\rm shellE}^2(t_{\rm breE}) v_{\rm shellE}(t_{\rm breE}) / \tilde{c}_{\rm s} \right]^{\frac{1}{2}}, & t_{\rm acc} \lesssim t_{\rm bre}. \end{cases} \tag{4.54}$$

Here, for the case $t_{\rm acc} \gtrsim t_{\rm bre}$, $r_{\rm shellb}(t)$ and $v_{\rm shellb}(t)$ denote the radius and velocity of the expanding shell after shock breakout; whereas for $t_{\rm acc} \lesssim t_{\rm bre}$, $r_{\rm shellE}(t_{\rm breE})$ and $v_{\rm shellE}(t_{\rm breE})$ correspond to the radius and velocity at the moment of shock breakout, following Chen et al. (2023a).

Accordingly, the refilling timescale of the cavity can be approximated as the cavity radius divided by the local sound speed:

$$t_{\rm ref} = \frac{r_{\rm cav}}{\tilde{c}_{\rm s}}. \tag{4.55}$$

The duty cycle then is given by the ratio of the effective accretion duration to the total cycle time (expansion plus recovery), expressed as:

$$\xi = \frac{t_{\rm acc}}{t_{\rm cav} + t_{\rm ref}}, \tag{4.56}$$

as shown in Fig. 4.7 for the fiducial setting. After accounting for feedback, the average accretion rate onto the NS is given by $\dot{m}$ times the duty cycle ξ.

4.4 White Dwarf Accretion in AGN Disks

The surface magnetic fields of WDs are generally weak ($< 10^5$ G) and thus have little influence on their accretion flows. Consequently, the corresponding accretion structure of a WD embedded in an AGN disk still follows an "outer envelope–inner disk" configuration. But unlike NSs, WDs do not form accretion columns within a magnetosphere. Instead, the inner radius of the circum-WD disk is simply the physical radius of the WD.

Its accretion rate, $\dot{m}_{\rm wd}$, is generally much higher than that of sBHs or NSs of similar mass due to its significantly larger radius, $r_{\rm wd}$. The accretion rate can be estimated as (Pan et al., 2021a)

$$\dot{m}_{\rm wd} = \max\left\{ \dot{m}_{\rm in}(r_{\rm cir}) \times \frac{r_{\rm wd}}{r_{\rm cir}}, \dot{m}_{\rm wd}^{\rm Edd} \right\}. \tag{4.57}$$

At sufficiently high accretion rates, exceeding 3 $\dot{m}_{\rm wd,stable}$ (where $\dot{m}_{\rm wd,stable} \approx 2 \times 10^{-8} - 4 \times 10^{-7}\ M_\odot\ {\rm yr}^{-1}$ is the critical accretion rate marking the transition from nova ignition to stable hydrogen burning), the rate of stable hydrogen burning becomes lower than the accretion rate, resulting in hydrogen accumulation on the WD surface. This results in the formation of a radially expanding envelope, analogous to that of a red giant, until optically thick winds ultimately regulate the net accretion. Given that WDs in AGN disks typically accrete at rates above 3 $\dot{m}_{\rm wd,stable}$, the accumulated gas forms an extended red-giant-like structure with $r_{\rm rg} \gg r_{\rm wd}$. Over a short period, $\delta t \ll m_{\rm wd}/\dot{m}_{\rm wd}$, this expanded structure is spun up to its shedding limit, $\Omega = \sqrt{Gm_{\rm wd}/r_{\rm rg}^3}$, at which point accretion ceases. Consequently, it appears challenging for WDs embedded in AGN disks to grow to the Chandrasekhar limit through accretion. This scenario holds across different AGN disk models.

4.5 Discussion and Conclusions

In this chapter, we presented AGN disk profiles and studied the accretion of different COs across various scales within them, leading to the following concluding remarks.

(i) Accretion of BHs in AGN disks exhibits an "outer spherical, inner disk" structure. It occurs in an approximately spherical manner on Bondi scales. On scales smaller than the Bondi radius by one to two orders of magnitude, a circum-BH disk forms due to the differential rotation of AGN disk gas. Additionally, BH accretion may give rise to jets. If the disk material is dense, the jet may be choked within the disk, potentially producing high-energy cosmic rays and neutrinos. In contrast, if the disk material is thin (Zhang et al., 2024a), the jet may penetrate the AGN disk—an event that could be associated with a GRB.

(ii) The accretion of NSs in the disk qualitatively resembles that of BHs at both the Bondi radius and the circum-NS disk scales. However, due to NSs' different magnetic field configurations and the presence of a hard surface, the accretion flow configuration near the NS differs significantly from that of a BH. As the accretion flow approaches the magnetosphere of the NS, the magnetic field guides the accretion flow, forming accretion columns that fall onto the NS with hyper-Eddington rates (Figs. 4.4 and 4.6). Therefore, accretion of NSs in AGN disks exhibits a hierarchical structure in general (Fig. 4.3).

(iii) The accreting WDs in AGN disks do not exceed the Chandrasekhar limit, as hyper-Eddington accretion leads the white dwarfs up to their shedding limit. Consequently, a white dwarf in an AGN disk cannot trigger a thermonuclear explosion, and cannot result in a Type Ia supernova solely through accretion.

Some aspects of the study remain limited and warrant careful attention:

A uniform density within the AGN disk's scale height is assumed in this work. However, this simplification neglects the disk's vertical structure and the influence of pressure gradients caused by expansion perpendicular to the disk plane. Accounting for this structure could modify the cavity's shape, size, and breakout position (Mac Low et al., 1988; Tagawa et al., 2022). In addition, thermal pressure—not just momentum conservation—may contribute to shell dynamics. These effects may introduce corrections, though the overall magnitudes and physical interpretation remain robust.

The circum-CO disk plays a critical role in shaping both the CO's spin evolution and the feedback on the AGN disk. Here we assume accretion from a Keplerian AGN disk, although turbulence could disrupt the circum-CO disk (Chen et al., 2023b), leading to a spherical-like accretion geometry. If the CO follows an eccentric orbit around the SMBH, retrograde accretion may occur, possibly even reversing the disk's rotation (Li et al., 2022d; Chen et al., 2022).

Strong magnetic fields and rapid NS rotation (e.g., $B \gtrsim 10^{13}$ G, $f \gtrsim 100$ Hz) may trigger the propeller effect, reducing the accretion rate (e.g. Davidson et al., 1973; Parfrey et al., 2016). For weakly magnetized NSs, however, the magnetospheric radius r_m is often below or comparable to the corotation radius, and accretion proceeds normally. Even when r_m slightly exceeds the corotation radius, accretion may still occur in the mild propeller regime (Ghosh et al., 1979; Pan et al., 2021a). Our model naturally accommodates intermittent accretion, including scenarios with the propeller effect. In such cases, while accretion onto the NS is suppressed, the Bondi-scale inflow remains high, enhancing wind-driven feedback. This leads to a larger value of the parameter ”s” in Eq. 4.40, which we currently treat as a free parameter due to the complexity of the underlying physics.

Chapter 5 White Dwarf Collisions in AGN Disks and Electromagnetic Signatures

5.1 Background

The last chapter has shown that WDs in AGN disks are unlikely to accrete sufficient mass to reach the Chandrasekhar limit (see also Pan et al. (2021a)). Therefore, the focus is shifted toward dynamical interactions among WDs.

AGN disks are anticipated to contain a higher number of WDs compared to BHs (Kroupa, 2001), although the mass function of stars in AGN disks tends to be ”top heavy” (Derdzinski et al., 2022). A substantial rate of WD-WD mergers has been predicted in AGN disks (e.g., McKernan et al., 2020); nevertheless, the detailed physical processes governing interactions among WDs in AGN disks, along with their possible observational signatures, remain poorly understood. The dynamics of BHs offer us insights to study those of WDs. Samsing et al. (2022) indicate that disk-assisted three-body encounters can produce highly eccentric binary mergers. Additionally, studies by Wang et al. (2021b); Rowan et al. (2022); Kaaz et al. (2021) suggest that BHs embedded in AGN disks may capture one another and form binaries, emitting both GWs and electromagnetic signals across multiple bands. Further investigations (Li et al., 2022a; Boekholt et al., 2023) reveal that Jacobi capture within the disk can generate eccentric BH binaries, which may coalesce within just a few orbits.

While WDs and their binary systems in AGN disks are expected to evolve differently from BHs and NSs, mainly because WDs have larger sizes, Jacobi capture tends to enable two WDs to collide directly instead of forming a binary system. If they collide, it potentially leads to a Type Ia supernova (SN Ia) explosion (Rosswog et al., 2009; Raskin et al., 2009; Hawley et al., 2012). Theoretical frameworks, numerical simulations (e.g., Mazzali et al., 2001; Iwamoto et al., 2006; Rosswog et al., 2009; Raskin et al., 2009), and observations (Hayden et al., 2010) all suggest that the explosion energy is mainly stored in the ejecta as kinetic energy, while only a small portion is emitted as neutrinos and electromagnetic radiation. Within the AGN disk environment, which contains dense gas, the motion of the ejecta should be influenced by the gravitational field of the SMBH. Thus, it is interesting to explore what the observational effects would be, and how they differ from normal SNe Ia.

From an observational standpoint, phenomena such as AGN variability (e.g., Gopal-Krishna et al., 2019), changing-look AGNs (e.g., Ricci et al., 2020; Trakhtenbrot et al., 2019), and the super-solar metallicities observed in quasars (Warner et al., 2003; Nagao et al., 2006; Shin et al., 2013; Du et al., 2014; Maiolino et al., 2019) remain not fully understood. Key unresolved questions involve how the extreme conditions in AGNs provide and transfer energy, as well as how heavy elements are produced in these environments.

In this chapter, we focus on the collision of two WDs via Jacobi capture in the AGN disk, and explore the subsequent observable effects caused by the interaction between the explosion's ejecta and the AGN disk material. Our findings highlight a possible link between these events and various observed AGN phenomena, including variability, changing-look behavior, and enhanced metallicity.

5.2 Theoretic Model

In this section, we present a detailed explanation of the collision and resulting explosion of two WDs in an AGN disk.

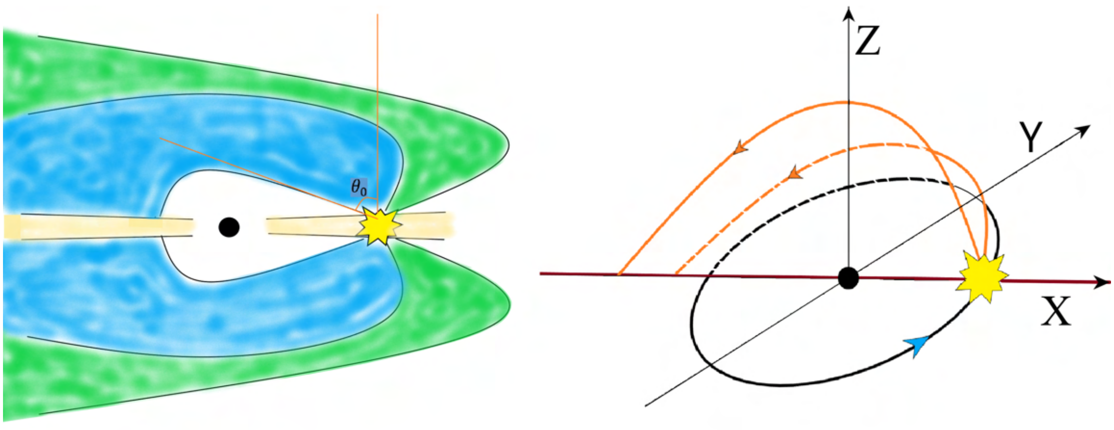

Figure 5.1 Schematic diagram of a WD-WD collision occurring within an AGN disk. Left panel: The collision of two WDs triggers thermonuclear explosion, causing the ejecta to rapidly leave the AGN disk. And due to the SMBH's gravitational influence, a considerable fraction of the ejecta falls back onto the AGN disk, while some escapes the system entirely. In our model, ejecta launched at angles $\theta < \theta_0 = 89^\circ$ are assumed to successfully escape the disk. The unbound ejecta are shown in green, and the bound ejecta—those that fall back onto the disk—are indicated in blue. Right panel: Illustration of the coordinate system used in this description. The black ellipse marks the trajectory of the two WDs' center of mass prior to the collision. The X-axis is defined along the line connecting the collision point and the SMBH. The ejecta's trajectory after the explosion is depicted by orange curves. Points where the fallback material reenters the AGN disk lie along the X-axis.

5.2.1 WD-WD Close Encounters in AGN Disks

Our analysis builds upon the models of Li et al. (2022a) and Boekholt et al. (2023), which study close encounters between stellar-mass BHs in AGN disks. Recent studies including gas effects can be found in Rowan et al. (2022). In AGN disks, such encounters are more likely in regions with migration traps or varying aspect ratios, though the relative velocity is often too high to form bound binaries. A bound system can only form through an extremely close encounter, where gravitational wave emission (and/or gas dissipation) removes enough kinetic energy. Following the approach in Li et al. (2022a), we investigate the close interaction of two WDs in an AGN disk. More details are available in Luo et al. (2023).

1. Qualitative estimation

Consider a three-body system, as illustrated in Fig. 4.3 (a), where two WDs orbit a central SMBH in nearly coplanar, quasi-circular orbits. In the AGN accretion disk environment, after migration and orbital circularization, the orbital separation between the two WDs can become extremely small. In this system, let the mass of the SMBH be $M_{\rm SMBH}$, and the masses of the two WDs be m_1 and m_2, with initial semi-major axes a_1 and a_2, respectively. Define $p = a_2 - a_1$ as the initial orbital separation. Due to their slightly different orbital periods, the separation p evolves over time. If p is much larger than the Hill radius of the system, the three-body configuration remains stable. However, when p becomes comparable to the Hill radius, the system transitions to an unstable regime, leading to chaotic evolution. Specifically, neglecting the short-term effects of the AGN disk on the compact objects' orbits, the critical separation between "stable" and "unstable" states is given by (Gladman, 1993)

$$p_{\rm c} = 2\sqrt{3}R_{\rm H} \quad , \tag{5.1}$$

where the Hill radius is

$$R_{\rm H} \equiv \frac{a_1 + a_2}{2}\left(\frac{m_1 + m_2}{3M_{\rm SMBH}}\right)^{\frac{1}{3}} \approx a_1\left(\frac{m_1 + m_2}{3M_{\rm SMBH}}\right)^{\frac{1}{3}} . \tag{5.2}$$

When $p < p_{\rm c}$, close encounters between the WDs can lead to mutual capture, significantly influencing the subsequent evolution of the system.

Unstable close encounters can bring the two WDs extremely close to each other. For them to form a stable binary, the energy loss must exceed the binding energy

$$E_{\rm b} = \frac{Gm_1m_2}{2R_{\rm H}}. \tag{5.3}$$

GW radiation serves as a primary energy loss mechanism, with an energy dissipation given by (Peters, 1964b)

$$\Delta E_{\rm GW} = \frac{85\pi}{12\sqrt{2}} \frac{G^{7/2}(m_1 m_2)^2 (m_1 + m_2)^{1/2}}{c^5 r_{\rm p}^{7/2}}. \tag{5.4}$$

By requiring $\Delta E_{\rm GW} \gtrsim E_{\rm b}$, we obtain the critical pericenter distance for gravitational binding:

$$r_{\rm p} \lesssim r_{\rm b} \equiv 3.48 \left(\frac{m_1 m_2}{(m_1 + m_2)^2}\right)^{7/2} \times \left(\frac{m_1 + m_2}{M_{\rm SMBH}}\right)^{10/21} \left(\frac{G M_{\rm SMBH}/c^2}{a_1}\right)^{5/7} R_{\rm H}. \tag{5.5}$$

Thus, for given $M_{\rm SMBH}$ and a_1, if the separation between the WDs falls below $r_{\rm b}$, sufficient energy can be dissipated via GW emission to overcome the tidal influence of the SMBH, allowing the formation of a stable binary. Additionally, if one WD is ejected from the system during a close encounter, the required condition is

$$\frac{G m_1 m_2}{r_{\rm e}} \gtrsim \frac{1}{2} \frac{m_1 m_2}{m_1 + m_2} v_{\rm orb}^2, \tag{5.6}$$

where $r_{\rm e}$ is the scattering distance, and $v_{\rm orb}$ is the orbital velocity. For typical WDs with $m_1 = m_2 = 0.6 M_\odot$, the collision radius is approximately twice the WD radius, i.e.,

$$r_{\rm c} = 2 r_{\rm WD} \approx 1.5 \times 10^7 \text{ m}. \tag{5.7}$$

For example, assuming $M_{\rm SMBH} = 10^6 M_\odot$ and $a_1 = 100 G M_{\rm SMBH}/c^2$, the gravitational wave-induced binding radius is

$$r_{\rm b} \lesssim 1.76 \times 10^5 \text{ m}, \tag{5.8}$$

which is much smaller than the collision radius $r_{\rm c}$. Similarly, the scattering distance required to eject a WD is

$$r_{\rm e} \lesssim 3.6 \times 10^5 \text{ m}, \tag{5.9}$$

which is also much smaller than $r_{\rm c}$. Therefore, before the WDs can form a stable binary or one gets ejected, they are likely to collide.

Actually, as confirmed by numerical simulations below, close encounters between WDs in AGN disks generally result in two possible outcomes:

- The two WDs undergo a relatively soft interaction and scatter onto a ”stable” orbit.
- The two WDs undergo a direct collision.

Table 5.1 The initial input model parameters for numerical simulations. The second column lists the mass of the WD. The third column shows the separation between the orbits of the two WDs. In particular, Run1 refers to a uniform distribution of orbital separations within the range[$0.8\ R_{\rm H}$, $4\ R_{\rm H}$]. The fourth column gives the inclination angle between the orbital planes of the two WDs. The final column indicates the number of simulation samples.

Name	$m_1, m_2\ (M_{\rm SMBH})$	$p/R_{\rm H}$	Δi	N
Run1	6×10^{-7}	[0.8,4]	0	4000
Run2	6×10^{-7}	3.0	$10^{-3}\frac{R_{\rm H}}{a_1}$	1000
Run3	6×10^{-7}	3.0	$10^{-2}\frac{R_{\rm H}}{a_1}$	1000
Run4	6×10^{-7}	3.0	$10^{-1}\frac{R_{\rm H}}{a_1}$	1000
Run5	6×10^{-7}	3.0	$\frac{R_{\rm H}}{a_1}$	1000
Run6	6×10^{-8}	3.0	0	1000
Run7	6×10^{-9}	3.0	0	1000

2. Numerical simulations

For the simulation of this hierarchical three-body system, we utilized the N-body simulation software REBOUND (Rein et al., 2012), employing the IAS15 integrator (Rein et al., 2015). We considered two WDs with masses $m_1 = m_2 = 0.6M_\odot$, and set the initial orbital separation p to range from $0.8R_{\rm H}$ to $4.0R_{\rm H}$. The initial orbital eccentricities of the two WDs are chosen as $e_1 = 0$ and $e_2 = 10^{-5}$. The initial difference in longitude is uniformly distributed in the range $[0, 2\pi]$. The orbital planes of the two WDs may not be perfectly aligned with the AGN disk plane. We define their inclinations relative to the disk as i_1 and i_2, and $\delta i = i_2 - i_1$. A detailed list of all initial parameters is provided in Table 5.1.

Fig. 5.2 presents the minimum separation between the two WDs and the WD-WD collision fraction over 10^5 orbital periods in Run1, for different values of $p/R_{\rm H} \in [0.8, 4]$. We find that nearly all close encounters occur in the dynamically ”unstable” region ($p < p_{\rm c}$). However, not all samples with $p < p_{\rm c}$ experience WD-WD close encounters. Notably, at $p = 1.1R_{\rm H}$, the occurrence of close encounters significantly decreases, and the minimum separation tends to increase as the initial orbital separation decreases. This phenomenon can be explained as follows: for smaller initial separations, the WDs reside in horseshoe orbits in a rotating reference frame. When they approach each other, one WD moves inward while the other moves outward, leading to an orbital exchange. Nonetheless, a small fraction of samples still undergo close encounters due to their exceptionally small initial separations, placing them outside the horseshoe orbit regime.

Beyond the initial orbital separation and semi-major axes, the effects of relative

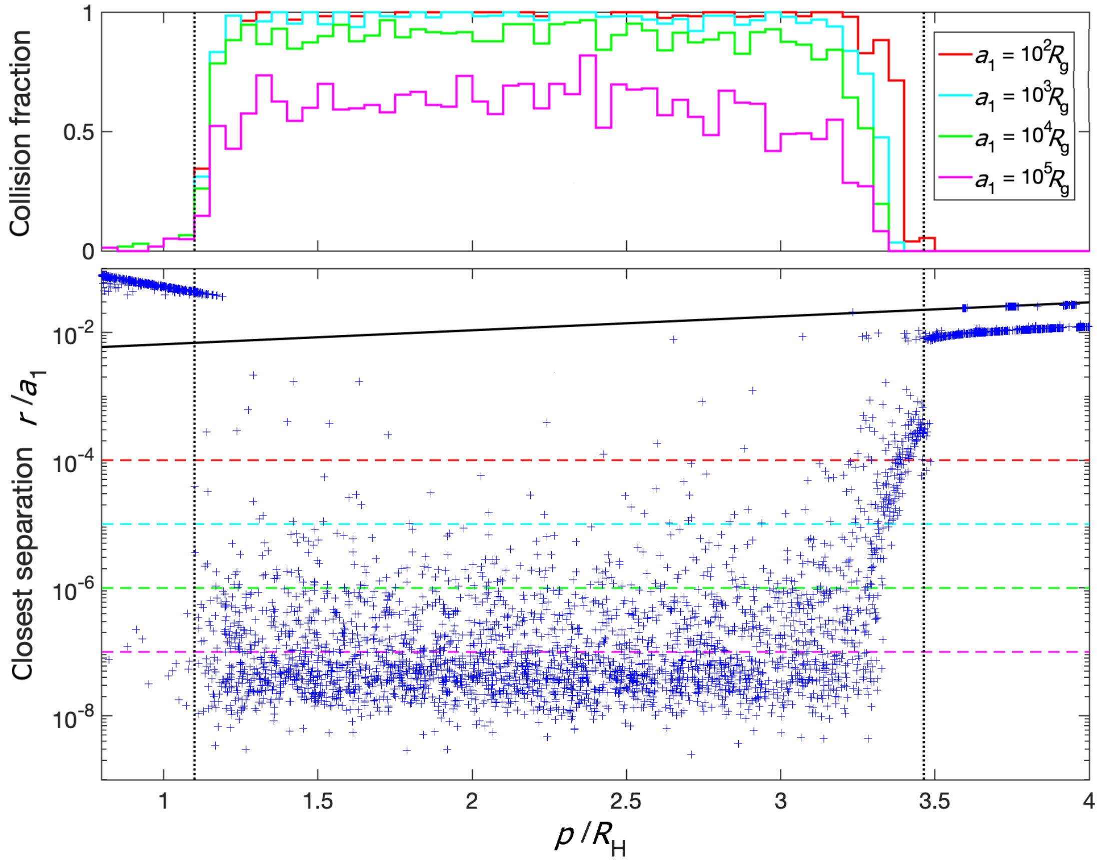

Figure 5.2 Top panel: The fraction of WD–WD collisions as a function of their initial orbital separation, for various fixed values of the inner orbit a_1. Each color represents a different a_1. Bottom panel: The minimum separation reached between the two WDs as a function of their initial orbital spacing. The solid black curve indicates the initial spacing, while the dashed red, cyan, green, and magenta lines represent the WD–WD collision thresholds for $a_1 = 10^2, 10^3, 10^4, 10^5\ R_g$, respectively. The vertical dotted black line marks the critical separation distinguishing stable from unstable configurations, defined by $p_c = 2\sqrt{3}R_H$. This figure is originally taken from our collaboration work Luo et al. (2023).

orbital inclination Δi and SMBH mass $M_{\rm SMBH}$ on WD collisions are also investigated (Luo et al., 2023), corresponding to Runs 2–5 and Runs 6–7, respectively. It is found that as the relative inclination increases, the peak of the minimum separation distribution shifts toward larger values, and the WD–WD collision fraction decreases. In cases with different SMBH masses, the minimum separation distributions remain similar, but the WD-WD collision fraction decreases with increasing SMBH mass. Overall, in the AGN disk environment, the gravitational influence of the central SMBH facilitates highly efficient WD-WD collisions during close encounters.

3. Event rate estimation

The number of stellar mass BHs in the nuclear star cluster surrounding an SMBH is estimated to be approximately $(1-4)\times 10^4$ (Generozov et al., 2018). Based on the initial mass function of stars, the number of WDs is expected to be about ten times that of BHs (Kroupa, 2001). Therefore, the total number of WDs around a central SMBH is expected to be $\sim 2 \times 10^5$. Assuming a cuspy stellar mass distribution and that the initial number density of WDs follows the relation $\mathrm{d}N_{\mathrm{WD}}(\tilde{R})/\mathrm{d}\tilde{R} \propto \tilde{R}^{-0.5}$ (Tagawa et al., 2021), where $N_{\mathrm{WD}}(\tilde{R})$ represents the total number of WDs within a distance $\tilde{R}$ from the SMBH.

Due to Type I migration, the orbital separations between WDs evolve over time. When their separation reaches $\sim 3R_{\mathrm{H}}$, they form an "SMBH+WD+WD" system. For such a system, the WD-WD collision rate can be expressed as (Luo et al., 2023)

$$\mathcal{R} = N_{\mathrm{GN}} \times f_{\mathrm{AGN}} \times \frac{N_{\mathrm{WD}} \times f_{\mathrm{d}} \times f_{\mathrm{3b}} \times f_{\mathrm{c}}}{\tau_{\mathrm{AGN}}}, \tag{5.10}$$

where N_{GN} is the number density of galactic nuclei hosting nuclear star clusters in the universe, f_{AGN} is the fraction of galaxies hosting an AGN, τ_{AGN} is the AGN lifetime, N_{WD} represents the total number of WDs within $10^6 \tilde{R}_{\mathrm{g}}$ of the central SMBH, f_d is the fraction of WDs that eventually migrate into the AGN disk, f_{3b} is the probability of forming a bound three-body system, and f_{c} denotes the fraction of WD-WD collisions in such three-body systems.

We find that if the simulation time extends to the AGN lifetime, nearly all WDs in the inner disk region ($\tilde{R} < 10^4 \tilde{R}_{\mathrm{g}}$) undergo WD-WD collisions, whereas the collision fraction decreases significantly in the outer disk region ($a_1 > 10^4 \tilde{R}_{\mathrm{g}}$), especially for more massive SMBHs. Hence, we assume that when WDs migrate to $\tilde{R} < 10^4 \tilde{R}_{\mathrm{g}}$, the collision fraction is $f_{\mathrm{c}} = 1$; otherwise, $f_{\mathrm{c}} = 0$. We further assume that half of the WDs in the AGN disk can migrate to $\tilde{R} < 10^4 \tilde{R}_{\mathrm{g}}$ and form bound three-body systems, leading to $f_{\mathrm{3b}} = 0.25$. Consequently, the WD-WD collision rate can be approximated as (Luo et al., 2023):

$$\mathcal{R} = 300\ \mathrm{Gpc}^{-3}\mathrm{yr}^{-1} \frac{N_{\mathrm{GN}}}{0.006\ \mathrm{Mpc}^{-3}} \frac{N_{\mathrm{WD}}}{2 \times 10^5} \times \frac{f_{\mathrm{AGN}}}{0.1} \frac{f_{\mathrm{d}}}{0.1} \frac{f_{\mathrm{3b}}}{0.25} \frac{f_{\mathrm{c}}}{1} \left(\frac{\tau}{10\mathrm{Myr}} \right)^{-1}. \tag{5.11}$$

If all such WD-WD collisions lead to Type Ia supernovae, the total event rate in AGN disks would be 300 $\mathrm{Gpc}^{-3}\mathrm{yr}^{-1}$. The observed Type Ia supernova rate in the local universe is $2.5 \pm 0.5 \times 10^4\ \mathrm{Gpc}^{-3}\mathrm{yr}^{-1}$ (Cappellaro et al., 2015). Therefore, WD-WD collisions account for approximately 1% of the observed SN Ia rate.

It is important to note that our study so far does not consider the effects of the surrounding gas on WDs. In the AGN disk environment, WDs may develop circumstellar gas disks, which can interact during close encounters (Li et al., 2023b), potentially accelerating collisions or enabling mergers in cases where collisions do not occur in the current simulation.

5.2.2 Motion of Ejecta

1. The explosion ejecta rush out of AGN disks

Once two WDs collide, a thermonuclear explosion could be triggered, potentially resulting in a SN Ia. Typically, this explosion releases a total energy of $\sim 1.5 \times 10^{51}$ erg, with neutrinos and electromagnetic radiation carrying away approximately 10^{50} erg and 10^{49} erg, respectively (Mazzali et al., 2001; Iwamoto et al., 2006; Hayden et al., 2010). As a result, most of the explosion energy is transferred into the kinetic energy of the ejecta, while only a small portion is lost through neutrinos and electromagnetic radiation. Numerical simulations further confirm that thermonuclear explosions triggered by WD collisions can produce homologous outflows with velocities of 1.3×10^4 – 1.6×10^4 km s^{-1}, corresponding to a kinetic energy of approximately 10^{51} erg (Rosswog et al., 2009; Raskin et al., 2009; Hawley et al., 2012). This emitted EM signal resembles that of normal SNe Ia events.

The mass of the disk material swept up by the ejecta resulting from the thermonuclear explosion within an AGN disk can be estimated. The AGN disk is modeled using the standard thin disk, which remains valid in the region of interest ($\lesssim 10^3 R_g$). In our analysis, an accretion rate of $\dot{M} = 0.1\dot{M}_{\rm Edd}$ and a viscosity parameter of $\tilde{\alpha} = 0.1$ are adopted in the AGN disk model. The values of disk mass swept up by the ejecta under various SMBH masses and explosion radii are listed in Table 5.2. For the representative scenarios considered here (i.e., $M_{\rm SMBH} \lesssim 10^8 M_\odot$ and $\tilde{R}_{\rm ej} \lesssim 10^3 R_g$), the amount of swept-up material is significantly smaller than the ejecta mass ($\sim 1 M_\odot$). It is worth noting that in other AGN disk models (e.g. TQM05), the swept-up mass may be even smaller. Evidently, the AGN disk gas is not dense enough (i.e., the quantity $\tilde{\rho} \times \tilde{H}^3$ is too small, though the disk remains optically thick) to significantly decelerate the ejecta. As a result, the ejecta locally escape the AGN disk at velocities very close to those of the initial explosion.

The following motion of the ejecta is dominated by the gravity of the central SMBH. At radial distances around $\sim 100 R_g$, the escape speed is approximately $v_{\rm esc} \sim 3\sqrt{2} \times 10^4$ km s^{-1}. Once the ejecta leaves the disk, it experiences the gravitational pull of the central SMBH, causing part of it to return toward the disk while the rest may leave the system entirely. These dynamics give rise to several potential observational signatures: (i) the early emission mimics that of a normal SN Ia, powered by radioactive decay and peaking in the optical band (Pereira et al., 2013); (ii) as fallback ejecta re-impacts the AGN disk, interactions can generate hard X-ray and soft gamma-ray transients; (iii) the disruption of the disk by this fallback leads to a temporary rise and subsequent decline in the accretion rate and luminosity before returning to a steady state (McKernan et al., 2022), reminiscent of the changing-look AGN phenomenon (Ricci et al., 2020; Trakhtenbrot et al., 2019; Li et al., 2022c).

The interaction between the fallback ejecta and the AGN disk, alongside the thermonuclear explosion of the WD system, introduces notable new phenomena. In the following section, we develop a model to investigate the observational signatures associated with this interaction (ii), while effects (i) and (iii) will be examined more thoroughly in the Discussion section.

Table 5.2 Mass of AGN disk gas swept up by the ejecta as it propagates outward from the disk midplane. The explosion is assumed to originate within the midplane, and the disk structure follows the standard thin-disk model.

$M_{\rm SMBH} = 10^6 M_\odot$, $\dot{M} = 0.1\dot{M}_{\rm Edd}$, $\tilde{\alpha} = 0.1$			
Explosion radius ($R_{\rm g}$)	100	200	500
Swept disk mass (g)	2.51×10^{27}	7.78×10^{27}	3.31×10^{28}
$M_{\rm SMBH} = 10^7 M_\odot$, $\dot{M} = 0.1\dot{M}_{\rm Edd}$, $\tilde{\alpha} = 0.1$			
Explosion radius ($R_{\rm g}$)	100	200	500
Swept disk mass (g)	2.51×10^{29}	7.78×10^{29}	3.31×10^{30}
$M_{\rm SMBH} = 10^8 M_\odot$, $\dot{M} = 0.1\dot{M}_{\rm Edd}$, $\tilde{\alpha} = 0.1$			
Explosion radius ($R_{\rm g}$)	100	200	500
Swept disk mass (g)	2.51×10^{31}	7.78×10^{31}	3.31×10^{32}

2. Fallback model

As illustrated in Fig. 5.1, the explosion is assumed to originate in the midplane of the AGN disk, leading to a symmetric expansion of the ejecta relative to the disk plane. Prior to the explosion, the center of mass of the colliding WDs is assumed to orbit the SMBH in a circular Keplerian trajectory. The collision triggers a thermonuclear detonation, resulting in homologous ejecta expansion with a characteristic velocity of 1.5×10^4 km s^{-1}. The ejecta subsequently exits the disk with nearly this initial velocity. Subject to the gravitational field of the central SMBH, a portion of the ejecta falls back along the negative X-direction of the disk, as shown in the right panel of Fig. 5.1, while the remainder may escape the system. The primary interest here is the radiation that arises from the interaction between the fallback ejecta and the disk material. For this analysis, a typical explosion radius of $\sim 100 R_{\rm g}$ is adopted, and the SMBH's gravity is treated in the Newtonian regime. Notably, some unbound ejecta may still re-interact with the disk if their hyperbolic trajectories intersect it.

Table 5.3 Fraction of fallback ejecta under various model configurations. From left to right, the table columns list: SMBH mass, explosion radius, ejecta velocity, and the resulting fallback ejecta fraction.

$M_{\rm SMBH}$	$\tilde{R}_{\rm ej}$	$v_{\rm ej}$	Ratio
$10^6 M_\odot$	$100 R_{\rm g}$	$1.5 \times 10^4\ {\rm km\,s^{-1}}$	0.8873
$10^6 M_\odot$	$200 R_{\rm g}$	$1.5 \times 10^4\ {\rm km\,s^{-1}}$	0.7107
$10^6 M_\odot$	$300 R_{\rm g}$	$1.5 \times 10^4\ {\rm km\,s^{-1}}$	0.6204
$10^6 M_\odot$	$500 R_{\rm g}$	$1.5 \times 10^4\ {\rm km\,s^{-1}}$	0.5121
$10^6 M_\odot$	$100 R_{\rm g}$	$1.0 \times 10^4\ {\rm km\,s^{-1}}$	1
$10^6 M_\odot$	$100 R_{\rm g}$	$2.0 \times 10^4\ {\rm km\,s^{-1}}$	0.7385
$10^7 M_\odot$	$100 R_{\rm g}$	$1.5 \times 10^4\ {\rm km\,s^{-1}}$	0.8873
$10^8 M_\odot$	$100 R_{\rm g}$	$1.5 \times 10^4\ {\rm km\,s^{-1}}$	0.8873

In our scenario, the supernova ejecta is assumed to be initially distributed in a spherically symmetric manner at the explosion site. The ejecta is divided into $N = 2 \times 10^5$ elements. A Monte Carlo approach is employed to randomly assign polar and azimuthal angles to each ejecta element. For each part of the ejecta, the initial position is set to the explosion point, and the initial velocity corresponds to the explosion velocity. Their subsequent paths are tracked to determine whether they re-interact with the disk, and if so, their fallback time, location, and velocity are recorded.

Due to the broad spread of the fallback material upon its return to the disk, the mass deposited per unit $R_{\rm g}$ is generally less than the disk gas mass in the same region (with specific exceptions addressed in the next Section). As this fallback material collides with the rapidly orbiting disk gas, shock waves form, efficiently converting kinetic energy into internal energy and producing electromagnetic emission.

We assume that when each part of the ejecta sweeps up a disk mass equal to its own, all of its kinetic energy is converted into internal energy. The energy dissipated by each part of the ejecta is given by:

$$E_{\rm i} = \frac{1}{2}\frac{m_{\rm ej}}{N} v_{\rm rel}^2, \tag{5.12}$$

where $m_{\rm ej}$ is the total ejecta mass and $v_{\rm rel}$ is the relative speed between the ejecta and local disk gas. Note that $v_{\rm rel}$ varies across different parts of ejecta.

However, not all of this energy can be radiated electromagnetically; only a fraction $\eta \sim 5\%$ is assumed to be converted into observable radiation. This choice reflects uncertainties in the physical modeling while preserving the integrity of the qualitative conclusions. Meanwhile, the remaining energy may be redistributed into the gas's internal energy, gravitational potential energy, large-scale motions such as vortices, turbulence, and expansion, as well as into the acceleration of high-energy particles. Thus, for each part of ejecta, the radiative energy is taken as ηE_{i}. This efficiency is consistent with the assumptions made in simulations by Jiang et al. (2016), which examined collisions in TDE scenarios, where radiation efficiencies fall in the range of 2% - 8%. Similarly, Wilson et al. (2004) provided an order-of-magnitude estimate for radiation output from a SN Ia impacting an AGN disk, yielding $\sim 10^{50}$ erg, which corresponds to a radiation efficiency of roughly 5%.

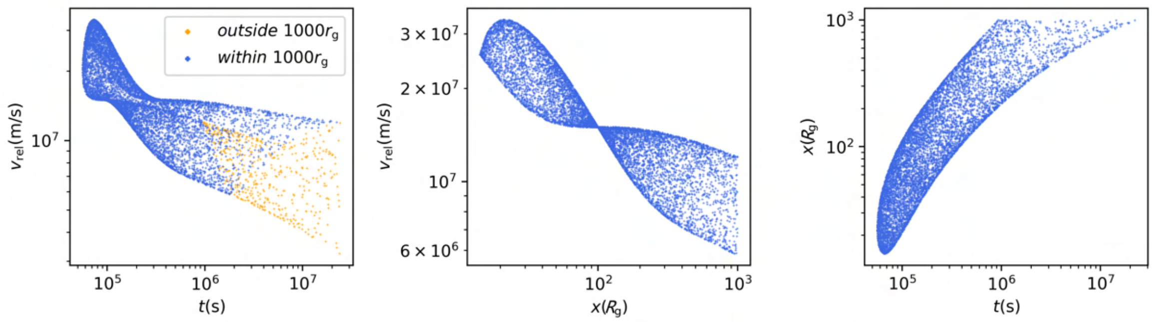

Figure 5.3 Scatter plots of fallback ejecta properties in the fiducial model.The left panel presents the correlation between υ_{rel} and fallback time, where blue markers indicate ejecta returning within $10^3 R_{\mathrm{g}}$, and orange markers denote those falling back beyond $10^3 R_{\mathrm{g}}$. The middle panel depicts the relation between υ_{rel} and the fallback location, while the right panel displays how the fallback position evolves with fallback time.

Using the fiducial parameters of our model (SMBH mass $M_{\mathrm{SMBH}} = 10^7 M_{\odot}$, explosion radius $\tilde{R}_{\mathrm{ej}} = 100 R_{\mathrm{g}}$, explosion velocity $\upsilon_{\mathrm{ej}} \sim 1.5 \times 10^4\ \mathrm{km\ s^{-1}}$, and ejecta mass $m_{\mathrm{ej}} = 1.8 M_{\odot}$) the resulting fallback fraction (i.e., the ratio of fallback mass to total ejecta mass) is calculated to be 0.8873. Table 6.2 illustrates how this ratio varies with different model parameters. Since the escape velocity declines as the explosion radius increases, both a larger explosion radius and a higher explosion velocity tend to reduce the fallback fraction. In contrast, the SMBH mass has no impact on this ratio. Across all examined scenarios, more than 50% of the ejecta returns to the disk.

5.3 Observational Signatures

5.3.1 Light Curve

Using the specified set of model parameters for a supernova explosion described above, the fallback ratio and detailed information of the falling ejecta—such as time, position, and velocity—can be determined.This enables the calculation of the ejecta fallback rate and energy dissipation rate over time, thereby allowing the derivation of the light curve.

Fig. 5.3 presents scatter plots illustrating the fallback information about the ejecta. Each data point corresponds to a portion of the fallback ejecta. To enhance clarity, the scatter plots use a reduced sample size of $N = 2 \times 10^4$. At early times, the relative velocities are broadly distributed and can reach values as high as 3.5×10^7 m s^{-1}, resulting in higher average energy dissipation per ejecta segment. At later times (beyond 10^6 s), relative velocities mostly remain below 1.5×10^7 m s^{-1}, and their distribution evolves more slowly, with the average dissipated energy gradually decreasing. Similarly, the middle panel shows that for fallback positions within roughly $100 R_g$, relative velocities exhibit greater dispersion and higher average values, leading to increased energy dissipation per ejecta segment. Beyond $100 R_g$, the relative velocity tends to be lower, corresponding to reduced energy dissipation. Generally, relative velocity generally decreases as fallback position increases, with a notable clustering of points around $100 R_g$ at approximately 1.5×10^7 m s^{-1}. The right panel reveals that at early times, fallback occurs close to the inner disk region (around $15 R_g$), but as time progresses, fallback locations become more dispersed and the average fallback radius increases rapidly, since ejecta falling back farther from the SMBH naturally require longer travel times. Overall, fallback ejecta are dispersed both temporally and spatially.

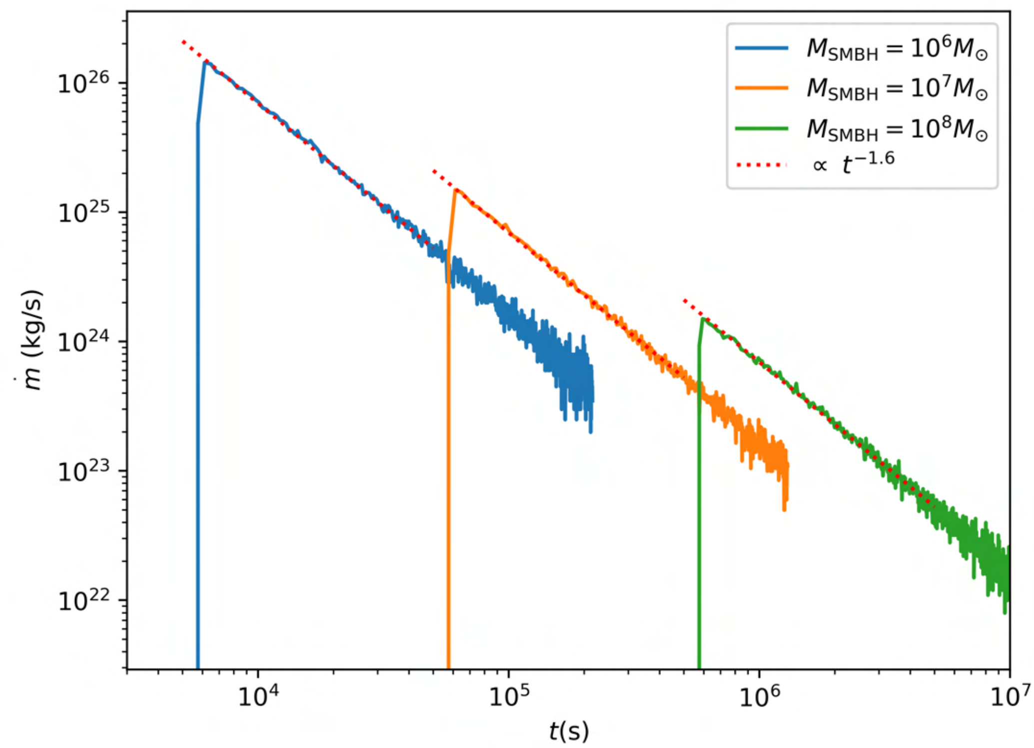

Figure 5.4 Time evolution of the fallback mass rate for various SMBH masses. Each solid line represents a different SMBH mass scenario, while the red dotted line indicates a $L \propto t^{-1.6}$ trend. All other parameters follow those of the fiducial model.

In what follows, we investigate the influence of the SMBH mass, keeping all other parameters identical to those of the fiducial model. At a radius of $100R_{\rm g}$, the Keplerian velocity reaches $c/10$, which exceeds the typical explosion velocity. Consequently, in the fiducial setup, the ejecta remain directed along the center-of-mass motion, meaning the Y-components of all ejecta velocities are positive. We also note that the relativistic correction at $v_{\rm rel} = c/10$ is less than 1%, implying that relativistic effects on the ejecta are minimal in this context.

Fig. 5.4 illustrates how the fallback mass rate evolves over time for different SMBH masses: $M_{\rm SMBH} = 10^6 M_\odot$, $10^7 M_\odot$, and $10^8 M_\odot$. Although the overall shapes of the curves remain similar, variations in the fallback time-scale emerge due to differences in the SMBH mass. Given that all models assume the same total ejecta mass—representing the material expelled by a SN Ia—the peak fallback rate diminishes by roughly an order of magnitude as the SMBH mass increases by a factor of ten. The irregularities in the curves stem from the finite particle number ($N = 2 \times 10^5$) used in the simulations, which could be smoothed by adopting a higher resolution.

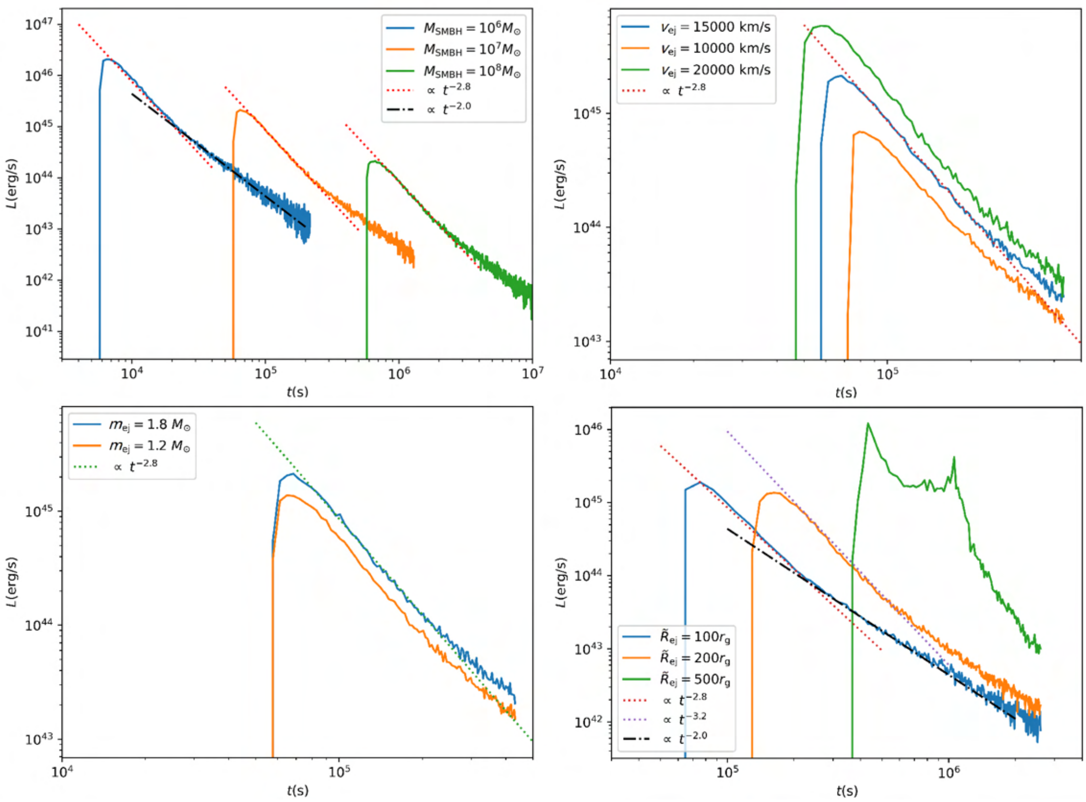

Figure 5.5 Upper left: Light curves resulting from the energy dissipation as fallback ejecta interact with the disk gas. Except for the SMBH mass, all other parameters are consistent with those in the fiducial model. Upper right: Light curves for various explosion velocities, shown alongside the fiducial model for comparison. Lower left: Light curves corresponding to different ejecta masses, contrasted with the fiducial scenario. Lower right: Light curves for varying explosion locations, compared against the fiducial case.

Fig. 5.5 presents the light curves, which resemble the temporal behavior of the matter fallback rate, showing a rapid rise followed by a power-law decay. However, the light curve depends not only on the fallback rate but also on the relative velocity $v_{\rm rel}$ and the efficiency parameter η. For reference, the power-law curves $L \propto t^{-2.8}$ and $L \propto t^{-2.0}$ are included. Shortly after the peak, the luminosity declines steeply following $L \propto t^{-2.8}$, then transitions to a slower decay described by $L \propto t^{-2.0}$. The overall steep decline indicates a rapid change in luminosity. While different SMBH masses (upper left panel) do not alter the shape of the light curve, they affect both the variability timescale and the peak luminosity. Specifically, increasing the SMBH mass by one order of magnitude results in a corresponding increase in variability timescale by the same factor and a decrease in peak luminosity by one order of magnitude. These patterns suggest that the variability timescale may serve as a diagnostic to constrain the SMBH mass.

The influence of various parameters, as compared to those in the fiducial model, is further illustrated in different panels of Fig. 5.5. The upper right panel compares the light curves for different explosion velocities. As shown in Table 5.3, the fallback fraction of the ejecta decreases as the explosion velocity increases. However, the light curves reveal that a higher explosion velocity, which leads to greater relative velocity $v_{\rm rel}$, results in an earlier peak time and a higher peak luminosity, while the overall power-law form of the light curve remains consistent. A lower explosion velocity (e.g., $v_{\rm rel} = 10^4 {\rm km\ s^{-1}}$) means that the ejecta experiences interaction and partial deceleration by the AGN disk during the initial phase, or it may indicate that the explosion deviates from an ideal head-on collision with zero impact parameter (Raskin et al., 2009).

The lower left panel of Fig. 5.5 compares the light curves for different ejecta masses. Variations in ejecta mass only affect the peak luminosity, while the timing of the peak and the shape of the light curves remain unchanged.

The effects of varying explosion radii on the light curves are shown in the lower right panel of Fig. 5.5. Different explosion radii influence the light curve profiles. Notably, the green curve corresponding to an explosion radius of $500 R_{\rm g}$ exhibits two distinct peaks. This occurs because the Keplerian velocity at $500 R_{\rm g}$ is lower than the explosion velocity. Unlike the explosion at $100 R_{\rm g}$, where all ejecta move roughly in the direction of the center of mass motion, some ejecta in the $500 R_{\rm g}$ case move opposite to this direction (i.e., some ejecta have negative Y-velocity components). These opposing ejecta cause the light curve to display two peaks.

As indicated in Table 5.3, larger explosion radii or higher explosion velocities correspond to smaller fallback fractions. Nevertheless, it is clear that the peak luminosity of the light curve is not solely determined by the fallback fraction. Generally, two physical factors shape the power-law slopes of the light curves: the ejecta fallback rate and the temporal variation of the average relative velocity between fallback ejecta and the disk gas. For a single light curve, although the ejecta fallback rate follows a power-law decline over time (Fig. 5.4), the relative velocity does not vary according to a power law (Fig. 5.3). Thus, changes in the average relative velocity over time are responsible for the different power-law slopes observed at various stages of the same light curve. However, for different light curves, variations in both the fallback rates and the evolution of the average relative velocities result in distinct curve shapes and power-law behaviors.

5.3.2 Spectral Energy Distribution

Assume that when the fallback ejecta collide with AGN disc gas of comparable mass, their entire kinetic energy is converted into thermal energy via shock heating. The resulting radiation can be approximated as a blackbody emission. The optical depth at the shock region is estimated by

$$\tau \sim \sigma \frac{\Sigma}{2m_{\rm H}}, \tag{5.13}$$

where σ is the photon cross section, and Σ is the mean column density of the fallback material, which can be inferred from Fig. 5.9. The expression for σ follows from Rybicki et al. (1991) and is given by

$$\sigma = \frac{3}{4}\sigma_{\rm T}\left\{\frac{1+\Gamma}{\Gamma^3}\left[\frac{2\Gamma(1+\Gamma)}{1+2\Gamma} - \ln(1+2\Gamma)\right] + \frac{\ln(1+2\Gamma)}{2\Gamma} - \frac{1+3\Gamma}{(1+2\Gamma)^2}\right\}, \tag{5.14}$$

where $\sigma_{\rm T}$ is the Thomson scattering cross section and Γ is the dimensionless photon energy, defined as the ratio between the photon energy and the electron rest mass energy:

$$\Gamma = \frac{h\nu}{m_{\rm e}c^2}, \tag{5.15}$$

with h being Planck's constant, $m_{\rm e}$ the electron rest mass, and ν the photon frequency. For the fiducial scenario, the fallback occurs near $100R_{\rm g}$, corresponding to $\Gamma \sim 10$. At this location, the optical depth is approximately $\tau \sim 80$, which is significantly greater than unity, justifying the blackbody approximation. The full SED over time can be regarded as the sum of all these individual blackbody spectra.

Let the average molecular weight of the ejecta be expressed as $m_{\rm A} = Am_{\rm H}$. Assume that the AGN disk primarily consists of ionized hydrogen, the temperature T can be derived via the equipartition theorem,

$$\frac{1}{2}m_{\rm A}v_{\rm rel}^2 = \frac{3}{2}(1 + A + \frac{3}{2}A)k_{\rm B}T. \tag{5.16}$$

This yields the relation,

$$T = \frac{2Am_{\mathrm{H}}v_{\mathrm{rel}}^2}{3(2+5A)k_{\mathrm{B}}}, \tag{5.17}$$

where k_{B} denotes the Boltzmann constant. In the case where $A \gg 1$, the equation simplifies to

$$T \simeq \frac{2m_{\mathrm{H}}v_{\mathrm{rel}}^2}{15k_{\mathrm{B}}}. \tag{5.18}$$

While in the case of a SMBH mass of $M_{\mathrm{SMBH}} = 10^6 M_\odot$, and when the fallback ejecta resides within the inner portion of the AGN disk (specifically $< 100R_{\mathrm{g}}$), the ejecta is expected to predominantly interact with its symmetric counterpart. In this case, we have

$$\frac{1}{2}m_{\mathrm{A}}v_{\mathrm{rel}}^2 = \frac{3}{2}(2+A)k_{\mathrm{B}}T, \tag{5.19}$$

leading to the temperature expression,

$$T = \frac{Am_{\mathrm{H}}v_{\mathrm{rel}}^2}{3(2+A)k_{\mathrm{B}}}. \tag{5.20}$$

In the limit where $A \gg 1$, this further reduces to

$$T \simeq \frac{m_{\mathrm{H}}v_{\mathrm{rel}}^2}{3k_{\mathrm{B}}}. \tag{5.21}$$

Fig. 5.6 presents the SEDs at peak luminosity for various SMBH masses. It is evident that a decrease in SMBH mass corresponds to an increase in peak luminosity, consistent with the findings shown in Fig. 5.5. Each of these SEDs displays characteristics of multi-temperature blackbody radiation, with their peaks located in the soft γ-ray region. Particularly, for $M_{\mathrm{SMBH}} = 10^6 M_\odot$, the SED reaches its maximum at a higher frequency. This arises from the relatively low gas density in the inner AGN disk region when the central SMBH is less massive, causing the fallback ejecta to interact primarily with its symmetric counterpart. Consequently, the resulting emission tends to be of higher energy. In contrast, for SMBHs with $M_{\mathrm{SMBH}} \gtrsim 10^7 M_\odot$, energy dissipation mainly occurs through collisions between the fallback ejecta and the disk material. This difference in interaction mechanism is reflected in the comparison between Equations(5.17) and (5.20). This is because, under the equipartition theorem, the average energy acquired by each particle from the dissipation of kinetic energy differs, owing to the distinct compositions of the fallback ejecta and the AGN disk gas. Nevertheless, the term v_{rel} in Equations (5.16) and (5.19) consistently denotes the relative velocity between the fallback material and the disk gas. Given the symmetry of the fallback ejecta with respect to the AGN disk plane, the vertical (Z-direction) components of velocity

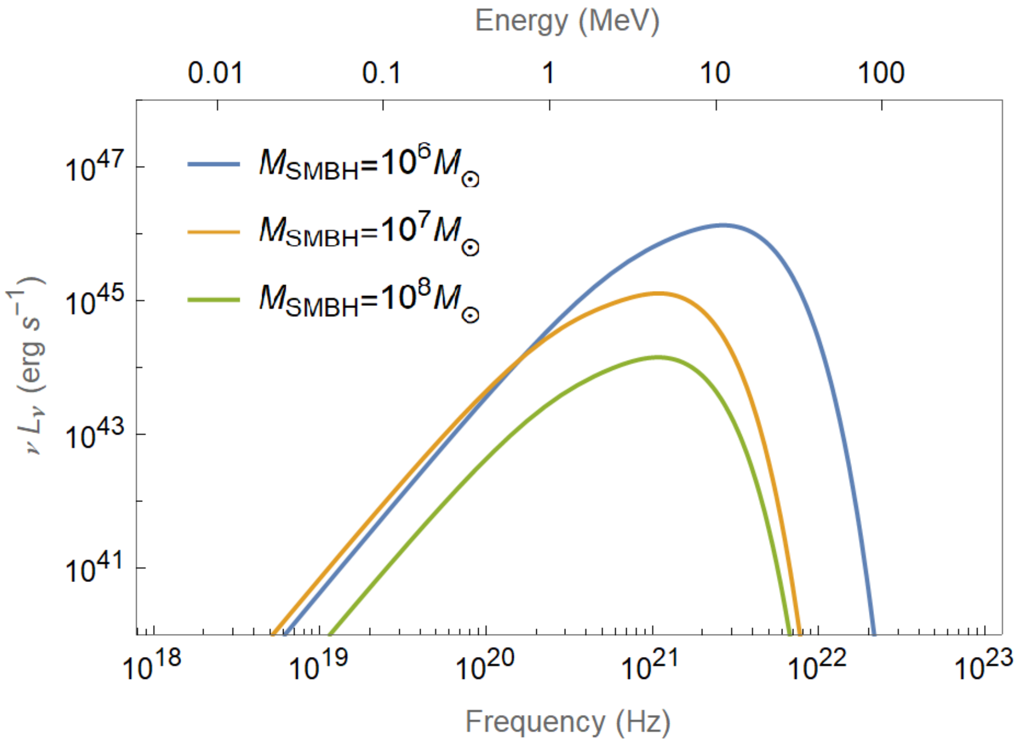

Figure 5.6 Spectral energy distributions at peak luminosity for various SMBH masses, with all other parameters following the fiducial model.

cancel out, and the final state is the same in both cases, i.e., the fallback ejecta settles into the disk material.

Fig. 5.7 display the SEDs corresponding to $M_{\rm SMBH} = 10^7 M_\odot$ and $M_{\rm SMBH} = 10^6 M_\odot$, respectively. Different colors represent SEDs at various moments in time. At the peak of the light curve, the SEDs exhibit maxima in the soft γ-ray band due to the high value of $v_{\rm rel}$. As time progresses, the peak frequency gradually shifts toward the hard X-ray regime. Excluding certain blazars, typical AGNs have average luminosities below 10^{40}erg s^{-1} in the MeV range (Hubeny et al., 2001). Hence, the emission generated by the fallback ejecta interacting with the disk gas significantly outshines the AGN background, making it potentially observable.

Fig. 5.8 presents light curves with different energies in the soft γ-ray band based on the fiducial model. The figure indicates that higher-energy radiation shows more rapid luminosity changes. For example, though the emission at 10 MeV reaches a peak luminosity above 10^{40} erg s^{-1}, it decays by nearly ten orders of magnitude within six days. In contrast, at 1 MeV, the luminosity drops by about one order over the same period, and at 0.1 MeV, the luminosity remains nearly unchanged. Thus, high-energy ($\gtrsim$ 10 MeV) radiation is mostly concentrated near the moment of luminosity peak, whereas lower-energy radiation persists for longer durations. This behavior remains consistent across different SMBH masses, although the time-scales vary depending on the SMBH mass.

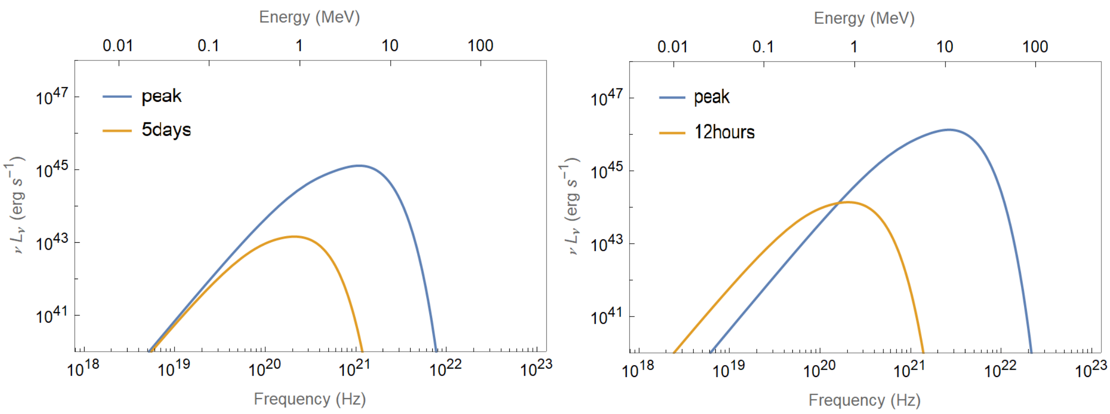

Figure 5.7 Left: SEDs at different epochs under the fiducial setting. The blue curve indicates the time of maximum luminosity, and the orange curve corresponds to 5 days after the explosion. Right: SEDs at various times for $M_{\rm SMBH} = 10^6 M_\odot$. The blue line represents the SED at the peak of the light curve, while the orange line shows the SED 12 hours post-explosion. All other parameters are based on the fiducial model.

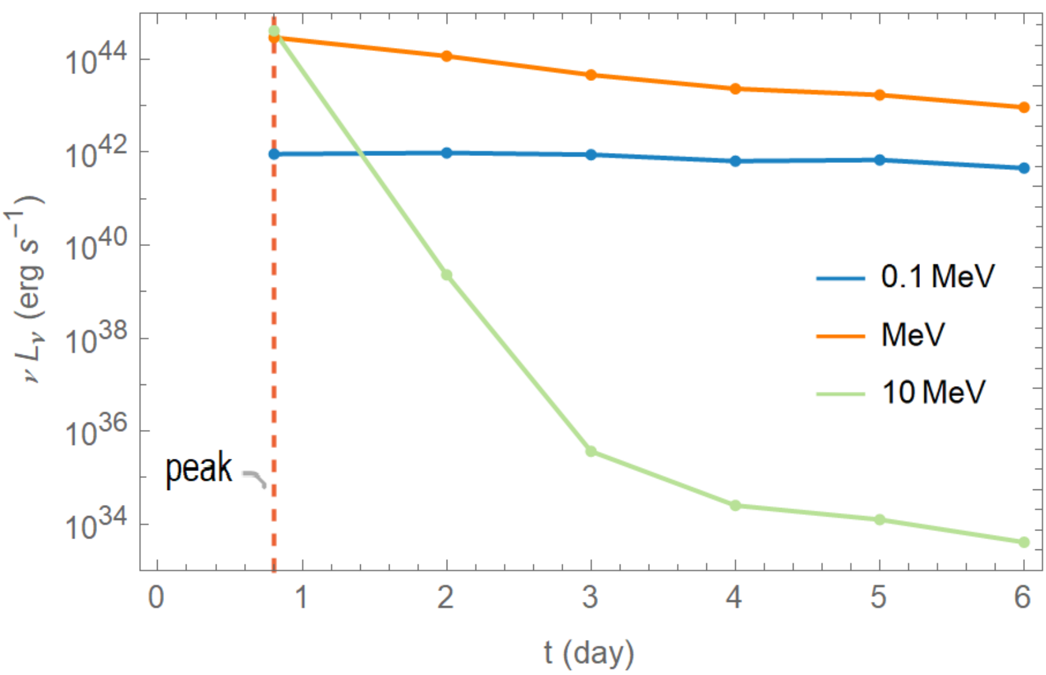

Figure 5.8 Light curves at several energies near the MeV **range under the fiducial setting. The red dashed line marks the time of the total luminosity peak, with the light curves plotted starting from this moment.**

Interestingly, for $M_{\rm SMBH} = 10^6 M_\odot$, the 0.1 MeV luminosity even increases after the total luminosity peak. This phenomenon, also visible in the right panel of Fig. 5.7, results from collisions between symmetric fallback ejecta in the AGN disk's inner region. In contrast, the light curve originating from the initial thermonuclear explosion and radioactive decay of SNe Ia does not vary with SMBH mass, as the decay timescales of radioactive isotopes are intrinsic and independent of external conditions.

It is worth noting that when estimating the radiation temperature, we only considered the partition of kinetic energy into ions and electrons, without allocating any fraction to radiation. If the dissipated kinetic energy were partly transferred into radiation, the resulting temperature would be significantly reduced. However, repeated Compton scattering could substantially increase the effective temperature (i.e., the Compton temperature) (Chan et al., 2021). Therefore, our present calculation should be regarded as preliminary, with many aspects that merit further consideration and improvement, as elaborated in the discussion section. Nevertheless, for reference, Wilson et al. (2004) estimated that the peak photon energy resulting from SNe Ia ejecta colliding with an AGN disc is around 400 keV. In addition, Chan et al. (2021) found that the fallback material from a TDE interacting with an AGN disc can produce photon energies peaking near ~ 1 MeV. Thus, these results are consistent with our qualitative expectations, and it is reasonable that the emitted radiation peaks in the hard X-ray to γ-ray range.

The MeV gamma-ray sky remains largely unexplored at present. As shown in Fig. 5.8, the luminosity at 1 MeV predicted by the fiducial model reaches $\sim 10^{43}$ erg s^{-1}. The *Fermi* Gamma-ray Burst Monitor (GBM) (Meegan et al., 2009) is capable of detecting such events for ~ 1 MeV gamma-ray emission only up to a distance of ~ 1 Mpc. Nevetheless, some of the events we predict, with peak energies in the 10−50 MeV range, could potentially be identified in *Fermi* data through the Large Area Telescope (LAT) Low-Energy analysis, which extends the effective area down to 30 MeV (Pelassa et al., 2010). Our predicted signals might also be observable by upcoming MeV missions such as the Compton Spectrometer and Imager (COSI) (Tomsick et al., 2022), Cube Sat MeV telescope (MeVCube) (Lucchetta et al., 2022), e-ASTROGAM (de Angelis et al., 2018), ComPare (Shy et al., 2022; Moiseev et al., 2015), the All-sky Medium Energy Gamma-Ray Observatory eXplorer (AMEGO-X) (Fleischhack, 2021), the Galactic Explorer with a Coded aperture mask Compton telescope (GECCO) (Orlando et al., 2022), and the Advanced Particle-astrophysics Telescope (APT) (Buckley et al., 2022). For example, AMEGO-X's sensitivity at 1 MeV is approximately 5×10^{-6} MeV cm^{-2}s^{-1} (Fleischhack, 2021), enabling it to detect our predicted bursts out to distances of ~ 100 Mpc. This range greatly exceeds the distance to the nearest known Seyfert galaxy (Filippenko et al., 2003).

5.3.3 Other Observational Effects

Apart from the MeV-band variability, collisions between WDs in AGN disks can lead to additional effects.

In sufficiently thin AGN disks or when the central SMBH has a relatively low mass,

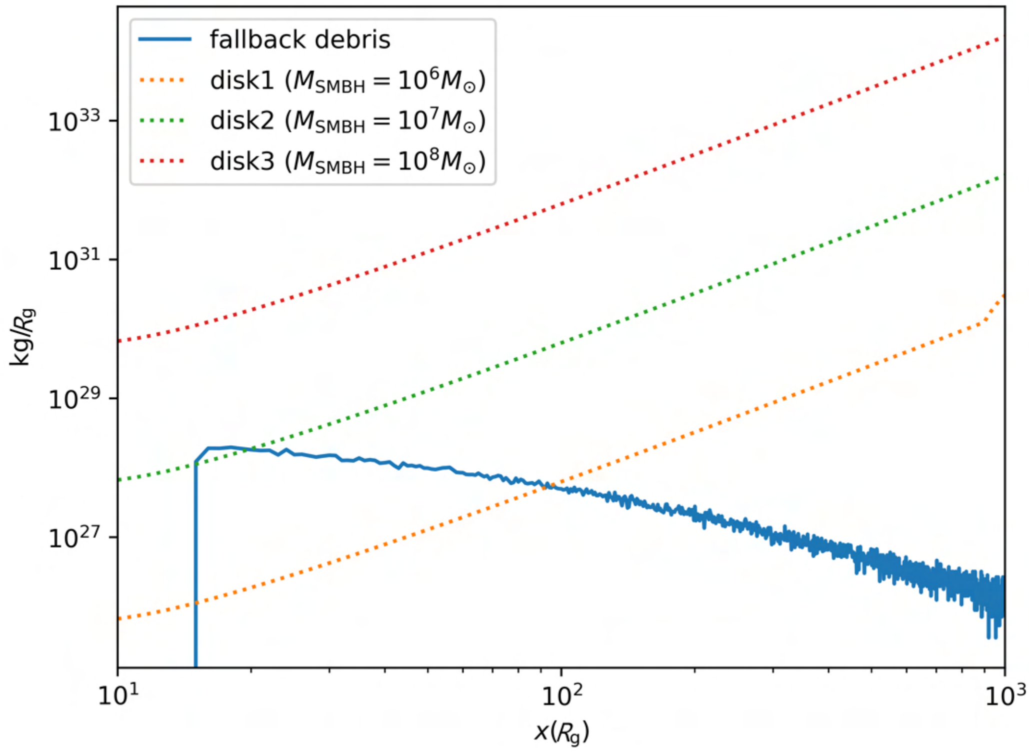

Figure 5.9 The cumulative distribution of fallback ejecta within the AGN disk is shown by the blue curve, while the dotted orange, green, and red curves represent the spatial distributions of AGN disk gas for central SMBH masses of $10^6 M_\odot$, $10^7 M_\odot$, and $10^8 M_\odot$, respectively. All results are derived using fiducial model parameters, with variations only in the SMBH mass.

the fallback mass per unit area may surpass the local gas mass density of the AGN disk, as illustrated in the case of $M_{\rm SMBH} = 10^6 M_\odot$ in Fig. 5.9. This imbalance can lead to a temporary disturbance in the AGN accretion flow, causing a transient decline in luminosity. However, over an accretion timescale, the AGN luminosity is expected to recover. Such behavior is consistent with the observational phenomenon of "changing-look AGNs," where the luminosity exhibits a transition from bright to dim and then back to bright, as modeled for the source 1ES 1927+654 (Trakhtenbrot et al., 2019; Ricci et al., 2020; Li et al., 2022c). Intriguingly, polarization studies of changing-look AGNs provide evidence that these luminosity variations are indeed driven by intrinsic fluctuations in the accretion rate rather than external obscuration (Hutsemékers et al., 2017).

Additionally, ejecta produced by supernova explosions can significantly enhance the metallicity of AGNs. Observations indicate that AGNs exhibit super-solar metallicity that remains nearly unchanged with redshift evolution. Moreover, colliding WDs will emit GWs. However, the GWs generated by WD collisions are likely to be short-lived, burst-like pulses, making them difficult to detect even within the Milky Way (Lorén-Aguilar et al., 2010). Nevertheless, the memory effect of GWs warrants further investigation.

5.4 Discussion

5.4.1 Collision Position

While numerous studies have suggested that migration traps could exist, Dittmann et al. (2020) reported the absence of migration traps in their disk models. Similarly, Pan et al. (2021b) argued that the inclusion of headwind effects can entirely eliminate these traps. Nevertheless, our conclusions are not entirely contingent on the existence of migration traps. We still anticipate that the novel events proposed in our study will predominantly emerge within radii $\lesssim 10^3 R_\mathrm{g}$. The rationale is as follows:

(1) Even in the absence of migration traps, a concentration of compact objects may naturally arise in disk regions with varying aspect ratios or where migration timescales differ significantly (McKernan et al., 2014). According to McKernan et al. (2012), the migration timescale for $1 M_\odot$ compact objects tends to increase inward of $\sim 10^3 R_\mathrm{g}$—a conclusion based solely on Type I torques. Moreover, Fig. 3 of Peng et al. (2021), which incorporates both gas and GW torques, shows that in the outer disk region ($\sim 10^3 R_\mathrm{g}$, outside of trap zones), torque magnitudes decrease or migration becomes slower with decreasing radius. This difference in migration velocity could facilitate collisions before WDs reach the putative trap region.

(2) Our numerical results demonstrate that even when two WDs have closely spaced orbits (separated by less than $2\sqrt{3}\ R_\mathrm{H}$), the probability of collision in the outer disk remains low (Luo et al., 2023).

(3) Even some collisions between WDs occur in the outer AGN disk, their detectability may be limited by the surrounding gas, unless the generated shock wave can successfully break through the disk surface (Zhu et al., 2021c). Though the outermost parts of AGN disks (e.g., at $\gtrsim 10^4 R_\mathrm{g}$) may initially be neutral, prompt radiation from the explosion can ionize this gas on a short timescale (Perna et al., 2021a). This resulting ionization renders the disk optically thick and prevents the ejecta from escaping, suppressing obvious signals. In such cases, while the explosion may contribute to the disk feedback, its impact is generally minor compared to the disk luminosity, as noted in Gilbaum et al. (2022). Alternatively, Grishin et al. (2021) proposed that ejecta not located on the disk midplane could escape if their velocity exceeds the escape threshold. However, if the ejecta are partially slowed before leaving the disk and fall back, this would require an unrealistic

fine-tuning of the explosion height.

5.4.2 Uncertainties in SEDs

For SMBHs with relatively low masses, corrections are required for both the light curves and SEDs. As illustrated in Fig. 5.9, the fallback ejecta near the inner boundary of an SMBH with $M_{\rm SMBH} \sim 10^6 M_\odot$ is sufficiently dense to alter the AGN disk's structure. Given that only a portion of the fallback ejecta's kinetic energy is converted into thermal energy, some deviation from a perfect blackbody spectrum is possible.

In the last section, we argue that blackbody radiation requires optical thickness. But note that it also needs highly efficient radiative processes to emit blackbody emission. When fallback occurs at small radii ($\lesssim 10^3 R_{\rm g}$), free-free cooling dominates. However, the paucity of high-energy photons from this process can cause deviations from a standard blackbody shape. Specifically, the spectrum may take on a Wien form at high frequencies (due to inverse Compton processes) and appear flatter at low frequencies where free-free emission is dominant (Nakar et al., 2010; Linial et al., 2023). Even so, this deviation is expected to remain moderate because there are typically sufficient soft photons (Katz et al., 2010) to interact with energetic electrons, and soft photons from the AGN disk can also serve as seed photons for inverse Compton scattering.

When estimating the radiation temperature, we only considered the partition of kinetic energy into ions and electrons, without allocating any fraction to radiation. If the dissipated kinetic energy were partly transferred to radiation, the resulting temperature would be significantly reduced. However, at larger radii ($\gtrsim 10^3 R_{\rm g}$), the fallback ejecta tend to become more diffuse and optically thin, causing inverse Compton scattering to dominate. Even in relatively inner regions, repeated Compton scattering could substantially increase the effective temperature (i.e., the Compton temperature) (Chan et al., 2021). In this regime, the AGN disk remains the main source of seed photons. Nevertheless, the actual radiation spectrum is likely a mixture of several components that evolve over time. Additional physical processes—such as pair production and magnetic field effects—should also be considered for a comprehensive picture. Therefore, while the multi-temperature blackbody model adopted in this work offers a useful first-order estimate of the radiation output, it has inherent limitations. More accurate modeling of the radiation mechanisms and transport will be necessary to obtain realistic spectra.

5.4.3 Potential Implications

In this work, both the trajectory computations and the adopted disk model neglect general relativistic (GR) effects. The analysis assumes that collisions primarily occur at radii $\sim 10^2 - 10^3 R_{\rm g}$, i.g., before the WDs reach the innermost regions. For instance, at distances around $\sim 10^2 R_{\rm g}$, the influence of GR—such as modifications to the debris fallback time and relative velocities due to orbital precession—is significantly weaker than other factors like the mass of the SMBH and the explosion velocity. Thus, using Newtonian mechanics for trajectory calculations provides a valid first-order approximation. Nonetheless, GR becomes essential when collisions happen deep in the potential well, e.g. $\sim 10 R_{\rm g}$.Similarly, relativistic corrections to the AGN disk structure remain subdominant unless the region is very close to the SMBH. Moreover, when the accretion rate remains moderate, the deviation of the disk gas's angular velocity from the Keplerian value is minimal (Peng et al., 2021), indicating that the classical model of Kato et al. (2008) remains adequate for our purposes.

If some WDs manage to avoid collisions in the outer regions, they may continue migrating inward, eventually merging near the final migration trap (Peng et al., 2021) or being accreted by the central SMBH. In scenarios where such collisions occur in the innermost disk region, GR corrections become significant. One expected GR effect pertains to the optical emission from SN Ia, which primarily arises from radioactive decay. Since decay processes are governed by local proper time, GR time dilation causes the observed decay duration to appear longer for distant observers than in SN Ia events. However, detecting this time dilation observationally is difficult, as it requires monitoring the source well after peak brightness—when the emission may already be outshone by the AGN's optical background.

In addition, several other phenomena may also occur. Firstly, if an EMRI formed before the WD collision, its sudden termination due to the collision could produce a characteristic gravitational wave signal. Secondly, the initial explosion may significantly disrupt the AGN disk structure, resulting in a sharp drop in AGN brightness, while the supernova luminosity—particularly in the optical band—may increase substantially. Thirdly, in the innermost regions of the AGN disk, where the explosion velocity is too low to overcome the local gravitational potential, fallback material may accrete onto the central SMBH, forming a transient accretion disk. This temporary emission source could mimic the features of a TDE. Fully resolving these scenarios would require advanced modeling, including general relativistic magnetohydrodynamics and detailed radiative transfer simulations, which will be explored in future research.

Moreover, early interaction between the ejecta and disk material could generate a brief, sharp peak in the light curve shortly after the explosion (Piro et al., 2016; Jiang et al., 2021). A further issue is whether the explosion can cause substantial structural changes to the AGN disk. We can estimate the size of the cavity formed by the explosion. In our fiducial setup, where the ejecta sweeps away a disk mass comparable to its own, the resulting cavity radius is estimated to be only $\sim 5R_{\rm g}$. This suggests that at distances $\gtrsim 100\ R_{\rm g}$ from the SMBH, the AGN disk remains nearly intact. However, for systems with lower SMBH masses or thinner accretion disks, the initial explosion may significantly disrupt the local disk environment—a possibility warranting more detailed study.

5.5 Conclusions

In this work, we have presented the study of WD collisions within AGN disks. We first qualitatively analyzed why WDs can collide in AGN disks, then revisited N-body simulations to reveal the statistical characteristics of such collisions. Finally, we discussed the potential observational effects of these events. The main conclusions are as follows:

(i) WDs in AGN accretion disks can migrate to the inner disk region and form dynamically unstable three-body systems. Due to the strong dynamical interactions, these systems do not evolve into binary configurations via gravitational wave radiation but instead lead to close encounters and direct collisions. The estimated collision rate is up to $\sim 300\ \rm Gpc^{-3}\ yr^{-1}$, accounting for approximately 1% of the observed rate of SNe Ia.

(ii) Close encounters between WDs primarily occur when their initial orbital separation lies in the range $1.1\ R_{\rm H} < p < 2\sqrt{3}\ R_{\rm H}$. When $p < 1.1\ R_{\rm H}$, most WDs follow horseshoe orbits, with only a small fraction undergoing close encounters due to their initial orbital phase differences. At $p = 3.0\ R_{\rm H}$, the majority of samples experience WD-WD collisions within 10^5 orbital periods. As the mutual inclination becomes higher or the SMBH mass increases, the WD−WD collision probability decreases.

(iii) WD collisions trigger thermonuclear explosions, making them a potential channel for producing SNe Ia. In the inner region of AGN accretion disks, the disk material is typically insufficient to significantly decelerate the ejected debris, leading to symmetric ejection along both sides of the disk. Under the gravitational influence of the SMBH, the ejecta eventually fall back onto the AGN disk, where their kinetic energy is dissipated into thermal radiation. This results in a rapid luminosity rise, followed by a decay as $L \propto t^{-2.8}$, with timescales ranging from hours to months depending on the SMBH mass.

(iv) The interaction between the ejecta and the AGN disk can generate high-energy radiation spanning from hard X-rays to soft gamma-rays. Future MeV observatories, such as AMEGO-X, are expected to detect these high-energy transients within a range of $\sim$ 100 Mpc. The subsequent disruption of the AGN disk by these impacts may also lead to the phenomenon of changing-look AGNs. Additionally, the metal enrichment from thermonuclear explosions can significantly enhance the metallicity of AGN disks, consistent with the observed supersolar metallicity in AGNs across different redshifts.

WD collisions in AGN disks represent one class of compact object mergers within AGN environments. Other similar events may include WD-BH, WD-NS, and star-BH collisions. If such collisions also result in energetic outbursts, they may produce analogous observational signatures, particularly in the MeV band. As observational gaps in the MeV regime are gradually filled, the study of explosive events in AGN disks will become more comprehensive.

Chapter 6 Multimessenger Implications for Neutron Star Accretions in AGN Disks

6.1 Background

Recall that Chapter 4 introduced the hierarchical pattern in the accretion behavior of NSs in AGN disks. The accretion of NSs in AGN disks is unique on the scale of the NS's magnetosphere. Due to their small radii and solid surfaces, NSs exhibit a mass-to-energy conversion efficiency during accretion that is roughly three times greater than that of Schwarzschild BHs. Additionally, magnetic field lines channel the inflowing material toward the NS's polar caps (Shapiro et al., 2008), concentrating the accretion onto small surface areas. This localized infall tends to significantly heat the polar regions, causing neutrino production to commence at relatively lower critical accretion rates (Mushtukov et al., 2018, 2019). Since neutrinos transport a large fraction of the accretion energy, they effectively limit the electromagnetic output to around the Eddington luminosity (Basko et al., 1976; Mushtukov et al., 2018). Consequently, the contribution of electromagnetic feedback on the AGN disk is negligible in comparison to that from disk outflows, as most of the surplus energy is removed by neutrino emission.

Furthermore, at high accretion rates, NSs may develop mass quadrupole deformations that emit GWs. Potential mechanisms include non-axisymmetric ”mountains” supported by the elastic crust (Bildsten, 1998; Ushomirsky et al., 2000) or magnetic stresses (Melatos et al., 2005; Haskell et al., 2015), as well as unstable stellar oscillation modes (Andersson, 1998; Andersson et al., 1999). However, current models of NS accretion in AGN disks generally neglect GW and neutrino emission, both of which critically influence accretion dynamics and electromagnetic feedback by mediating energy and angular momentum loss. Their inclusion could also yield unique multi-messenger signals, offering observational avenues to identify compact objects in AGN environments.

The accretion rate of NSs in AGN disks further determines their lifetimes and, consequently, has a direct impact on the binary NS merger rate.The origin, composition, and formation pathways of compact objects in the low-mass gap, as well as their connection to GW events involving binary NS mergers, are still uncertain. Some studies propose that these objects may form within AGN disks (Yang et al., 2020; Perna et al., 2021b; Tagawa et al., 2021; Pan et al., 2022). Binary NS mergers in AGN disks have been investigated by Zhu et al. (2021d); Kathirgamaraju et al. (2023). Perna et al. (2021b) estimated that the NS merger rate in such environments could reach ~ 0.1–$5\ \mathrm{Gpc^{-3}yr^{-1}}$ if the NSs accrete at the Eddington limit. However, these analyses often overlook the detailed effects of accretion. If NSs are capable of forming binaries in AGN disks and merging at significant rates, a correspondingly large NS merger rate is expected. Yet, among nearly 200 GW events detected by ground-based observatories to date (see the Gravitational-Wave Candidate Event Database (GraceDB, 2024)), fewer than 10% are attributed to NS–NS or NS–BH mergers, with the vast majority being BH–BH events. This highlights the importance of accurately modeling NS accretion in AGN disks to assess whether these systems predominantly undergo accretion-induced collapse (AIC) or binary mergers.

This chapter aims to explore how NSs accreting in AGN disks, taking into account the impact of neutrinos and GWs production, and discuss potential observable multimessenger signals.

6.2 The Roles of Neutrinos

6.2.1 Classification of Accretion

We explored the accretion behavior of NSs in AGN disks following the hierarchical pattern illustrated in Fig. 4.3, which generally applies to typical AGN disk environments. Nevertheless, the wide range of disk parameters—such as magnetic field strength, angular momentum, and accretion rate—may introduce subtle differences or reveal finer details in the accretion process. This section offers a more detailed classification of NS accretion regimes in AGN disks based on neutrino production.

Fig. 6.1 presents a classification scheme for various accretion scenarios and associated neutrino emission from NSs within AGN disks. The framework is divided into two main branches as determined by the angular momentum of the inflow. In cases where the accreted material possesses sufficient angular momentum to form a circum-NS disk, accretion proceeds through three hierarchical stages. Conversely, if the angular momentum is too low to sustain a disk, the accretion process is nearly spherical until it interacts with the magnetic barrier or reaches the NS surface.

In the rightmost column of Fig. 6.1, red boxes denote regimes where neutrino emission dominates, while green boxes correspond to cases with negligible neutrino production. A specific example is the scenario labeled “Disk accretion –Weak magnetic field –$\dot{m} \lesssim \dot{m}_{\rm cn}$”, where the green box indicates an expectation of minimal neutrino out-

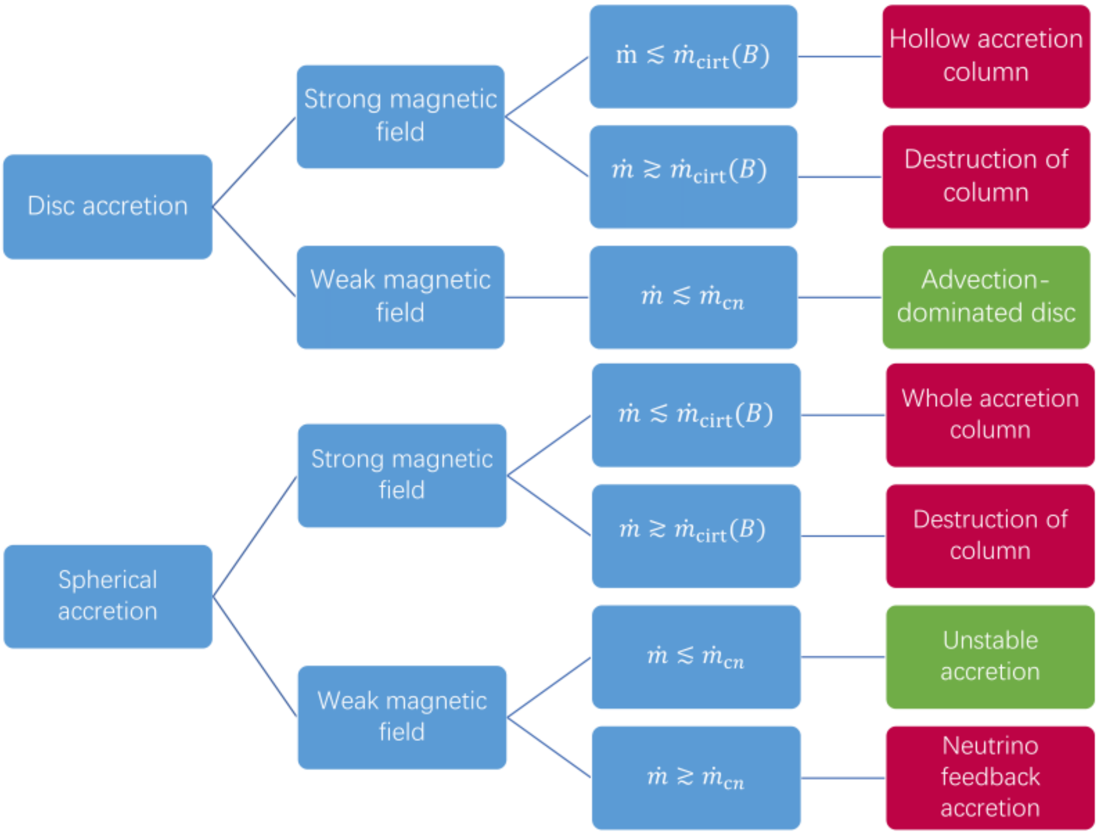

Figure 6.1 Categorization of NS accretion modes in AGN disks and the corresponding neutrino emission, determined by the accretion flow's angular momentum, magnetic field intensity, and accretion rate. Red boxes on the right denote scenarios where neutrino emission is dominant, whereas green boxes represent cases with negligible neutrino output. Here, a strong magnetic field refers to conditions where the Alfvén radius is substantially greater than the NS radius.

put. Nonetheless, it remains possible that sporadic or non-steady neutrino-cooled accretion could occur (Chevalier, 1996). It should also be emphasized that the thresholds $\dot{m}_{\rm crit}(B, S)$ and $\dot{m}_{\rm cn}$ are not universal constants. The value of $\dot{m}_{\rm crit}(B, S)$—the critical accretion rate at which the base of the accretion column is disrupted—depends on both the magnetic field strength and whether a circum-NS disk is present (i.e., the effective cross-sectional area S of the accretion column), as elaborated in Eq. (6.3). Meanwhile, the critical rate for neutrino-dominated accretion, denoted $\dot{m}_{\rm cn}$, is determined by the mode through which material reaches the NS surface. Three distinct regimes are identified: (1) for spherical accretion, $\dot{m}_{\rm cn} \gtrsim 10^4\ \dot{m}_{\rm Edd}$ (Chevalier, 1989); (2) for disk accretion, $\dot{m}_{\rm cn} \sim 1\ {\rm M_\odot s^{-1}}$; and (3) for accretion via columns, where $\dot{m}_{\rm cn} \approx 500\ \dot{m}_{\rm Edd}$.

Because of the specific physical conditions in AGN disks, Fig. 6.1 does not include all theoretically possible NS accretion scenarios reported in the literature. For instance, the scenario "Disk accretion -Weak magnetic field -$\dot{m} \gtrsim \dot{m}_{\rm cn}$" is excluded, as Fig. 4.5 indicates that such a scenario is unlikely to occur in AGN disks. Instead, it may occur under much higher accretion rates, such as those found in fallback accretion following supernovae (Chevalier, 1996). Similarly, the case of strong magnetic fields combined with accretion rates below the neutrino-cooling threshold (i.e., column accretion $\lesssim 500\dot{m}_{\rm Edd}$ with negligible neutrino production) is not shown, since Figures 4.4 and 4.6 indicate that such conditions are rarely met in AGN disks. Nevertheless, this regime could potentially arise temporarily during episodes of intermittent accretion, especially when a cavity is present.

The dominant accretion modes also vary with radial distance from the AGN center. In the inner regions, the higher sound speed generally leads to nearly spherical accretion. In contrast, the outer parts of the disk more commonly give rise to circum-NS disks. Throughout the disk, the net accretion rate onto the NS tends to be relatively low near both the inner edge and the outer regions, with a peak around $\sim 100R_{\rm g}$. In conclusion, except for a few marginal cases, NS accretion within AGN disks is primarily characterized by strong neutrino emission.

6.2.2 Column Bottom Destruction and Neutrino Energy Spectrum

The following analysis concentrates on the typical scenario, exploring the accretion column in detail. When the accretion rate exceeds the critical threshold of approximately $500\dot{m}_{\rm Edd}$, the electromagnetic luminosity produced by the accretion column no longer increases significantly, remaining around or slightly above $\sim L_{\rm Edd}$ (Basko et al., 1976; Mushtukov et al., 2018). Although this peak luminosity depends strongly on the geometry of the accretion flow and can exceed $L_{\rm Edd}$, it remains small compared to the gravitational energy released during accretion. This occurs because, at accretion rates far exceeding the Eddington limit, the accretion column becomes optically thick to photons, preventing most of them from escaping sideways. Instead, photons are advected inward with the inflowing material and become trapped near the base of the column, leading to greatly increased radiation energy density and temperature. When the temperature reaches sufficiently high values, neutrino emission dominates energy losses over photons, and neutrino emission efficiently removes the surplus energy flux.

The scale height of the accretion column is characterized by the location of the shock within it. As the accretion rate increases, this shock moves upward until one of two conditions is met: (i) it reaches the Alfvén radius, or (ii) the ram pressure from the inflowing material becomes comparable to the magnetic pressure at the NS surface (Basko et al., 1976). Namely, a sufficiently high accretion rate can destabilize the base of the column. Assuming a proton number density at the column base of $n_{\rm p}$, the critical temperature $T_{\rm crit}(B, S)$ beyond which disruption occurs is obtained by solving the inequality:

$$P_{\rm tot}(S, B, T) < P_{\rm crit}(B, T), \tag{6.1}$$

where the two pressure terms are given by:

$$P_{\rm crit} \approx 3 \times 10^{23} S_{10}^{1/2} B_{12}^{2} T_{10}^{-1} \text{ erg cm}^{-3}, \tag{6.2a}$$

$$P_{\rm tot} = P_{\rm gas} + P_{\rm rad} = n k_{\rm B} T + \frac{1}{3} a T^4, \tag{6.2b}$$

with $P_{\rm crit}$ representing the magnetic-pressure-limited threshold at which the column base becomes unstable (Bildsten et al., 1997), and $P_{\rm tot}$ denoting the combined gas and radiation pressure. Here, S is the cross-sectional area of the accretion column, and n is the total number density of massive particles, including protons and both species of leptons: $n = n_{\rm p} + n_{+} + n_{-}$. The radiation constant is denoted by a. For geometry, typical values are $S \sim 10^{10}$ cm^2 for hollow columns and $S \sim 10^{12}$ cm^2 for filled (solid) columns. Importantly, the critical temperature $T_{\rm crit}$ is relatively insensitive to the exact value of $n_{\rm p}$; we adopt $n_{\rm p} = 5.98 \times 10^{29}$ cm^{-3} (equivalent to a mass density of $\rho = 10^6$ g cm^{-3}) for calculations. The equilibrium number densities of electrons and positrons, $n_{\mp}(T, B)$, are evaluated by integrating over the longitudinal momentum distribution and summing over Landau levels, as described in Kaminker et al. (1992); Harding et al. (2006); Mushtukov et al. (2018). We follow the method in Mushtukov et al. (2018) and assume a fully ionized hydrogen plasma to compute $n_{\mp}$ numerically.

Since the neutrino-emitting region is confined within the magnetosphere and does not extend beyond the scale height of the accretion column, the maximum sustainable accretion rate $\dot{m}_{\rm crit}$ can be constrained by the condition:

$$r_{\rm m}(B, \dot{m})\ S\ Q_{\nu}^{-}(T_{\rm crit}) \gtrsim \frac{\eta \dot{m} c^2}{2}, \tag{6.3}$$

where $Q_{\nu}^{-}(T_{\rm crit})$ denotes the volumetric energy loss rate due to neutrino emission via electron−positron annihilation. For temperatures $T \gtrsim 10^9$ K and magnetic fields $B \lesssim 10^{15}$ G, this rate is approximated by (Kaminker et al., 1994)

$$Q_{\nu}^{-} \approx 4 \times 10^{24} T_{10}^{9} \text{ erg cm}^{-3}\text{s}^{-1}. \tag{6.4}$$

As illustrated in Fig. 6.2, when a NS accretes material within AGN disks, the base of a *hollow* accretion column can be readily destroyed if the magnetic field strength satisfies $B \lesssim 5 \times 10^{13}$ G. Following this disruption, the infalling matter escapes the confinement of the column walls, leading to a partial infill of the hollow structure and gradually transitioning into a *solid* column configuration. In contrast, breaking the base of a *solid* accretion column proves more difficult, primarily because its larger cross-sectional area (S) and elevated critical pressure ($P_{\rm crit}$) act to stabilize it, as described by Eqs. (6.2) and (6.3). Therefore, when NSs are located in the innermost region of the AGN disk without forming circum-NS disks, the initially established solid columns tend to remain stable and are unlikely to be disrupted.

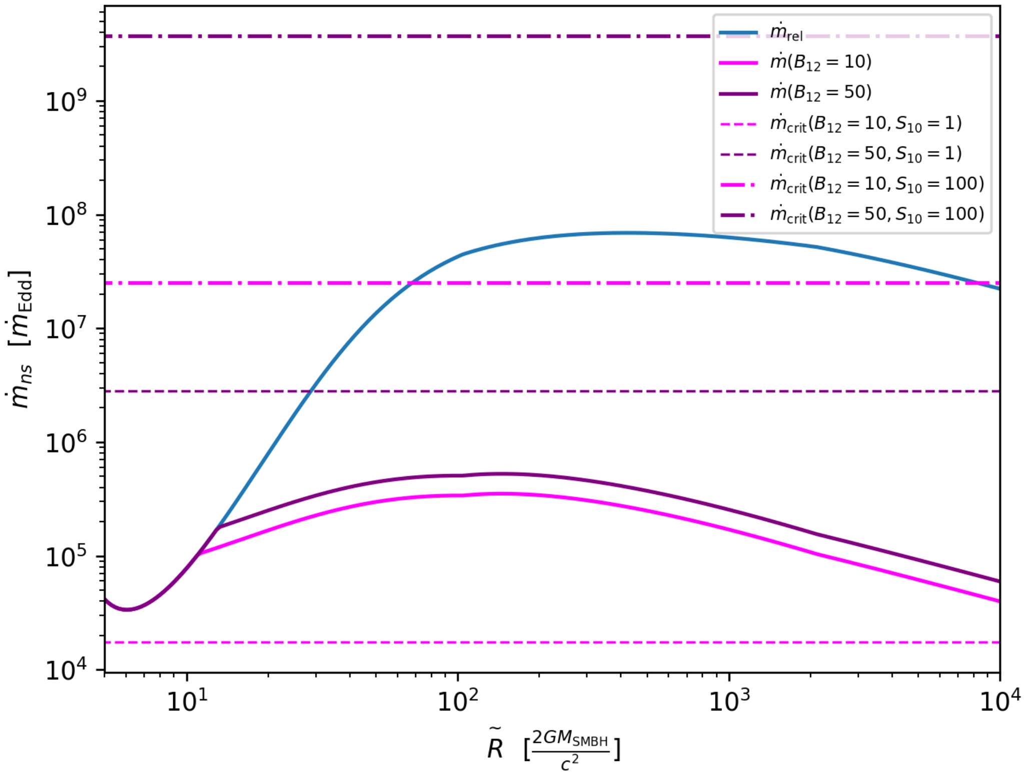

Figure 6.2 Comparison between the accretion rates of NSs in the AGN disk and the critical rates required to disrupt the base of accretion columns. The blue curve, identical to the right panel of Fig. 4.4, shows the Bondi-scale accretion rate under fiducial settings. Solid purple curves indicate the accretion rates at the inner edge of circum-NS disks for various magnetic field strengths. Dashed lines represent the critical rates at which the base of a hollow column becomes disrupted, while dash-dotted lines correspond to the disruption threshold for solid columns. The fiducial settings are the same as in the last chapter.

Table 6.1 Critical temperature and accretion rate responsible for disrupting the bases of hollow accretion columns ($S \sim 10^{10}$ cm^2) as a function of the NS's dipole magnetic field strength.

B[G]	10^{13}	5×10^{13}	10^{14}	2×10^{14}
$T_{\rm crit}$[K]	9.43×10^{9}	1.76×10^{10}	2.32×10^{10}	3.05×10^{10}
$\dot{m}_{\rm crit}[\dot{m}_{\rm Edd}]$	1.82×10^{4}	2.93×10^{6}	2.76×10^{7}	2.55×10^{8}

Table 6.1 lists examples of the critical temperature and accretion rate required for material to spread over the NS surface at the base of hollow accretion columns with dif-

ferent magnetic field strengths. It is evident that the critical accretion rate is quite sensitive to the magnetic field, whereas the critical temperature shows less variation. The temperature at the column base generally remains near 1 MeV, due to the neutrino emission rate being highly sensitive to temperature, as described by Eq. (6.4). Additionally, beyond the critical value, increased temperature leads to disruption at the column base, enlarging its cross section and expanding the neutrino emission zone. This feedback limits any substantial temperature increase. As a result, the neutrino energy spectrum is confined to a narrow energy band, characterized by a temperature of approximately ~ 1 MeV at the neutrino production site.

Once the temperature is obtained, one can compute both the mean energy and the energy spectrum of the emitted neutrinos. The neutrinos mainly result from electron-positron pair annihilation, and the environment is optically thin to neutrinos. Thus, the normalized neutrino spectrum follows the form (Misiaszek et al., 2006):

$$\phi(E_\nu; \langle E_\nu \rangle, \sigma_\nu^2) = \frac{\left(\langle E_\nu \rangle^2/\sigma_\nu^2\right)^{\langle E_\nu \rangle^2/\sigma_\nu^2}}{\Gamma\left(\langle E_\nu \rangle^2/\sigma_\nu^2\right)} \frac{E_\nu^{\langle E_\nu \rangle^2/\sigma_\nu^2 - 1}}{\langle E_\nu \rangle^{\langle E_\nu \rangle^2/\sigma_\nu^2}} \exp\left(-\frac{\langle E_\nu \rangle E_\nu}{\sigma_\nu^2}\right), \tag{6.5}$$

where $\langle E_\nu \rangle(T)$ and $\sigma_\nu^2(T)$ denote the neutrino mean energy and the variance of neutrino energy, respectively, which can be obtained from the tables in PSNS (2001); Misiaszek et al. (2006).

Due to the gravitational redshift experienced by neutrinos emitted close to the NS surface, the observed neutrino spectrum at infinity is modified as:

$$\phi_\infty(E_\nu) = (1 + z_{\rm g})\phi\left((1 + z_{\rm g})E_\nu\right), \tag{6.6}$$

where the gravitational redshift factor is given by

$$1 + z_{\rm g} = \left(1 - \frac{2Gm_{\rm ns}}{r_{\rm ns}c^2}\right)^{-\frac{1}{2}} \tag{6.7}$$

Correspondingly, the average neutrino energy observed shifts to $\langle E_\nu \rangle/(1 + z_{\rm g})$.

As emphasized earlier, temperature is the key parameter governing these spectra; it is ~ 1 MeV for NS accretion within AGN disks. Fig. 6.3 illustrates the spectra detected by a distant observer for temperatures of 0.5 MeV, 1 MeV, and 1.5 MeV. The associated average neutrino energies at the NS surface are 2.26 MeV, 4.11 MeV, and 6.16 MeV, respectively. After accounting for gravitational redshift, these average energies shift to 1.88 MeV, 3.40 MeV, and 5.09 MeV, respectively. At leading order, the spectral shapes are nearly identical for different neutrino flavors (i.e., e, μ, and τ types) (Misiaszek et al., 2006). The resulting spectra are applicable to computations of the neutrino background.

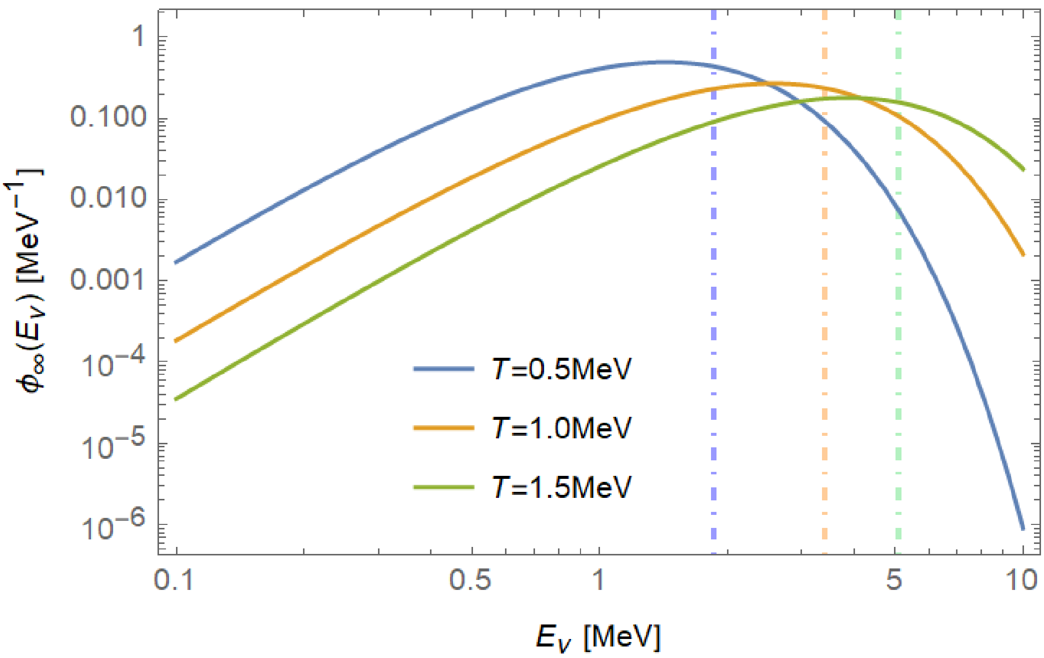

Figure 6.3 Normalized neutrino energy spectra (solid curves) and corresponding average energies (dot-dashed curves) resulting from NS accretion as seen by a remote observer. The temperature refers to that of the hot plasma at the neutrino generation site.

6.2.3 Neutrino Background at MeV Scope

We first evaluate the potential detectability of neutrinos emitted by a single accreting NS in a nearby AGN using the Hyper-Kamiokande (HK) detector. The number of detectable neutrino events depends on several factors: the sensitivity of the detector, the distance to the source, the neutrino luminosity, and the total observation time. The expected number of events can be estimated following Scholberg (2015):

$$N_{ev} \simeq \frac{t}{4\pi d^2 \langle E_\nu \rangle} \frac{V_{\rm det} N_{\rm A} \rho_{\rm N} \sigma_{\rm cc}^{\bar{\nu}_e p} L_\nu}{6}. \tag{6.8}$$

Here, $N_{\rm A}$ is Avogadro's number, $\rho_{\rm N} = 2/18\ {\rm g\ cm^{-3}}$ is the nucleon density in water (Mohapatra et al., 2004), and the cross-section is approximated by $\sigma_{\rm cc}^{\bar{\nu}_e p} \simeq 9{\times}10^{-44} E_\nu^2/{\rm MeV}^2$ (Bahcall, 1989), and the factor of 6 accounts for flavor oscillations reducing the flux of electron antineutrinos. Assuming a detector volume of $V_{\rm det} = 560$ kton for HK (Abe et al., 2011; Scholberg, 2015), a source distance of $d \sim 5$ Mpc, a neutrino luminosity of $L_\nu \sim 2 \times 10^5 L_{\rm Edd}$, and an integration time of $t = 10$ years, the expected number of events is approximately $N_{ev} \sim 10^{-3}$. Clearly, existing and upcoming detectors are incapable of identifying individual neutrino events from NS accretion in AGN environments.

Nevertheless, most of the energy released during NS accretion in AGN disks is carried away by neutrinos; the total energy emitted in neutrinos over the NS's lifetime —from formation to collapse—is estimated to be on the order of $\eta M_{\odot} c^2 \sim 3\times 10^{53}$ erg, comparable to that from a typical core-collapse supernova. However, neutrino emission from accreting NSs in AGNs occurs over relatively long timescales, significantly reducing the likelihood of detection. For comparison, nearly all neutrinos from a supernova are released within $\sim$ 10 seconds (Kotake et al., 2006), leading to a sufficiently high flux to be detected. In addition, the mean energy of neutrinos emitted by NS accretion is slightly lower than that of supernova neutrinos; while supernova neutrino spectra can be approximated by a thermal (Fermi-Dirac) distribution, the spectra from NS accretion follow Eq. (6.5).

Although detecting individual events is difficult, it is worthwhile to investigate the neutrino background generated by NS accretion in AGN disks across the entire sky. Similar to the contribution of supernova neutrinos to the background (Horiuchi et al., 2009; Beacom, 2010), the neutrino number flux from NS accretion in AGNs integrated over the sky can be estimated as

$$\frac{dF(E_\nu)}{dE_\nu} = c\int N_{\rm AGN}(z) n_{\rm ns/AGN} \frac{\overline{L}_\nu}{\langle E_\nu \rangle} \phi_\infty(E_\nu')(1+z)\left|\frac{dt}{dz}\right| dz, \tag{6.9}$$

where $E_\nu' = E_\nu(1+z)$, $|\frac{dz}{dt}| = H_0(1+z)\left[\Omega_{\rm m}(1+z)^3 + \Omega_\Lambda\right]^{1/2}$, and $\overline{L}_\nu$ denotes the average neutrino luminosity including the duty cycle, as introduced in the last chapter. The AGN number density as a function of redshift z is modeled as

$$N_{\rm AGN}(z) = N_{\rm AGN}(0) e(z), \tag{6.10}$$

with the local AGN density $N_{\rm AGN}(0) \sim 10^{-4}$ Mpc^{-3} and

$$e(z) = \begin{cases} (1+z)^{p_1}, & z \leqslant z_{\rm c} \\ (1+z_{\rm c})^{p_1}\left(\frac{1+z}{1+z_{\rm c}}\right)^{p_2}, & z \geqslant z_{\rm c}, \end{cases} \tag{6.11}$$

where $p_1 = 4.1$, $p_2 = 0.03$, and $z_{\rm c} = 1.03$ (Ueda et al., 2003; Fotopoulou, 2012). Over the course of an AGN activity phase with a duration of $\sim 10^6$ yr, a cumulative number of $\sim 10^4$ NSs are expected to have appeared within the disk (Perna et al., 2021b). Therefore, the mean number of NSs coexisting in an AGN disk can be estimated by

$$n_{\rm ns/AGN} \sim \frac{10^4}{10{\rm Myr}} \frac{\eta M_{\odot} c^2}{\overline{L}_\nu}. \tag{6.12}$$

The integral in Equation (6.9) is evaluated numerically up to a maximum redshift of $z = 5$.

Fig. 6.4 illustrates the contribution of neutrinos produced by NS accretion in AGN disks to the neutrino background. The neutrino background from NS accretion primarily falls within the $\sim$ MeV energy range, whereas the MeV neutrino background has previously been attributed mainly to supernovae. As shown, at energies around 1 MeV, neutrinos from NS accretion in AGNs contribute approximately 25% of the supernova neutrino background; at around 0.3 MeV, the background flux from NS accretion in AGN disks becomes comparable to that from supernovae. It should be noted that the abundance of NSs in AGNs significantly influences the overall neutrino background level. While mass segregation may decrease the NS population within AGN nuclear clusters (McKernan et al., 2020), the occurrence of repeated AGNs (Shankar et al., 2009) can instead lead to an increase, thereby enhancing the corresponding neutrino background contribution.

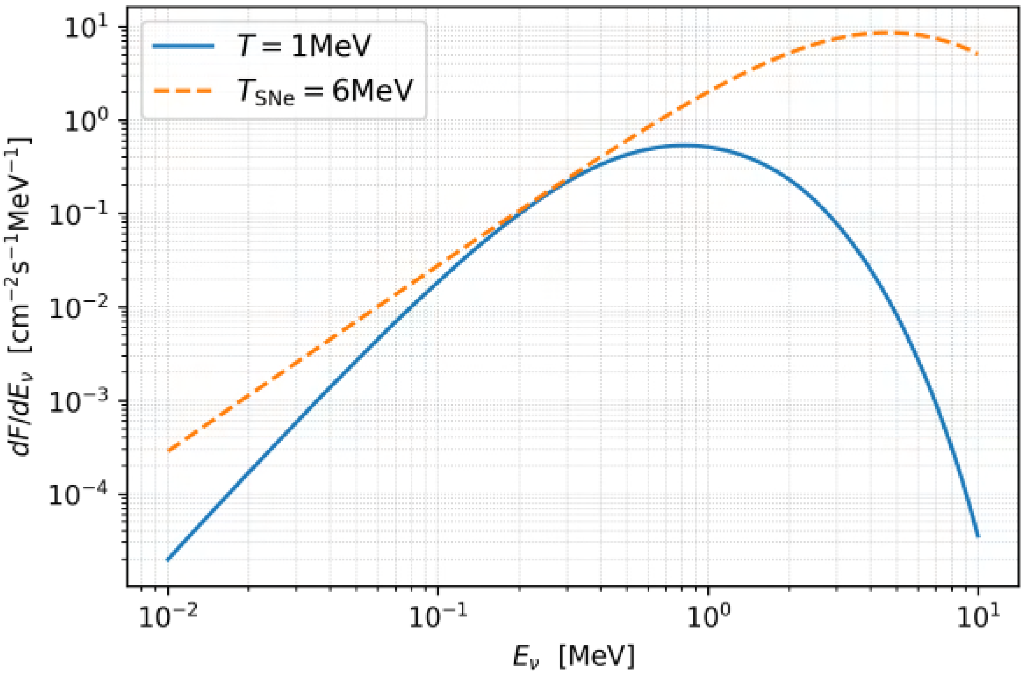

Figure 6.4 Neutrino background (all flavors) resulting from NS accretion within AGN disks is depicted by the blue solid line. For comparison, the Diffuse Supernova Neutrino Background (all-flavor), based on Horiuchi et al. (2009), is shown as the yellow dashed line.

We are aware that emissions from terrestrial nuclear reactors primarily contribute to neutrino backgrounds at energies $\lesssim$ 1 MeV, which significantly exceed the estimated background produced by NS accretion in AGN disks. Thus, detecting the neutrino background at energies $\lesssim$ 1 MeV remains a significant challenge. Nonetheless, since reactor neutrinos originate from identifiable locations on Earth, their effects can potentially be reduced by employing multiple detectors or utilizing techniques such as spectral analysis and temporal correlation.

6.2.4 Angular Momentum Carried Away by Neutrinos

Assuming that neutrinos are emitted isotropically at the emission points in the frame co-rotating with a NS rotating at angular velocity Ω, the star's rotation can lead to a net angular momentum being carried away by the neutrinos when observed in the laboratory frame. For simplicity, we consider the NS's rotation axis to be aligned with its magnetic pole and oriented perpendicular to the AGN disk plane. As accreting matter moves along the magnetic column toward the NS surface, it generates neutrino emission. Each neutrino carries momentum, and thus contributes to angular momentum. In the co-rotating frame, the mean angular momentum carried by neutrinos vanishes. However, in the laboratory frame, the average angular momentum transported by a single neutrino with energy E_ν is given by

$$d\bar{J} = \frac{E_\nu \Omega \frac{r_{\rm cap}^2}{c^2}}{\sqrt{1 - \frac{\Omega^2 r_{\rm cap}^2}{c^2}}}, \tag{6.13}$$

where the polar cap radius $r_{\rm cap}$ is related to the magnetospheric radius $r_{\rm m}$ by the relation (Shapiro et al., 2008)

$$r_{\rm cap} = r_{\rm ns}\sqrt{\frac{r_{\rm ns}}{r_{\rm m}}}. \tag{6.14}$$

Therefore, the total rate of angular momentum loss due to neutrino emission can be expressed as:

$$\dot{J} = \frac{dN_\nu}{dt} d\bar{J} = \frac{L_\nu \Omega \frac{r_{\rm cap}^2}{c^2}}{\sqrt{1 - \frac{\Omega^2 r_{\rm cap}^2}{c^2}}}. \tag{6.15}$$

Table 6.2 The angular momentum loss rates via neutrino emission for NSs with different masses and spin rates. The columns from left to right show the NS masses, angular velocities, neutrino-induced angular momentum loss rates, accretion-driven gain rates, and their respective ratios.

$m_{\rm ns}$ [$M_\odot$]	Ω [s^{-1}]	$\dot{J}_\nu$ [$\frac{\dot{m}}{\dot{m}_{\rm Edd}}$ g cm^{2}s^{-2}]	$\dot{J}_{\rm acc}$ [$\frac{\dot{m}}{\dot{m}_{\rm Edd}}$ g cm^{2}s^{-2}]	$-\dot{J}_\nu/\dot{J}_{\rm acc}$
1.4	0	0	4.22×10^{34}	0
1.4	3.0×10^3	-1.12×10^{32}	4.22×10^{34}	0.27%
1.4	$\Omega_{\rm K}$	-3.48×10^{32}	4.22×10^{34}	0.82%
2.2	$\Omega_{\rm K}$	-7.18×10^{33}	5.29×10^{34}	1.36%

Table 6.2 summarizes the angular momentum loss via neutrino emission, the angular momentum gained through accretion, and their ratio for NSs with varying masses

and spin rates. The fraction of angular momentum carried away by neutrinos depends on both the emission site and the location of the magnetosphere. In this table, the magnetospheric radius is fixed at 10^7 cm; however, this ratio tends to decline slightly as the magnetosphere expands. Based on these estimates, it appears that although neutrinos may carry off most of the energy released during accretion, they typically account for only a small portion of the angular momentum compared to that delivered by the accreting matter. This is primarily because neutrino emission is limited to the base of the accretion column. The residual angular momentum is either absorbed by the NS resulting in a spin-up or offset through mechanisms such as GW radiation.

6.3 Gravitational Waves Implications

NS accretion may lead to the emission of GWs from individual NSs and influence the merger of NS-involved binaries.

6.3.1 GWs from NS Mountains

The non-axisymmetry of a neutron star, often referred to as its ”mountains,” primarily arises from asymmetrical deformations in its solid crust. Uneven accretion onto the NS can induce asymmetries in both its composition and thermal distribution, thereby causing crustal deformations. These asymmetries may be driven by the gravitational energy released during accretion or by nuclear reactions occurring within the NS. When a NS accretes material from AGN disks, a variety of nuclear processes—such as electron captures, neutron emissions, and pycnonuclear reactions—are triggered in its surface layers and crust (Meisel et al., 2018). These reactions give rise to large-scale temperature asymmetries misaligned with the spin axis, increasing the NS's mass quadrupole. In addition, Ushomirsky et al. (2000) demonstrated that the mass quadrupole tends to increase with higher accretion rates.

The referred mass quadrupole is essentially the specific perturbation's multipole moment $Q_{\rm lm}$, defined by(Ushomirsky et al., 2000)

$$Q_{\rm lm} = \int \delta\rho_{\rm lm}(r) r^{l+1} dr, \tag{6.16}$$

where $\delta\rho_{\rm lm}$ is the spherical harmonic decomposition coefficient of the density perturbation from spherical symmetry $\delta\rho$, i.e.,

$$\delta\rho \equiv \mathrm{Re}\{\delta\rho_{\rm lm}(r) Y_{\rm lm}(\theta, \phi)\}. \tag{6.17}$$

Although uncertainties persist regarding the asymmetry in heating caused by nuclear reactions, sustained accretion onto the NS enables a gradual buildup of "mountains," eventually approaching the maximum allowable quadrupole moment (Ushomirsky et al., 2000). This upper limit arises because excessive stress can destroy the crust (Horowitz et al., 2009). According to Haskell et al. (2015), the NS crust can support a quadrupole moment as large as $Q_{22} \sim 10^{40}$ g cm^2. This maximum value in turn constrains the amplitude of GW emission. The connection between the mass quadrupole and the resulting GW strain is given by (Ushomirsky et al., 2000)

$$h_{\mathrm{a1}} = \frac{16}{5}\left(\frac{\pi}{3}\right)^{\frac{1}{2}} \frac{G Q_{22} \Omega^2}{d c^2}, \tag{6.18}$$

where d denotes the distance to the source. Although numerous studies have proposed that GWs could counterbalance the angular momentum delivered by accretion (Papaloizou et al., 1978; Wagoner, 1984; Bildsten, 1998), the accretion rates experienced by NSs within AGN disks can be extremely high, often exceeding $\gtrsim 10^5 \dot{m}_{\mathrm{Edd}}$. Under such conditions, even if the crustal mass quadrupole of the NS reaches its theoretical maximum, the resulting GWs may still be insufficient to counteract the angular momentum introduced by accretion.

On the other hand, if one takes into account the mass quadrupole sustained by magnetic fields, a substantially larger quadrupole moment may be produced. This enhanced quadrupole could, in principle, enable the GW emission to offset the accretion-driven angular momentum. In such a case, the associated GW strain is

$$h_{\mathrm{a2}} = \left(\frac{G\dot{m}}{\Omega c^3}\right)^{\frac{1}{2}} \frac{\left(G m_{\mathrm{ns}} r_{\mathrm{m}}\right)^{\frac{1}{4}}}{d}. \tag{6.19}$$

Fig. 6.5 shows the sensitivity curves of GW detectors alongside potential upper bounds on GW emission resulting from NS accretion. A coherent integration over an observation duration t_{obs} can detect a strain level approximately given by

$$h \approx 11.4\sqrt{\frac{S_{\mathrm{n}}(f)}{t_{\mathrm{obs}}}}, \tag{6.20}$$

where $S_{\mathrm{n}}(f)$ denotes the detector's noise power spectral density. The factor 11.4 corresponds to a 10% false dismissal probability and a 1% false alarm probability per trial, as described in Abbott et al. (2007). The sensitivity profiles (i.e., $S_{\mathrm{n}}(f)$) for Advanced LIGO (aLIGO), the Einstein Telescope (ET), and the Cosmic Explorer (CE) are adopted from Moore et al. (2015). For GWs arising from NS accretion within AGN disks, a source distance of $d = 5$ Mpc is adopted—greater than that of the closest observed AGN (Filippenko et al., 2003). Two possible GW upper limits are shown: the purple shaded area in the figure corresponds to the strain associated with the maximal mass quadrupole the NS's crust can support, whereas the red region indicates the strain expected if the GW is strong enough to counterbalance the angular momentum from accretion at an accretion rate of approximately $2 \times 10^5 \dot{m}_{\rm Edd}$. Both cases produce strain levels exceeding the sensitivity thresholds of the ET and CE detectors. Consequently, gravitational waves generated by NS accretion in AGN disks may become detectable by third-generation GW detectors given a two-year observation window.

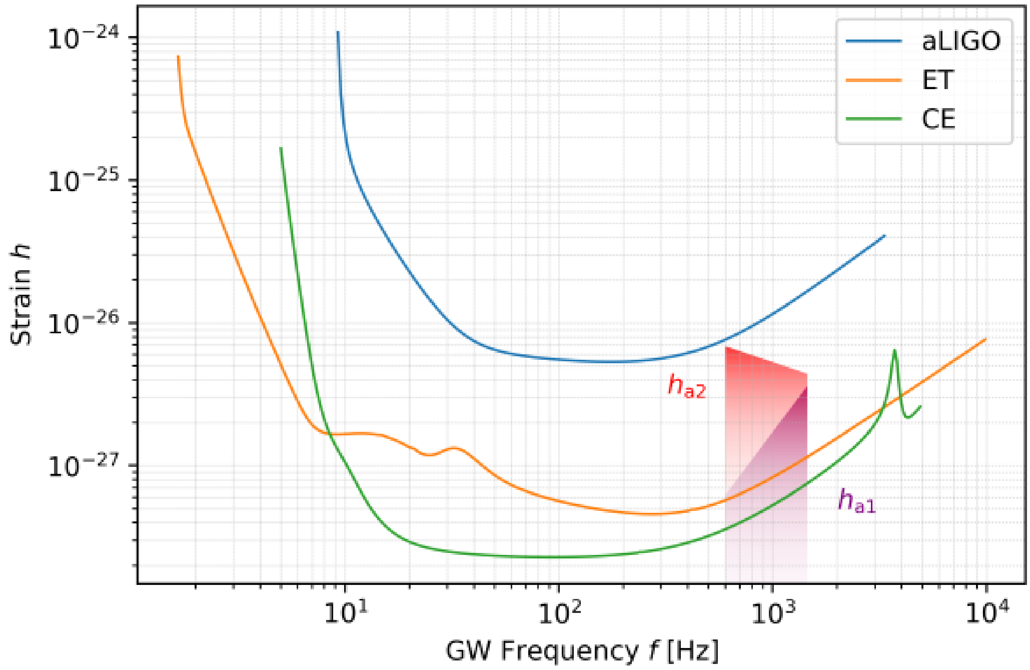

Figure 6.5 The expected range of GW strain generated by a neutron star accreting in a nearby AGN disk. The purple shaded area denotes the strain associated with the maximum quadrupole moment the crust can support, whereas the red area indicates the strain range where GW emission offsets the angular momentum gained through accretion. The NS spin frequency is assumed to lie between 300 and 730 Hz, corresponding to GW frequencies in the 600−1460 Hz interval. For reference, sensitivity curves of different GW detectors for an observation duration of $t_{\rm obs} = 2$ yr are also plotted.

The GWs emitted by NSs embedded in AGN disks may exhibit distinct features due to the special environmental, particularly duo to influences of the central SMBH. These include: (1) periodic modulation of the GW signal caused by variations in the path length along the line of sight as the NS orbits the SMBH; (2) phase variations arising from relativistic beaming, Doppler shifts, and gravitational redshift; (3) Shapiro delay, resulting from variations in the effective "light" travel time through the SMBH's gravitational potential (Meiron et al., 2017); (4) gravitational lensing effects that may give rise to GW echoes, which resemble the primary waveform but arrive after a time lag (Gondán et al., 2022). Moreover, the intermittent accretion processes experienced by NSs in AGN disks can result in intermittent GW emission. Taking these signatures into account, the GW signals originating from such NSs may be distinguishable from those produced in X-ray binaries (Bildsten, 1998; Watts et al., 2008). Detection of these GWs would provide compelling evidence for the presence of NSs in AGN disks and contribute to our understanding of compact object astrophysics in these environments.

The extraction of angular momentum from NSs via GWs plays a critical role. For example, Pan et al. (2021a) explored whether accretion could spin a NS up to the shedding limit and found that the results were near the threshold. Depending on the choice of parameters, their outcomes varied, often lying close to the dividing line between reaching and not reaching the shedding limit. However, their analysis did not include the angular momentum loss due to GWs. Consequently, even if GWs remove part of the angular momentum during accretion, it becomes less probable for NSs within AGN disks to attain the shedding limit. This, in turn, sustains accretion and increases the likelihood of collapse.

6.3.2 Implications for Binary NS Merger

In AGN disks, NS accretion is accompanied by feedback processes that influence the surrounding AGN gas. This feedback modifies the accretion rate and, in turn, impacts the binary merger rate. If the NS maintains a hyper-Eddington accretion rate, it can rapidly surpass its critical mass and undergo collapse, thereby reducing the likelihood of binary NS mergers within AGN disks. However, strong outflows from the circum-NS disk carve out a cavity before accretion resumes at hyper-Eddington levels. Thus, the corresponding feedback-regulated duty cycle must be taken into account.

Compared to the BH case presented by Chen et al. (2023a), the relatively larger duty cycle associated with NS accretion primarily stems from the impact of magnetic fields and neutrino emission. While Chen et al. (2023a) also considers the accretion-driven feedback of NSs onto AGN disks, their model neglects the role of neutrinos and assumes that the full gravitational energy released by accretion contributes to gas feedback. This simplification results in an overestimation of the feedback strength and, consequently, a relatively smaller duty cycle in their analysis. In reality, a larger accretion duty cycle increases the likelihood that NSs within AGN disks collapse. To strengthen this conclusion, we also compare the AIC timescale and the migration timescale. As for migration, both Type I migration and GW-induced migration are considered. Although other mechanisms could influence the migration process, they're not expected to change the order of magnitude of the timescale. Within the fiducial setting, our results show

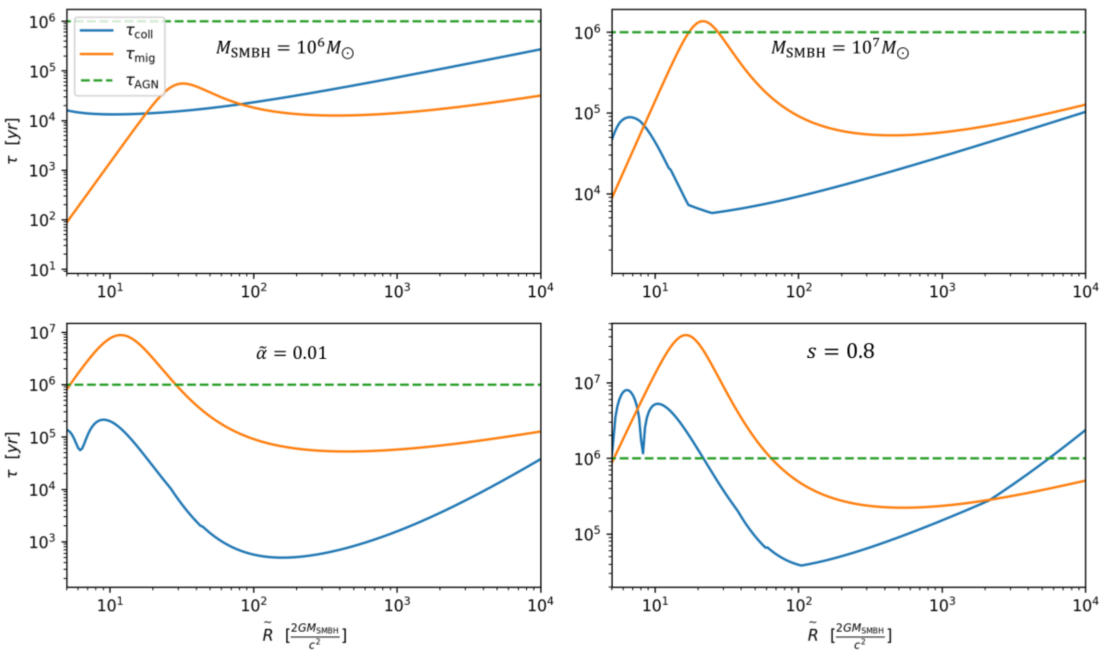

Figure 6.6 Timescales for NS AIC (blue) and migration (yellow) in AGN disks under varying parameter conditions. Apart from the parameters indicated in each panel, all other parameters are consistent with those in the fiducial setup.

that the timescale for migration exceeds that of collapse, and both remain below the typical AGN lifetime of $\sim$ 10 Myr. Since binaries in AGN disks generally form in regions of differential migration or near migration traps, the migration timescale offers a lower bound for the timescale of binary coalescence. These findings imply that NS-NS or NS-BH mergers are unlikely to occur within AGN disks.

Beyond the fiducial model, Fig. 6.6 comprises the AIC timescale and the migration timescale across different parameter choices. The overall trend remains consistent with the fiducial case—namely, the collapse timescale is generally shorter than the migration timescale. This suggests that NSs embedded in AGN disks are likely to undergo collapse before encountering mergers or collisions. An exception arises in scenarios involving AGNs hosting lower-mass SMBHs, where the collapse timescale may surpass the migration timescale, as shown in the upper left panel of Fig. 6.6. As discussed in the last chapter (see also Luo et al. (2023)), hierarchical triple systems composed of two WDs and an SMBH within AGN disks are investigated, and it is found that systems with lower-mass SMBHs more readily lead to binary encounters or collisions. Nevertheless, compared to WDs in AGN environments, NS mergers remain infrequent, even with lower-mass SMBHs, because GW emission (or gas dissipation) is required to shrink the binary separation below the capture radius. These theoretical results align with observational evidence: as of May 15, 2024, nearly 200 GW sources have been detected by ground-based observatories, yet only two binary NS mergers (GW170817 and GW190425) have been confirmed, alongside roughly five candidate NS-BH events (GraceDB, 2024).

It is important to highlight that although most of the energy released during matter accretion onto a NS is carried away by neutrinos, a small portion (approximately at the Eddington luminosity level) escapes as electromagnetic radiation and is deposited into the AGN disk due to its high opacity. Nonetheless, this radiative contribution is minimal when compared to the mass outflows from the circum-NS disk into the AGN environment. Moreover, for NSs embedded in AGN disks, the dipolar magnetic field truncates the circum-NS disk at relatively large distances, thereby limiting the strength of outflows. As a result, NS-induced feedback in AGN disks is weaker than that from BHs.

6.4 Electromagnetic Signatures

The accretion of NSs within AGN disks can also give rise to electromagnetic emission. This radiation primarily originates from shocks formed by the interaction between outflows from the circum-NS disk and the surrounding AGN disk material, with the shock eventually breaking out on the AGN disk surface. The characteristic luminosity of this process can be estimated by:

$$L_{\rm bre} \approx \begin{cases} \left(\pi \tilde{H}^2 v_{\rm shellb}(t_{\rm bre})\right) \times \left(\frac{1}{2}\tilde{\rho}_0 v_{\rm shellb}(t_{\rm bre})^2\right) \times \frac{9}{2} = \frac{9\pi \tilde{H}^2 \tilde{\rho}_0 v_{\rm shellb}(t_{\rm bre})^3}{4}, & t_{\rm acc} \gtrsim t_{\rm bre} \\ \left(\pi \tilde{H}^2 v_{\rm shellE}(t_{\rm breE})\right) \times \left(\frac{1}{2}\tilde{\rho}_0 v_{\rm shellE}(t_{\rm breE})^2\right) \times \frac{9}{2} = \frac{9\pi \tilde{H}^2 \tilde{\rho}_0 v_{\rm shellE}(t_{\rm breE})^3}{4}, & t_{\rm acc} \lesssim t_{\rm bre}, \end{cases} \tag{6.21}$$

Here, the first term in each expression represents the volume traversed by the shock per unit time, while the second term gives the kinetic energy density at the time of shock breakout. The numerical factor $\frac{9}{2}$ accounts for corrections (Kimura et al., 2021; Chen et al., 2023a). The emitted radiation is approximately thermal, and its characteristic temperature can be estimated as:

$$T_{\rm rad} \approx \begin{cases} \left[\frac{9\tilde{\rho}_0 v_{\rm shellb}(t_{\rm bre})^2}{4a}\right]^{1/4}, & t_{\rm acc} \gtrsim t_{\rm bre} \\ \left[\frac{9\tilde{\rho}_0 v_{\rm shellE}(t_{\rm breE})^2}{4a}\right]^{1/4}, & t_{\rm acc} \lesssim t_{\rm bre}, \end{cases} \tag{6.22}$$

where a is the radiation constant.

Fig. 6.7 shows the typical luminosity and temperature of flares powered by shock breakout on the disk surface, evaluated across a range of model parameters. The luminosity reaches up to $\sim 10^{42}$ erg s^{-1}, with temperatures in the range of $\sim 10^4 - 10^6$ K, corresponding to ultraviolet emission. To evaluate the observational prospects, Fig. 6.8 dis-

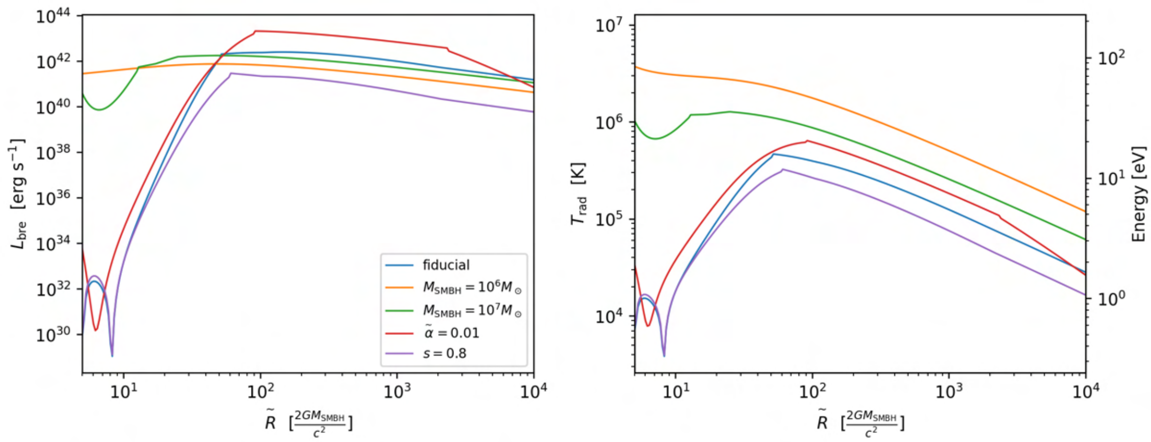

Figure 6.7 Left panel: Estimated luminosity of the shocked shell produced by outflow breakout under various parameter configurations. Right panel: Corresponding characteristic temperature of the shocked shell during breakout for the same parameter variations. Unless otherwise specified in the legend, all other parameters adopt the values from the fiducial setting.

plays the SEDs for a fixed luminosity of 10^{42} erg s^{-1} across different breakout temperatures, alongside the mean SEDs of AGNs derived from observations (Shang et al., 2011). The AGN SEDs are normalized to a bolometric luminosity of $L_{\rm AGN,bol} = 10^{44}$ erg s^{-1}. In general, the radiation from NS-induced flares within AGN disks is fainter than the underlying AGN emission, thus posing significant challenges for detection. Nonetheless, in AGNs with moderate luminosities, the signals induced from such NS accretion may still be observable.

It is also essential to account for the cumulative radiation emitted by all NSs embedded within an AGN disc. Over the course of a typical AGN activity lifetime ($\sim$ 10 Myr), about 10^4 NSs are expected to be present (Perna et al., 2021b). Thus, the mean number of NSs simultaneously residing in the AGN disc can be estimated by Eq. (6.12). By combining this estimate with the results in Fig. 6.6, the average number of concurrently accreting NSs is found to be on the order of $n_{\rm ns/AGN} \sim 100$. However, it is unlikely that these NSs generate flares in a synchronized manner. Given the estimated duty cycle of accretion—ranging from $\sim$ 1/1000 to $\sim$ 1/10 (see Fig. 4.7)—the total luminosity of the associated electromagnetic variability would at most reach levels comparable to the background emission of the AGN itself. Consequently, detecting the combined radiation signal remains challenging due to the absence of strong or distinctive observational signatures.

The preceding analysis has primarily addressed thermal radiation. However, NS accretion within AGN discs is also expected to generate non-thermal emission and high-energy neutrinos. Given the typical optical depth of AGN discs being $\gtrsim 1$ (refer to Fig. 4.1), both internal eruptive activity and shock breakouts on the disc surface can be

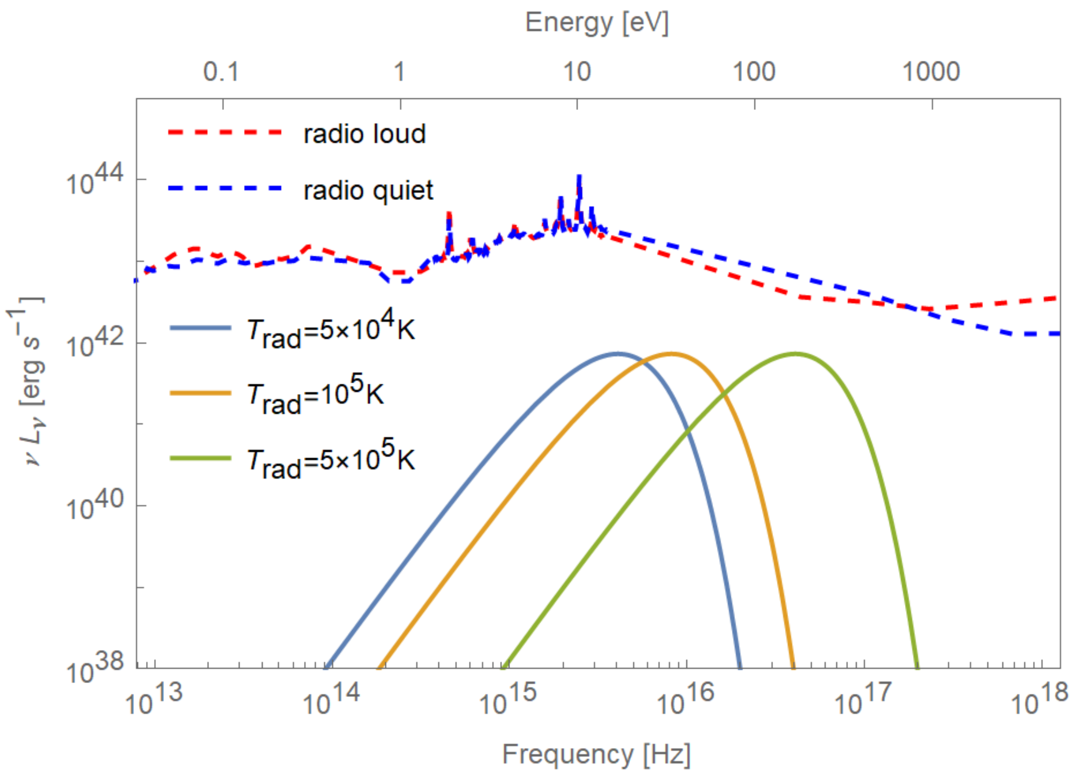

Figure 6.8 SEDs of thermal radiation corresponding to various breakout temperatures, assuming a fixed luminosity of 10^{42} erg s^{-1} (solid lines). These are shown alongside the average AGN SEDs from observations Shang et al. (2011) (dashed lines), which are normalized to a bolometric luminosity of $L_{\rm AGN,bol} = 10^{44}$ erg s^{-1}.

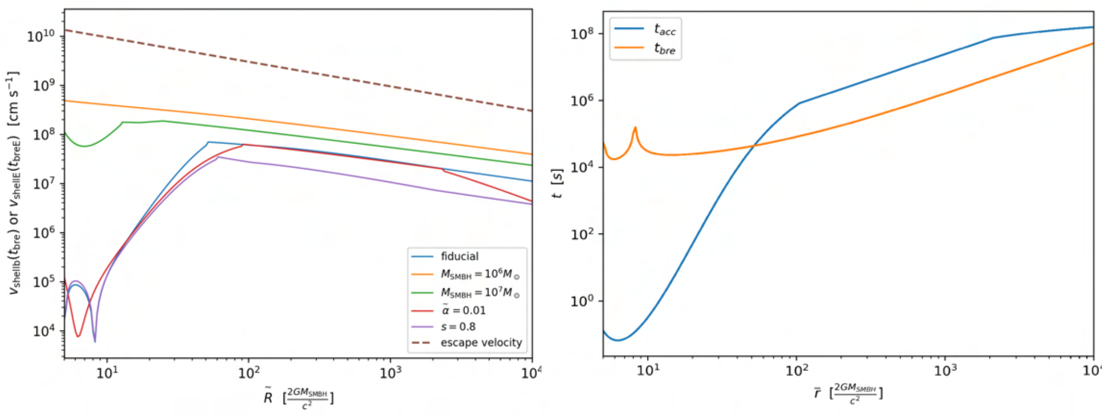

Figure 6.9 Left: Comparison between the breakout velocities of shocked shells driven by outflows and the corresponding escape velocities. Right: Comparison between the accretion timescale and the breakout timescale under the fiducial assumptions.

reasonably modeled as thermal processes. Even in cases where the outer disc regions start as optically thin, the ionization of ambient material by radiation from NS accretion will eventually render the medium optically thick. Despite this, several scenarios can give rise to non-thermal radiation:

(1) Shocks traveling outward to the broad-line region may cool via synchrotron or inverse Compton mechanisms (Wang et al., 2021a).

(2) Momentum-driven outflows that escape the disk may be pulled back by the gravitational influence of the central SMBH (see, e.g., Fig. 6.9); upon re-impacting the disk surface, such fallback material could produce non-thermal emission.

(3) The interaction between outflows and the disk may form low-density channels or cavities, allowing previously trapped non-thermal photons from accretion processes to escape.

(4) Finally, magnetic reconnection events triggered by the AIC of a NS may give rise to transient phenomena resembling FRBs (Falcke et al., 2014; Perna et al., 2021b).

Moreover, the shocks associated with NS accretion and its aftermath can accelerate particles to relativistic speeds, thereby producing high-energy neutrinos through hadronic interactions (Ma et al., 2024). Altogether, the thermal luminosity estimated above represents an approximate upper limit on the total electromagnetic output. However, contributions from non-thermal channels—particularly in the high-energy and radio bands—may be observationally significant due to reduced contamination from the AGN background in those wavelengths.

6.5 Discussion and Conclusions

In this chapter, the multi-messenger implications of NS accretion in AGN disks have been studied, leading to the following concluding remarks.

(i) The presence of a hard surface on NSs enables highly efficient accretion, and their potential strong magnetic fields can direct inflowing material into narrow accretion columns. Consequently, NSs undergoing hyper-Eddington accretion within AGN disks are capable of emitting neutrinos via electron-positron annihilation. A more comprehensive categorization of the possible accretion states of NSs in AGN disks is presented in Fig. 6.1. In this context, neutrino emission serves as a cooling mechanism that limits the electromagnetic luminosity. These neutrinos are characterized by a non-thermal energy spectrum (see Fig. 6.3) and are produced in regions with characteristic temperatures of approximately 1MeV, as shown in Table 6.1. The resulting neutrino flux from NS accretion processes contributes notably to the sub-MeV and MeV diffuse background, reaching levels comparable to the supernova contribution near 0.3MeV (Fig. 6.4).

(ii) The process of accretion onto a NS can induce a mass quadrupole moment, thereby leading to the emission of GWs as it rotates. The estimated upper bound on the resulting GW strain may fall within the sensitivity range of third-generation GW observatories (see Fig. 6.5). These gravitational signals may also exhibit distinct features such as periodic modulation and echoes. Furthermore, as shown in Table 6.2, GWs can carry away angular momentum from the accreting material, helping to relax the shedding limit and allowing continued mass accumulation onto the NS.

(iii) The presence of a magnetosphere can truncate the circum-NS disk at a relatively large radius r_{m}, consequently suppressing outflows from the disk and weakening the associated feedback on the AGN disk. In most cases, the duty cycle remains high, and the typical timescale for AIC is shorter than the migration timescale (and thus the merger timescale) within AGN disks (see Figs. 4.7 and 6.6). Therefore, AIC of NSs are expected to take place before binary mergers occur in AGN disks.

Magnetic fields are fundamentally important in processes such as neutrino generation, feedback onto the AGN disk, and the overall evolution of NSs. Massive stars formed within AGN disks might exhibit a higher incidence of magnetars with surface fields $\gtrsim 10^{13}$ G, though their post-formation evolution remains intricate. During accretion, magnetic fields may decay via mechanisms like Ohmic dissipation, eventually stabilizing at values around $\sim 10^{9}$–10^{10} G (Pan et al., 2021a). Conversely, magnetic fields are typically included in disk models (Eardley et al., 1975), and observational data indicate average field strengths on the order of $\sim 10^{4}$ G within AGN disks (Silant'ev et al., 2009; Daly, 2019). As a NS accretes material from the AGN environment, conservation of magnetic flux may lead to an amplification of the NS magnetic field. Investigating these interactions through future magnetohydrodynamic simulations would be valuable. Additionally, this work adopts a dipolar magnetic field structure for simplicity. However, both theory and observation suggest the presence of higher-order multipole components (e.g. Roberts, 1979; Gil et al., 2001; Pétri, 2015), which could suppress the formation of accretion columns. Given the substantial uncertainties associated with multipolar field geometries, their influence is not considered in the current analysis.

Further investigation is needed into the nucleosynthesis processes occurring in accreted material and their influence on the NS's mass quadrupole moment. While nuclear reactions within the surface layers and crust of NSs have been extensively studied, the conditions present during accretion in AGN disks—characterized by extremely high accretion rates and potentially strong magnetic fields—differ significantly. The specific behavior of nuclear reactions under such extreme conditions remains poorly understood.

Current understanding suggests that at sufficiently high accretion rates, nuclear burning on the NS surface may proceed in a continuous rather than episodic manner (Meisel et al., 2018). Moreover, intense magnetic fields can modify the structure of the NS's outer layers (Chamel et al., 2008; Meisel et al., 2018), thereby affecting nucleosynthesis. These nuclear processes, in turn, play a critical role in determining the composition and thermal asymmetry of the NS crust, ultimately impacting GW emission.

At present, our study focuses on qualitative analyses of representative models or specific evolutionary stages, rather than tracking the full dynamical evolution. For example, the physical processes at the interface between accretion models on different scales, as well as the time-dependent development of accretion columns and circum-NS disks, remain uncertain. Additionally, the spin and magnetic field of NSs may affect the threshold mass for collapse, though these factors are not expected to substantially alter our current qualitative estimates. Addressing these uncertainties will require dedicated high-resolution numerical simulations to resolve their complex structures and evolutionary pathways.

In conclusion, NS accretion within AGN disks plays a pivotal role. Advancing this research through more refined simulations and coordinated multi-messenger observations may confirm the existence of compact objects embedded in AGN environments, shed light on the underlying physics of such extreme systems, and help pinpoint potential hosts of GWs.

Chapter 7 Binary Black Hole Merger Produces Short GRB in AGN Disk: The Case of S241125n

7.1 Background

Short GRBs are typically thought to arise from the mergers of compact binaries involving at least one neutron star (Berger, 2014). In contrast, binary black hole mergers are usually not associated with GRB production. Nonetheless, under specific conditions, such associations become feasible—for instance, if the BHs carry electric charge (Zhang, 2019), reside in dense gaseous environments such as AGN disks (Tagawa et al., 2023b), or when the BH binary forms from two clumps in a dumbbell configuration (Loeb, 2016).

As introduced in Chapter 1, AGN disks are natural astrophysical sites for binary BH mergers and can lead to hyper-Eddington accretion onto the merger remnants, which are characterized by fast spin and strong surrounding magnetic fields. Under these conditions, both GWs and jets are expected to be launched. The jets interacts with the surrounding disk material, resulting in the formation of shocks. In the early stages, photon diffusion lags behind the shock front, leading to the trapping of photons within the flow (Zhu et al., 2021b; Yuan et al., 2022). As the shock advances to a height where the photon diffusion timescale becomes shorter than the shock propagation timescale, photons can escape, giving rise to GRB emission (Nakar et al., 2010, 2012). These GRBs are theoretically expected to differ from conventional ones in both their duration and the SED of the prompt (Tagawa et al., 2023b) and afterglow phases (Lazzati et al., 2022; Wang et al., 2022). Additionally, in some cases, the jet may fail to break out, depending on the disk's density profile (Zhu et al., 2021b; Zhang et al., 2024a).

GW events associated with GRBs serve as important targets for multi-messenger astronomy. They offer a means to investigate the underlying processes behind GRB emission, identify the host environments of GW sources (Veronesi et al., 2022, 2023, 2025), and improve constraints on cosmological parameters (Mukherjee et al., 2020; Gayathri et al., 2021; Alves et al., 2024; Bom et al., 2024; Mancarella et al., 2024). In addition, when such events occur within AGN disks, they present an opportunity to probe the physical conditions of the disk itself. Despite this potential, only a small number of GRBs have been proposed as possible counterparts to binary mergers in AGN disks (e.g., GRB 191019 (Levan et al., 2023; Lazzati et al., 2023) and GW 150914-GBM (Connaughton et al., 2016)). Even fewer events exhibit tentative associations with GWs (e.g., Bagoly et al., 2016), and the interpretation remains a subject of debate (Greiner et al., 2016; Connaughton et al., 2018; Tagawa et al., 2023b).

In this chapter, we argue that S241125n could represent a new GRB – GW association. We present a summary of its GW and multi-wavelength electromagnetic observations, examine the consistency between theoretical expectations and observed properties, and suggest that its most probable origin is a binary BH merger occurring within an AGN disk.

7.2 Observation

7.2.1 Gravitational Wave

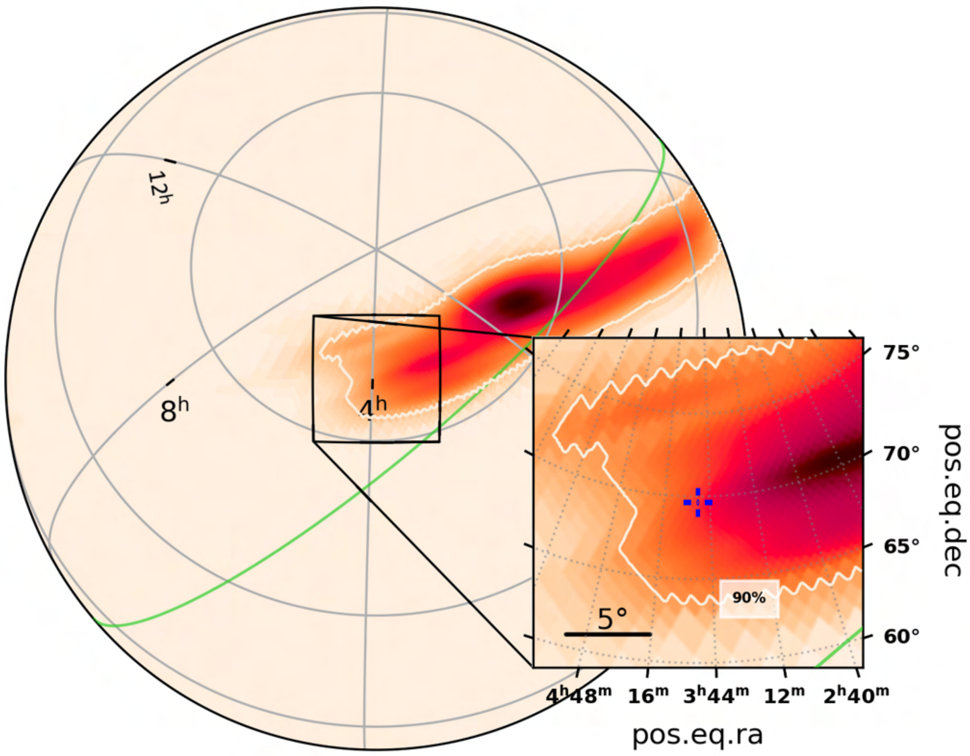

Figure 7.1 GW skymap for LVK S241125n, overlaid with the GRB position marked by a blue cross in the inset plot. The color bar represents the relative probability distribution of the GW source location, and the white solid contour marks the 90% confidence level, and the green curve indicates the Galactic plane.

The compact binary merger candidate LIGO/Virgo/KAGRA (LVK) S241125n was detected through real-time data processing on 2024 November 25 at 01:01:16.780 UTC (T_0), with contributions from the LIGO Hanford (H1), LIGO Livingston (L1), and Virgo (V1) observatories. The inferred luminosity distance was $d_{\rm L} = 4173 \pm 1590$ Mpc, corresponding to a redshift of $z = 0.73$ (LIGO Scientific Collaboration et al., 2024).

The GW signal was categorized with high confidence as a binary black hole (BBH) merger (> 99%), with low probabilities for terrestrial origin (< 1%), binary neutron star (BNS; < 1%), or neutron star−black hole (NSBH; < 1%) mergers. The presence of noise transients (glitches) in the LIGO Hanford data could influence the inferred parameters of the signal or reduce its statistical significance (LIGO Scientific Collaboration et al., 2024).

Fig. 7.1 presents the GW skymap for LVK S241125n, visualized using the Bilby analysis pipeline (Ashton et al., 2019) with the file `Bilby.offline0.multiorder.fits`, available at https://gracedb.ligo.org/superevents/S241125n/view/. The 90% credible region spans 2196 deg^2, corresponding to f_{sky} = 5.32% of the celestial sphere. The candidate electromagnetic co

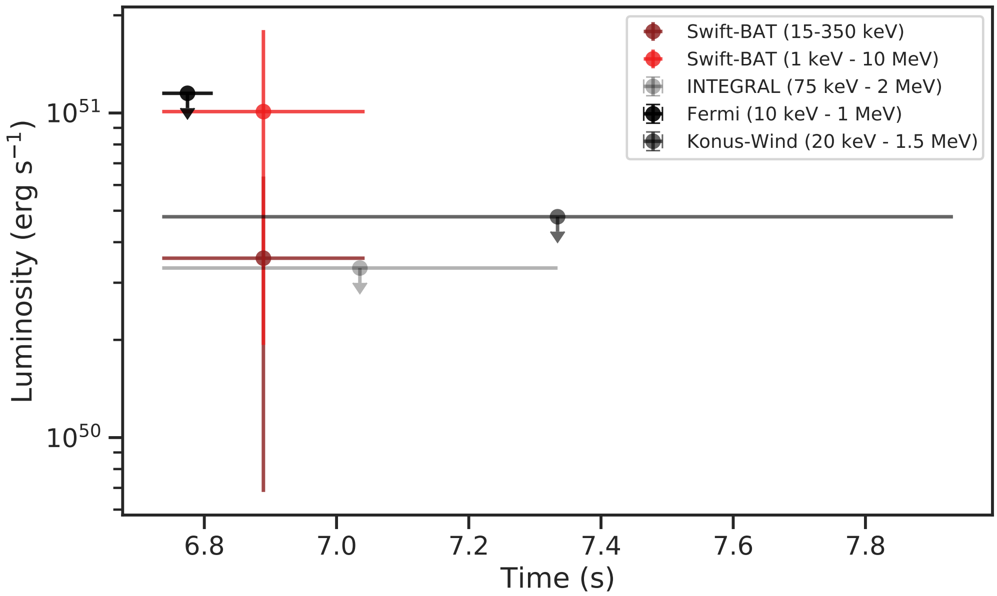

Figure 7.2 Prompt emission luminosity as measured by the Swift, INTEGRAL, Fermi, and Konus-Wind satellites. The GW trigger time is adopted as the reference start time (T_0), and all times are presented in the rest frame.

7.2.2 Gamma-ray Counterparts

After the detection of LVK S241125n, the Swift Burst Alert Telescope (Swift-BAT) responded to the alert issued by the Gamma-ray Urgent Archiver for Novel Opportunities (GUANO, Tohuvavohu et al., 2020) and found a possible gamma-ray counterpart with trigger ID 754189311. This candidate exhibited a square root of the test statistic value of 7.41, beginning at T_0 + 11.264 s and analyzed within a 0.512 s time bin (GCN Circulars 38308). The position reported for this candidate by BAT was RA = 58.079°, Dec = +69.689°, with an estimated positional uncertainty of 5 arcminutes (50% con-

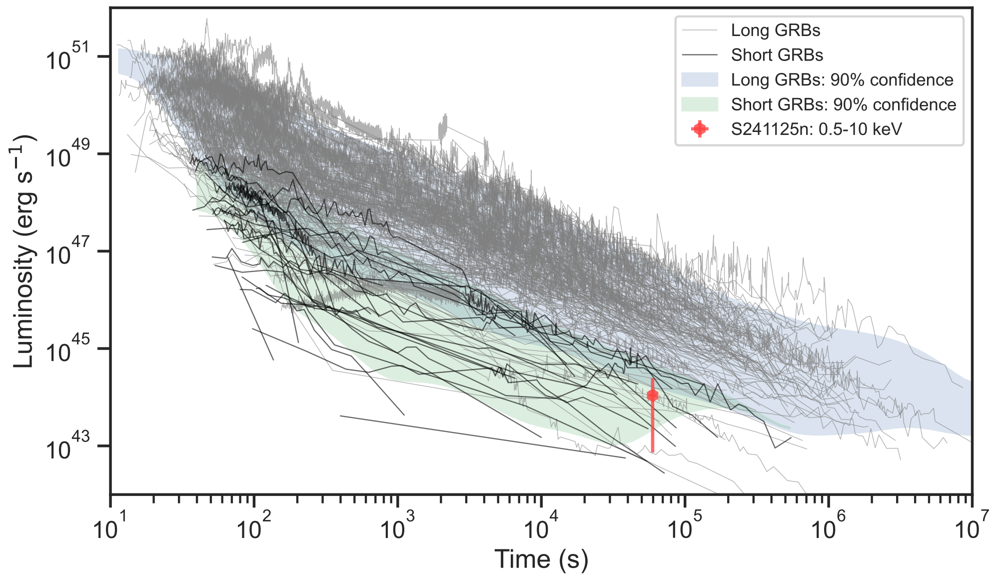

Figure 7.3 X-ray afterglow data point of S241125n (red), obtained from EP observations in the 0.5–10 keV energy range. For comparison, background samples from Swift-XRT include 217 long GRBs (gray) and 31 short GRBs (black), covering 0.3 – 10 keV. Shaded regions indicate the 90% **confidence intervals derived directly from the data. S241125n's luminosity is consistent with that of short GRBs. Time is given in the rest frame.**

tainment) (DeLaunay et al., 2024a).

Spectral fitting of the gamma-ray counterpart indicated a Comptonized (cutoff power-law) spectrum characterized by a peak energy $E_{\text{peak}} = 49$ keV, photon index of -2.2, and a flux in the 15–350 keV band of $f = 1.1^{+0.2}_{-0.3} \times 10^{-7}$ erg cm^{-2}s^{-1} (DeLaunay et al., 2024b). However, the photon index is poorly constrained, ranging between -1.4 and -3.0, with corresponding variations in the allowed values of E_{peak} (DeLaunay et al., 2024b).

Assuming during the LVK O4 observing run that the all-sky GW event rate is $R_{\text{GW}} = 1$ event/day $= \frac{1}{86400}$Hz, and the GRB detection rate is similarly $R_{\text{GRB}} =$ 1 event/day $= \frac{1}{86400}$ Hz, the chance coincidence rate within a time window of $t_{\text{delay}} =$ 11.264s and restricted to the 90% credible region of LVK S241125n can be estimated as:

$$\begin{aligned} R_{\text{coinc}} &= R_{\text{time}}\, f_{\text{sky}} \\ &= t_{\text{delay}}\, R_{\text{GW}}\, R_{\text{GRB}}\, f_{\text{sky}} \\ &\approx 8.03 \times 10^{-11}\ \text{Hz}. \end{aligned} \tag{7.1}$$

This implies that if the GW and GRB signals were completely unrelated, such a coincident detection would be expected roughly once every 400 years. Including the correlation with the X-ray counterpart candidate observed by the Einstein Probe (EP; discussed in the next subsection) would further reduce the coincidence probability, making R_{coinc} even smaller.

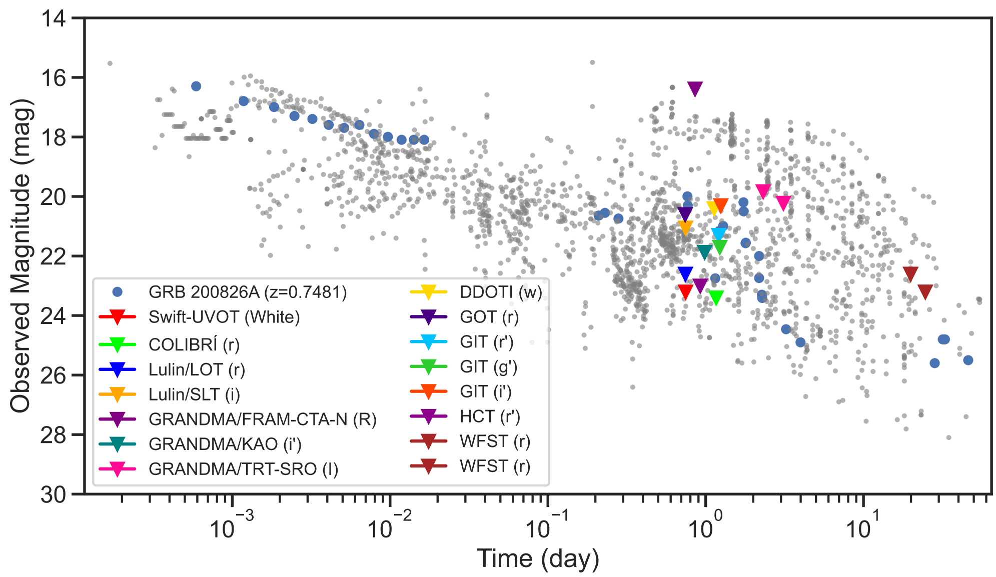

Figure 7.4 Optical constraints of S241125n provided by Swift, COLIBRÍ, Lulin, GRANDMA, DDOTI, GOT, GIT, HCT and WFST telescopes. For comparison, gray data points are drawn from multi-band optical observations of 29 short GRBs compiled by Dainotti et al. (2024). Among these, GRB 200826A (marked in blue), which shares a similar redshift with S241125n, is specifically highlighted. Both time and magnitude are presented in the observer's frame. The reference magnitudes of gray points have been corrected for Galactic extinction, whereas the S241125n data mainly represent raw measurements directly sourced from the GRB Coordinates Network (GCN). Based on the Milky Way extinction toward S241125n, with $E(B-V) = 0.4678$ mag (Schlafly et al., 2011), the extinction-corrected magnitudes for S241125n would be roughly 0.5 to 2 magnitudes brighter than those shown in the figure; for example, $A_{i'} = 0.927$ mag, $A_{r'} = 1.224$ mag, and $A_{g'} = 1.739$ mag.

We then proceeded to compute the isotropic-equivalent luminosity ($L_{\gamma,\rm iso}$) of the gamma-ray counterpart by combining the observed flux with the luminosity distance inferred from the GW signal, i.e., assuming the GW and GRB are associated. Using the standard formula $L = 4\pi k d_{\rm L}^2 f$, where k represents the k-correction accounting for cosmological redshift (Bloom et al., 2001), the rest-frame luminosity in the 15−350 keV band was estimated to be $3.57^{+2.80}_{-2.89} \times 10^{50}$ erg s^{-1}, applying a k-correction factor of 1.56. Extrapolating this using the Comptonized spectral model to the wider energy range of 1 keV−10 MeV yields a luminosity of $1.01^{+0.79}_{-0.82} \times 10^{51}$ erg s^{-1} with a k-correction factor of 4.40. The uncertainties incorporate errors from both the flux measurement and the luminosity distance estimation. Given the burst duration $\Delta t = 0.512$ s, the isotropic-equivalent energy in the 15−350 keV band is calculated as $E_{\gamma,\rm iso} = L_{\gamma,\rm iso} \times \Delta t/(1+z)$, resulting in $1.09^{+0.86}_{-0.88} \times 10^{50}$ erg. Similarly, the energy within the 1 keV−10 MeV range amounts to $3.09^{+2.42}_{-2.50} \times 10^{50}$ erg.

No gamma-ray counterpart was observed by INTEGRAL (Savchenko et al., 2024), Fermi (Scotton et al., 2024), or Konus-Wind (Ridnaia et al., 2024), with only upper limits established. INTEGRAL provided a 3σ upper limit of 1.6×10^{-7} erg cm^{-2} in the 75 – 2000 keV band, assuming a burst shorter than 1 s and using a typical short GRB spectral model (Savchenko et al., 2024), corresponding to a luminosity limit of 3.33×10^{50} erg s^{-1}. Fermi, adopting a hard-spectrum template characteristic of short GRBs, set a 3σ upper limit on the flux in the 10 – 1000 keV band at 5.5×10^{-7} erg s^{-1}cm^{-2} over 0.128 s (Scotton et al., 2024), translating to a luminosity upper bound of 1.15×10^{51} erg s^{-1}. Konus-Wind estimated a 90% confidence upper limit on flux in the 20–1500 keV range as 2.3×10^{-7} erg s^{-1}cm^{-2} for a burst spectrum similar to GRB 170817A (Ridnaia et al., 2024), which corresponds to a luminosity upper limit of 4.79×10^{50} erg s^{-1}. Note that no k-correction was applied when calculating these luminosity upper limits.

Fig. 7.2 presents the prompt emission data collected from these instruments. The isotropic luminosity is found to lie $\sim 10^{50} - 10^{51}$ erg s^{-1}, consistent with typical short GRB luminosities. Based on BAT observations, the isotropic gamma-ray energy is $E_{\gamma,\mathrm{iso}} = 3.09^{+2.42}_{-2.50} \times 10^{50}$ erg, and the rest-frame peak energy is $E_{p,\mathrm{rest}} = 49\ \mathrm{keV} \times (1+z) = 85$ keV. This agrees with the empirical correlation between $E_{p,\mathrm{rest}}$ and $E_{\gamma,\mathrm{iso}}$ observed for short GRBs (Willingale et al., 2017), supporting the association assumption between the GW event and the GRB. However, the burst's photon index is measured to be $-2.2^{+0.6}_{-0.8}$, which is softer than the typical low-energy spectral index of around -1.5 seen in short GRB prompt emissions. This discrepancy might imply a unique radiation mechanism or different propagation effects affecting the prompt emission.

7.2.3 X-Ray Candidates

Swift XRT carried out follow-up observations from about $T_0 + 55$ ks to $T_0 + 74$ ks after the GW trigger (Page et al., 2024). Initially, 5 previously uncatalogued X-ray sources were reported (Page et al., 2024), which were later updated to a total of 15 new uncatalogued sources (see https://www.swift.ac.uk/LVC/S241125n/). However, none of these sources showed sufficient brightness to be confidently identified as counterparts to the GW event, nor have any been confirmed to be associated with a galaxy.

EP performed follow-up observations at approximately T_0+94 ks with an exposure time around 11 ks (Wang et al., 2024a). Within the 5-arcminute BAT error region, one X-ray source was detected by both EP modules at RA = 58.1097°, Dec = +69.6392°, with a positional uncertainty of 10 arcseconds (90% confidence). Spectral analysis in the 0.5 – 10 keV band favored an absorbed power-law model with a photon index of

$0.43^{+0.76}_{-0.74}$ and a flux of $1.17^{+1.18}_{-0.63} \times 10^{-13}$ erg s^{-1}cm^{-2} (Wang et al., 2024a). Applying a k-correction factor of 0.45, the corresponding luminosity is $1.09^{+1.37}_{-1.01} \times 10^{44}$erg s^{-1}.

Currently, no other publicly available data confirm an associated X-ray transient. Assuming the EP source is related to LVK S241125n, Fig. 7.3 shows that the EP data point lies within the typical luminosity range for short GRB afterglows. The photon index measured by EP, $0.43^{+0.76}_{-0.74}$, is significantly softer than the standard afterglow index of about -2. This difference could suggest a distinct radiation mechanism or a different local environment, such as a host galaxy with high hydrogen density that causes strong absorption of soft X-rays.

7.2.4 Optical Observations

Despite extensive follow-up campaigns conducted by many observatories, no confirmed optical counterpart to the GW event LVK S241125n has been found, with only upper limits reported. These campaigns include observations from Lulin Observatory, COLIBRÍ telescope, Himalayan Chandra Telescope (HCT), GROWTH-India telescope, Gaoyazi/GOT telescope, DDOTI/OAN wide-field imager, MMT telescope, Swift-UVOT, and the GRANDMA network (Chen et al., 2024b; Watson et al., 2024; Swain et al., 2024; Mohan et al., 2024; Jiang et al., 2024; Becerra et al., 2024; Rastinejad et al., 2024; Akl et al., 2024b; Klingler et al., 2024; Akl et al., 2024a), summarized in Fig. 7.4.

Most observations were performed approximately one day post-event, with no data available prior to 0.5 days. Additionally, we utilized the Wide Field Survey Telescope (WFST) (Wang et al., 2023c) in the r-band to monitor candidate sources reported by EP (Wang et al., 2024a) at later epochs (2024-12-14T22:17 and 2024-12-19T16:51 UTC). Within the EP error region, no significant variability was detected, with 5σ limiting magnitudes ranging from 22.5 to 23.5 mag (see Fig. 7.4), compared against archival Pan-STARRS1 images (Finkbeiner et al., 2016; Flewelling et al., 2020). The current upper limits are consistent with typical values for short GRBs (Dainotti et al., 2024), and no transient optical source has yet been confirmed.

Data from MMT (Rastinejad et al., 2024) are not included in Fig. 7.4. The MMT observations targeted the error circle of S241125n_X2 (the second X-ray source detected by Swift-XRT within the BAT error region (Page et al., 2024)) and revealed five optical sources with magnitudes between 18.9 and 25.4; however, association with LVK S241125n remains unconfirmed.

Compared with these data and the reference GRB 200826A, which has a similar redshift, the optical brightness of S241125n is likely fainter than 24 mag a few days after the event, assuming it follows a similar light curve evolution. Moreover, this GRB lies near the Galactic plane, at a Galactic latitude around 10 degrees (see Fig. 7.1), which poses additional observational difficulties. Detecting such a faint source typically requires large-aperture ground-based telescopes or space-based instruments. If the host galaxy has significant dust extinction, follow-up observations with infrared space telescopes such as the James Webb Space Telescope ((JWST), Gardner et al., 2006) would be essential.

7.2.5 Light-curve Comparison

The light curve of S241125n (Fig. 7.5), has been compared to that of the typical short GRB 090510 (Ackermann et al., 2010; Ruffini et al., 2016) as well as the GW-associated GRB 170817A (Abbott et al., 2017; Rueda et al., 2018). The behavior of S241125n shows greater resemblance to GRB 090510, with both its prompt gamma-ray emission and X-ray afterglow matching the typical short GRB profile. Although the optical flux of S241125n remains uncertain, Fig. 7.4 suggests that at around 10^6 s post-trigger, the optical luminosity upper limit is roughly 24 magnitudes, equivalent to approximately 10^{42} erg s^{-1}, which also aligns well with known short GRB properties.

In summary, the observations indicate that the energy output and luminosity (assuming the luminosity distance inferred from the GW signal) for S241125n are comparable to those seen in short GRBs, despite differences in the observed spectral features.

7.3 BH Binary Merger in an AGN Disk as a Possible Scenario

7.3.1 Prompt Emergence

The GRB linked to LVK S241125n exhibits an unusual property in its prompt emission phase—specifically, a photon index of -2.2 within the 15 - 350 keV range. We show that such spectral characteristics are well explained within the framework of a BBH merger occurring in an AGN disk.

To model the SED of a GRB triggered by such a merger within an AGN disk, we consider the scenario where the newly formed BH accretes surrounding gas, launching a jet through the BZ mechanism. As the jet propagates, it interacts with the disk material and eventually breaks through the disk surface, producing emission observable by current instruments. Our modeling follows the approach developed by Tagawa et al.

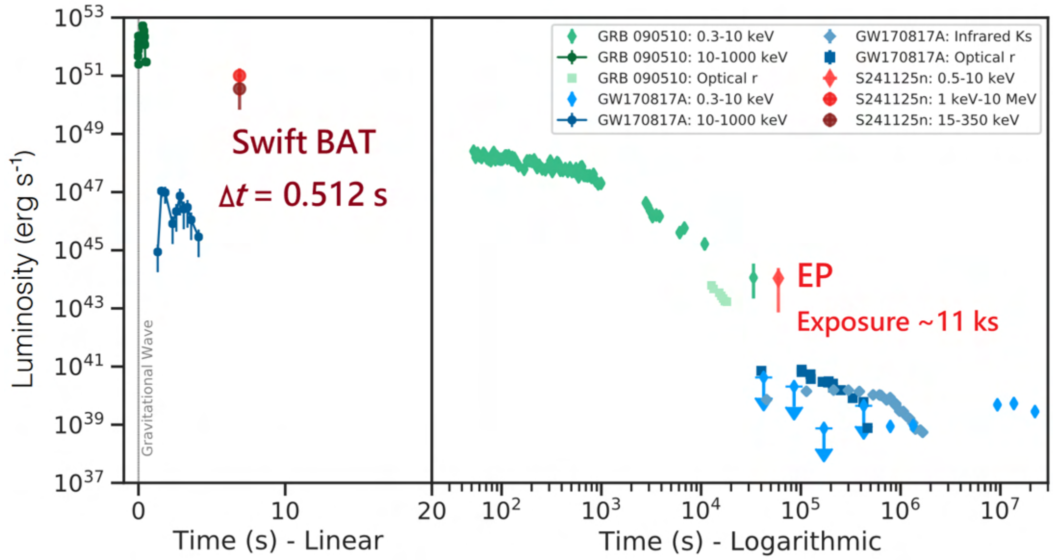

Figure 7.5 The lightcurve of S241125n (in red), i.e., the luminosity evolution from the prompt to the afterglow phase. For comparison, the typical short GRB 090510 (in green) and the neutron star merger event GRB 170817A (in blue) are also plotted. The GW trigger time is adopted as the event start time for both S241125n and GRB 170817A. Time is given in the rest frame.

(2023b). For the AGN disk structure, we adopt the standard thin disk model. In our fiducial setup, the accretion rate is set to $\dot{M} = 0.01\dot{M}_{\rm Edd}$ and the viscosity parameter to $\tilde{\alpha} = 0.05$. The GRB is assumed to occur at a radial distance of $10^3 R_{\rm Sch}$ from the central SMBH. We also set the AGN disk's outer edge at $2 \times 10^4 R_{\rm Sch}$, beyond which gravitational instability may arise.

The accretion rate onto the remnant BH immediately after the binary merger is estimated using the Bondi-Hoyle-Lyttleton formula, with corrections accounting for the disk's vertical scale height and tidal effects, and further enhanced by a factor of $f_{\rm acc} = 15$ due to the recoil velocity imparted by the merger. To estimate the jet energy, we assume a linear relationship between the jet luminosity and the accretion rate, scaled by an efficiency factor $\eta_{\rm j} = 0.5$. The jet's propagation through the disk is calculated following the method of Tagawa et al. (2022), which provides the velocity of the jet head during this phase. Radiation output is then computed based on Tagawa et al. (2023b), accounting for both thermal and non-thermal contributions as the jet emerges from the disk. The non-thermal processes include synchrotron radiation, synchrotron self-Compton (SSC), and second-order inverse Compton scattering (2ndIC). All plasma parameters related to the non-thermal emission are taken directly from Tagawa et al. (2023b).

In our model, we adopt a merging BH mass of $150M_{\odot}$, inspired by the remnant mass observed in GW190521. To justify this choice, we estimate the minimum detectable mass based on the luminosity distance, utilizing a scaling relation for the signal-to-noise ratio (SNR) during the inspiral phase. The SNR follows the proportionality

$$\mathrm{SNR} \propto \frac{M_{\mathrm{c}}^{5/6}}{d_{\mathrm{L}}}, \tag{7.2}$$

where M_{c} denotes the chirp mass (Cutler et al., 1994). As a benchmark, an equal-mass binary neutron star system has a chirp mass of $M_{\mathrm{c}} = m_{\mathrm{ns}}/2^{\frac{1}{5}} \sim 1.2M_{\odot}$, and LIGO can detect such events out to 177 Mpc (Capote et al., 2024). For a source located at d_{L} = 4173 Mpc, scaling the chirp mass yields $M_c \approx 1.2M_{\odot} \times \left(\frac{4173}{177}\right)^{\frac{6}{5}} \approx 53M_{\odot}$. Assuming an equal-mass binary, the corresponding total mass becomes $m_{\mathrm{bh}} = 2 \times M_c \times 2^{\frac{1}{5}} \approx 122M_{\odot}$. Hence, adopting $150M_{\odot}$as the fiducial BH mass is a justified approximation.

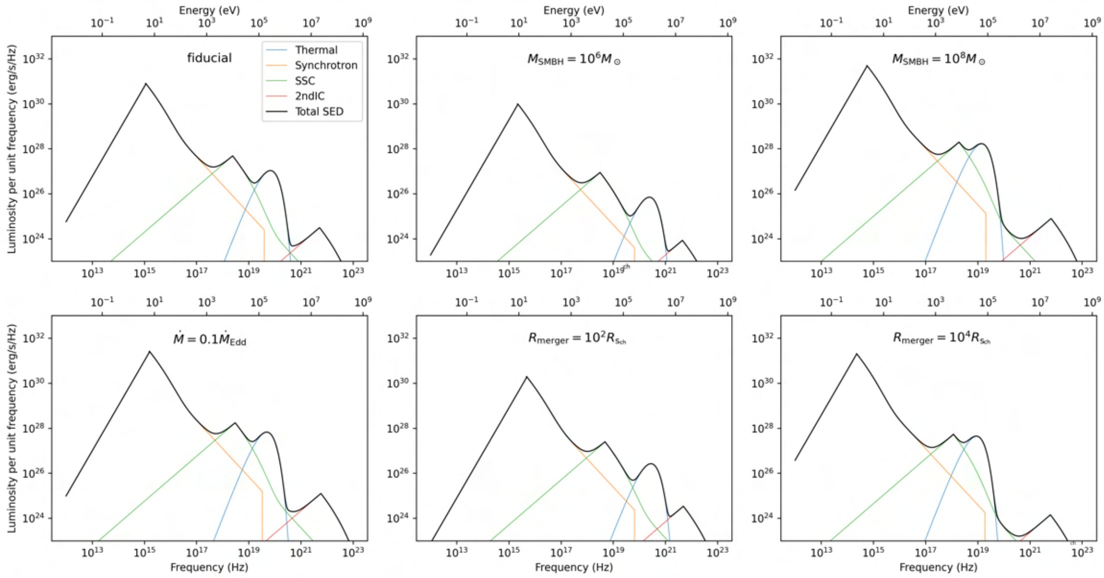

Figure 7.6 The predicted SEDs of a GRB resulting from a BBH merger within an AGN disk. In each panel, only the parameter indicated is varied, while all other parameters are fixed to the fiducial values. The fiducial model adopts the following settings: $M_{\mathrm{SMBH}} = 10^7 M_{\odot}$, $\dot{M} = 0.01\dot{M}_{\mathrm{Edd}}$, $\tilde{\alpha} = 0.05$, $\tilde{R} = 10^3 R_{\mathrm{Sch}}$, and $m_{\mathrm{BH}} = 150M_{\odot}$.

Fig. 7.6 shows the modeled SED of the prompt emission from a GRB powered by an accreting BH remnant embedded in an AGN disk. We explore a range of parameters relative to the fiducial scenario, including different SMBH masses, varying accretion rates, and distinct explosion locations within the AGN disk. Despite these variations, the general features of the results remain consistent. In the low-energy region, synchrotron radiation is the dominant process; SSC becomes prominent around 10 keV, and 2ndIC contributes mainly in the gamma-ray domain. In particular, within the energy range of ∼ 10−100 keV, which corresponds to the observational band of Swift-BAT, thermal emission is dominant and declines steeply at higher frequencies. The thermal peak may partially overlap with the SSC component, together forming the main energy-emitting band and leading to a steep spectral index.

After outlining the mechanism and typical observational signatures of GRBs that may arise from BBH mergers within AGN disks, we turn our attention back to S241125n. The observed broken power-law spectrum with a photon index of -2.2 over the 15–350 keV band (observer frame) can be explained either as the high-energy tail of thermal emission or as the high-energy extension of SSC. We have also examined both the SG and TQM disk models. The SG model produces an overall SED and photon index behavior in the 15 – 300 keV range similar to that of the standard thin disk. In contrast, the TQM model generally predicts lower luminosities, which do not align well with the observations of S241125n.

According to Tagawa et al. (2023b), the time delay between the GW and GRB and the isotropic equivalent breakout luminosity of the relativistic shock are expressed as:

$$t_{\rm delay} \approx (1+z)\frac{\tilde{H}}{4\gamma_{\rm sf}^2 c}, \tag{7.3}$$

and

$$L_{\rm breakout} \approx \pi f_{\rm beaming}\theta_{\rm j}^2 \tilde{H}^2 \tilde{\rho} v_{\rm FS}\gamma_{\rm FS}^2 c^2 \frac{\gamma_{\rm sf,f}}{4\gamma_{\rm sf}}, \tag{7.4}$$

where $f_{\rm beaming} = 2\gamma_{\rm sf,f}^2$; $\gamma_{\rm sf}$ and $\gamma_{\rm sf,f}$ denote the Lorentz factor and the final Lorentz factor of the shocked fluid, respectively; $v_{\rm FS}$ and $\gamma_{\rm FS}$ represent the velocity and Lorentz factor of the shock front.

From the above two equations, by equating them to the observational results, i.e., $t_{\rm delay} = 11.264$ s and $L_{\rm breakout} = 1.01 \times 10^{51}$ erg s^{-1}, the AGN disk thickness $\tilde{H}$ and density $\tilde{\rho}$ at the GRB site can be estimated. By setting the final Lorentz factor of the shocked fluid as $\gamma_{\rm sf,f} = 15$ (corresponding to the final shock Lorentz factor $\gamma_{\rm FS,f} \approx 40$), we solve the AGN disk thickness and density at the GRB site to be $\tilde{H} \approx 5.69 \times 10^{12}$ cm and $\tilde{\rho} \approx 4.20 \times 10^{-9}$ g cm^{-3}, respectively, assuming a jet opening angle of $\theta_{\rm j} = 0.1$. These inferred values correspond to a standard AGN disk characterized by an accretion rate of $\dot{M} = 0.01\dot{M}_{\rm Edd}$, a central SMBH mass of $M_{\rm SMBH} = 10^7 M_\odot$, and viscosity parameter $\tilde{\alpha} = 0.05$, located at a radius of about $\tilde{R}_{\rm merger} \sim 8 \times 10^2 R_{\rm S}$. Then, the predicted burst duration from the model is

$$\Delta t = (1+z)\tilde{H}/(2\gamma_{{\rm sf},f}^2 c) \approx 0.729\,{\rm s}, \tag{7.5}$$

consistent with typical short GRB durations, yet slightly longer than the observed value of S241125n (0.512 s). This may be because some parts of the signal did not trigger the detection bin, leading to a slightly shorter observed duration. Nevertheless, this measurement effect could not be significant; namely, S2411125n cannot be a long GRB in reality, since if it were and the flux within the observed time bin were sufficiently high, the flux in adjacent bins would not abruptly fall below the detection threshold.

The ambient material of the AGN disk influences not only the prompt emission of the GRB but also its afterglow. The afterglow's emission region may be offset from the disk mid-plane, which would reduce the column density of intervening gas.

7.3.2 Afterglow

1. X-ray: photoelectric absorption

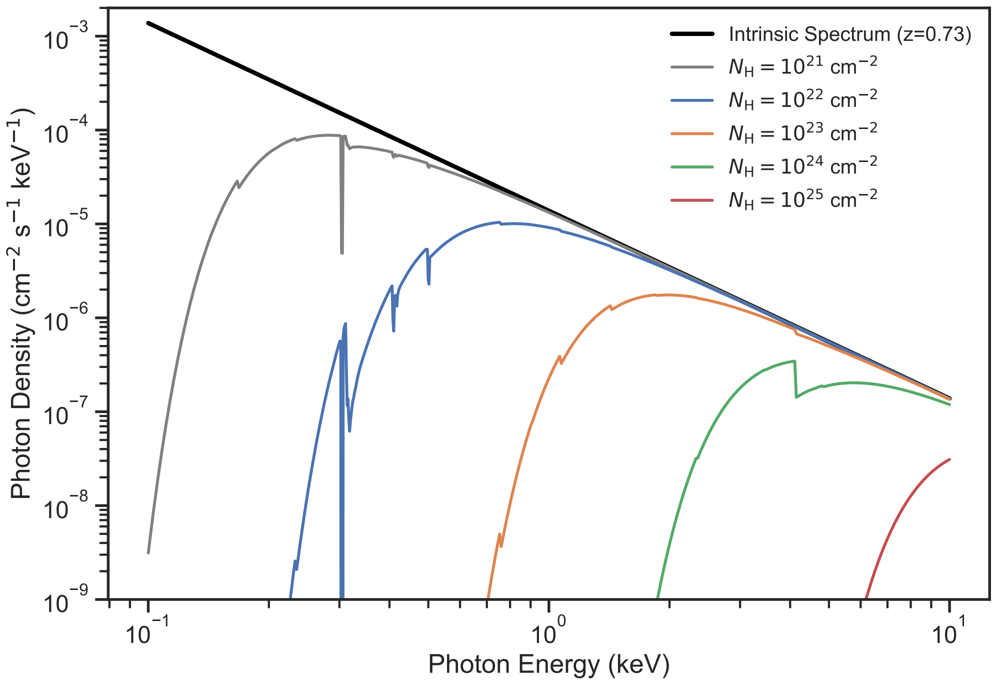

Figure 7.7 Illustration of X-ray absorption effects on a power-law spectrum (photon index = 2) emitted at redshift $z = 0.73$ and observed at $z = 0$. The black curve represents the unabsorbed spectrum with a total flux of 2.20×10^{-13} erg cm^{-2} s^{-1} over the 0.1–10 keV energy range. Colored curves display the spectra after absorption with varying neutral hydrogen column densities ($\tilde{N}_{\rm H}$), ranging from 10^{21} to 10^{25} cm^{-2}. As $\tilde{N}_{\rm H}$ increases, the absorption cutoff energy shifts to higher values, resulting in a harder observed spectrum and a flattened slope above the cutoff.

X-ray photons can be absorbed when their energies surpass the ionization thresholds of bound electrons in atoms or ions, primarily through photoelectric absorption. In this process, an X-ray photon ionizes an atom by ejecting an inner-shell electron. The optical depth τ at a given photon energy ϵ can be expressed as:

$$\tau(\epsilon) = \tilde{N}_{\rm H} \cdot \sigma_{\rm eff}(\epsilon), \tag{7.6}$$

where $\tilde{N}_{\rm H}$ denotes the hydrogen column density and $\sigma_{\rm eff}$ represents the effective photoelectric cross-section. This cross-section incorporates the contributions from hydrogen (dominant at energies below roughly 0.3 keV), helium (important in the 0.3–1 keV soft X-ray regime), and heavier elements (contribute notably via K- and L-shell absorption edges) (Morrison et al., 1983; Balucinska-Church et al., 1992).

Observationally, high column densities ($\tilde{N}_{\rm H} > 10^{21}{\rm cm}^{-2}$) are found to suppress soft X-ray emission ($\epsilon < 1$ keV) (Campana et al., 2010; Schady et al., 2010). At higher energies, the impact of absorption weakens due to the steep energy dependence of the cross-section, which approximately follows $\sigma_{\rm eff} \propto \epsilon^{-3}$. Additionally, specific absorption edges associated with heavy elements can produce distinct flux drops, such as the K-edge of oxygen at 0.54 keV, silicon at around 1.8 keV, and iron at approximately 7.1 keV (Wilms et al., 2000).

AGN disks are typically characterized by high column densities in the range of $\tilde{N}_{\rm H} \sim 10^{22} - 10^{25}$ cm^{-2} (Risaliti et al., 1999). Given such high $\tilde{N}_{\rm H}$, the AGN environment can heavily attenuate GRB afterglow emission in the X-ray band, especially for energies below 10 keV. This results in spectral hardening and a low-energy cutoff in the observed signal (Campana et al., 2010; Schady et al., 2010). To model these effects, we adopt the interstellar grain absorption models provided in XSPEC (see: https://heasarc.gsfc.nasa.gov/xanadu/xspec/manual/node275.html), utilizing elemental abundances from Wilms et al. (2000) and cross-section data from Verner et al. (1996). The intrinsic emission is assumed to follow a power-law (see: https://heasarc.gsfc.nasa.gov/xanadu/xspec/manual/node220.html) with photon index 2 and a normalization of 0.003 cm^{-2} s^{-1} keV^{-1} at 1 keV, emitted at $z = 0.73$, under the assumption of solar metallicity.

Fig. 7.7 displays the resulting absorbed spectra for hydrogen column densities ranging $\sim 10^{21} - 10^{25}$ cm^{-2}, observed at $z = 0$. The simulations show a progressive increase in the low-energy absorption cutoff—from about 0.2 keV at $\tilde{N}_{\rm H} = 10^{21}$ cm^{-2} to beyond 10 keV at $\tilde{N}_{\rm H} = 10^{25}$ cm^{-2}. Simultaneously, the spectral shape flattens, with the photon index approaching zero at $\tilde{N}_{\rm H} = 10^{24}$ cm^{-2}. These results suggest that strong absorption can substantially alter the observed photon index. For instance, the EP-detected afterglow of S241125n exhibits a photon index of $(0.43^{+0.76}_{-0.74}$, significantly harder than the standard value of 2. This observation is consistent with a scenario involving X-ray absorption by an AGN disk with column densities in the range $\sim 10^{23}$–10^{24} cm^{-2}.

2. Infrared, optical and UV: extinction

Fig. 7.4 displays the available optical data for S241125n, which consists solely of upper limits reported by various observatories, alongside a comparative sample of other

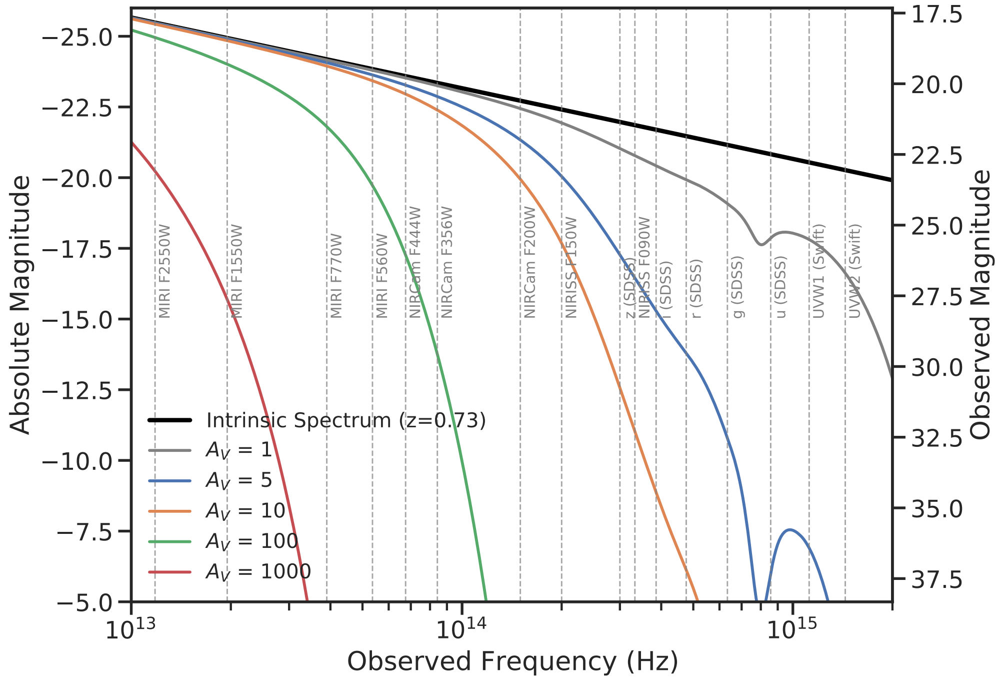

Figure 7.8 Illustration of extinction effects on a synchrotron afterglow spectrum spanning infrared, optical, and ultraviolet wavelengths, emitted at redshift $z = 0.73$ and observed at $z = 0$. The black curve depicts the intrinsic spectrum, following a power-law with spectral index 1 (photon index = 2), typical of short GRB afterglows at around one day post-burst. Colored curves show how this spectrum is altered under varying extinction levels ($A_V = 1 - 1000$). Vertical dashed lines mark the central wavelengths of common observational filters, including SDSS optical bands (u, g, r, i, z), JWST's NIRISS, NIRCam, and MIRI instruments in the infrared, as well as UV bands used by Swift-UVOT. While dust in AGN environments may heavily obscure UV and optical emission, the infrared component of the GRB afterglow is comparatively less affected.

short GRBs. The absence of a confirmed optical counterpart suggests that the optical afterglow from this event was either intrinsically dim or subject to significant extinction.

A major contributing factor to the non-detection of optical afterglows is substantial dust extinction. GRBs occurring within dense regions—such as those rich in star formation or embedded within AGN disks—can be completely obscured in optical wavelengths. Previous studies have found a population of GRBs lacking optical detections, often categorized as "dark GRBs" (Jakobsson et al., 2004), many of which are associated with host galaxies characterized by high hydrogen column densities (Greiner et al., 2010; Perley et al., 2009).

The level of extinction is commonly quantified by the visual extinction parameter A_V, which correlates with $N_{\rm H}$. For the Milky Way's interstellar medium, the typical relation is approximately (Bohlin et al., 1978; Predehl et al., 1995; Foight et al., 2012)

$$A_V(\mathrm{MW}) \approx 5 \times 10^{-22} N_{\rm H}. \tag{7.7}$$

In AGNs, however, the dust-to-gas ratio is generally reduced—likely due to grain destruction by strong radiation, shocks, and turbulence—yielding a lower proportionality (Maiolino et al., 2001; Burtscher et al., 2016):

$$A_V(\mathrm{AGN}) \approx 5 \times 10^{-23} \tilde{N}_\mathrm{H}. \tag{7.8}$$

This implies that for AGN environments with $\tilde{N}_\mathrm{H} \sim 10^{23} - 10^{24}\ \mathrm{cm}^{-2}$, one expects:

$$A_V \approx 5 - 50. \tag{7.9}$$

Applying the extinction law from Fitzpatrick et al. (2007), we estimate its impact on the afterglow spectrum in Fig. 7.8. The extinction effect is more severe at shorter wavelengths—UV and optical photons are particularly vulnerable to absorption. When $A_V > 5$, the ultraviolet emission is almost entirely absorbed, and the optical flux is diminished by several magnitudes, making afterglows invisible even in deep optical surveys. While delayed UV/optical flares may be produced by powerful AGN jets (Chen et al., 2025b), such emissions are likely to be heavily obscured by dust extinction, consistent with the observational constraints from WFST. In contrast, infrared emission suffers significantly less extinction.

In this context, infrared follow-up becomes essential. Instruments like JWST's NIRCam and MIRI, which cover wavelengths from 1 to 25 μm (Gardner et al., 2006), are well-suited to detecting GRB afterglows in obscured environments. As illustrated in Fig. 7.8, even with $A_V \sim 10$, the afterglow remains detectable in JWST's mid-infrared bands such as MIRI/F560W and F770W. Assuming a typical power-law decay with index -1.5 (Li et al., 2018; Dainotti et al., 2025) and an initial brightness of ~ 20 mag at 1 day, the infrared afterglow is expected to fade to around 25.5 mag after 1 month, and roughly 27 mag after 3 months. Given MIRI's sensitivity to sources fainter than 28 - 29 mag in deep exposures, such afterglows should remain observable for weeks to months post-burst. Unfortunately, S241125n did not benefit from timely infrared follow-up. Similar future events would strongly benefit from dedicated deep infrared observations.

Overall, the absence of an optical counterpart for S241125n can be reasonably attributed to significant extinction in a dust-rich environment, consistent with conclusions drawn from the X-ray spectral analysis.

7.4 Discussion on Host Galaxy

Once a GRB is localized, astronomers typically perform deep imaging of the surrounding sky region to search for potential host galaxies (Bloom et al., 2002). The most probable host is generally identified as the galaxy closest to the afterglow position. Spectroscopic observations can then determine the redshift of the candidate galaxy, and if it matches that of the GRB afterglow, the association is considered confirmed. In the case of S241125n, however, the 5-arcminute localization uncertainty from BAT covers a relatively wide area, and no deep imaging observations have been reported in public datasets that specifically target this region after the GRB event.

Another approach to identifying the host galaxy involves comparing the GRB localization with data from large-scale astronomical surveys. These surveys often provide photometric—and occasionally spectroscopic—information across wide regions of the sky, enabling cross-referencing with known galaxy positions. Nevertheless, for S241125n, no host galaxy has been found within the reported uncertainty radius in any available catalog. This raises an open question: is the absence due to the observational limitations of current surveys, or does S241125n originate from a truly host-less or extremely faint extragalactic environment?

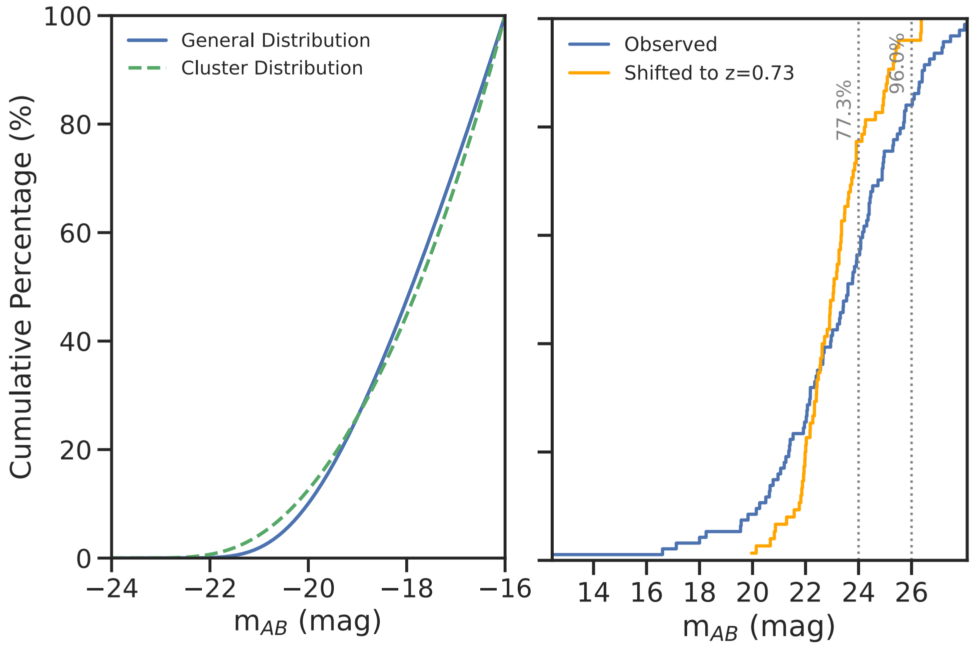

Figure 7.9 Left: Cumulative percentage of absolute magnitude obtained by integrating the luminosity function for the general galaxy distribution (solid blue line) and the composite cluster galaxy distribution (dashed green line). Right: Cumulative distributions of the observed AB magnitudes (blue step line, sample size = 94) and the AB magnitudes shifted to a redshift of 0.73 (orange step line, sample size = 75) for the host galaxies of short GRBs. Vertical grey dotted lines indicate $m_{\rm AB} = 24$ and 26, with the corresponding cumulative percentages labeled accordingly.

In optical bands, various surveys offer different detection limits: SDSS typically reaches a limiting magnitude of around $\sim$ 22 mag (York et al., 2000), Pan-STARRS can probe sources as faint as $\sim$ 23 mag (Chambers et al., 2016), while deeper surveys like DES and DESI extend this limit to approximately $\sim$ 24 mag (Abbott et al., 2021; DESI Collaboration et al., 2016). In the near-infrared range, 2MASS and WISE provide sensitivity down to $\sim$ 16.5 mag (Skrutskie et al., 2006; Wright et al., 2010), and the GAMA spectroscopic survey achieves depths of about $\sim$ 20 mag (Alpaslan et al., 2015). Therefore, galaxies with apparent magnitudes fainter than 24 mag would lie below the detection thresholds of these surveys and hence would not be recorded in their catalogs. Some ultra-deep field surveys, such as the Hyper Suprime-Cam Subaru Strategic Program (HSC-SSP) (Aihara et al., 2018), the Hubble Ultra Deep Field (HUDF) (Beckwith et al., 2006), UltraVISTA (McCracken et al., 2012), and the Spitzer Extended Deep Survey (SEDS) (Ashby et al., 2013), do reach depths beyond 24 mag, in some cases even exceeding 26 mag. However, their limited coverage of the sky does not include the region where S241125n is located.

We then begin by examining the possibility of intrinsic faintness. For a galaxy with absolute magnitude M in a specific band, its apparent magnitude m can be estimated using the distance modulus formula: $m = M + \mu + K$, where $\mu = 5\log_{10}(d_L/10\ \mathrm{pc})$ denotes the distance modulus and K represents the k-correction. At the distance of S241125n, the distance modulus is $\mu = 43.2$. Therefore, a typical galaxy with $M \sim -21$ would appear at $m = 22.2$ mag, while a sub-luminous galaxy with $M \sim -19$ would correspond to $m = 24.2$ mag, assuming K-corrections are negligible.

Another factor to account for is dust extinction. In typical galaxies, the optical extinction A_V usually falls between 0.5 and 1.0 magnitudes. However, in galaxies with active star formation or undergoing starburst activity, A_V can reach 1–2 magnitudes or even higher (Calzetti et al., 1994, 2000). In the case of AGNs, the degree of extinction can vary significantly. For example, obscured AGNs (Type 2) often exhibit A_V values exceeding 5 magnitudes, with some reaching up to 10 magnitudes or more (Richards et al., 2003; Barquín-González et al., 2024). If we assume $A_V \sim 1$, the observed apparent magnitude would become fainter by about 1 magnitude, shifting from 22.2 to 23.2 mag, or from 24.2 to 25.2 mag. In addition, cosmological surface brightness dimming follows a $(1+z)^4$ dependence (Tolman, 1930). At redshift $z = 0.73$, this factor is approximately 9. As a result, even if the total magnitude of the host galaxy is within detection limits, its extended, faint structures might fall below the surface brightness threshold, making them difficult to identify in surveys.

The Schechter luminosity function (Schechter, 1976; Blanton et al., 2001) can be used to quantify the proportion of galaxies with luminosities below a certain magnitude threshold. As illustrated in Fig. 7.9, the cumulative fractions derived from integrating this function are shown for both the general field galaxy population and a composite sample of cluster galaxies. The results indicate that more than 70% of galaxies are dimmer than −19 mag, and over 90% fall below −20 mag. Consequently, for a survey with a limiting magnitude around 24 mag, a significant fraction of galaxies at redshift $z = 0.73$ would fall below the detection limit and remain undetected.

Based on GRB host galaxy statistics, Lyman et al. (2017) performed a Snapshot survey using the Hubble Space Telescope (HST) WFC3/F160W instrument, targeting 39 host galaxies of long-duration GRBs. Their analysis revealed that these hosts are, on average, fainter than typical field galaxies. Specifically, 17 of the host galaxies exhibited magnitudes dimmer than 24 mag, accounting for 43.6% of the sample. In addition, 5 hosts were undetected, implying that their magnitudes likely exceed 26 mag or they may be heavily obscured.

In another study, Fong et al. (2022) investigated the host galaxies of 94 short GRBs. The cumulative distribution of their observed AB magnitudes is shown as the blue step line in the right panel of Fig. 7.9. To examine how observable these hosts would be at a redshift of $z = 0.73$, the host magnitudes were redshift-corrected. Among the 94 GRBs, 19 have no redshift measurements, likely due to the faintness of their hosts, which have magnitude lower limits between 23.6 and 28.1. The remaining 75 GRBs, after redshift shifting, yield the orange step line in the same figure. This analysis shows that 17 of the 75 shifted hosts would be fainter than 24 mag at $z = 0.73$. Including the 19 hosts without redshifts, the estimated fraction of host galaxies dimmer than 24 mag at this redshift lies between 18% and 38%. This percentage is smaller than the fraction predicted by the Schechter luminosity function, likely because more luminous galaxies contain more stars and thus have a higher likelihood of producing GRBs.

As for S241125n, which may represent a unique class of GRBs, whether its host follows the typical patterns of GRB host galaxies remains unclear. Still, based on the observational evidence and estimations above, the absence of a host galaxy detection for S241125n in current surveys is consistent with expectations, with the non-detection probability likely ranging from about 20% up to over 50%.

While the above represents the general scenario, the detectability of host galaxies is also influenced by the BH formation channels if the GRB originates in an AGN disk. This is because the central SMBH may be biased—either below or above $10^7 M_\odot$ —depending on the formation pathway of the black holes. If BHs are captured from nuclear star clusters, theoretical models suggest they are more likely to be embedded in AGN disks surrounding lower-mass SMBHs, as such captures are more efficient in that regime (Xue et al., 2025). On the other hand, if BHs form in situ via star formation within the disk, the merger rate tends to follow the AGN luminosity function, peaking for SMBHs in the $10^7 - 10^8 M_\odot$ mass range. Therefore, one should be cautious when interpreting the detectability of the host. In particular, the in-situ formation scenario may face constraints due to the absence of a confirmed host galaxy.

Additionally, although the probability that the association between the GW and EM signals (Swift and/or EP) is due to random coincidence is very low, we cannot completely rule out the possibility that they are unrelated, since the redshift of the GRB has not been confirmed by either spectroscopy or host galaxy identification. If the GRB and GW signals are unrelated, the GRB may have originated from a much greater distance. Even if they are physically associated, the GW's poor localization means the actual source could still lie farther away. In either case, identifying the host galaxy becomes even more challenging.

7.5 Conclusions

LVK S241125n stands as the only currently known gravitational-wave candidate from a binary BH merger that exhibits an associated short GRB detected across multiple wavelengths. In this work, we explore the possibility that S241125n originates from a BH merger embedded within an AGN disk. Within this framework, a set of physically reasonable parameters can account for the main observational characteristics.

(i) Relativistic Jet Production: Binary BH mergers in AGN disks can lead to super-Eddington accretion onto the remnant BH, triggering the formation of relativistic jets that produce both thermal and non-thermal emission through shock interactions with the disk material.

(ii) Spectral Features Explained: The observed photon index of -2.2 during the prompt GRB phase can be attributed to the high-energy tail of thermal emission or the SSC component, while the unusually hard photon index in the afterglow phase is likely a result of absorption in a dense environment. The lack of an optical counterpart is also consistent with the significant dust extinction expected in AGN disks.

(iii) Parameter Consistency: The time delay between the GW and GRB signals, as well as the GRB duration and luminosities, align well with theoretical expectations for a BH merger occurring within an AGN disk, assuming appropriate model parameters.

Given the limited signal quality and the absence of a confirmed host galaxy, our interpretation remains cautious. Nonetheless, future studies of S241125n and similar events (e.g., searching for the host using deep-field telescopes, fitting the merger eccentricity from GW data, and conducting timely infrared and/or even high-energy neutrino follow-up observations) could shed light on the physical mechanisms underlying BH mergers and provide new insights into the connection between GW, electromagnetic counterparts, and their astrophysical environments.

Chapter 8 Summary and Outlook

8.1 Roles of Irreducible Mass in BH Physics

One of my main research focuses during my Ph.D. is on the critical role of irreducible mass (Mirr) in BH physics. This work explored the feedback of Mirr in processes like BH accretion and energy extraction, accurately calculating how rotational energy in the BH is gained or lost and determining the total extractable energy. The square of Mirr is proportional to the BH's area and thus to its entropy, so quantifying the growth of Mirr offers a measure of the irreversibility of these processes. The irreducible mass is considered just as fundamental as the mass and angular momentum in describing black hole physics.

8.1.1 Extended Plans

As for energy extraction processes in black holes, there are numerous equally important questions worth exploring. For example, in the Penrose process, one should further investigate the case where the decay point does not coincide with the turning point, as well as the analysis of the negative root solution in Eq. (2.10). The negative root solution may not be intuitively obvious from a physical standpoint. However, since it is also a solution of the Einstein field equations, it warrants further consideration. This may be related to the motion of antimatter in the reverse direction of time. Additionally, various energy extraction processes, such as the confined Penrose process (Zaslavskii, 2022), collisional Penrose processes (Piran et al., 1975), and the Blandford-Znajek(BZ) process (Blandford et al., 1977), are worth studying in terms of their feedback to BHs. Furthermore, the Pollock process (Pollock, 1976; King et al., 1977) and accretion processes are also relevant for understanding the irreducible mass and irreversibility of BHs. These physical processes either involve consideration of BH magnetic fields (such as the BZ mechanism and Pollock process) or complex systems with many particles (such as collisional Penrose processes). When considering magnetic fields, not only may the magnetic field itself interact with the BH, altering its mass and irreducible mass, but it may also extend the ergosphere of the BH, leading to the appearance of a wider range of negative-energy orbits, thereby resulting in different energy extraction and feedback from the BH compared to the Penrose processes considered in the current manuscript. When considering complex multi-particle systems, we intend to statistically account for the energy extracted from the BH and the feedback on the BH, rather than considering the trajectory of each individual particle and its impact on the BH.

As for the mass increase process, we have shown that EMRIs exhibit similar feedback on the irreducible mass as accretion processes. A further open question is whether a scaling relation exists between EMRIs and near-equal-mass binaries, and, if so, what physical mechanism underlies it. In particular, the role of irreducible mass in binary systems, as well as its evolution throughout the merger process, remains to be clarified. These issues will be addressed in future work.

8.2 The Dynamics and Accretion of Compact Objects in AGN Disks

Another main research focus during my PhD, leaning more toward processes related to observational effects, is on the accretion and dynamics of compact objects in AGN disks. These works form a series on compact objects (stellar-mass BHs, NSs, and WDs) embedded in AGN disks, aiming to explore their evolutionary fates, to interpret AGN variability and certain GRB sources, and to account for the super-solar metallicities observed in quasars. Moreover, the predicted corresponding multi-messenger signals are valuable for uncovering the origins of GWs and neutrinos.

8.2.1 Extended Plans

My Ph.D. studies have inspired me to pursue a broader research: exploring the role of compact objects in AGNs through multi-messenger approaches.

Firstly, our study is general and adaptable. WD–WD collisions represent one type of compact object interaction in AGN disks. The underlying dynamical mechanisms are general and could also apply to WD–BH, WD–NS, or star–BH systems, potentially leading to micro-TDEs, which warrant further investigation. Furthermore, these explosive events in AGN disks naturally lead to interactions between disk material and ejected (i.e., non-disk) components. This can be generalized to a broader class of problems involving the interaction between disk and non-disk components. While accretion disk theory has seen great success and has been validated by observations, the disk component alone cannot capture the impact of non-disk components on energy and angular momentum transfer, and consequently, their observational signatures. Non-disk components are prevalent in the nuclear regions of AGNs and include: (1) fallback material from explosive events in the disk; (2) jet ISM interactions producing backflows; and (3) failed winds from the disk. These components are often related to stellar or compact object activity within the AGN disk. Understanding these interactions is therefore essential for tracing angular momentum redistribution, accretion physics, and compact object evolution in AGN disks.

Gas in AGN disks damps the motion of compact objects, so the GW signals from EMRIs or IMRIs of such “wet” origin will show phase differences compared to those from “dry” origins. Since compact objects in the disk are often super-Eddington accretors with intermittent accretion, how does this process affect EMRI signals? Not all nuclear compact objects remain confined to the disk; when their orbits are inclined relative to the disk plane, how are the corresponding EMRI signals modified? In particular, what are the effects of accretion as the object crosses the disk? These issues render EMRIs in AGN disks both excellent targets for LISA and valuable probes of the accretion behavior of compact objects. Meanwhile, current studies are mostly based on the assumption that AGN disks follow the standard thin-disk model and are idealized as fluid disks. In reality, however, the gas within the disk may not be uniformly distributed but instead clumpy and turbulent. At the same time, accreting gas flows may give rise to unstable circumbinary disk structures in binary systems. All these factors could significantly affect the evolutionary pathways of compact objects. Therefore, more refined models of compact object accretion in AGN disks are warranted.

While we have conducted preliminary research on NS accretion in AGN disks, several questions still need to be solved about NSs evolutions in AGN disks: (1) How do the spin and magnetic field of NSs evolve in AGN disks, and how do they interact with the disk's magnetic field? (2) What are the nucleosynthesis outcomes under hyper-Eddington accretion onto NSs? (3) How do the internal structure and crust evolve, and how does the NS's mass quadrupole moment change? (4) What is the distribution of NS progenitor stars and their natal kick velocities in AGN disks? Does the disk facilitate or hinder the escape of newborn NSs, and what is their final spatial distribution?

During a binary BH merger, GWs carry away both angular and linear momentum from the system. The loss of angular momentum leads to orbital decay, while the linear momentum carried by GWs imparts a recoil velocity —referred to as the kick—to the merger remnant relative to the binary's center of mass. Such a kick can enhance the post-merger accretion rate, significantly affecting the detectability and characteristics of the associated electromagnetic radiation and high-energy neutrinos. Moreover, the kick itself leaves a distinct signature in the GW signal, offering a promising avenue for multi-messenger studies of compact objects in AGN disks. However, the kick characteristics of binary black hole mergers in AGN disks remain poorly understood, highlighting the need for dynamical modeling of their distribution.

In addition, how the formation and growth of massive “seed” BHs in the early universe occurred is still lacking clarification. Observations suggest that more massive galaxies often lack nuclear star clusters, while less massive ones do not (Georgiev et al., 2016), hinting that compact objects may play a significant role in the growth of SMBHs. In addition, compact objects or stars embedded in AGN disks can alter the accretion structure, possibly producing observable spectral features like the “V” -shaped spectra seen in little red dots. These studies suggest that compact objects in AGNs may play a key role in the cosmological evolution of SMBHs, involving the co-evolution of galaxies, AGNs, and SMBHs. With this in mind, we plan to study the growth of SMBHs and the distribution of compact objects within the framework of the cosmological evolution of galaxies.

Meanwhile, we will integrate electromagnetic, GW, and neutrino observations to search for more sources. Currently, only a few candidates in AGN disks have been reported, and most studies remain theoretical. This is because of challenges in detecting compact objects in AGN disks, including: (1) the strong optical background of AGNs; (2) the typically large distances to AGNs and the poor localization of GW sources; (3) the lack of smoking-gun observational evidence for individual events; and (4) insufficient sample sizes for statistical analysis. Future searches need to address these challenges accordingly. Given the strong optical background in AGNs and the relatively lower background at higher energies, our search will focus on the high-energy regime, e.g., the radio, X-ray, MeV, and GeV bands. Combining increasing multimessenger observations with ML-assisted data mining holds promise for pushing the study of compact objects in AGNs into a population-level regime. More and more LVK O4 (and O5) GW sources are being detected with improved parameter estimation and localization, enabling statistical assessments. Meanwhile, we will theoretically explore distinct signatures—including eccentricity and kick velocities—to guide identification and interpretation.

Combining these further investigations holds great potential for understanding how compact objects regulate the transport and redistribution of mass, energy, and angular momentum across various scales in AGNs, how the central “monster” evolves over comic time, and how to search for the associated multi-wavelength and multi-messenger observational signatures. Such multi-messenger information could even open a new window for probing cosmology.

Bibliography

Abbott B, Abbott R, Adhikari R, et al. 2007. Searches for periodic gravitational waves from unknown isolated sources and Scorpius X-1: Results from the second LIGO science run[J/OL]. Phys. Rev. D, 76(8): 082001. DOI: 10.1103/PhysRevD.76.082001.

Abbott B P, Abbott R, Abbott T D, et al. 2017. Gravitational Waves and Gamma-Rays from a Binary Neutron Star Merger: GW170817 and GRB 170817A[J/OL]. Astrophys. J. Lett., 848(2): L13. DOI: 10.3847/2041-8213/aa920c.

Abbott R, Abbott T D, Abraham S, et al. 2020. GW190521: A Binary Black Hole Merger with a Total Mass of 150 M⊙[J/OL]. Phys. Rev. Lett., 125(10): 101102. DOI: 10.1103/PhysRevLett.125.101102.

Abbott T M C, Adamów M, Aguena M, et al. 2021. The Dark Energy Survey Data Release 2[J/OL]. Astrophys. J. Suppl., 255(2): 20. DOI: 10.3847/1538-4365/ac00b3.

Abe K, Abe T, Aihara H, et al. 2011. Letter of Intent: The Hyper-Kamiokande Experiment — Detector Design and Physics Potential —[A/OL]. arXiv:1109.3262. arXiv: 1109.3262.

Ackermann M, Asano K, Atwood W B, et al. 2010. Fermi Observations of GRB 090510: A Short-Hard Gamma-ray Burst with an Additional, Hard Power-law Component from 10 keV TO GeV Energies[J/OL]. Astrophys. J., 716(2): 1178-1190. DOI: 10.1088/0004-637X/716/2/1178.

Aihara H, Armstrong R, Bickerton S, et al. 2018. First data release of the Hyper Suprime-Cam Subaru Strategic Program[J/OL]. Publications of the Astronomical Society of Japan, 70: S8. DOI: 10.1093/pasj/psx081.

Akl D, Andrade C, de Bruin E, et al. 2024a. LIGO/Virgo/KAGRA S241125n: GRANDMA Optical Upper Limits[J]. GRB Coordinates Network, 38396: 1.

Akl D, Antier S, Ducoin J G, et al. 2024b. LIGO/Virgo/KAGRA S241125n: COLIBRÍ Upper Limits on Optical Counterparts to Two of the Swift/XRT Sources[J]. GRB Coordinates Network, 38334: 1.

Alexander D R, Ferguson J W. 1994. Low-Temperature Rosseland Opacities[J/OL]. Astrophys. J., 437: 879. DOI: 10.1086/175039.

Ali-Dib M, Lin D N C. 2023. The impermanent fate of massive stars in AGN discs[J/OL]. Mon. Not. R. Astron. Soc., 526(4): 5824-5838. DOI: 10.1093/mnras/stad2774.

Alpaslan M, Driver S, Robotham A S G, et al. 2015. Galaxy And Mass Assembly (GAMA): trends in galaxy colours, morphology, and stellar populations with large-scale structure, group, and pair environments[J/OL]. Mon. Not. R. Astron. Soc., 451(3): 3249-3268. DOI: 10.1093/mnras/stv1176.

Alves L M B, Sullivan A G, Yang Y, et al. 2024. Determining the Hubble constant with AGN-assisted black hole mergers[J/OL]. Mon. Not. R. Astron. Soc., 531(3): 3679-3683. DOI: 10.1093/mnras/stae1360.

Ananna T T, Bogdán Á, Kovács O E, et al. 2024. X-Ray View of Little Red Dots: Do They Host Supermassive Black Holes?[J/OL]. Astrophys. J. Lett., 969(1): L18. DOI: 10.3847/2041-8213/ad5669.

Andersson N. 1998. A New Class of Unstable Modes of Rotating Relativistic Stars[J/OL]. Astrophys. J., 502(2): 708-713. DOI: 10.1086/305919.

Andersson N, Kokkotas K D, Stergioulas N. 1999. On the Relevance of the R-Mode Instability for Accreting Neutron Stars and White Dwarfs[J/OL]. Astrophys. J., 516(1): 307-314. DOI: 10.1086/307082.

Antoni A, MacLeod M, Ramirez-Ruiz E. 2019. The Evolution of Binaries in a Gaseous Medium: Three-dimensional Simulations of Binary Bondi-Hoyle-Lyttleton Accretion[J/OL]. Astrophys. J., 884(1): 22. DOI: 10.3847/1538-4357/ab3466.

Antonini F. 2014. On the Distribution of Stellar Remnants around Massive Black Holes: Slow Mass Segregation, Star Cluster Inspirals, and Correlated Orbits[J/OL]. Astrophys. J., 794(2): 106. DOI: 10.1088/0004-637X/794/2/106.

Ashby M L N, Willner S P, Fazio G G, et al. 2013. SEDS: The Spitzer Extended Deep Survey. Survey Design, Photometry, and Deep IRAC Source Counts[J/OL]. Astrophys. J., 769(1): 80. DOI: 10.1088/0004-637X/769/1/80.

Ashton G, Hübner M, Lasky P D, et al. 2019. BILBY: A User-friendly Bayesian Inference Library for Gravitational-wave Astronomy[J/OL]. Astrophys. J. Suppl., 241(2): 27. DOI: 10.3847/1538-4365/ab06fc.

Asthana A, Mushtukov A A, Dobrynina A A, et al. 2023. Bright X-ray pulsars as sources of MeV neutrinos in the sky[J/OL]. Mon. Not. R. Astron. Soc., 522(3): 3405-3411. DOI: 10.1093/mnras/stad1118.

Bagoly Z, Szécsi D, Balázs L G, et al. 2016. Searching for electromagnetic counterpart of LIGO gravitational waves in the Fermi GBM data with ADWO[J/OL]. Astron. Astrophys., 593: L10. DOI: 10.1051/0004-6361/201628569.

Bahcall J N. 1989. Neutrino Astrophysics[M].

Bai X N, Stone J M. 2011. Effect of Ambipolar Diffusion on the Nonlinear Evolution of Magnetorotational Instability in Weakly Ionized Disks[J/OL]. Astrophys. J., 736(2): 144. DOI: 10.1088/0004-637X/736/2/144.

Balucinska-Church M, McCammon D. 1992. Photoelectric Absorption Cross Sections with Variable Abundances[J/OL]. Astrophys. J., 400: 699. DOI: 10.1086/172032.

Bardeen J M, Press W H, Teukolsky S A. 1972. Rotating Black Holes: Locally Nonrotating Frames, Energy Extraction, and Scalar Synchrotron Radiation[J/OL]. Astrophys. J., 178: 347-370. DOI: 10.1086/151796.

Barquín-González L, Mateos S, Carrera F J, et al. 2024. Extinction and AGN over host galaxy contrast effects on the optical spectroscopic classification of AGN[J/OL]. Astron. Astrophys., 687: A159. DOI: 10.1051/0004-6361/202348948.

Basko M M, Sunyaev R A. 1976. The limiting luminosity of accreting neutron stars with magnetic fields.[J/OL]. Mon. Not. R. Astron. Soc., 175: 395-417. DOI: 10.1093/mnras/175.2.395.

Beacom J F. 2010. The Diffuse Supernova Neutrino Background[J/OL]. Annual Review of Nuclear and Particle Science, 60: 439-462. DOI: 10.1146/annurev.nucl.010909.083331.

Becerra R L, Troja E, Angulo Valdez C, et al. 2024. LIGO/Virgo/KAGRA S241125n: DDOTI Optical Upper Limits[J]. GRB Coordinates Network, 38329: 1.

Beckmann V, Shrader C R. 2012. Active Galactic Nuclei[M].

Beckwith S V W, Stiavelli M, Koekemoer A M, et al. 2006. The Hubble Ultra Deep Field[J/OL]. Astron. J., 132(5): 1729-1755. DOI: 10.1086/507302.

Bekenstein J D. 1973a. Extraction of Energy and Charge from a Black Hole[J/OL]. Phys. Rev. D, 7(4): 949-953. DOI: 10.1103/PhysRevD.7.949.

Bekenstein J D. 1973b. Black Holes and Entropy[J/OL]. Phys. Rev. D, 7(8): 2333-2346. DOI: 10.1103/PhysRevD.7.2333.

Bekenstein J D, Schiffer M. 1998. The many faces of superradiance[J/OL]. Phys. Rev. D, 58(6): 064014. DOI: 10.1103/PhysRevD.58.064014.

Bellovary J M, Mac Low M M, McKernan B, et al. 2016. Migration Traps in Disks around Supermassive Black Holes[J/OL]. Astrophys. J. Lett., 819(2): L17. DOI: 10.3847/2041-8205/819/2/L17.

Berger E. 2014. Short-Duration Gamma-Ray Bursts[J/OL]. Annu. Rev. Astron. Astrophys., 52: 43-105. DOI: 10.1146/annurev-astro-081913-035926.

Bernal C G, Lee W H, Page D. 2010. Hypercritical accretion onto a magnetized neutron star surface: a numerical approach[J]. Rev. Mex. Astron. Astrofis., 46: 309-322.

Bildsten L. 1998. Gravitational Radiation and Rotation of Accreting Neutron Stars[J/OL]. Astrophys. J. Lett., 501(1): L89-L93. DOI: 10.1086/311440.

Bildsten L, Brown E F. 1997. Thermonuclear Burning on the Accreting X-Ray Pulsar GRO J1744-28 [J/OL]. Astrophys. J., 477(2): 897-904. DOI: 10.1086/303752.

Bisnovatyi-Kogan G S, Blinnikov S I. 1977. Disk accretion onto a black hole at subcritical luminosity.[J]. Astron. Astrophys., 59: 111-125.

Blandford R D, Payne D G. 1982. Hydromagnetic flows from accretion disks and the production of radio jets.[J/OL]. Mon. Not. R. Astron. Soc., 199: 883-903. DOI: 10.1093/mnras/199.4.883.

Blandford R D, Znajek R L. 1977. Electromagnetic extraction of energy from Kerr black holes. [J/OL]. Mon. Not. R. Astron. Soc., 179: 433-456. DOI: 10.1093/mnras/179.3.433.

Blandford R D, Begelman M C. 1999. On the fate of gas accreting at a low rate on to a black hole [J/OL]. Mon. Not. R. Astron. Soc., 303(1): L1-L5. DOI: 10.1046/j.1365-8711.1999.02358.x.

Blanton M R, Dalcanton J, Eisenstein D, et al. 2001. The Luminosity Function of Galaxies in SDSS Commissioning Data[J/OL]. Astron. J., 121(5): 2358-2380. DOI: 10.1086/320405.

Bloom J S, Kulkarni S R, Djorgovski S G. 2002. The Observed Offset Distribution of Gamma-Ray Bursts from Their Host Galaxies: A Robust Clue to the Nature of the Progenitors[J/OL]. Astron. J., 123(3): 1111-1148. DOI: 10.1086/338893.

Bloom J S, Frail D A, Sari R. 2001. The Prompt Energy Release of Gamma-Ray Bursts using a Cosmological k-Correction[J/OL]. Astron. J., 121(6): 2879-2888. DOI: 10.1086/321093.

Boekholt T C N, Rowan C, Kocsis B. 2023. On the Jacobi capture origin of binaries with applications to the Earth-Moon system and black holes in galactic nuclei[J/OL]. Mon. Not. R. Astron. Soc., 518(4): 5653-5669. DOI: 10.1093/mnras/stac3495.

Bohlin R C, Savage B D, Drake J F. 1978. A survey of interstellar H I from Lalpha absorption measurements. II.[J/OL]. Astrophys. J., 224: 132-142. DOI: 10.1086/156357.

Bom C R, Palmese A. 2024. Standard siren cosmology with gravitational waves from binary black hole mergers in active galactic nuclei[J/OL]. Phys. Rev. D, 110(8): 083005. DOI: 10.1103/PhysRevD.110.083005.

Boyer R H, Lindquist R W. 1967. Maximal Analytic Extension of the Kerr Metric[J/OL]. Journal of Mathematical Physics, 8(2): 265-281. DOI: 10.1063/1.1705193.

Buckley J, APT Team. 2022. The Advanced Particle-astrophysics Telescope (APT)[C]//AAS/High Energy Astrophysics Division: Vol. 54 AAS/High Energy Astrophysics Division. 404.04.

Burke O, Gair J, Simón J. 2020. Transition from inspiral to plunge: A complete near-extremal trajectory and associated waveform[J/OL]. Phys. Rev. D, 101(6): 064026. DOI: 10.1103/PhysRevD.101.064026.

Burtscher L, Davies R I, Graciá-Carpio J, et al. 2016. On the relation of optical obscuration and X-ray absorption in Seyfert galaxies[J/OL]. Astron. Astrophys., 586: A28. DOI: 10.1051/0004-6361/201527575.

Callister T A, Haster C J, Ng K K Y, et al. 2021. Who Ordered That? Unequal-mass Binary Black Hole Mergers Have Larger Effective Spins[J/OL]. Astrophys. J. Lett., 922(1): L5. DOI: 10.3847/2041-8213/ac2ccc.

Calzetti D, Kinney A L, Storchi-Bergmann T. 1994. Dust Extinction of the Stellar Continua in Starburst Galaxies: The Ultraviolet and Optical Extinction Law[J/OL]. Astrophys. J., 429:

582. DOI: 10.1086/174346.

Calzetti D, Armus L, Bohlin R C, et al. 2000. The Dust Content and Opacity of Actively Star-forming Galaxies[J/OL]. Astrophys. J., 533(2): 682-695. DOI: 10.1086/308692.

CAMENZIND M. 2007. Compact objects in astrophysics[M]. Springer.

Campana S, Thöne C C, de Ugarte Postigo A, et al. 2010. The X-ray absorbing column densities of Swift gamma-ray bursts[J/OL]. Mon. Not. R. Astron. Soc., 402(4): 2429-2435. DOI: 10.1111/j.1365-2966.2009.16006.x.

Cantiello M, Jermyn A S, Lin D N C. 2021. Stellar Evolution in AGN Disks[J/OL]. Astrophys. J., 910(2): 94. DOI: 10.3847/1538-4357/abdf4f.

Cao X. 2011. The Large-scale Magnetic Fields of Advection-dominated Accretion Flows[J/OL]. Astrophys. J., 737(2): 94. DOI: 10.1088/0004-637X/737/2/94.

Cao Z, Aharonian F, Axikegu, et al. 2024. Discovery of Very High Energy Gamma-Ray Emissions from the Low-luminosity AGN NGC 4278 by LHAASO[J/OL]. Astrophys. J. Lett., 971(2): L45. DOI: 10.3847/2041-8213/ad5e6d.

Capote E, Jia W, Aritomi N, et al. 2024. Advanced LIGO detector performance in the fourth observing run[A/OL]. arXiv:2411.14607. arXiv: 2411.14607.

Cappellaro E, Botticella M T, Pignata G, et al. 2015. Supernova rates from the SUDARE VST-OmegaCAM search. I. Rates per unit volume[J/OL]. Astron. Astrophys., 584: A62. DOI: 10.1051/0004-6361/201526712.

Carter B. 1968. Global Structure of the Kerr Family of Gravitational Fields[J/OL]. Physical Review, 174(5): 1559-1571. DOI: 10.1103/PhysRev.174.1559.

Chambers K C, Magnier E A, Metcalfe N, et al. 2016. The Pan-STARRS1 Surveys[A/OL]. arXiv:1612.05560. arXiv: 1612.05560.

Chamel N, Haensel P. 2008. Physics of Neutron Star Crusts[J/OL]. Living Reviews in Relativity, 11(1): 10. DOI: 10.12942/lrr-2008-10.

Chan C H, Piran T, Krolik J H, et al. 2019. Tidal Disruption Events in Active Galactic Nuclei[J/OL]. Astrophys. J., 881(2): 113. DOI: 10.3847/1538-4357/ab2b40.

Chan C H, Piran T, Krolik J H. 2020. Light Curves of Tidal Disruption Events in Active Galactic Nuclei[J/OL]. Astrophys. J., 903(1): 17. DOI: 10.3847/1538-4357/abb776.

Chan C H, Piran T, Krolik J H. 2021. High-energy Emission from Tidal Disruption Events in Active Galactic Nuclei[J/OL]. Astrophys. J., 914(2): 107. DOI: 10.3847/1538-4357/abf0a7.

CHANDRASEKHAR S. 1998. The mathematical theory of black holes: Vol. 69[M]. Oxford university press.

Chen K, Li Z, Inayoshi K, et al. 2025a. Dust Budget Crisis in Little Red Dots[A/OL]. arXiv:2505.22600. arXiv: 2505.22600.

Chen K, Dai Z G. 2024a. Electromagnetic Counterparts Powered by Kicked Remnants of Black Hole Binary Mergers in AGN Disks[J/OL]. Astrophys. J., 961(2): 206. DOI: 10.3847/1538-4357/ad0dfd.

Chen K, Dai Z G. 2025b. Observational Properties of Thermal Emission from Relativistic Jets Embedded in AGN Disks[A/OL]. arXiv:2505.16390. arXiv: 2505.16390.

Chen K, Ren J, Dai Z G. 2023a. The Role of Outflow Feedback on Accretion of Compact Objects in Accretion Disk of Active Galactic Nuclei[J/OL]. Astrophys. J., 948(2): 136. DOI: 10.3847/1538-4357/acc45f.

Chen T W, Brennan S J, Ronchini S, et al. 2024b. LIGO/Virgo/KAGRA S241125n: Kinder optical upper limit in the BAT error region[J]. GRB Coordinates Network, 38314: 1.

Chen Y X, Lin D N C. 2023b. Chaotic gas accretion by black holes embedded in AGN discs as cause of low-spin signatures in gravitational wave events[J/OL]. Mon. Not. R. Astron. Soc., 522(1): 319-329. DOI: 10.1093/mnras/stad992.

Chen Y X, Lin D N C. 2024c. The Population of Massive Stars in Active Galactic Nuclei Disks [J/OL]. Astrophys. J., 967(2): 88. DOI: 10.3847/1538-4357/ad3c3a.

Chen Y X, Bailey A, Stone J, et al. 2022. Prograde and Retrograde Gas Flow around Disk-embedded Companions: Dependence on Eccentricity, Mass, and Disk Properties[J/OL]. Astrophys. J. Lett., 939(2): L23. DOI: 10.3847/2041-8213/ac9b3e.

Chen Y X, Jiang Y F, Goodman J, et al. 2024d. Radiation Hydrodynamic Simulations of Massive Stars in Gas-rich Environments: Accretion of AGN Stars Suppressed by Thermal Feedback [J/OL]. Astrophys. J., 974(1): 106. DOI: 10.3847/1538-4357/ad6dd4.

Chevalier R A. 1989. Neutron Star Accretion in a Supernova[J/OL]. Astrophys. J., 346: 847. DOI: 10.1086/168066.

Chevalier R A. 1996. Neutrino-cooled Accretion: Rotation and Stellar Equation of State[J/OL]. Astrophys. J., 459: 322. DOI: 10.1086/176895.

Chiaberge M, Capetti A, Macchetto F D. 2005. The Hubble Space Telescope View of LINER Nuclei: Evidence for a Dual Population?[J/OL]. Astrophys. J., 625(2): 716-726. DOI: 10.1086/429612.

Christodoulou D. 1970. Reversible and Irreversible Transformations in Black-Hole Physics[J/OL]. Phys. Rev. Lett., 25(22): 1596-1597. DOI: 10.1103/PhysRevLett.25.1596.

Christodoulou D, Ruffini R. 1971. Reversible Transformations of a Charged Black Hole[J/OL]. Phys. Rev. D, 4(12): 3552-3555. DOI: 10.1103/PhysRevD.4.3552.

Clark J A, Bauswein A, Stergioulas N, et al. 2016. Observing gravitational waves from the post-merger phase of binary neutron star coalescence[J/OL]. Classical and Quantum Gravity, 33 (8): 085003. DOI: 10.1088/0264-9381/33/8/085003.

Compère G, Fransen K, Jonas C. 2020. Transition from inspiral to plunge into a highly spinning black hole[J/OL]. Classical and Quantum Gravity, 37(9): 095013. DOI: 10.1088/1361-6382/ab79d3.

Connaughton V, Burns E, Goldstein A, et al. 2016. Fermi GBM Observations of LIGO Gravitational-wave Event GW150914[J/OL]. Astrophys. J. Lett., 826(1): L6. DOI: 10.3847/2041-8205/826/1/L6.

Connaughton V, Burns E, Goldstein A, et al. 2018. On the Interpretation of the Fermi-GBM Transient Observed in Coincidence with LIGO Gravitational-wave Event GW150914[J/OL]. Astrophys. J. Lett., 853(1): L9. DOI: 10.3847/2041-8213/aaa4f2.

Cutler C, Flanagan É E. 1994. Gravitational waves from merging compact binaries: How accurately can one extract the binary's parameters from the inspiral waveform\?[J/OL]. Phys. Rev. D, 49 (6): 2658-2697. DOI: 10.1103/PhysRevD.49.2658.

Dainotti M G, De Simone B, Mohideen Malik R F, et al. 2024. An optical gamma-ray burst catalogue with measured redshift - I. Data release of 535 gamma-ray bursts and colour evolution[J/OL]. Mon. Not. R. Astron. Soc., 533(4): 4023-4043. DOI: 10.1093/mnras/stae1484.

Dainotti M G, Bhardwaj S, Bissaldi E, et al. 2025. Analysis of Gamma-Ray Burst Closure Relationship in Multiple Wavelengths[J/OL]. Astrophys. J., 978(1): 51. DOI: 10.3847/1538-4357/ad93b5.

Daly R A. 2019. Black Hole Spin and Accretion Disk Magnetic Field Strength Estimates for More Than 750 Active Galactic Nuclei and Multiple Galactic Black Holes[J/OL]. Astrophys. J., 886 (1): 37. DOI: 10.3847/1538-4357/ab35e6.

Davidson K, Ostriker J P. 1973. Neutron-Star Accretion in a Stellar Wind: Model for a Pulsed X-Ray Source[J/OL]. Astrophys. J., 179: 585-598. DOI: 10.1086/151897.

de Angelis A, Tatischeff V, Grenier I A, et al. 2018. Science with e-ASTROGAM. A space mission for MeV-GeV gamma-ray astrophysics[J/OL]. Journal of High Energy Astrophysics, 19: 1-106. DOI: 10.1016/j.jheap.2018.07.001.

DeLaunay J, Tohuvavohu A, Ronchini S, et al. 2024a. LIGO/Virgo/KAGRA S241125n: Swift/BAT-GUANO candidate counterpart[J]. GRB Coordinates Network, 38308: 1.

DeLaunay J, Tohuvavohu A, Ronchini S, et al. 2024b. LIGO/Virgo/KAGRA S241125n: Preliminary flux estimate and spectral analysis of the Swift/BAT-GUANO candidate counterpart[J]. GRB Coordinates Network, 38351: 1.

Deng Z L, Li X D, Shao Y, et al. 2024. On the Formation of Double Neutron Stars in the Milky Way: Influence of Key Parameters[J/OL]. Astrophys. J., 963(2): 80. DOI: 10.3847/1538-4357/ad2357.

Derdzinski A, Mayer L. 2022. In-situ extreme mass ratio inspirals via sub-parsec formation and migration of stars in thin, gravitationally unstable AGN discs[A]. arXiv:2205.10382. arXiv: 2205.10382.

Derdzinski A, Mayer L. 2023. In situ extreme mass ratio inspirals via subparsec formation and migration of stars in thin, gravitationally unstable AGN discs[J/OL]. Mon. Not. R. Astron. Soc., 521(3): 4522-4543. DOI: 10.1093/mnras/stad749.

DESI Collaboration, Aghamousa A, Aguilar J, et al. 2016. The DESI Experiment Part I: Science,Targeting, and Survey Design[A/OL]. arXiv:1611.00036. arXiv: 1611.00036.

Di Clemente F, Drago A, Pagliara G. 2022. Is the compact object associated with HESS J1731-347 a strange quark star?[A/OL]. arXiv:2211.07485. arXiv: 2211.07485.

Dittmann A J, Miller M C. 2020. Star formation in accretion discs and SMBH growth[J/OL]. Mon. Not. R. Astron. Soc., 493(3): 3732-3743. DOI: 10.1093/mnras/staa463.

Dittmann A J, Cantiello M, Jermyn A S. 2021. Accretion onto Stars in the Disks of Active Galactic Nuclei[J/OL]. Astrophys. J., 916(1): 48. DOI: 10.3847/1538-4357/ac042c.

Doroshenko V, Suleimanov V, Pühlhofer G, et al. 2022. A strangely light neutron star within a supernova remnant[J/OL]. Nature Astronomy, 6: 1444-1451. DOI: 10.1038/s41550-022-01800-1.

Du P, Wang J M, Hu C, et al. 2014. Outflows from active galactic nuclei: the BLR-NLR metallicity correlation[J/OL]. Mon. Not. R. Astron. Soc., 438(4): 2828-2838. DOI: 10.1093/mnras/stt2386.

Dutta Roy P, Mahapatra P, Samajdar A, et al. 2025. Identifying intermediate mass binary black hole mergers in AGN disks using LISA[A/OL]. arXiv:2503.11721. arXiv: 2503.11721.

Eardley D M, Lightman A P. 1975. Magnetic viscosity in relativistic accretion disks.[J/OL]. Astrophys. J., 200: 187-203. DOI: 10.1086/153777.

East W E, Pretorius F, Stephens B C. 2012. Eccentric black hole-neutron star mergers: Effects of black hole spin and equation of state[J/OL]. Phys. Rev. D, 85(12): 124009. DOI: 10.1103/PhysRevD.85.124009.

Esteban I, Beacom J F, Kopp J. 2025. Detectable MeV Neutrino Signals from Neutron-Star Common-Envelope Systems[J/OL]. Phys. Rev. Lett., 134(18): 181003. DOI: 10.1103/PhysRevLett.134.181003.

Event Horizon Telescope Collaboration, Akiyama K, Alberdi A, et al. 2019. First M87 Event Horizon Telescope Results. I. The Shadow of the Supermassive Black Hole[J/OL]. Astrophys. J. Lett., 875(1): L1. DOI: 10.3847/2041-8213/ab0ec7.

Fabj G, Nasim S S, Caban F, et al. 2020. Aligning nuclear cluster orbits with an active galactic nucleus accretion disc[J/OL]. Mon. Not. R. Astron. Soc., 499(2): 2608-2616. DOI: 10.1093/mnras/staa3004.

Fabj G, Dittmann A J, Cantiello M, et al. 2024. Mapping the Outcomes of Stellar Evolution in the Disks of Active Galactic Nuclei[A/OL]. arXiv:2408.16050. arXiv: 2408.16050.

Falcke H, Rezzolla L. 2014. Fast radio bursts: the last sign of supramassive neutron stars[J/OL]. Astron. Astrophys., 562: A137. DOI: 10.1051/0004-6361/201321996.

Filippenko A V, Ho L C. 2003. A Low-Mass Central Black Hole in the Bulgeless Seyfert 1 Galaxy NGC 4395[J/OL]. Astrophys. J. Lett., 588(1): L13-L16. DOI: 10.1086/375361.

Finkbeiner D P, Schlafly E F, Schlegel D J, et al. 2016. Hypercalibration: A Pan-STARRS1-based Recalibration of the Sloan Digital Sky Survey Photometry[J/OL]. Astrophys. J., 822(2): 66. DOI: 10.3847/0004-637X/822/2/66.

Finn L S, Thorne K S. 2000. Gravitational waves from a compact star in a circular, inspiral orbit, in the equatorial plane of a massive, spinning black hole, as observed by LISA[J/OL]. Phys. Rev. D, 62(12): 124021. DOI: 10.1103/PhysRevD.62.124021.

Fitzpatrick E L, Massa D. 2007. An Analysis of the Shapes of Interstellar Extinction Curves. V. The IR-through-UV Curve Morphology[J/OL]. Astrophys. J., 663(1): 320-341. DOI: 10.1086/518158.

Fleischhack H. 2021. AMEGO-X: MeV gamma-ray Astronomy in the Multi-messenger Era[J/OL]. PoS, ICRC2021: 649. DOI: 10.22323/1.395.0649.

Flewelling H A, Magnier E A, Chambers K C, et al. 2020. The pan-starrs1 database and data products [J/OL]. The Astrophysical Journal Supplement Series, 251(1): 7. https://dx.doi.org/10.3847/1538-4365/abb82d.

Foight D, Slane P, Guver T, et al. 2012. The Relation Between Hydrogen Column Density and Optical Extinction for Supernova Remnants from the Chandra Archive[C]//American Astronomical Society Meeting Abstracts: Vol. 220 American Astronomical Society Meeting Abstracts #220. 523.01.

Fong W F, Nugent A E, Dong Y, et al. 2022. Short GRB Host Galaxies. I. Photometric and Spectroscopic Catalogs, Host Associations, and Galactocentric Offsets[J/OL]. Astrophys. J., 940 (1): 56. DOI: 10.3847/1538-4357/ac91d0.

Fotopoulou S. 2012. Active Galactic Nuclei Luminosity Function and the Lockman Hole Deep Field [D]. Technische Universitaet Muenchen, Germany.

Foucart F, Deaton M B, Duez M D, et al. 2014. Neutron star-black hole mergers with a nuclear equation of state and neutrino cooling: Dependence in the binary parameters[J/OL]. Phys. Rev. D, 90(2): 024026. DOI: 10.1103/PhysRevD.90.024026.

Fryer C L, Huang J, Ali-Dib M, et al. 2025. Stellar population and metal production in AGN discs [J/OL]. Mon. Not. R. Astron. Soc., 537(2): 1556-1570. DOI: 10.1093/mnras/staf130.

Gangardt D, Trani A A, Bonnerot C, et al. 2024. pAGN: the one-stop solution for AGN disc modelling[J/OL]. Mon. Not. R. Astron. Soc., 530(4): 3689-3705. DOI: 10.1093/mnras/stae1117.

Gardner J P, Mather J C, Clampin M, et al. 2006. The James Webb Space Telescope[J/OL]. Space Science Reviews, 123(4): 485-606. DOI: 10.1007/s11214-006-8315-7.

Gayathri V, Healy J, Lange J, et al. 2021. Measuring the Hubble Constant with GW190521 as an Eccentric black hole Merger and Its Potential Electromagnetic Counterpart[J/OL]. Astrophys. J. Lett., 908(2): L34. DOI: 10.3847/2041-8213/abe388.

Generozov A, Stone N C, Metzger B D, et al. 2018. An overabundance of black hole X-ray binaries in the Galactic Centre from tidal captures[J/OL]. Mon. Not. R. Astron. Soc., 478(3): 4030-4051. DOI: 10.1093/mnras/sty1262.

Georgiev I Y, Böker T, Leigh N, et al. 2016. Masses and scaling relations for nuclear star clusters, and their co-existence with central black holes[J/OL]. Mon. Not. R. Astron. Soc., 457(2): 2122-2138. DOI: 10.1093/mnras/stw093.

Ghosh P, Lamb F K. 1979. Accretion by rotating magnetic neutron stars. III. Accretion torques and period changes in pulsating X-ray sources.[J/OL]. Astrophys. J., 234: 296-316. DOI: 10.1086/157498.

Gil J, Mitra D. 2001. Vacuum Gaps in Pulsars and PSR J2144-3933[J/OL]. Astrophys. J., 550(1): 383-391. DOI: 10.1086/319714.

Gilbaum S, Stone N C. 2022. Feedback-dominated Accretion Flows[J/OL]. Astrophys. J., 928(2): 191. DOI: 10.3847/1538-4357/ac4ded.

Gladman B. 1993. Dynamics of Systems of Two Close Planets[J/OL]. Icarus, 106(1): 247-263. DOI: 10.1006/icar.1993.1169.

Gondán L, Kocsis B. 2022. Astrophysical gravitational-wave echoes from galactic nuclei[J/OL]. Mon. Not. R. Astron. Soc., 515(3): 3299-3318. DOI: 10.1093/mnras/stac1985.

Gopal-Krishna, Britzen S, Wiita P. 2019. The diversity of AGN variability: Some highlights and challenges[J]. Bulletin de la Societe Royale des Sciences de Liege, 88: 132-142.

GraceDB. 2024. GraceDB | The Gravitational-Wave Candidate Event Database[EB/OL]. [2024-03-09]. https://gracedb.ligo.org/.

Graham M J, Ford K E S, McKernan B, et al. 2020. Candidate Electromagnetic Counterpart to the Binary Black Hole Merger Gravitational-Wave Event S190521g*[J/OL]. Phys. Rev. Lett., 124 (25): 251102. DOI: 10.1103/PhysRevLett.124.251102.

Graham M J, Djorgovski S G, Stern D, et al. 2015. A possible close supermassive black-hole binary in a quasar with optical periodicity[J/OL]. Nature, 518(7537): 74-76. DOI: 10.1038/nature14143.

Greene J E, Labbe I, Goulding A D, et al. 2024. UNCOVER Spectroscopy Confirms the Surprising Ubiquity of Active Galactic Nuclei in Red Sources at $z > 5$[J/OL]. Astrophys. J., 964(1): 39.

DOI: 10.3847/1538-4357/ad1e5f.

Greiner J, Krühler T, Klose S, et al. 2010. The nature of “dark” gamma-ray bursts[C/OL]//Kawai N, Nagataki S. American Institute of Physics Conference Series: Vol. 1279 Deciphering the Ancient Universe with Gamma-ray Bursts. AIP: 144-151. DOI: 10.1063/1.3509253.

Greiner J, Burgess J M, Savchenko V, et al. 2016. On the Fermi-GBM Event 0.4 s after GW150914 [J/OL]. Astrophys. J. Lett., 827(2): L38. DOI: 10.3847/2041-8205/827/2/L38.

Grishin E, Bobrick A, Hirai R, et al. 2021. Supernova explosions in active galactic nuclear discs [J/OL]. Mon. Not. R. Astron. Soc., 507(1): 156-174. DOI: 10.1093/mnras/stab1957.

Haardt F, Maraschi L. 1993. X-Ray Spectra from Two-Phase Accretion Disks[J/OL]. Astrophys. J., 413: 507. DOI: 10.1086/173020.

Hankla A M, Jiang Y F, Armitage P J. 2020. Local Simulations of Heating Torques on a Luminous Body in an Accretion Disk[J/OL]. Astrophys. J., 902(1): 50. DOI: 10.3847/1538-4357/abb4df.

Harada T, Kimura M. 2011. Collision of two general geodesic particles around a Kerr black hole [J/OL]. Phys. Rev. D, 83(8): 084041. DOI: 10.1103/PhysRevD.83.084041.

Harding A K, Lai D. 2006. Physics of strongly magnetized neutron stars[J/OL]. Reports on Progress in Physics, 69(9): 2631-2708. DOI: 10.1088/0034-4885/69/9/R03.

Haskell B, Priymak M, Patruno A, et al. 2015. Detecting gravitational waves from mountains on neutron stars in the advanced detector era[J/OL]. Mon. Not. R. Astron. Soc., 450(3): 2393-2403. DOI: 10.1093/mnras/stv726.

Hawking S W. 1971. Gravitational Radiation from Colliding Black Holes[J/OL]. Phys. Rev. Lett., 26(21): 1344-1346. DOI: 10.1103/PhysRevLett.26.1344.

Hawking S W. 1972. Black holes in general relativity[J/OL]. Communications in Mathematical Physics, 25(2): 152-166. DOI: 10.1007/BF01877517.

Hawley W P, Athanassiadou T, Timmes F X. 2012. Zero Impact Parameter White Dwarf Collisions in FLASH[J/OL]. Astrophys. J., 759(1): 39. DOI: 10.1088/0004-637X/759/1/39.

Hayden B T, Garnavich P M, Kessler R, et al. 2010. The Rise and Fall of Type Ia Supernova Light Curves in the SDSS-II Supernova Survey[J/OL]. Astrophys. J., 712(1): 350-366. DOI: 10.1088/0004-637X/712/1/350.

Hillebrandt W, Kromer M, Röpke F K, et al. 2013. Towards an understanding of Type Ia supernovae from a synthesis of theory and observations[J/OL]. Frontiers of Physics, 8(2): 116-143. DOI: 10.1007/s11467-013-0303-2.

HOBSON M P, EFSTATHIOU G P, LASENBY A N. 2006. General relativity: an introduction for physicists[M]. Cambridge University Press.

Horiuchi S, Beacom J F, Dwek E. 2009. Diffuse supernova neutrino background is detectable in Super-Kamiokande[J/OL]. Phys. Rev. D, 79(8): 083013. DOI: 10.1103/PhysRevD.79.0830

13.

Horowitz C J, Kadau K. 2009. Breaking Strain of Neutron Star Crust and Gravitational Waves [J/OL]. Phys. Rev. Lett., 102(19): 191102. DOI: 10.1103/PhysRevLett.102.191102.

Horvath J E, Rocha L S, de Sá L M, et al. 2023. A light strange star in the remnant HESS J1731−347: Minimal consistency checks[J/OL]. Astron. Astrophys., 672: L11. DOI: 10.1051/0004-6361/202345885.

Hoyle F, Fowler W A. 1960. Nucleosynthesis in Supernovae.[J/OL]. Astrophys. J., 132: 565. DOI: 10.1086/146963.

Hubeny I, Blaes O, Krolik J H, et al. 2001. Non-LTE Models and Theoretical Spectra of Accretion Disks in Active Galactic Nuclei. IV. Effects of Compton Scattering and Metal Opacities[J/OL]. Astrophys. J., 559(2): 680-702. DOI: 10.1086/322344.

Hutsemékers D, Agís González B, Sluse D, et al. 2017. Polarization of the changing-look quasar J1011+5442[J/OL]. Astron. Astrophys., 604: L3. DOI: 10.1051/0004-6361/201731397.

IceCube Collaboration, Abbasi R, Ackermann M, et al. 2022. Evidence for neutrino emission from the nearby active galaxy NGC 1068[J/OL]. Science, 378(6619): 538-543. DOI: 10.1126/science.abg3395.

Iglesias C A, Rogers F J. 1996. Updated Opal Opacities[J/OL]. Astrophys. J., 464: 943. DOI: 10.1086/177381.

Isbell J W, Meisenheimer K, Pott J U, et al. 2022. The dusty heart of Circinus. I. Imaging the circumnuclear dust in N-band[J/OL]. Astron. Astrophys., 663: A35. DOI: 10.1051/0004-6361/202243271.

Iwamoto K, Kunugise T. 2006. Neutrino Emission from Type Ia Supernovae[C/OL]//Kubono S, Aoki W, Kajino T, et al. American Institute of Physics Conference Series: Vol. 847 Origin of Matter and Evolution of Galaxies. 406-408. DOI: 10.1063/1.2234440.

Jakobsson P, Hjorth J, Fynbo J P U, et al. 2004. Swift Identification of Dark Gamma-Ray Bursts [J/OL]. Astrophys. J. Lett., 617(1): L21-L24. DOI: 10.1086/427089.

Jermyn A S, Dittmann A J, Cantiello M, et al. 2021. Stellar Evolution in the Disks of Active Galactic Nuclei Produces Rapidly Rotating Massive Stars[J/OL]. Astrophys. J., 914(2): 105. DOI: 10.3847/1538-4357/abfb67.

Jermyn A S, Dittmann A J, McKernan B, et al. 2022. Effects of an Immortal Stellar Population in AGN Disks[J/OL]. Astrophys. J., 929(2): 133. DOI: 10.3847/1538-4357/ac5d40.

Jiang J A, Maeda K, Kawabata M, et al. 2021. Discovery of the Fastest Early Optical Emission from Overluminous SN Ia 2020hvf: A Thermonuclear Explosion within a Dense Circumstellar Environment[J/OL]. Astrophys. J. Lett., 923(1): L8. DOI: 10.3847/2041-8213/ac375f.

Jiang S Q, Liu X, Fu S Y, et al. 2024. LIGO/Virgo/KAGRA S241125n: Gaoyazi/GOT optical observations[J]. GRB Coordinates Network, 38328: 1.

Jiang Y F, Guillochon J, Loeb A. 2016. Prompt Radiation and Mass Outflows from the Stream-Stream Collisions of Tidal Disruption Events[J/OL]. Astrophys. J., 830(2): 125. DOI: 10.3847/0004-637X/830/2/125.

Jiao C L, Mineshige S, Takeuchi S, et al. 2015. Comparison between Radiation-Hydrodynamic Simulation of Supercritical Accretion Flows and a Steady Model with Outflows[J/OL]. Astrophys. J., 806(1): 93. DOI: 10.1088/0004-637X/806/1/93.

Kaaz N, Schrøder S L, Andrews J J, et al. 2021. The hydrodynamic evolution of binary black holes embedded within the vertically stratified disks of active galactic nuclei[A/OL]. arXiv:2103.12088. arXiv: 2103.12088.

Kaminker A D, Gnedin O Y, Yakovlev D G, et al. 1992. Neutrino emissivity from e^-e^+ annihilation in a strong magnetic field: Hot, nondegenerate plasma[J/OL]. Phys. Rev. D, 46(10): 4133-4139. DOI: 10.1103/PhysRevD.46.4133.

Kaminker A D, Gnedin O Y, Yakovlev D G, et al. 1994. Neutrino emissivity from e-e annihilation in a strong magnetic field: Non-degenerate plasma[J/OL]. Astronomical and Astrophysical Transactions, 4(4): 283-289. DOI: 10.1080/10556799408205385.

Kathirgamaraju A, Li H, Ryan B R, et al. 2023. Afterglows from binary neutron star post-merger systems embedded in AGN disks[A/OL]. arXiv:2311.03571. arXiv: 2311.03571.

Kato S, Fukue J, Mineshige S. 2008. Black-hole accretion disks[M]. Kyoto University Press, Kyoto, Japan, iSBN.

Katz B, Budnik R, Waxman E. 2010. Fast Radiation Mediated Shocks and Supernova Shock Breakouts[J/OL]. Astrophys. J., 716(1): 781-791. DOI: 10.1088/0004-637X/716/1/781.

Kerr R P. 1963a. Gravitational Field of a Spinning Mass as an Example of Algebraically Special Metrics[J/OL]. Phys. Rev. Lett., 11(5): 237-238. DOI: 10.1103/PhysRevLett.11.237.

Kerr R P. 1963b. Gravitational Field of a Spinning Mass as an Example of Algebraically Special Metrics[J/OL]. Phys. Rev. Lett., 11(5): 237-238. DOI: 10.1103/PhysRevLett.11.237.

Kimura S S, Murase K, Bartos I. 2021. Outflow Bubbles from Compact Binary Mergers Embedded in Active Galactic Nuclei: Cavity Formation and the Impact on Electromagnetic Counterparts [J/OL]. Astrophys. J., 916(2): 111. DOI: 10.3847/1538-4357/ac0535.

King A R, Lasota J P. 1977. Magnetic alignment of rotating black holes and accretion discs.[J]. Astron. Astrophys., 58(1-2): 175-179.

Klingler N J, Oates S R, Tohuvavohu A, et al. 2024. LIGO/Virgo/KAGRA S241125n: Swift-UVOT Upper Limits[J]. GRB Coordinates Network, 38350: 1.

Kocevski D D, Onoue M, Inayoshi K, et al. 2023. Hidden Little Monsters: Spectroscopic Identification of Low-mass, Broad-line AGNs at $z > 5$ with CEERS[J/OL]. Astrophys. J. Lett., 954

(1): L4. DOI: 10.3847/2041-8213/ace5a0.

Kocevski D D, Finkelstein S L, Barro G, et al. 2025. The Rise of Faint, Red Active Galactic Nuclei at $z > 4$: A Sample of Little Red Dots in the JWST Extragalactic Legacy Fields[J/OL]. Astrophys. J., 986(2): 126. DOI: 10.3847/1538-4357/adbc7d.

Kocsis B, Yunes N, Loeb A. 2011. Observable signatures of extreme mass-ratio inspiral black hole binaries embedded in thin accretion disks[J/OL]. Phys. Rev. D, 84(2): 024032. DOI: 10.1103/PhysRevD.84.024032.

Kokubo M, Harikane Y. 2024. Challenging the AGN scenario for JWST/NIRSpec broad Hα emitters/Little Red Dots in light of non-detection of NIRCam photometric variability and X-ray [A/OL]. arXiv:2407.04777. arXiv: 2407.04777.

Konar S, Bhattacharya D. 1997. Magnetic field evolution of accreting neutron stars[J/OL]. Mon. Not. R. Astron. Soc., 284(2): 311-317. DOI: 10.1093/mnras/284.2.311.

Kotake K, Sato K, Takahashi K. 2006. Explosion mechanism, neutrino burst and gravitational wave in core-collapse supernovae[J/OL]. Reports on Progress in Physics, 69(4): 971-1143. DOI: 10.1088/0034-4885/69/4/R03.

Kratter K M, Matzner C D, Krumholz M R. 2008. Global Models for the Evolution of Embedded, Accreting Protostellar Disks[J/OL]. Astrophys. J., 681(1): 375-390. DOI: 10.1086/587543.

Kroupa P. 2001. On the variation of the initial mass function[J/OL]. Mon. Not. R. Astron. Soc., 322 (2): 231-246. DOI: 10.1046/j.1365-8711.2001.04022.x.

Kyutoku K, Ioka K, Okawa H, et al. 2015. Dynamical mass ejection from black hole-neutron star binaries[J/OL]. Phys. Rev. D, 92(4): 044028. DOI: 10.1103/PhysRevD.92.044028.

Labbe I, Greene J E, Bezanson R, et al. 2025. UNCOVER: Candidate Red Active Galactic Nuclei at $3 < z < 7$ with JWST and ALMA[J/OL]. Astrophys. J., 978(1): 92. DOI: 10.3847/1538-4357/ad3551.

Laskos-Patkos P, Koliogiannis P S, Moustakidis C C. 2024. Hybrid stars in light of the HESS J1731-347 remnant and the PREX-II experiment[J/OL]. Phys. Rev. D, 109(6): 063017. DOI: 10.1103/PhysRevD.109.063017.

Latif M A, Aftab A, Whalen D J, et al. 2025. Radio emission from little red dots may reveal their true nature[J/OL]. Astron. Astrophys., 694: L14. DOI: 10.1051/0004-6361/202453194.

Lazzati D, Soares G, Perna R. 2022. Prompt Emission of γ-Ray Bursts in the High-density Environment of Active Galactic Nucleus Accretion Disks[J/OL]. Astrophys. J. Lett., 938(2): L18. DOI: 10.3847/2041-8213/ac98ad.

Lazzati D, Perna R, Gompertz B P, et al. 2023. GRB 191019A: A Short Gamma-Ray Burst in Disguise from the Disk of an Active Galactic Nucleus[J/OL]. Astrophys. J. Lett., 950(2): L20. DOI: 10.3847/2041-8213/acd18c.

Levan A J, Malesani D B, Gompertz B P, et al. 2023. A long-duration gamma-ray burst of dynamical origin from the nucleus of an ancient galaxy[J/OL]. Nature Astronomy, 7: 976-985. DOI: 10.1038/s41550-023-01998-8.

Li G, Bhaskar H G, Kocsis B, et al. 2023a. Secular Spin-Orbit Resonances of Black Hole Binaries in AGN Disks[J/OL]. Astrophys. J., 950(1): 48. DOI: 10.3847/1538-4357/acccf1.

Li G P. 2022. Time-dependent stellar-mass binary black hole mergers in AGN disks: Mass distribution of hierarchical mergers[J/OL]. Phys. Rev. D, 105(6): 063006. DOI: 10.1103/PhysRevD.105.063006.

Li J, Lai D, Rodet L. 2022a. Long-term Evolution of Tightly Packed Stellar Black Holes in AGN Disks: Formation of Merging Black Hole Binaries via Close Encounters[J/OL]. Astrophys. J., 934(2): 154. DOI: 10.3847/1538-4357/ac7c0d.

Li J, Dempsey A M, Li H, et al. 2023b. Hydrodynamical Simulations of Black Hole Binary Formation in AGN Disks[J/OL]. Astrophys. J. Lett., 944(2): L42. DOI: 10.3847/2041-8213/acb934.

Li L, Wang Y, Shao L, et al. 2018. A Large Catalog of Multiwavelength GRB Afterglows. I. Color Evolution and Its Physical Implication[J/OL]. Astrophys. J. Suppl., 234(2): 26. DOI: 10.3847/1538-4365/aaa02a.

Li R, Lai D. 2022b. Hydrodynamical evolution of black-hole binaries embedded in AGN discs [J/OL]. Mon. Not. R. Astron. Soc., 517(2): 1602-1624. DOI: 10.1093/mnras/stac2577.

Li R, Lai D. 2023c. Hydrodynamical evolution of black hole binaries embedded in AGN discs: II. dependence on equation of state, binary mass, and separation scales[J/OL]. Mon. Not. R. Astron. Soc., 522(2): 1881-1894. DOI: 10.1093/mnras/stad1117.

Li R, Lai D. 2024. Hydrodynamical evolution of black-hole binaries embedded in AGN discs - III. The effects of viscosity[J/OL]. Mon. Not. R. Astron. Soc., 529(1): 348-359. DOI: 10.1093/mnras/stae504.

Li R, Ho L C, Ricci C, et al. 2022c. The Host Galaxy and Rapidly Evolving Broad-line Region in the Changing-look Active Galactic Nucleus 1ES 1927+654[J/OL]. Astrophys. J., 933(1): 70. DOI: 10.3847/1538-4357/ac714a.

Li Y P, Dempsey A M, Li S, et al. 2021. Orbital Evolution of Binary Black Holes in Active Galactic Nucleus Disks: A Disk Channel for Binary Black Hole Mergers?[J/OL]. Astrophys. J., 911 (2): 124. DOI: 10.3847/1538-4357/abed48.

Li Y P, Chen Y X, Lin D N C, et al. 2022d. Spin Evolution of Stellar-mass Black Holes Embedded in AGN Disks: Orbital Eccentricity Produces Retrograde Circumstellar Flows[J/OL]. Astrophys. J. Lett., 928(1): L1. DOI: 10.3847/2041-8213/ac5b61.

Li Y P, Dempsey A M, Li H, et al. 2022e. Hot Circumsingle Disks Drive Binary Black Hole Mergers in Active Galactic Nucleus Disks[J/OL]. Astrophys. J. Lett., 928(2): L19. DOI: 10.3847/20

41-8213/ac60fd.

LIGO Scientific Collaboration, VIRGO Collaboration, Kagra Collaboration. 2024. LIGO/Virgo/KAGRA S241125n: Identification of a GW compact binary merger candidate[J]. GRB Coordinates Network, 38305: 1.

Lin D N C, Pringle J E. 1987. A viscosity prescription for a self-gravitating accretion disc[J/OL]. Mon. Not. R. Astron. Soc., 225: 607-613. DOI: 10.1093/mnras/225.3.607.

Linial I, Metzger B D. 2023. EMRI + TDE = QPE: Periodic X-Ray Flares from Star-Disk Collisions in Galactic Nuclei[J/OL]. Astrophys. J., 957(1): 34. DOI: 10.3847/1538-4357/acf65b.

Liska M, Tchekhovskoy A, Quataert E. 2020. Large-scale poloidal magnetic field dynamo leads to powerful jets in GRMHD simulations of black hole accretion with toroidal field[J/OL]. Mon. Not. R. Astron. Soc., 494(3): 3656-3662. DOI: 10.1093/mnras/staa955.

Loeb A. 2016. Electromagnetic Counterparts to Black Hole Mergers Detected by LIGO[J/OL]. Astrophys. J. Lett., 819(2): L21. DOI: 10.3847/2041-8205/819/2/L21.

Lorén-Aguilar P, Isern J, García-Berro E. 2010. Smoothed particle hydrodynamics simulations of white dwarf collisions and close encounters[J/OL]. Mon. Not. R. Astron. Soc., 406(4): 2749-2763. DOI: 10.1111/j.1365-2966.2010.16878.x.

Lucchetta G, Ackermann M, Berge D, et al. 2022. Introducing the MeVCube concept: a CubeSat for MeV observations[J/OL]. J. Cosmol. Astropart. Phys., 2022(8): 013. DOI: 10.1088/1475-7516/2022/08/013.

Luo Y, Wu X J, Zhang S R, et al. 2023. White dwarf-white dwarf collisions in AGN discs via close encounters[J/OL]. Mon. Not. R. Astron. Soc., 524(4): 6015-6023. DOI: 10.1093/mnras/stad2188.

Lyman J D, Levan A J, Tanvir N R, et al. 2017. The host galaxies and explosion sites of long-duration gamma ray bursts: Hubble Space Telescope near-infrared imaging[J/OL]. Mon. Not. R. Astron. Soc., 467(2): 1795-1817. DOI: 10.1093/mnras/stx220.

Lyu Z, Pan Z, Mao J, et al. 2024. Science Opportunities of Wet Extreme Mass-Ratio Inspirals[A/OL]. arXiv:2501.03252. arXiv: 2501.03252.

Ma Z P, Wang K. 2024. High-energy Neutrinos from Outflows Powered by the Kicked Remnants of Binary Black Hole Mergers in Active Galactic Nucleus Accretion Disks[J/OL]. Astrophys. J., 970(2): 127. DOI: 10.3847/1538-4357/ad5678.

Mac Low M M, McCray R. 1988. Superbubbles in Disk Galaxies[J/OL]. Astrophys. J., 324: 776. DOI: 10.1086/165936.

Maiolino R, Mannucci F. 2019. De re metallica: the cosmic chemical evolution of galaxies[J/OL]. Astron. Astrophys. Rev., 27(1): 3. DOI: 10.1007/s00159-018-0112-2.

Maiolino R, Marconi A, Oliva E. 2001. Dust in active nuclei. II. Powder or gravel?[J/OL]. Astron.

Astrophys., 365: 37-48. DOI: 10.1051/0004-6361:20000012.

Mancarella M, Iacovelli F, Foffa S, et al. 2024. Accurate Standard Siren Cosmology with Joint Gravitational-Wave and <inline-formula><mml:math display=“inline”><mml:mi>γ</mml:mi></mml:math></inline-formula>-Ray Burst Observations[J/OL]. Phys. Rev. Lett., 133(26): 261001. DOI: 10.1103/PhysRevLett.133.261001.

Maoz D, Mannucci F, Nelemans G. 2014. Observational Clues to the Progenitors of Type Ia Supernovae[J/OL]. Annu. Rev. Astron. Astrophys., 52: 107-170. DOI: 10.1146/annurev-astro-082812-141031.

Mazzali P A, Nomoto K, Cappellaro E, et al. 2001. Can Differences in the Nickel Abundance in Chandrasekhar-Mass Models Explain the Relation between the Brightness and Decline Rate of Normal Type IA Supernovae?[J/OL]. Astrophys. J., 547(2): 988-994. DOI: 10.1086/318428.

McCracken H J, Milvang-Jensen B, Dunlop J, et al. 2012. UltraVISTA: a new ultra-deep near-infrared survey in COSMOS[J/OL]. Astron. Astrophys., 544: A156. DOI: 10.1051/0004-6361/201219507.

McCutcheon C, Zeng Y, Liu Z W, et al. 2022. Type Ia supernova ejecta-donor interaction: explosion model comparison[J/OL]. Mon. Not. R. Astron. Soc., 514(3): 4078-4086. DOI: 10.1093/mnras/stac1275.

McKernan B, Ford K E S, Lyra W, et al. 2012. Intermediate mass black holes in AGN discs - I. Production and growth[J/OL]. Mon. Not. R. Astron. Soc., 425(1): 460-469. DOI: 10.1111/j.1365-2966.2012.21486.x.

McKernan B, Ford K E S, Kocsis B, et al. 2014. Intermediate-mass black holes in AGN discs - II. Model predictions and observational constraints[J/OL]. Mon. Not. R. Astron. Soc., 441(1): 900-909. DOI: 10.1093/mnras/stu553.

McKernan B, Ford K E S, O’Shaughnessy R. 2020. Black hole, neutron star, and white dwarf merger rates in AGN discs[J/OL]. Mon. Not. R. Astron. Soc., 498(3): 4088-4094. DOI: 10.1093/mnras/staa2681.

McKernan B, Ford K E S, Cantiello M, et al. 2022. Starfall: a heavy rain of stars in ’turning on’ AGN[J/OL]. Mon. Not. R. Astron. Soc., 514(3): 4102-4110. DOI: 10.1093/mnras/stac1310.

Meegan C, Lichti G, Bhat P N, et al. 2009. The Fermi Gamma-ray Burst Monitor[J/OL]. Astrophys. J., 702(1): 791-804. DOI: 10.1088/0004-637X/702/1/791.

Meiron Y, Kocsis B, Loeb A. 2017. Detecting Triple Systems with Gravitational Wave Observations [J/OL]. Astrophys. J., 834(2): 200. DOI: 10.3847/1538-4357/834/2/200.

Meisel Z, Deibel A, Keek L, et al. 2018. Nuclear physics of the outer layers of accreting neutron stars[J/OL]. Journal of Physics G Nuclear Physics, 45(9): 093001. DOI: 10.1088/1361-6471/aad171.

Melatos A, Payne D J B. 2005. Gravitational Radiation from an Accreting Millisecond Pulsar with a Magnetically Confined Mountain[J/OL]. Astrophys. J., 623(2): 1044-1050. DOI: 10.1086/428600.

Miniutti G, Giustini M, Arcodia R, et al. 2023. Repeating tidal disruptions in GSN 069: Long-term evolution and constraints on quasi-periodic eruptions' models[J/OL]. Astron. Astrophys., 670: A93. DOI: 10.1051/0004-6361/202244512.

Misiaszek M, Odrzywołek A, Kutschera M. 2006. Neutrino spectrum from the pair-annihilation process in the hot stellar plasma[J/OL]. Phys. Rev. D, 74(4): 043006. DOI: 10.1103/PhysRevD.74.043006.

MISNER C W, THORNE K S, WHEELER J A. 1973. Gravitation[M]. San Francisco: W. H. Freeman.

Mohan T, Waratkar G, Saikia A P, et al. 2024. LIGO/VIRGO/KAGRA S241125n: GROWTH-India telescope optical observations[J]. GRB Coordinates Network, 38325: 1.

Mohapatra R N, Pal P B. 2004. Massive Neutrinos in Physics and Astrophysics (Third Edition) [M/OL]. World scientific. DOI: 10.1142/5024.

Moiseev A A, Ajello M, Buckley J H, et al. 2015. Compton-Pair Production Space Telescope (ComPair) for MeV Gamma-ray Astronomy[A]. arXiv:1508.07349. arXiv: 1508.07349.

Moore C J, Cole R H, Berry C P L. 2015. Gravitational-wave sensitivity curves[J/OL]. Classical and Quantum Gravity, 32(1): 015014. DOI: 10.1088/0264-9381/32/1/015014.

Morrison R, McCammon D. 1983. Interstellar photoelectric absorption cross sections, 0.03-10 keV. [J/OL]. Astrophys. J., 270: 119-122. DOI: 10.1086/161102.

Mukherjee S, Ghosh A, Graham M J, et al. 2020. First measurement of the Hubble parameter from bright binary black hole GW190521[A/OL]. arXiv:2009.14199. arXiv: 2009.14199.

Müller B, Heger A, Powell J. 2025. Minimum Neutron Star Mass in Neutrino-Driven Supernova Explosions[J/OL]. Phys. Rev. Lett., 134(7): 071403. DOI: 10.1103/PhysRevLett.134.071403.

Mummery A, Balbus S. 2022. Inspirals from the Innermost Stable Circular Orbit of Kerr Black Holes: Exact Solutions and Universal Radial Flow[J/OL]. Phys. Rev. Lett., 129(16): 161101. DOI: 10.1103/PhysRevLett.129.161101.

Murase K. 2022. Hidden Hearts of Neutrino Active Galaxies[J/OL]. Astrophys. J. Lett., 941(1): L17. DOI: 10.3847/2041-8213/aca53c.

Murase K, Kimura S S, Mészáros P. 2020. Hidden Cores of Active Galactic Nuclei as the Origin of Medium-Energy Neutrinos: Critical Tests with the MeV Gamma-Ray Connection[J/OL]. Phys. Rev. Lett., 125(1): 011101. DOI: 10.1103/PhysRevLett.125.011101.

Mushtukov A A, Tsygankov S S, Suleimanov V F, et al. 2018. Ultraluminous X-ray sources as neutrino pulsars[J/OL]. Mon. Not. R. Astron. Soc., 476(3): 2867-2873. DOI: 10.1093/mnras/

sty379.

Mushtukov A A, Ognev I S, Nagirner D I. 2019. Electron-positron pairs in hot plasma of accretion column in bright X-ray pulsars[J/OL]. Mon. Not. R. Astron. Soc., 485(1): L131-L135. DOI: 10.1093/mnrasl/slz047.

Nagao T, Maiolino R, Marconi A. 2006. Gas metallicity in the narrow-line regions of high-redshift active galactic nuclei[J/OL]. Astron. Astrophys., 447(3): 863-876. DOI: 10.1051/0004-6361:20054127.

Nakar E, Sari R. 2010. Early Supernovae Light Curves Following the Shock Breakout[J/OL]. Astrophys. J., 725(1): 904-921. DOI: 10.1088/0004-637X/725/1/904.

Nakar E, Sari R. 2012. Relativistic Shock Breakouts—A Variety of Gamma-Ray Flares: From Low-luminosity Gamma-Ray Bursts to Type Ia Supernovae[J/OL]. Astrophys. J., 747(2): 88. DOI: 10.1088/0004-637X/747/2/88.

Nasim S S, Fabj G, Caban F, et al. 2023. Aligning Retrograde Nuclear Cluster Orbits with an Active Galactic Nucleus Accretion Disc[J/OL]. Mon. Not. R. Astron. Soc., 522(4): 5393-5401. DOI: 10.1093/mnras/stad1295.

Netzer H. 2013. The physics and evolution of active galactic nuclei[M]. Cambridge university press.

Neumayer N, Seth A, Böker T. 2020. Nuclear star clusters[J/OL]. The Astronomy and Astrophysics Review, 28(1): 4. DOI: 10.1007/s00159-020-00125-0.

Newman E T, Couch E, Chinnapared K, et al. 1965. Metric of a Rotating, Charged Mass[J/OL]. Journal of Mathematical Physics, 6(6): 918-919. DOI: 10.1063/1.1704351.

Nordström G. 1918. On the Energy of the Gravitation field in Einstein's Theory[J]. Koninklijke Nederlandse Akademie van Wetenschappen Proceedings Series B Physical Sciences, 20: 1238-1245.

Ori A, Thorne K S. 2000. Transition from inspiral to plunge for a compact body in a circular equatorial orbit around a massive, spinning black hole[J/OL]. Phys. Rev. D, 62(12): 124022. DOI: 10.1103/PhysRevD.62.124022.

Orlando E, Bottacini E, Moiseev A A, et al. 2022. Exploring the MeV sky with a combined coded mask and Compton telescope: the Galactic Explorer with a Coded aperture mask Compton telescope (GECCO)[J/OL]. J. Cosmol. Astropart. Phys., 2022(7): 036. DOI: 10.1088/1475-7516/2022/07/036.

Ostriker E C. 1999. Dynamical Friction in a Gaseous Medium[J/OL]. Astrophys. J., 513(1): 252-258. DOI: 10.1086/306858.

Paczynski B. 1978. A model of selfgravitating accretion disk.[J]. Acta Astronomica, 28: 91-109.

Page K L, Evans P A, Kennea J A, et al. 2024. LIGO/Virgo S241125n: Swift XRT observations, 5 X-ray sources[J]. GRB Coordinates Network, 38324: 1.

Pan Z, Yang H. 2021a. Supercritical Accretion of Stellar-mass Compact Objects in Active Galactic Nuclei[J/OL]. Astrophys. J., 923(2): 173. DOI: 10.3847/1538-4357/ac249c.

Pan Z, Yang H. 2021b. Formation rate of extreme mass ratio inspirals in active galactic nuclei[J/OL]. Phys. Rev. D, 103(10): 103018. DOI: 10.1103/PhysRevD.103.103018.

Pan Z, Lyu Z, Yang H. 2022. Mass-gap extreme mass ratio inspirals[J/OL]. Phys. Rev. D, 105(8): 083005. DOI: 10.1103/PhysRevD.105.083005.

Papaloizou J, Pringle J E. 1978. Gravitational radiation and the stability of rotating stars.[J/OL]. Mon. Not. R. Astron. Soc., 184: 501-508. DOI: 10.1093/mnras/184.3.501.

Papenfort L J, Gold R, Rezzolla L. 2018. Dynamical ejecta and nucleosynthetic yields from eccentric binary neutron-star mergers[J/OL]. Phys. Rev. D, 98(10): 104028. DOI: 10.1103/PhysRevD.98.104028.

Parfrey K, Spitkovsky A, Beloborodov A M. 2016. Torque Enhancement, Spin Equilibrium, and Jet Power from Disk-Induced Opening of Pulsar Magnetic Fields[J/OL]. Astrophys. J., 822(1): 33. DOI: 10.3847/0004-637X/822/1/33.

Passy J C, Mac Low M M, De Marco O. 2012. On the Survival of Brown Dwarfs and Planets Engulfed by Their Giant Host Star[J/OL]. Astrophys. J. Lett., 759(2): L30. DOI: 10.1088/2041-8205/759/2/L30.

Pelassa V, Preece R, Piron F, et al. 2010. The LAT Low-Energy technique for Fermi Gamma-Ray Bursts spectral analysis[A/OL]. arXiv:1002.2617. arXiv: 1002.2617.

Peng P, Chen X. 2021. The last migration trap of compact objects in AGN accretion disc[J/OL]. Mon. Not. R. Astron. Soc., 505(1): 1324-1333. DOI: 10.1093/mnras/stab1419.

Peng P, Chen X. 2023. Synchronizing the EMRIs and IMRIs in AGN Accretion Disks[J/OL]. Astrophys. J., 950(1): 3. DOI: 10.3847/1538-4357/acce3b.

Penrose R, Floyd R M. 1971. Extraction of Rotational Energy from a Black Hole[J/OL]. Nature Physical Science, 229(6): 177-179. DOI: 10.1038/physci229177a0.

Pereira R, Thomas R C, Aldering G, et al. 2013. Spectrophotometric time series of SN 2011fe from the Nearby Supernova Factory[J/OL]. Astron. Astrophys., 554: A27. DOI: 10.1051/0004-6361/201221008.

Perley D A, Cenko S B, Bloom J S, et al. 2009. The Host Galaxies of Swift Dark Gamma-ray Bursts: Observational Constraints on Highly Obscured and Very High Redshift GRBs[J/OL]. Astron. J., 138(6): 1690-1708. DOI: 10.1088/0004-6256/138/6/1690.

Perlmutter S, Aldering G, Goldhaber G, et al. 1999. Measurements of Ω and Λ from 42 High-Redshift Supernovae[J/OL]. Astrophys. J., 517(2): 565-586. DOI: 10.1086/307221.

Perna R, Lazzati D, Cantiello M. 2021a. Electromagnetic Signatures of Relativistic Explosions in the Disks of Active Galactic Nuclei[J/OL]. Astrophys. J. Lett., 906(2): L7. DOI: 10.3847/20

41-8213/abd319.

Perna R, Tagawa H, Haiman Z, et al. 2021b. Accretion-Induced Collapse of Neutron Stars in the Disks of Active Galactic Nuclei[J/OL]. Astrophys. J., 915(1): 10. DOI: 10.3847/1538-4357/abfdb4.

Peters P C. 1964a. Gravitational Radiation and the Motion of Two Point Masses[J/OL]. Physical Review, 136: 1224-1232. DOI: 10.1103/PhysRev.136.B1224.

Peters P C. 1964b. Gravitational Radiation and the Motion of Two Point Masses[J/OL]. Physical Review, 136(4B): 1224-1232. DOI: 10.1103/PhysRev.136.B1224.

Peters P C, Mathews J. 1963. Gravitational Radiation from Point Masses in a Keplerian Orbit[J/OL]. Physical Review, 131: 435-440. DOI: 10.1103/PhysRev.131.435.

Pétri J. 2015. Multipolar electromagnetic fields around neutron stars: exact vacuum solutions and related properties[J/OL]. Mon. Not. R. Astron. Soc., 450(1): 714-742. DOI: 10.1093/mnras/stv598.

Piran T, Shaham J, Katz J. 1975. High Efficiency of the Penrose Mechanism for Particle Collisions [J/OL]. Astrophys. J. Lett., 196: L107. DOI: 10.1086/181755.

Piro A L, Morozova V S. 2016. Exploring the Potential Diversity of Early Type Ia Supernova Light Curves[J/OL]. Astrophys. J., 826(1): 96. DOI: 10.3847/0004-637X/826/1/96.

POLLOCK M. 1976. The interaction between a weak magnetic field and a slowly rotating black hole[J]. Proceedings of the Royal Society of London. A. Mathematical and Physical Sciences, 350(1661): 239-252.

Prasad C, Wang Y, Perna R, et al. 2024. Tidal disruption events from three-body scatterings and eccentricity pumping in the discs of active galactic nuclei[J/OL]. Mon. Not. R. Astron. Soc., 531(1): 1409-1421. DOI: 10.1093/mnras/stae1263.

Predehl P, Schmitt J H M M. 1995. X-raying the interstellar medium: ROSAT observations of dust scattering halos.[J]. Astron. Astrophys., 293: 889-905.

PSNS. 2001. PSNS - Pre Supernova Neutrino Spectrum homepage[EB/OL]. [2023-11-01]. http://th.if.uj.edu.pl/~odrzywolek/psns/index.html.

Radice D, Galeazzi F, Lippuner J, et al. 2016. Dynamical mass ejection from binary neutron star mergers[J/OL]. Mon. Not. R. Astron. Soc., 460(3): 3255-3271. DOI: 10.1093/mnras/stw1227.

Raskin C, Timmes F X, Scannapieco E, et al. 2009. On Type Ia supernovae from the collisions of two white dwarfs[J/OL]. Mon. Not. R. Astron. Soc., 399(1): L156-L159. DOI: 10.1111/j.1745-3933.2009.00743.x.

Rastinejad J C, Shrestha M, Hosseinzadeh G, et al. 2024. LIGO/Virgo/KAGRA S241125n: SAGUARO follow-up observations with the MMT[J]. GRB Coordinates Network, 38333: 1.

Ray M, Lazzati D, Perna R. 2023. The effects of time-variable absorption due to gamma-ray bursts in active galactic nucleus accretion discs[J/OL]. Mon. Not. R. Astron. Soc., 521(3): 4233-4245. DOI: 10.1093/mnras/stad816.

Raynaud R, Guilet J, Janka H T, et al. 2020. Magnetar formation through a convective dynamo in protoneutron stars[J/OL]. Science Advances, 6(11): eaay2732. DOI: 10.1126/sciadv.aay2732.

REES M, RUFFINI R, WHEELER J A. 1974. Black holes, gravitational waves, and cosmology: an introduction to current research[J]. Topics in Astrophysics and Space Physics.

Rein H, Liu S F. 2012. REBOUND: an open-source multi-purpose N-body code for collisional dynamics[J/OL]. Astron. Astrophys., 537: A128. DOI: 10.1051/0004-6361/201118085.

Rein H, Spiegel D S. 2015. IAS15: a fast, adaptive, high-order integrator for gravitational dynamics, accurate to machine precision over a billion orbits[J/OL]. Mon. Not. R. Astron. Soc., 446(2): 1424-1437. DOI: 10.1093/mnras/stu2164.

Reissner H. 1916. Über die Eigengravitation des elektrischen Feldes nach der Einsteinschen Theorie [J/OL]. Annalen der Physik, 355(9): 106-120. DOI: 10.1002/andp.19163550905.

Ricci C, Kara E, Loewenstein M, et al. 2020. The Destruction and Recreation of the X-Ray Corona in a Changing-look Active Galactic Nucleus[J/OL]. Astrophys. J. Lett., 898(1): L1. DOI: 10.3847/2041-8213/ab91a1.

Ricci C, Trakhtenbrot B. 2023. Changing-look active galactic nuclei[J/OL]. Nature Astronomy, 7: 1282-1294. DOI: 10.1038/s41550-023-02108-4.

Richards G T, Hall P B, Vanden Berk D E, et al. 2003. Red and Reddened Quasars in the Sloan Digital Sky Survey[J/OL]. Astron. J., 126(3): 1131-1147. DOI: 10.1086/377014.

Ridnaia A, Frederiks D, Lysenko A, et al. 2024. LIGO/Virgo/KAGRA S241125n: Upper limits from Konus-Wind observations[J]. GRB Coordinates Network, 38321: 1.

Riess A G, Filippenko A V, Challis P, et al. 1998. Observational Evidence from Supernovae for an Accelerating Universe and a Cosmological Constant[J/OL]. Astron. J., 116(3): 1009-1038. DOI: 10.1086/300499.

Risaliti G, Maiolino R, Salvati M. 1999. The Distribution of Absorbing Column Densities among Seyfert 2 Galaxies[J/OL]. Astrophys. J., 522(1): 157-164. DOI: 10.1086/307623.

Roberts W J. 1979. Electromagnetic multipole fields of neutron stars.[J/OL]. Astrophys. J. Suppl., 41: 75-86. DOI: 10.1086/190608.

Rodriguez J F, Rueda J A, Ruffini R. 2018. On the Final Gravitational Wave Burst from Binary Black Holes Mergers[J/OL]. Astronomy Reports, 62(12): 940-952. DOI: 10.1134/S1063772918120338.

Rodríguez J F, Rueda J A, Ruffini R. 2018. Comparison and contrast of test-particle and numerical-relativity waveform templates[J/OL]. J. Cosmol. Astropart. Phys., 2018(2): 030. DOI: 10.1

088/1475-7516/2018/02/030.

Romero-Shaw I, Lasky P D, Thrane E, et al. 2020. GW190521: Orbital Eccentricity and Signatures of Dynamical Formation in a Binary Black Hole Merger Signal[J/OL]. Astrophys. J. Lett., 903(1): L5. DOI: 10.3847/2041-8213/abbe26.

Rosswog S, Kasen D, Guillochon J, et al. 2009. Collisions of White Dwarfs as a New Progenitor Channel for Type Ia Supernovae[J/OL]. Astrophys. J. Lett., 705(2): L128-L132. DOI: 10.1088/0004-637X/705/2/L128.

Rowan C, Boekholt T, Kocsis B, et al. 2022. Black Hole Binary Formation in AGN Discs: From Isolation to Merger[A/OL]. arXiv:2212.06133. arXiv: 2212.06133.

Rowan C, Whitehead H, Kocsis B. 2024. Black Hole Merger Rates in AGN: contribution from gas-captured binaries[A/OL]. arXiv:2412.12086. arXiv: 2412.12086.

Rowan C, Whitehead H, Fabj G, et al. 2025. Prompt gravitational-wave mergers aided by gas in Active Galactic Nuclei: The hydrodynamics of binary-single black hole scatterings[A/OL]. arXiv:2501.09017. arXiv: 2501.09017.

Rueda J A, Ruffini R, Wang Y, et al. 2018. GRB 170817A-GW170817-AT 2017gfo and the observations of NS-NS, NS-WD and WD-WD mergers[J/OL]. J. Cosmol. Astropart. Phys., 2018 (10): 006. DOI: 10.1088/1475-7516/2018/10/006.

Rueda J A, Ruffini R, Kerr R P. 2022. Gravitomagnetic Interaction of a Kerr Black Hole with a Magnetic Field as the Source of the Jetted GeV Radiation of Gamma-Ray Bursts[J/OL]. Astrophys. J., 929(1): 56. DOI: 10.3847/1538-4357/ac5b6e.

RUEDA J, RUFFINI R. 2023. Extracting the energy and angular momentum of a kerr black hole [A].

Ruffini R, Wheeler J A. 1971a. Relativistic cosmology and space platforms.[J]. ESRO, 52: 45-174.

Ruffini R, Wilson J R. 1975. Relativistic magnetohydrodynamical effects of plasma accreting into a black hole[J/OL]. Phys. Rev. D, 12(10): 2959-2962. DOI: 10.1103/PhysRevD.12.2959.

Ruffini R, Muccino M, Aimuratov Y, et al. 2016. GRB 090510: A Genuine Short GRB from a Binary Neutron Star Coalescing into a Kerr-Newman Black Hole[J/OL]. Astrophys. J., 831 (2): 178. DOI: 10.3847/0004-637X/831/2/178.

Ruffini R, Moradi R, Rueda J A, et al. 2019. On the GeV Emission of the Type I BdHN GRB 130427A[J/OL]. Astrophys. J., 886(2): 82. DOI: 10.3847/1538-4357/ab4ce6.

Ruffini R, Wheeler J A. 1971b. Introducing the black hole[J/OL]. Physics Today, 24(1): 30. DOI: 10.1063/1.3022513.

Ruffini R, Prakapenia M, Quevedo H, et al. 2025. Single versus the Repetitive Penrose Process in a Kerr Black Hole[J/OL]. Phys. Rev. Lett., 134(8): 081403. DOI: 10.1103/PhysRevLett.134.081403.

Rybicki G B, Lightman A P. 1991. Radiative processes in astrophysics[M]. John Wiley & Sons.

Ryu T, McKernan B, Ford K E S, et al. 2024. In-plane tidal disruption of stars in discs of active galactic nuclei[J/OL]. Mon. Not. R. Astron. Soc., 527(3): 8103-8117. DOI: 10.1093/mnras/stad3487.

Sagun V, Giangrandi E, Dietrich T, et al. 2023. What Is the Nature of the HESS J1731-347 Compact Object?[J/OL]. Astrophys. J., 958(1): 49. DOI: 10.3847/1538-4357/acfc9e.

Saio H, Nomoto K. 1985. Evolution of a merging pair of C + O white dwarfs to form a single neutron star[J]. Astron. Astrophys., 150(1): L21-L23.

Samsing J, Bartos I, D'Orazio D J, et al. 2022. AGN as potential factories for eccentric black hole mergers[J/OL]. Nature, 603(7900): 237-240. DOI: 10.1038/s41586-021-04333-1.

Santini A, Gerosa D, Cotesta R, et al. 2023. Black-hole mergers in disklike environments could explain the observed q -χ_{eff} correlation[J/OL]. Phys. Rev. D, 108(8): 083033. DOI: 10.1103/PhysRevD.108.083033.

Sasaki M, Nakamura T. 1982a. Gravitational Radiation from a Kerr Black Hole. I —Formulation and a Method for Numerical Analysis—[J/OL]. Progress of Theoretical Physics, 67: 1788-1809. DOI: 10.1143/PTP.67.1788.

Sasaki M, Nakamura T. 1982b. A class of new perturbation equations for the Kerr geometry[J/OL]. Physics Letters A, 89: 68-70. DOI: 10.1016/0375-9601(82)90507-2.

Savchenko V, Ferrigno C, Rodi J, et al. 2024. LIGO/Virgo/KAGRA S241125n: No counterpart candidates in INTEGRAL SPI-ACS prompt observation, comparisong with Swift/BAT counterpart[J]. GRB Coordinates Network, 38311: 1.

Schady P, Page M J, Oates S R, et al. 2010. Dust and metal column densities in gamma-ray burst host galaxies[J/OL]. Mon. Not. R. Astron. Soc., 401(4): 2773-2792. DOI: 10.1111/j.1365-2966.2009.15861.x.

Schechter P. 1976. An analytic expression for the luminosity function for galaxies.[J/OL]. Astrophys. J., 203: 297-306. DOI: 10.1086/154079.

Schlafly E F, Finkbeiner D P. 2011. Measuring Reddening with Sloan Digital Sky Survey Stellar Spectra and Recalibrating SFD[J/OL]. Astrophys. J., 737(2): 103. DOI: 10.1088/0004-637X/737/2/103.

Schmidt B P, Suntzeff N B, Phillips M M, et al. 1998. The High-Z Supernova Search: Measuring Cosmic Deceleration and Global Curvature of the Universe Using Type IA Supernovae[J/OL]. Astrophys. J., 507(1): 46-63. DOI: 10.1086/306308.

Schmidt M. 1963. 3C 273 : A Star-Like Object with Large Red-Shift[J/OL]. Nature, 197(4872): 1040. DOI: 10.1038/1971040a0.

Scholberg K. 2015. Supernova neutrino detection[C/OL]//American Institute of Physics Conference

Series: Vol. 1666 XXVI International Conference on Neutrino Physics and AstroPhysics: Neutrino 2014. 070002. DOI: 10.1063/1.4915561.

Schwarzschild K. 1916. On the Gravitational Field of a Mass Point According to Einstein's Theory [J]. Abh. Konigl. Preuss. Akad. Wissenschaften Jahre 1906,92, Berlin,1907, 1916: 189-196.

Scott N, Graham A W. 2013. Updated Mass Scaling Relations for Nuclear Star Clusters and a Comparison to Supermassive Black Holes[J/OL]. Astrophys. J., 763(2): 76. DOI: 10.1088/0004-637X/763/2/76.

Scotton L, Fermi-GBM Team. 2024. LIGO/Virgo/KAGRA S241125n: Upper limits from Fermi-GBM Observations[J]. GRB Coordinates Network, 38316: 1.

Shakura N I, Sunyaev R A. 1973. Black holes in binary systems. Observational appearance.[J]. Astron. Astrophys., 24: 337-355.

Shang Z, Brotherton M S, Wills B J, et al. 2011. The Next Generation Atlas of Quasar Spectral Energy Distributions from Radio to X-Rays[J/OL]. Astrophys. J. Suppl., 196(1): 2. DOI: 10.1088/0067-0049/196/1/2.

Shankar F, Weinberg D H, Miralda-Escudé J. 2009. Self-Consistent Models of the AGN and Black Hole Populations: Duty Cycles, Accretion Rates, and the Mean Radiative Efficiency[J/OL]. Astrophys. J., 690(1): 20-41. DOI: 10.1088/0004-637X/690/1/20.

Shapiro S L, Teukolsky S A. 2008. Black holes, white dwarfs, and neutron stars: The physics of compact objects[M]. John Wiley & Sons.

Sheng Z, Wang T, Jiang N, et al. 2017. Mid-infrared Variability of Changing-look AGNs[J/OL]. Astrophys. J. Lett., 846(1): L7. DOI: 10.3847/2041-8213/aa85de.

Shin J, Woo J H, Nagao T, et al. 2013. The Chemical Properties of Low-redshift QSOs[J/OL]. Astrophys. J., 763(1): 58. DOI: 10.1088/0004-637X/763/1/58.

Shy D, Kierans C, Cannady N, et al. 2022. Development of the ComPair gamma-ray telescope prototype[C/OL]//den Herder J W A, Nikzad S, Nakazawa K. Society of Photo-Optical Instrumentation Engineers (SPIE) Conference Series: Vol. 12181 Society of Photo-Optical Instrumentation Engineers (SPIE) Conference Series. 121812G. DOI: 10.1117/12.2628811.

Silant'ev N A, Piotrovich M Y, Gnedin Y N, et al. 2009. Magnetic fields of AGNs and standard accretion disk model: testing by optical polarimetry[J/OL]. Astron. Astrophys., 507(1): 171-182. DOI: 10.1051/0004-6361/200810892.

Sirko E, Goodman J. 2003. Spectral energy distributions of marginally self-gravitating quasi-stellar object discs[J/OL]. Mon. Not. R. Astron. Soc., 341(2): 501-508. DOI: 10.1046/j.1365-8711.2003.06431.x.

Skrutskie M F, Cutri R M, Stiening R, et al. 2006. The Two Micron All Sky Survey (2MASS)[J/OL]. Astron. J., 131(2): 1163-1183. DOI: 10.1086/498708.

Song J R, Shu X W, Sun L M, et al. 2020. Possible ~0.4 h X-ray quasi-periodicity from an ultrasoft active galactic nucleus[J/OL]. Astron. Astrophys., 644: L9. DOI: 10.1051/0004-6361/2020 39410.

Sunyaev R A, Titarchuk L G. 1980. Comptonization of X-Rays in Plasma Clouds - Typical Radiation Spectra[J]. Astron. Astrophys., 86: 121.

Swain V, Teja R S, Mohan T, et al. 2024. LIGO/Virgo/KAGRA S241125n: HCT upper limit[J]. GRB Coordinates Network, 38322: 1.

Taam R E. 1980. The long-term evolution of accreting carbon white dwarfs[J/OL]. Astrophys. J., 242: 749-755. DOI: 10.1086/158509.

Tagawa H, Haiman Z, Kocsis B. 2020. Formation and Evolution of Compact-object Binaries in AGN Disks[J/OL]. Astrophys. J., 898(1): 25. DOI: 10.3847/1538-4357/ab9b8c.

Tagawa H, Kocsis B, Haiman Z, et al. 2021. Mass-gap Mergers in Active Galactic Nuclei[J/OL]. Astrophys. J., 908(2): 194. DOI: 10.3847/1538-4357/abd555.

Tagawa H, Kimura S S, Haiman Z, et al. 2022. Can Stellar-mass Black Hole Growth Disrupt Disks of Active Galactic Nuclei? The Role of Mechanical Feedback[J/OL]. Astrophys. J., 927(1): 41. DOI: 10.3847/1538-4357/ac45f8.

Tagawa H, Kimura S S, Haiman Z. 2023a. High-energy Electromagnetic, Neutrino, and Cosmic-Ray Emission by Stellar-mass Black Holes in Disks of Active Galactic Nuclei[J/OL]. Astrophys. J., 955(1): 23. DOI: 10.3847/1538-4357/ace71d.

Tagawa H, Kimura S S, Haiman Z, et al. 2023b. Observable Signature of Merging Stellar-mass Black Holes in Active Galactic Nuclei[J/OL]. Astrophys. J., 950(1): 13. DOI: 10.3847/1538 -4357/acc4bb.

Tagawa H, Kimura S S, Haiman Z, et al. 2023c. Observable Signatures of Stellar-mass Black Holes in Active Galactic Nuclei[J/OL]. Astrophys. J. Lett., 946(1): L3. DOI: 10.3847/2041-8213/ acc103.

Takeo E, Inayoshi K, Mineshige S. 2020. Hyper-Eddington accretion flows on to black holes accompanied by powerful outflows[J/OL]. Mon. Not. R. Astron. Soc., 497(1): 302-317. DOI: 10.1093/mnras/staa1906.

Tee W L, Fan X, Wang F, et al. 2025. Lack of Rest-frame Ultraviolet Variability in Little Red Dots Based on HST and JWST Observations[J/OL]. Astrophys. J. Lett., 983(1): L26. DOI: 10.3847/2041-8213/adc5e3.

Teukolsky S A. 1972. Rotating Black Holes: Separable Wave Equations for Gravitational and Electromagnetic Perturbations[J/OL]. Physical Review Letters, 29: 1114-1118. DOI: 10.1103/Ph ysRevLett.29.1114.

Teukolsky S A. 1973. Perturbations of a Rotating Black Hole. I. Fundamental Equations for Gravitational, Electromagnetic, and Neutrino-Field Perturbations[J/OL]. Astrophys. J., 185: 635-648. DOI: 10.1086/152444.

Teukolsky S A, Press W H. 1974. Perturbations of a rotating black hole. III. Interaction of the hole with gravitational and electromagnetic radiation.[J/OL]. Astrophys. J., 193: 443-461. DOI: 10.1086/153180.

Thompson T A, Quataert E, Murray N. 2005. Radiation Pressure-supported Starburst Disks and Active Galactic Nucleus Fueling[J/OL]. Astrophys. J., 630(1): 167-185. DOI: 10.1086/431923.

THORNE J, ROBOTHAM A, DAVIES L, et al. 2022. Agn unification diagram[M/OL]. Zenodo. https://doi.org/10.5281/zenodo.6381013.

Thorne K S. 1974. Disk-Accretion onto a Black Hole. II. Evolution of the Hole[J/OL]. Astrophys. J., 191: 507-520. DOI: 10.1086/152991.

Tohuvavohu A, Kennea J A, DeLaunay J, et al. 2020. Gamma-Ray Urgent Archiver for Novel Opportunities (GUANO): Swift/BAT Event Data Dumps on Demand to Enable Sensitive Subthreshold GRB Searches[J/OL]. Astrophys. J., 900(1): 35. DOI: 10.3847/1538-4357/aba94f.

Tolman R C. 1930. On the Estimation of Distances in a Curved Universe with a Non-Static Line Element[J/OL]. Proceedings of the National Academy of Science, 16(7): 511-520. DOI: 10.1073/pnas.16.7.511.

Tomsick J, COSI Collaboration. 2022. The Compton Spectrometer and Imager Project for MeV Astronomy[C/OL]//37th International Cosmic Ray Conference. 652. DOI: 10.22323/1.395.0652.

Trakhtenbrot B, Arcavi I, MacLeod C L, et al. 2019. 1ES 1927+654: An AGN Caught Changing Look on a Timescale of Months[J/OL]. Astrophys. J., 883(1): 94. DOI: 10.3847/1538-4357/ab39e4.

Trani A A, Quaini S, Colpi M. 2024. Three-body encounters in black hole discs around a supermassive black hole. The disc velocity dispersion and the Keplerian tidal field determine the eccentricity and spin-orbit alignment of gravitational wave mergers[J/OL]. Astron. Astrophys., 683: A135. DOI: 10.1051/0004-6361/202347920.

Tursunov A, Dadhich N. 2019. Fifty Years of Energy Extraction from Rotating Black Hole: Revisiting Magnetic Penrose Process[J/OL]. Universe, 5(5): 125. DOI: 10.3390/universe5050125.

Ueda Y, Akiyama M, Ohta K, et al. 2003. Cosmological Evolution of the Hard X-Ray Active Galactic Nucleus Luminosity Function and the Origin of the Hard X-Ray Background[J/OL]. Astrophys. J., 598(2): 886-908. DOI: 10.1086/378940.

Ushomirsky G, Cutler C, Bildsten L. 2000. Deformations of accreting neutron star crusts and gravitational wave emission[J/OL]. Mon. Not. R. Astron. Soc., 319(3): 902-932. DOI:

10.1046/j.1365-8711.2000.03938.x.

Veres P M, Franckowiak A, van Velzen S, et al. 2024. Back from the dead: AT2019aalc as a candidate repeating TDE in an AGN[A/OL]. arXiv:2408.17419. arXiv: 2408.17419.

Verner D A, Ferland G J, Korista K T, et al. 1996. Atomic Data for Astrophysics. II. New Analytic Fits for Photoionization Cross Sections of Atoms and Ions[J/OL]. Astrophys. J., 465: 487. DOI: 10.1086/177435.

Veronesi N, Rossi E M, van Velzen S, et al. 2022. Detectability of a spatial correlation between stellar mass black hole mergers and active galactic nuclei in the local Universe[J/OL]. Mon. Not. R. Astron. Soc., 514(2): 2092-2097. DOI: 10.1093/mnras/stac1346.

Veronesi N, Rossi E M, van Velzen S. 2023. The most luminous AGN do not produce the majority of the detected stellar-mass black hole binary mergers in the local Universe[J/OL]. Mon. Not. R. Astron. Soc., 526(4): 6031-6040. DOI: 10.1093/mnras/stad3157.

Veronesi N, van Velzen S, Rossi E M, et al. 2025. Constraining the AGN formation channel for detected black hole binary mergers up to z = 1.5 with the Quaia catalogue[J/OL]. Mon. Not. R. Astron. Soc., 536(1): 375-386. DOI: 10.1093/mnras/stae2575.

Vick M, Lai D. 2019. Tidal effects in eccentric coalescing neutron star binaries[J/OL]. Phys. Rev. D, 100(6): 063001. DOI: 10.1103/PhysRevD.100.063001.

Vijaykumar A, Kapadia S J, Ajith P. 2022. Can a binary neutron star merger in the vicinity of a supermassive black hole enable a detection of a post-merger gravitational wave signal?[J/OL]. Mon. Not. R. Astron. Soc., 513(3): 3577-3586. DOI: 10.1093/mnras/stac1131.

von Fellenberg S D, Gillessen S, Stadler J, et al. 2022. The Young Stars in the Galactic Center [J/OL]. Astrophys. J. Lett., 932(1): L6. DOI: 10.3847/2041-8213/ac68ef.

Wagoner R V. 1984. Gravitational radiation from accreting neutron stars[J/OL]. Astrophys. J., 278: 345-348. DOI: 10.1086/161798.

Wald R M. 1974. Energy Limits on the Penrose Process[J/OL]. Astrophys. J., 191: 231-234. DOI: 10.1086/152959.

Wang B, Han Z. 2012. Progenitors of type Ia supernovae[J/OL]. New Astron. Rev., 56(4): 122-141. DOI: 10.1016/j.newar.2012.04.001.

Wang B, Liu D. 2020a. The formation of neutron star systems through accretion-induced collapse in white-dwarf binaries[J/OL]. Research in Astronomy and Astrophysics, 20(9): 135. DOI: 10.1088/1674-4527/20/9/135.

Wang J M, Liu J R, Ho L C, et al. 2021a. Accretion-modified Stars in Accretion Disks of Active Galactic Nuclei: Slowly Transient Appearance[J/OL]. Astrophys. J. Lett., 911(1): L14. DOI: 10.3847/2041-8213/abee81.

Wang J M, Liu J R, Ho L C, et al. 2021b. Accretion-modified Stars in Accretion Disks of Active

Galactic Nuclei: Gravitational-wave Bursts and Electromagnetic Counterparts from Merging Stellar Black Hole Binaries[J/OL]. Astrophys. J. Lett., 916(2): L17. DOI: 10.3847/2041-8213/ac0b46.

Wang J M, Zhai S, Li Y R, et al. 2023a. Star Formation in Self-gravitating Disks in Active Galactic Nuclei. III. Efficient Production of Iron and Infrared Spectral Energy Distributions[J/OL]. Astrophys. J., 954(1): 84. DOI: 10.3847/1538-4357/acdf48.

Wang J S, Lai D. 2020b. Evolution of inspiralling neutron star binaries: Effects of tidal interactions and orbital eccentricities[J/OL]. Phys. Rev. D, 102(8): 083005. DOI: 10.1103/PhysRevD.102.083005.

Wang M, Ma Y, Wu Q. 2023b. Accretion-modified stellar-mass black hole distribution and milli-Hz gravitational wave backgrounds from galaxy centre[J/OL]. Mon. Not. R. Astron. Soc., 520(3): 4502-4516. DOI: 10.1093/mnras/stad422.

Wang T, Liu G, Cai Z, et al. 2023c. Science with the 2.5-meter Wide Field Survey Telescope (WFST)[J/OL]. Science China Physics, Mechanics, and Astronomy, 66(10): 109512. DOI: 10.1007/s11433-023-2197-5.

Wang Y L, Wen S X, Wang W X, et al. 2024a. LIGO/Virgo/KAGRA S241125n: EP-FXT follow-up observations[J]. GRB Coordinates Network, 38345: 1.

Wang Y H, Lazzati D, Perna R. 2022. The emergence of diffused gamma-ray burst afterglows from the discs of active galactic nuclei[J/OL]. Mon. Not. R. Astron. Soc., 516(4): 5935-5944. DOI: 10.1093/mnras/stac1968.

Wang Y, Lin D N C, Zhang B, et al. 2024b. Changing-look Active Galactic Nuclei Behavior Induced by Disk-captured Tidal Disruption Events[J/OL]. Astrophys. J. Lett., 962(1): L7. DOI: 10.3847/2041-8213/ad20e5.

Warner C, Hamann F, Dietrich M. 2003. A Relation between Supermassive Black Hole Mass and Quasar Metallicity?[J/OL]. Astrophys. J., 596(1): 72-84. DOI: 10.1086/377710.

Watson A M, Antier S, Basa S, et al. 2024. LIGO/Virgo/KAGRA S241125n: COLIBRÍ Upper Limits on a Optical Counterpart at the BAT Position[J]. GRB Coordinates Network, 38317: 1.

Watts A L, Krishnan B, Bildsten L, et al. 2008. Detecting gravitational wave emission from the known accreting neutron stars[J/OL]. Mon. Not. R. Astron. Soc., 389(2): 839-868. DOI: 10.1111/j.1365-2966.2008.13594.x.

Weaver R, McCray R, Castor J, et al. 1977. Interstellar bubbles. II. Structure and evolution.[J/OL]. Astrophys. J., 218: 377-395. DOI: 10.1086/155692.

Webbink R F. 1984. Double white dwarfs as progenitors of R Coronae Borealis stars and type I supernovae.[J/OL]. Astrophys. J., 277: 355-360. DOI: 10.1086/161701.

Whelan J, Iben J, Icko. 1973. Binaries and Supernovae of Type I[J/OL]. Astrophys. J., 186: 1007-1014. DOI: 10.1086/152565.

Willingale R, Mészáros P. 2017. Gamma-Ray Bursts and Fast Transients. Multi-wavelength Observations and Multi-messenger Signals[J/OL]. Space Science Reviews, 207(1-4): 63-86. DOI: 10.1007/s11214-017-0366-4.

Wilms J, Allen A, McCray R. 2000. On the Absorption of X-Rays in the Interstellar Medium[J/OL]. Astrophys. J., 542(2): 914-924. DOI: 10.1086/317016.

Wilson J R, Mathews G J. 2004. White Dwarfs near Black Holes: A New Paradigm for Type I Supernovae[J/OL]. Astrophys. J., 610(1): 368-377. DOI: 10.1086/421449.

Wright E L, Eisenhardt P R M, Mainzer A K, et al. 2010. The Wide-field Infrared Survey Explorer (WISE): Mission Description and Initial On-orbit Performance[J/OL]. Astron. J., 140 (6): 1868-1881. DOI: 10.1088/0004-6256/140/6/1868.

Wu W B, Gu W M, Sun M. 2022. Thermal Equilibrium Solutions of Black Hole Accretion Flows: Outflows versus Advection[J/OL]. Astrophys. J., 930(2): 108. DOI: 10.3847/1538-4357/ac6588.

Xin C, Ryu T, Wang Y, et al. 2023. “Tidal-Peeling Events”: low-eccentricity tidal disruption of a star by a stellar mass black hole in the AGN disk[C]//AAS/High Energy Astrophysics Division: Vol. 20 AAS/High Energy Astrophysics Division. 406.02.

Xue L, Tagawa H, Haiman Z, et al. 2025. What Determines the Maximum Mass of AGN-assisted Black Hole Mergers?[A]. arXiv:2504.19570. arXiv: 2504.19570.

Yang Y, Bartos I, Haiman Z, et al. 2019. AGN Disks Harden the Mass Distribution of Stellar-mass Binary Black Hole Mergers[J/OL]. Astrophys. J., 876(2): 122. DOI: 10.3847/1538-4357/ab16e3.

Yang Y, Gayathri V, Bartos I, et al. 2020. Black Hole Formation in the Lower Mass Gap through Mergers and Accretion in AGN Disks[J/OL]. Astrophys. J. Lett., 901(2): L34. DOI: 10.3847/2041-8213/abb940.

Yang Y, Bartos I, Fragione G, et al. 2022. Tidal Disruption on Stellar-mass Black Holes in Active Galactic Nuclei[J/OL]. Astrophys. J. Lett., 933(2): L28. DOI: 10.3847/2041-8213/ac7c0b.

York D G, Adelman J, Anderson J E, Jr., et al. 2000. The Sloan Digital Sky Survey: Technical Summary[J/OL]. Astron. J., 120(3): 1579-1587. DOI: 10.1086/301513.

Yuan C, Murase K, Guetta D, et al. 2022. GeV Signatures of Short Gamma-Ray Bursts in Active Galactic Nuclei[J/OL]. Astrophys. J., 932(2): 80. DOI: 10.3847/1538-4357/ac6ddf.

Zaslavskii O B. 2022. Confined Penrose process and black-hole bomb[J/OL]. Phys. Rev. D, 106 (2): 024037. DOI: 10.1103/PhysRevD.106.024037.

Zaslavskii O B. 2023. General properties of the Penrose process with neutral particles in the equatorial plane[A/OL]. arXiv:2307.06469. arXiv: 2307.06469.

Zhang B. 2019. Charged Compact Binary Coalescence Signal and Electromagnetic Counterpart of Plunging Black Hole-Neutron Star Mergers[J/OL]. Astrophys. J. Lett., 873(2): L9. DOI: 10.3847/2041-8213/ab0ae8.

Zhang C, Wu Q, Fan X, et al. 2025a. The Composite Spectrum of the Little Red Dots from an Inner Standard Disk and an Outer Gravitationally Unstable Disk[A/OL]. arXiv:2505.12719. arXiv: 2505.12719.

Zhang H H, Zhu J P, Yu Y W. 2024a. Propagation of Gamma-Ray Burst Relativistic Jets in Active Galactic Nucleus Disks and Its Implication for Gamma-Ray Burst Detection[J/OL]. Astrophys. J., 976(1): 63. DOI: 10.3847/1538-4357/ad8139.

Zhang S R, Rueda Hernandez J A, Negreiros R. 2025b. Can the Central Compact Object in HESS J1731–347 Be Indeed the Lightest Neutron Star Observed?[J/OL]. Astrophys. J., 978(1): 1. DOI: 10.3847/1538-4357/ad96b5.

Zhang S R. 2023. The Transformation of the Rotational Energy of an Accreting Kerr Black Hole [J/OL]. Astronomy Reports, 67: S97-S101. DOI: 10.1134/S1063772923140202.

Zhang S R, Prakapenia M. 2024b. The transformation of the rotational energy of a Kerr black hole [J/OL]. Classical and Quantum Gravity, 41(13): 135019. DOI: 10.1088/1361-6382/ad51c2.

Zhang S R, Luo Y, Wu X J, et al. 2023. Electromagnetic signatures of white dwarf collisions in AGN discs[J/OL]. Mon. Not. R. Astron. Soc., 524(1): 940-951. DOI: 10.1093/mnras/stad1855.

Zhang S R, Yuan Y F, Wang J M, et al. 2024c. Neutron star accretion events in AGN discs: mutimessenger implications[J/OL]. Mon. Not. R. Astron. Soc., 532(2): 1330-1344. DOI: 10.1093/mnras/stae1546.

Zhou Z H, Zhu J P, Wang K. 2023. High-energy Neutrino Production from AGN Disk Transients Impacted by the Circum-disk Medium[J/OL]. Astrophys. J., 951(1): 74. DOI: 10.3847/1538-4357/acd380.

Zhu J P. 2024. High-energy neutrinos from merging stellar-mass black holes in active galactic nuclei accretion disc[J/OL]. Mon. Not. R. Astron. Soc., 528(1): L88-L95. DOI: 10.1093/mnrasl/slad176.

Zhu J P, Wang K, Zhang B. 2021a. High-energy Neutrinos from Stellar Explosions in Active Galactic Nuclei Accretion Disks[J/OL]. Astrophys. J. Lett., 917(2): L28. DOI: 10.3847/2041-8213/ac1a17.

Zhu J P, Wang K, Zhang B, et al. 2021b. High-energy Neutrinos from Choked Gamma-Ray Bursts in Active Galactic Nucleus Accretion Disks[J/OL]. Astrophys. J. Lett., 911(2): L19. DOI: 10.3847/2041-8213/abf2c3.

Zhu J P, Yang Y P, Zhang B, et al. 2021c. Thermonuclear Explosions and Accretion-induced Collapses of White Dwarfs in Active Galactic Nucleus Accretion Disks[J/OL]. Astrophys. J. Lett., 914(1): L19. DOI: 10.3847/2041-8213/abff5a.

Zhu J P, Zhang B, Yu Y W, et al. 2021d. Neutron Star Mergers in Active Galactic Nucleus Accretion Disks: Cocoon and Ejecta Shock Breakouts[J/OL]. Astrophys. J. Lett., 906(2): L11. DOI: 10.3847/2041-8213/abd412.

Appendix A Particle Decaying in Kerr Spacetime

A.1 Kerr Metric and Effective Potential

In this Appendix, explicit formulas for quantities relevant to describing the Penrose process in Kerr spacetime are provided. In Boyer-Lindquist coordinates Boyer et al. (1967) and units where G = c = 1, the Kerr metric takes the form

$$
\begin{aligned}
ds^2 &= g_{\alpha\beta} dx^\alpha dx^\beta \\
&= -\left(1 = \frac{2Mr}{\Sigma}\right) dt^2 - \frac{4Mar\sin^2\theta}{\Sigma} dt d\phi + \frac{\Sigma}{\Delta} dr^2 + \Sigma d\theta^2 + \frac{A}{\Sigma}\sin^2\theta d\phi^2
\end{aligned}
\tag{A.1}
$$

where M is the mass of the BH, $\hat{a} \equiv a/M = J/M^2$ is its dimensionless spin, and

$$
\begin{aligned}
\Sigma &\equiv r^2 + a^2\cos^2\theta, \\
\Delta &\equiv a^2 + r^2 - 2Mr, \\
A &= \left(r^2 + a^2\right)^2 - \Delta a^2 \sin^2\theta.
\end{aligned}
\tag{A.2}
$$

For a test particle, the four-momentum is

$$
p^\alpha \equiv dx^\alpha/d\lambda = \left(\frac{dt}{d\lambda}, \frac{dr}{d\lambda}, \frac{d\theta}{d\lambda}, \frac{d\phi}{d\lambda}\right)
\tag{A.3}
$$

where λ is an affine parameter. The existence of a conserved energy, a conserved angular momentum, and a conserved rest mass of the particle

$$
\begin{aligned}
E &= -p_t, \\
L_z &= p_\phi, \\
\mu &= \left(-p^\alpha p_\alpha\right)^{\frac{1}{2}}.
\end{aligned}
\tag{A.4}
$$

Dimensionless quantities can be introduced for convenience: $\hat{r} = r/M$, $\hat{a} = a/M$ and for massive particles additionally have the constants of motion: $\hat{E} = E/\mu$, $\hat{p}_\phi = p_\phi/M/\mu$. The ergosphere is maximal in the equatorial plane; therefore, the decay of a particle falling onto the BH in the equatorial plane is considered.

The motion of a particle (both mass particle and massless particle) in the equatorial plane of Kerr BH is governed by effective potential, which is given by

$$
V(r) = \frac{\beta \pm \sqrt{\beta^2 - \alpha\gamma_0}}{\alpha},
\tag{A.5}
$$

where α, β and γ_0 given by

$$\alpha = \left(r^2 + a^2\right)^2 - \Delta a > 0 \tag{A.6}$$
$$\beta = 2Mrap_\phi$$
$$\gamma_0 = (r^2 - 2Mr)p_\phi^2 - \mu^2 r^2 \Delta.$$

Only the positive sign solution is considered in this paper. The allowed regions for a particle of E are the regions with $V \leqslant E$, and the turning points occur where $V = E$ Misner et al. (1973).

For massive particle,

$$\frac{V}{\mu} = \frac{2\hat{a}\hat{p}_\phi + \sqrt{\hat{r}\left[\hat{a}^2 + \hat{r}\left(\hat{r}-2\right)\right]\left(\hat{p}_\phi^2\hat{r} + \left[\hat{r}^3 + \hat{a}^2\left(2+\hat{r}\right)\right]\right)}}{\hat{r}^3 + \hat{a}^2\left(\hat{r}+2\right)}, \tag{A.7}$$

when $r \to r_+$, $\frac{V}{\mu} \to \frac{\hat{a}\hat{p}_\phi}{2+2\sqrt{1-\hat{a}^2}}$ where $r_+ = M + \sqrt{M^2 - a^2}$ is the radius of the outer horizon. Thus, we have that $\hat{E} > \frac{\hat{a}\hat{p}_\phi}{2+2\sqrt{1-\hat{a}^2}}$ for $\hat{r} > \hat{r}^+$. For the extreme Kerr BH ($a = M$),

$$\frac{V}{\mu} = \frac{2\hat{p}_\phi + (\hat{r}-1)\sqrt{\hat{r}\left(\hat{r}^3 + \hat{r} + 2\right) + \hat{p}_\phi^2\hat{r}^2}}{\hat{r}^3 + \hat{r} + 2}, \tag{A.8}$$

when $\frac{r}{M} \to 1$, $\frac{V}{\mu} \to \frac{\hat{p}_\phi}{2}$. Thus, we have that $\hat{E} > \frac{\hat{p}_\phi}{2}$ for $\hat{r} > \hat{r}^+ = 1$.

For massless particle,

$$V = \frac{2\hat{a}\frac{p_\phi}{M} + \hat{r}\sqrt{\left[\hat{a}^2 + \hat{r}\left(\hat{r}-2\right)\right]\frac{p_\phi^2}{M^2}}}{\hat{r}^3 + \hat{a}^2\left(\hat{r}+2\right)}, \tag{A.9}$$

when $r \to r_+$, $V \to \frac{\hat{a}\frac{p_\phi}{M}}{2+2\sqrt{1-\hat{a}^2}}$. Thus, we have that $E > \frac{\hat{a}\frac{p_\phi}{M}}{2+2\sqrt{1-\hat{a}^2}}$ for $\hat{r} > \hat{r}^+$. For the extreme Kerr BH,

$$V = \frac{\frac{2p_\phi}{M} + \hat{r}\left(\hat{r}-1\right)\sqrt{\frac{p_\phi^2}{M^2}}}{\hat{r}^3 + \hat{r} + 2}, \tag{A.10}$$

when $\frac{r}{M} \to 1$, $V \to \frac{p_\phi}{2M}$. Thus, have that $E > \frac{p_\phi}{2M}$ for $\hat{r} > \hat{r}^+ = 1$.

A.2 Particle Decaying Processes

We can imagine that test particle "1" was created by the decay of particle "0" at some turning point in the ergosphere of Kerr BH when particle "1" goes into the horizont and particle "2" goes out to infinity (Penrose process). Since the minimum energy of a particle is achieved when $p_r = p_\theta = 0$ Misner et al. (1973), we only analyze the decay of a particle at the turning point.

For any given

$$\hat{r}\ :\ \hat{r}_+ < \hat{r} < 2 \tag{A.11a}$$

$$E_1 < 0,\ \ p_{\phi 1} < 0\ :\ E_1 > \frac{\hat{a}\frac{p_{\phi 1}}{M}}{2 + 2\sqrt{1-\hat{a}^2}}. \tag{A.11b}$$

$$\mu_0,\ \ \mu_1,\ \ \mu_2\ :\ \mu_0 > \mu_1 + \mu_2, \tag{A.11c}$$

one can always find the corresponding positive values

$$\hat{E}_0,\ \ \hat{p}_{\phi 0},\ \ \hat{E}_2,\ \ \hat{p}_{\phi 2} \tag{A.12}$$

from the following set of equations:

$$\hat{p}_{r0} = 0, \tag{A.13a}$$

$$\mu_0 \hat{E}_0 = E_1 + \mu_2 \hat{E}_2, \tag{A.13b}$$

$$\mu_0 \hat{p}_{\phi 0} = p_{\phi 1} + \mu_2 \hat{p}_{\phi 2}, \tag{A.13c}$$

$$\mu_0 \hat{p}_{r0} = p_{r1} + \mu_2 \hat{p}_{r2}, \tag{A.13d}$$

where

$$\hat{p}_{r0} = \left\{ (\hat{E}_0^2 - 1)\hat{r}^3 + 2\hat{r}^2 + \left[\hat{a}^2(\hat{E}_0^2 - 1) - \hat{p}_{\phi 0}^2\right]\hat{r} + 2(\hat{a}\hat{E}_0 - \hat{p}_{\phi 0})^2 \right\}^{1/2}, \tag{A.14}$$

$$\hat{p}_{r2} = \left\{ (\hat{E}_2^2 - 1)\hat{r}^3 + 2\hat{r}^2 + \left[\hat{a}(\hat{E}_2^2 - 1) - \hat{p}_{\phi 2}^2\right]\hat{r} + 2(\hat{a}\hat{E}_2 - \hat{p}_{\phi 2})^2 \right\}^{1/2}. \tag{A.15}$$

And the explicit expression of p_{r1} depends on whether particle "1" has mass or not. For massive particle "1", conserved quantities can be expressed in a dimensionless form and

$$\hat{p}_{r1} = -\left\{ (\hat{E}_1^2 - 1)\hat{r}^3 + 2\hat{r}^2 + \left[\hat{a}(\hat{E}_1^2 - 1) - \hat{p}_{\phi 1}^2\right]\hat{r} + 2(\hat{a}\hat{E}_1 - \hat{p}_{\phi 1})^2 \right\}^{1/2}. \tag{A.16}$$

For massless particle "1", conserved quantities can't be expressed in a dimensionless form and

$$p_{r1} = -[E_1^2\hat{r}^3 + (\hat{a}^2E_1^2 - \frac{p_{\phi_1}^2}{M^2})\hat{r} + 2(\hat{a}E_1 - \frac{p_{\phi_1}}{M})^2]^{1/2}. \tag{A.17}$$

Eq. (A.26a) guarantees that the particle "0" decays at the turning point (see example Fig. 2.7), Eqs. (A.26b)–(A.26d) represents the conservation of energy, angular momentum, and radial momentum.

Furthermore, it is essential to note the following: 1) if we assume that the particle "1" is also generated at the turning point, we have $p_{r1} = 0$, and as a consequence, $\hat{p}_{r2} = 0$; 2) if particle "2" is massless, the physical quantity related to particle "2" should not be expressed as a dimensionless quantity, similar to the physical quantity associated with particle "1".

A.3 The Formalism of Energy Conservation During Particle Decay in the Kerr Spacetime

A.3.1 The Formula for the Relative Velocity of Two Particles

Here we will show a concise formula for the relative velocity of two particles in terms of the four-velocity of the two particles in curve spacetime. It is useful in many physical scenarios, including verify the energy conservation of the Penrose process.

Consider the collision or fission of two particles. Namely, let the masses of the two particles be m_1 and m_2, located at the same spacetime point but with different four-velocities u_1 and u_2. The four-momentum of each particle can be expressed as:

$$p_1^\alpha = m_1 u_1^\alpha, \quad p_2^\alpha = m_2 u_2^\alpha. \tag{A.18}$$

Thus, the total four-momentum of the two particles is:

$$(p_{\rm tot})^\alpha = p_1^\alpha + p_2^\alpha = m_1 u_1^\alpha + m_2 u_2^\alpha. \tag{A.19}$$

The center-of-mass energy of the two particles $E_{\rm cm}$ is then given by (e.g., Harada et al., 2011):

$$E_{\rm cm}^2 = -(p_{\rm tot})^\alpha (p_{\rm tot})_\alpha = m_1^2 + m_2^2 - 2m_1 m_2\, g_{\alpha\beta} u_1^\alpha u_2^\beta. \tag{A.20}$$

On the other hand, consider the local reference frame in which particle 1 is at rest. In this frame, the four-velocities of particle 1 and particle 2 are given by:

$$u_1 = (1, 0, 0, 0), \quad u_2 = (\gamma_{\rm r}, \gamma_{\rm r} \mathbf{v}_{\rm r}) \tag{A.21}$$

where $\gamma_{\rm r} = \frac{1}{\sqrt{1-v_{\rm r}^2}}$ is the relative gamma factor between the two particles. The center-of-mass energy of the two particles is then:

$$E_{\rm cm}^2 = m_1^2 + m_2^2 + 2m_1 m_2 \gamma_{\rm r} \tag{A.22}$$

When $\gamma_{\mathrm{r}} = 1$, i.e., when there is no relative velocity between the two particles, the expression is simplified to the obvious form:

$$E_{\mathrm{cm}} = m_1 + m_2 \tag{A.23}$$

It is worth noting that the center-of-mass energy of the two particles (collision or fission) is determined solely by their masses and relative velocity, regardless of the spacetime property and the reference frame used. Therefore, Equation (A.22) is always satisfy and equivalent to Equation (A.20). By comparing the right-hand sides of these two equations, an important identity is obtained.:

$$-g_{\alpha\beta} u_1^\alpha u_2^\beta = \gamma_{\mathrm{r}} = \frac{1}{\sqrt{1 - v_{\mathrm{r}}^2}}. \tag{A.24}$$

If the two particles have no relative velocity, $u_1 = u_2 = u$, the above equation is simplified to the well-known four-velocity normalization equation:

$$-g_{\alpha\beta} u^\alpha u^\beta = 1. \tag{A.25}$$

A.3.2 Energy Conservation During Particle Fission in Kerr Spacetime

In Kerr spacetime, when particle 0 (with mass m_0) decays into particle 1 (with mass m_1) and particle 2 (with mass m_2), momentum conservation in each direction must be satisfied, i.e.,

$$p_{\mathrm{t}0} = p_{\mathrm{t}1} + p_{\mathrm{t}2}, \tag{A.26a}$$

$$p_{\mathrm{r}0} = p_{\mathrm{r}1} + p_{\mathrm{r}2}, \tag{A.26b}$$

$$p_{\theta 0} = p_{\theta 1} + p_{\theta 2}, \tag{A.26c}$$

$$p_{\phi 0} = p_{\phi 1} + p_{\phi 2}, \tag{A.26d}$$

where $p_{\alpha i}$ represents the α component of four-momentum of particle i (i=0, 1, and 2). In this process, we want to verify that the sum of the two masses $m_1 + m_2$ is necessarily less than m_0; and the mass loss is converted into kinetic energy in the center-of-mass frame. Namely, we want to verify:

$$m_0 = m_1 \gamma_{01} + m_2 \gamma_{02}, \tag{A.27}$$

where γ_{01} is relative gamma factor between particle 0 and 1, and γ_{02} is relative gamma factor between particle 0 and 2. If $m_0 > m_1 + m_2$, then we naturally have $\gamma_{01}, \gamma_{02} > 1$, indicating that the two particles have a relative velocity and separate.

Using the previously derived Equation (A.24), the right-hand side of Equation (A.27) can be written as:

$$m_1\gamma_{01} + m_2\gamma_{02} = -g_{\alpha\beta}\left(m_1 u_0^\alpha u_1^\beta + m_2 u_0^\alpha u_2^\beta\right). \tag{A.28}$$

Note that u_{i}^{α} represents the four-velocity of the particle i, which is expressed in terms of the conserved quantities of the particle's motion. Similarly, the momenta of the particles in each direction in Equation (A.26) can also be expressed in terms of the conserved quantities of the particle's motion. Thus, substituting Equation (A.26) into the right-hand side of Equation (A.28), after a lengthy but straightforward calculation, the right-hand side of Equation (A.28) is found to equal m_0, i.e.,

$$-g_{\alpha\beta}\left(m_1 u_0^\alpha u_1^\beta + m_2 u_0^\alpha u_2^\beta\right) = m_0, \tag{A.29}$$

where $g_{\square\square}$ is the Kerr metric. Therefore, we have proved that Equation (A.27) holds generally in Kerr spacetime.

Moreover, it is straightforward to extend the above results to a more general case, where particle 0 decays into N particles ($N \geqslant 2$). The corresponding momentum conservation equations for each direction thus are:

$$p_{\alpha 0} = \sum_{i=1}^{N} p_{\alpha i} \text{ (, where } \alpha = t, r, \theta, \phi). \tag{A.30}$$

The corresponding formula (A.27) generalizes to:

$$m_0 = \sum_{i=1}^{N} m_i \gamma_{0i}, \tag{A.31}$$

where γ_{0i} is relative gamma factor between particle 0 and i, and it satisfies the Equation (A.24) in any curve spacetime. Additionally, at least

$$\begin{cases} N-1, & N > 2 \\ 2, & N = 2 \end{cases} \tag{A.32}$$

of these relative gamma factors are strictly lager than 1. In other words, at most one of the decay particles can follow the trajectory of particle 0, thus the corresponding relative gamma factor equals 1. Of course, any two of the decay particles must have a relative velocity (i.e., $\gamma_{ij} > 1$, where $i, j \geqslant 1$ & $i \neq j$) to ensure that the N particles are separated from each other.

A.3.3 Summary

We verified during particle decay in Kerr spacetime (e.g., Penrose process), the sum of the two masses, $m_1 + m_2$, cannot be equal to the initial particle mass m_0 in this process. If the masses remain equal, the solution of trajectories of m_1 and m_2 always coincide, and they do not separate, meaning that these two particles never have a relative velocity. From a physical perspective, mass loss is necessary to generate kinetic energy in the center of the mass frame, allowing the two particles to have a relative velocity and separate.

Acknowledgements

I am acknowledge the Joint International Relativistic Astrophysics Doctorate Program and support from the China Scholarship Council (CSC No. 202206340085).

During my PhD study, I have had the privilege of meeting many excellent mentors and friends. First and foremost, I would like to express my heartfelt gratitude to my three supervisors: Prof. Ye-Fei Yuan, Prof. Remo Ruffini, and Prof. Jorge Rueda. They not only guided me onto the right research path and imparted fundamental knowledge in relativistic astrophysics, but also taught me how to identify meaningful scientific problems. Their integrity, dedication to science, and pursuit of knowledge will remain a lifelong inspiration to me.

I am grateful to USTC for providing a supportive and vibrant academic environment. I would like to express my sincere gratitude to Prof. Tinggui Wang, Prof. Junxian Wang, Prof. Yongquan Xue, Prof. Fuzhen Cheng, Prof. Zigao Dai, Prof. Wen Zhao, Prof. Hongyan Zhou, Prof. Guilin Liu, Prof. Filipe Abdalla, Dr. Xuanbin Lin, and Dr. Qingfeng Zhu Dr. Xiaojun Wu, Dr. Xianger Fang, Dr. Rajiv Kumar, Dr. Zeyuan Tang, Dr. Tianle Zhao, Dr. Yan Luo, Dongfang Bai, Changxiang Mao, Yuan Feng, Jiahao Hou, Yewen Yang, Shunyao Han, Fanqi Zheng, Yiming Hu, Bowen Xu, Prof. Jian Li, Prof. Fei Yan, Shan Lu, Nan Zhou, and Weiran Xing from the Department of Astronomy of USTC.

I am grateful to ICRANet and the UNIFE for offering platforms that allowed me to engage, both formally and informally, with scientists from around the world. I also wish to thank Prof. Shesheng Xue, Prof. Yu Wang, and Prof. Liang Li; Prof. Rahim Moradi and Prof. Gregory; as well as Elisabetta, Cinzia, and Silvia at ICRANet, whose assistance with administrative matters spared me the burden of distractions outside research. My sincere thanks also go to Prof. Rosati, Prof. Guidorzi, Prof. Bulla, and to my colleagues Lisa, Lorenzo, Alice, Riccardo, Salvatore, Giorgia, Romain, Manuele, and Jin at UNIFE, for their valuable scientific discussions and daily support. There are many others who deserve my gratitude; any omissions are unintentional, and I kindly ask for your understanding.

Finally, I am indebted to all my collaborators for their insightful suggestions and guidance in my research, to the referees for carefully reviewing my thesis and providing constructive feedback, and to my family and friends for their unwavering support.

Research Achievements

Journal Articles

1. **S.-R. Zhang**, Y. Luo, X.-J. Wu, J.-M. Wang, L. C. Ho, and Y.-F. Yuan, "Electromagnetic signatures of white dwarf collisions in AGN discs," MNRAS, vol. 524, no. 1, pp. 940–951, Sep. 2023.DOI: 10.1093/mnras/stad1855.
2. **S.-R. Zhang**, Y.-F.Yuan, J.-M. Wang, and L. C. Ho, "Neutron star accretion events in AGN discs: mutimessenger implications," MNRAS, vol. 532, no. 2, pp. 1330–1344, Aug. 2024. DOI: 10.1093/mnras/stae1546.
3. **S.-R. Zhang**, Y. Wang, Y.-F.Yuan, et al., "S241125n: Binary Black Hole Merger Produces Short GRB in AGN Disk," ArXiv e-prints, May 2025 (Submitted). arXiv:2505.10395 [astro-ph].
4. **S.-R. Zhang** and M. Prakapenia, "The transformation of the rotational energy of a Kerr black hole," CQG, vol. 41, no. 13, 135019, p. 135019, Jul. 2024. DOI: 10.1088/1361-6382/ad51c2.
5. **S.-R. Zhang**, J.A. Rueda, and R. Negreiros, "Can the central compact object in hess j1731−347 be indeed the lightest neutron star observed?," ApJ, vol. 978, no. 1, p. 1, 2024. DOI: 10.3847/1538-4357/ad96b5.
6. Y. Luo, X.-J. Wu, **S.-R. Zhang**, J.-M. Wang, L. C. Ho, and Y.-F. Yuan, "White dwarf-white dwarf collisions in AGN discs via close encounters," MNRAS, vol. 524, no. 4, pp. 6015–6023, Oct. 2023. DOI: 10.1093/mnras/stad2188.
7. Y. Aimuratov, L.M. Becerra, C.L. Bianco, ..., and **S.-R. Zhang**, "GRB-SN Association within the Binary-driven Hypernova Model," ApJ, vol. 955, no. 2, 93, p. 93, Oct. 2023. DOI: 10.3847/1538-4357/ace721.
8. C.L. Bianco, M.T. Mirtorabi, R. Moradi, ..., and **S.-R. Zhang**, "Probing Electromagnetic Gravitational-wave Emission Coincidence in a Type I Binary-driven Hypernova Family of Long Gamma-Ray Bursts at Very High Redshift," ApJ, vol. 966, no. 2, 219, p. 219, May 2024. DOI: 10.3847/1538-4357/ad2fa9.
9. R. Ruffini, M. Prakapenia, H. Quevedo, and **S.-R. Zhang**, "Single versus the repetitive penrose process in a kerr black hole," PRL, vol. 134, p. 081403, 8 Feb. 2025. DOI: 10.1103/PhysRevLett.134.081403.
10. R. Ruffini, C.L. Bianco, M. Prakapenia, H. Quevedo, J.A. Rueda, and **S.-R. Zhang**, "Role of the irreducible mass in repetitive penrose energy extraction processes in a kerr black hole," PRR, vol. 7, p. 013203, 1 Feb. 2025. DOI:

10.1103/PhysRevResearch.7.013203.

Conference Proceedings

1. **S.-R. Zhang**, "The Transformation of the Rotational Energy of an Accreting Kerr Black Hole," in Proceedings of the Fifth Zeldovich meeting, Astron. Rep., vol. 67, Dec. 2023, S97–S101. DOI: 10.1134/S1063772923140202.